POLITECNICO DI TORINO
Repository ISTITUZIONALE

Optimization and Energy Maximizing Control Systems for Wave Energy Converters

Original
Optimization and Energy Maximizing Control Systems for Wave Energy Converters / Giorgi, Giuseppe; Sirigu, Sergej Antonello. - (2022). [10.3390/books978-3-0365-2825-0]

Availability:
This version is available at: 11583/2956476 since: 2022-02-27T10:59:58Z

Publisher:
Multidisciplinary Digital Publishing Institute

Published
DOI:10.3390/books978-3-0365-2825-0

Terms of use:

This article is made available under terms and conditions as specified in the corresponding bibliographic description in the repository

Publisher copyright

(Article begins on next page)

12 October 2024

Journal of
Marine Science
and Engineering

Optimization and Energy Maximizing Control Systems for Wave Energy Converters

Edited by
Giuseppe Giorgi and Sergej Antonello Sirigu

Printed Edition of the Special Issue Published in
Journal of Marine Science and Engineering

www.mdpi.com/journal/jmse

MDPI

Optimization and Energy Maximizing Control Systems for Wave Energy Converters

Optimization and Energy Maximizing Control Systems for Wave Energy Converters

Editors

Giuseppe Giorgi
Sergej Antonello Sirigu

MDPI • Basel • Beijing • Wuhan • Barcelona • Belgrade • Manchester • Tokyo • Cluj • Tianjin

Editors

Giuseppe Giorgi
Politecnico di Torino
Italy

Sergej Antonello Sirigu
Politecnico di Torino
Italy

Editorial Office
MDPI
St. Alban-Anlage 66
4052 Basel, Switzerland

This is a reprint of articles from the Special Issue published online in the open access journal *Journal of Marine Science and Engineering* (ISSN 2077-1312) (available at: https://www.mdpi.com/journal/jmse/special_issues/control_systems_wave_energy).

For citation purposes, cite each article independently as indicated on the article page online and as indicated below:

LastName, A.A.; LastName, B.B.; LastName, C.C. Article Title. *Journal Name* **Year**, *Volume Number*, Page Range.

ISBN 978-3-0365-2824-3 (Hbk)
ISBN 978-3-0365-2825-0 (PDF)

© 2021 by the authors. Articles in this book are Open Access and distributed under the Creative Commons Attribution (CC BY) license, which allows users to download, copy and build upon published articles, as long as the author and publisher are properly credited, which ensures maximum dissemination and a wider impact of our publications.
The book as a whole is distributed by MDPI under the terms and conditions of the Creative Commons license CC BY-NC-ND.

Contents

About the Editors . . . . . **vii**

Giuseppe Giorgi and Sergej Antonello Sirigu
Optimization and Energy Maximizing Control Systems for Wave Energy Converters
Reprinted from: *J. Mar. Sci. Eng.* **2021**, *9*, 1436, doi:10.3390/jmse9121436 . . . . . **1**

Sergej Antonello Sirigu, Ludovico Foglietta, Giuseppe Giorgi, Mauro Bonfanti, Giulia Cervelli, Giovanni Bracco and Giuliana Mattiazzo
Techno-Economic Optimisation for a Wave Energy Converter via Genetic Algorithm
Reprinted from: *J. Mar. Sci. Eng.* **2020**, *8*, 482, doi:10.3390/jmse8070482 . . . . . **5**

Marianna Giassi, Jens Engström, Jan Isberg and Malin Göteman
Comparison of Wave Energy Park Layouts by Experimental and Numerical Methods
Reprinted from: *J. Mar. Sci. Eng.* **2020**, *8*, 750, doi:10.3390/jmse8100750 . . . . . **35**

Demián García-Violini, Nicolás Faedo, Fernando Jaramillo-Lopez and John V. Ringwood
Simple Controllers for Wave Energy Devices Compared
Reprinted from: *J. Mar. Sci. Eng.* **2020**, *8*, 793, doi:10.3390/jmse8100793 . . . . . **59**

Josh Davidson and Tamás Kalmár-Nagy
A Real-Time Detection System for the Onset of Parametric Resonance in Wave Energy Converters
Reprinted from: *J. Mar. Sci. Eng.* **2020**, *8*, 819, doi:10.3390/jmse8100819 . . . . . **89**

Mauro Bonfanti, Andrew Hillis, Sergej Antonello Sirigu, Panagiotis Dafnakis, Giovanni Bracco, Giuliana Mattiazzo and Andrew Plummer
Real-Time Wave Excitation Forces Estimation: An Application on the ISWEC Device
Reprinted from: **2020**, *8*, 825, doi:10.3390/jmse8100825 . . . . . **113**

Enrico Anderlini, Gordon G. Parker and Giles Thomas
Towards Real-Time Reinforcement Learning Control of a Wave Energy Converter
Reprinted from: *J. Mar. Sci. Eng.* **2020**, *8*, 845, doi:10.3390/jmse8110845 . . . . . **143**

Alexis Mérigaud and Paolino Tona
Spectral Control of Wave Energy Converters with Non-Ideal Power Take-off Systems
Reprinted from: *J. Mar. Sci. Eng.* **2020**, *8*, 851, doi:10.3390/jmse8110851 . . . . . **159**

Jian Tan, Henk Polinder, Antonio Jarquin Laguna, Peter Wellens and Sape Miedema
The Influence of Sizing of Wave Energy Converters on the Techno-Economic Performance
Reprinted from: *J. Mar. Sci. Eng.* **2021**, *9*, 52, doi:10.3390/jmse9010052 . . . . . **175**

Mirko Previsic, Anantha Karthikeyan and Jeff Scruggs
A Comparative Study of Model Predictive Control and Optimal Causal Control for Heaving Point Absorbers
Reprinted from: *J. Mar. Sci. Eng.* **2021**, *9*, 805, doi:10.3390/jmse9080805 . . . . . **201**

Ali S. Haider, Ted K. A. Brekken and Alan McCall
Real-Time Nonlinear Model Predictive Controller for Multiple Degrees of Freedom Wave Energy Converters with Non-Ideal Power Take-Off
Reprinted from: *J. Mar. Sci. Eng.* **2021**, *9*, 890, doi:10.3390/jmse9080890 . . . . . **223**

Tania Demonte Gonzalez, Gordon G. Parker, Enrico Anderlini and Wayne W. Weaver
Sliding Mode Control of a Nonlinear Wave Energy Converter Model
Reprinted from: *J. Mar. Sci. Eng.* **2021**, *9*, 951, doi:10.3390/jmse9090951 . . . . . **241**

About the Editors

Giuseppe Giorgi, Ph.D., a research fellow, is currently working at the Marine Offshore Renewable Energy Lab (MOREnergy Lab) of Politecnico di Torino, Italy. He holds a Ph.D. in Engineering, obtained in the Centre for Ocean Energy Research (COER) of Maynooth University, Ireland, with major contributions in the nonlinear hydrodynamic modelling of wave energy conversion under controlled conditions. He is a Marie-Curie individual fellow alumni, working on computationally efficient nonlinear Froude–Krylov force calculation methods, applied to control and parametric resonance detection. His current research interests involve offshore renewable energy in general, numerical modelling and experimental testing.

Sergej Antonello Sirigu, Ph.D., a research fellow, is currently working at the Marine Offshore Renewable Energy Lab (MOREnergy Lab) of Politecnico di Torino, Italy. He holds a Ph.D. in Mechanical Engineering, with major contributions in design and testing of innovative wave energy converters, based on inertial coupling and resonance water tanks. His current research interests involve holistic techno-economic optimization based on genetic algorithms and evolutionary theory, as well as hardware-in-the-loop and wave tank experimental testing.

Journal of
Marine Science and Engineering

MDPI

Editorial

Optimization and Energy Maximizing Control Systems for Wave Energy Converters

Giuseppe Giorgi *and Sergej Antonello Sirigu

Marine Offshore Renewable Energy Lab (MOREnergy Lab), Department of Mechanical and Aerospace Engineering (DIMEAS), Politecnico di Torino, 10129 Turin, Italy; sergej.sirigu@polito.it
* Correspondence: giuseppe.giorgi@polito.it

In recent years, we have been witnessing great interest and activity in the field of wave energy converters' (WECs) development, striving for competitiveness and economic viability via increasing power conversion while decreasing costs and ensuring survivability. In the community, the consensus is that both optimization and control are sine qua non conditions for success, but many challenges, peculiar to WECs, need to be addressed. Unlike other traditional control applications, the control objective for WECs is to exaggerate the motion, potentially inducing strong nonlinearities in the system and stressing the power-conversion chain and mechanical structure. Therefore, it is crucial to include techno-economical constraints in both the optimization and control objective functions. Furthermore, although often considered as consecutive independent phases, optimization and control are mutually dependent and, ideally, should be considered together.

The book *Optimization and Energy Maximizing Control Systems for Wave Energy Converters* includes eleven contributions [1–11] to this Special Issue published during 2020–2021. The overall objective of this Special Issue is to draw the most updated picture of the heterogeneous challenges that still need to be addressed in the field of wave energy control and optimization, while also to gather novel and cutting-edge techniques and methods to advance the state-of-the-art. The scientific collection presented in this Special Issue will be valuable for both scientists and technology developers, since each paper within is moved by a bundle of theoretical and pragmatic spirits, with the objective of providing advanced and effective solutions to problems that are currently holding back the development of wave energy technologies.

From a critical analysis of the eleven different contributions of this special issue, it is possible to highlight four major connecting threads:

1. Conjunction of both technical and economic considerations to drive decision-making [1,2,8];
2. Inclusion of non-ideal power take-off (PTO) and nonlinear phenomena for the effectiveness of control strategies [4,7,10];
3. Real-time capabilities as a mandatory condition for applicability of estimation, detection, and control algorithms [3–6,10];
4. Various control strategies including all of the above [3,6,7,9–11].

Tan et al. [8] investigate the influence of the size of a heaving point absorber wave energy converter, considering the techno-economic impact of the resulting power take-off. An optimization method is proposed to reduce the Levelized Cost Of Energy (LCOE). The performance of the system is evaluated through a frequency domain model of the device considering three representative sea states for productivity assessment. In order to represent the effect of the PTO size on power production, PTO force constraints have been included in the model. A preliminary economic model is implemented to estimate costs and LCOE at an early development stage. A control-informed optimization is carried out, evaluating the influence of buoy geometry, PTO size, wave resource and control logic for LCOE reduction. The results show that, for this application, the main driver of LCOE is cost rather than productivity. In fact, smaller PTOs have lower productivity, but still

check for updates

Citation: Giuseppe, G.; Sirigu, S.A. Optimization and Energy Maximizing Control Systems for Wave Energy Converters. *J. Mar. Sci. Eng.* **2021**, *9*, 1436. https://doi.org/10.3390/jmse9121436

Received: 30 November 2021
Accepted: 14 December 2021
Published: 15 December 2021

Publisher's Note: MDPI stays neutral with regard to jurisdictional claims in published maps and institutional affiliations.

Copyright: © 2021 by the authors. Licensee MDPI, Basel, Switzerland. This article is an open access article distributed under the terms and conditions of the Creative Commons Attribution (CC BY) license (https://creativecommons.org/licenses/by/4.0/).

achieve an LCOE reduction of 24% to 31%. It is also interesting to note that wave resource and PTO size do not influence buoy size since the main techno-economic driver is cost.

Giassi et al. [2] perform an experimental campaign to evaluate the performance of different wave energy farm configurations, considering a bottom-tethered heaving point that can move in 6 DoF. The objective of this work is to evaluate the performance of the array considering different layouts and to compare the experimental results with a numerical frequency domain model. Array configurations were obtained by optimisation with genetic algorithms. The performance of the different configurations was evaluated experimentally under regular and long-crested waves. An important result is the calculation of the interaction factor (q-factor), which lies in the range of 0.77 up to 1.06, while the optimal configuration is the staggered layout. A frequency domain model of the array that predicts the heave motion of each device has been compared with the experimental tests.The numerical results are in agreement with the experimental ones when the test conditions do not involve strongly non-linear phenomena such as parametric resonance, slack line and wave breaking.

Sirigu et al. [1] present a holistic techno-economic optimization of the Pendulum Wave Energy Converter (PeWEC), using an evolutionary-based global optimization genetic algorithm. A strong and validated statement is provided and defended about the need for the inclusion of economic functions already during the first preliminary design. A genetic algorithm is implemented in order to optimize 13 different parameters, comprising shape, dimensions, mass properties and ballast, power take-off control torque and constraints, number and characteristics of the pendula and other subcomponents. Economic estimations are included, based on the mass of the hull and the pendula, as well as the size of the PTOs. Multiple optimization objectives are considered, Capture Width Ratio (CWR) and Capital expenditure over Productivity (CoP), demonstrating that CWR and CoP may be adverse objectives: the most effective device in absorbing and converting the incoming wave energy is not, in general, economically convenient, and vice versa.

Davidson and Kalmár-Nagy [4] propose a real-time detection system to identify when parametric resonance appears in wave energy converters. Parametric resonance is a dynamic instability due to the internal transfer of energy between degrees of freedom, which is known to cause large unstable pitch and/or roll motions, usually with detrimental effects on the power extraction performance and may increase loading on the WEC structure and mooring system. To remedy such negative effects, control systems can be designed to mitigate the onset of parametric resonance. Since real-time detection is key to enabling corrective actions, this paper presents the first application of a real-time detection system for the onset of parametric resonance in WECs. The proposed detection system achieved 95% accuracy across nearly 7000 sea states, producing 0.4% false negatives and 4.6% false positives.

Bonfanti et al. [5] are concerned with the real-time estimation of wave excitation forces, considering the case study of the Inertial Sea Wave Energy Converter (ISWEC). Energy-maximizing control strategies normally require the knowledge of the incoming wave force, which cannot be measured and should be estimated; moreover, since the input (PTO) control action must be provided in real-time, also the estimation should compute faster than real time. This paper investigates the wave excitation force estimation for a non-linear WEC, using both a model-based and a model-free approach. Firstly, a Kalman Filter is implemented considering the WEC linear model with the excitation force modelled as an unknown state to be estimated. Secondly, a feed-forward Neural Network is applied to map the WEC dynamics to the excitation force by training the network through a supervised learning algorithm. Sensitivity and robustness analyses are performed to investigate the estimation error in presence of un-modelled phenomena, model errors and measurement noise.

Garcia-Violiniet al. [3] present a critical comparison of a set of five simple controllers with the common ability to compute in real-time. In fact, it is argued that the computational cost of some complex control algorithms make them inapplicable to real devices; on the

other hand, having the objective of actual implementation, a number of energy-maximising wave energy controllers have been recently developed based on relatively simple strategies, stemming from the fundamentals behind impedance-matching. This paper documents this set of five controllers, which have been developed over the period 2010–2020: (i) Suboptimal causal reactive controller; (ii) Simple and effective real-time controller; (iii) Multi resonant feedback controller; (iv) Feedback resonating controller; (v) LiTe-Con. The comparison, carried out both analytically and numerically, encompass their characteristics, in terms of energy-maximising performance, the handling of physical constraints, and computational complexity. In particular, a scoring system is set, explicitly evaluating the following metrics: computational simplicity, stability, constraint handling, and resulting performance.

Mérigaud and Tona [7] propose an energy-maximisation spectral control that is able to include non-ideal PTO systems in the underlying model used to compute the optimal control law. The discontinuous PTO efficiency characteristic is included via a smooth function approximation to ensure computational efficiency. However, the cost function becomes non-quadratic, hence requires a slight generalisation of the derivative-based spectral control approach, initially introduced for quadratic cost functions. This generalisation is derived in the presented paper, providing details on its practical interest. Two application cases are considered, namely a single-body and a two-body heaving point absorbers inspired by real devices. In both cases, the spectral approach calculates WEC trajectory and control force solutions, for which the mean electrical power is shown to lie within a few percent of the true optimal electrical power. Regarding the effect of a non-ideal PTO efficiency upon achievable power production, the power achieved lies within 80–95% of that obtained by simply applying the efficiency factor to the optimal power with ideal PTO. This is a significantly less pessimistic result than the others found in the literature.

Anderlini et al. [6] implement a real-time reinforcement learning control for wave energy converters, to cope with the potential inaccuracies and uncertainties of the underlying mathematical description of model-based controllers. In particular, such uncertainties may be due to both initial limitations of the model (e.g., linear and nonlinear assumptions) and to variations of some parameters during the operative life of the device (e.g., ageing and wear). In this paper, an alternative solution is introduced to address such challenges, applying deep reinforcement learning (DRL) to the control of WECs. A DRL agent is initialised from data collected in multiple sea states under linear model predictive control in a linear simulation environment. The agent outperforms model predictive control for high wave heights and periods, but suffers close to the resonant period of the WEC. The computational cost at the deployment time of DRL is also much lower by diverting the computational effort from deployment time to training. In addition, model-free reinforcement learning can autonomously adapt to changes in the system dynamics, enabling fault-tolerant control.

Previsic et al. [9] tackle the comparison of model predictive control (MPC) and optimal causal control, applied to a heaving point absorber. In recent years, efforts by various researchers have been invested in the design of simple causal control laws, thanks to their simplicity of implementation in a real system. However, it is important to have a fair comparison, under representative conditions, with more complex non-causal controllers, in order to appropriately evaluate the trade-off between power yield and complexity, also including constraint handling ability. In this paper, a linear MPC is compared to a casual controller that incorporates constraint handling. The analysis demonstrates that the MPC provides significant performance advantages compared to an optimized causal controller, particularly if significant constraints on device motion and/or forces are imposed. It is further demonstrated that distinct control performance regions can be established that correlate well with classical point absorber and volumetric limits of the wave energy conversion device.

Haider et al. [10] propose a nonlinear model predictive controller for a wave energy converter with multiple degrees of freedom. The proposed control is computed in real-time and includes non-ideal power take-off and model non linearities. The inclusion of non-linearities in the model leads to a non-quadratic and non-standard cost function,

which is challenging to solve in a computationally effective manner. The considered device is the CENTIPOD, simulated in WEC-Sim, while the extracted power is re-written in pseudo-quadratic form and polynomial decomposition. Comparing linear to nonlinear MPC, despite a computational load that is only slightly higher (+35%), an appreciable improvement in power capture is achieved (up to +10.6%).

Demonte Gonzalez et al. [11] consider the application of sliding mode control for a floating heaving wave energy converter, including nonlinear hydrodynamic effects. In fact, the effectiveness of a control strategy is tightly linked to the representativeness of the underlying model, usually related to nonlinearities. Maximising energy extraction normally implies exaggerating the motion of the floater, inducing hydrodynamic nonlinearities: the most remarkable and often impactful are nonlinear static and dynamic Froude–Krylov forces, which are herein included. A sliding mode controller is proposed, which tracks a reference velocity that matches the phase of the excitation force to ensure higher energy absorption. The control algorithm is tested in regular linear waves and is compared to a complex-conjugate control and a nonlinear variation of the complex-conjugate control. Results show that the sliding mode control successfully tracks the reference and keeps the device displacement bounded while absorbing more energy than the other, although simple, control strategies. Furthermore, due to the robustness of the control law, it can also accommodate disturbances and uncertainties in the dynamic model of the wave energy converter.

Conflicts of Interest: The authors declare no conflict of interest.

References

1. Sirigu, S.A.; Foglietta, L.; Giorgi, G.; Bonfanti, M.; Cervelli, G.; Bracco, G.; Mattiazzo, G. Techno-Economic Optimisation for a Wave Energy Converter via Genetic Algorithm. *J. Mar. Sci. Eng.* **2020**, *8*, 482. [CrossRef]
2. Giassi, M.; Engström, J.; Isberg, J.; Göteman, M. Comparison of Wave Energy Park Layouts by Experimental and Numerical Methods. *J. Mar. Sci. Eng.* **2020**, *8*, 750. [CrossRef]
3. García-Violini, D.; Faedo, N.; Jaramillo-Lopez, F.; Ringwood, J.V. Simple controllers for wave energy devices compared. *J. Mar. Sci. Eng.* **2020**, *8*, 793. [CrossRef]
4. Davidson, J.; Kalmár-Nagy, T. A Real-Time Detection System for the Onset of Parametric Resonance in Wave Energy Converters. *J. Mar. Sci. Eng.* **2020**, *8*, 819. [CrossRef]
5. Bonfanti, M.; Hillis, A.; Sirigu, S.A.; Dafnakis, P.; Bracco, G.; Mattiazzo, G.; Plummer, A. Real-time wave excitation forces estimation: An application on the ISWEC device. *J. Mar. Sci. Eng.* **2020**, *8*, 825. [CrossRef]
6. Anderlini, E.; Husain, S.; Parker, G.G.; Abusara, M.; Thomas, G. Towards Real-Time Reinforcement Learning Control of a Wave Energy Converter. *J. Mar. Sci. Eng.* **2020**, *8*, 845. [CrossRef]
7. Mérigaud, A.; Tona, P. Spectral Control of Wave Energy Converters with Non-Ideal Power Take-off Systems. *J. Mar. Sci. Eng.* **2020**, *8*, 851. [CrossRef]
8. Tan, J.; Polinder, H.; Laguna, A.J.; Wellens, P.; Miedema, S.A. The Influence of Sizing of Wave Energy Converters on the Techno-Economic Performance. *J. Mar. Sci. Eng.* **2021**, *9*, 52. [CrossRef]
9. Previsic, M.; Karthikeyan, A.; Scruggs, J.; Giorgi, G.; Sirigu, S.A. A Comparative Study of Model Predictive Control and Optimal Causal Control for Heaving Point Absorbers. *J. Mar. Sci. Eng.* **2021**, *9*, 805. [CrossRef]
10. Haider, A.S.; Brekken, T.K.; McCall, A. Real-Time Nonlinear Model Predictive Controller for Multiple Degrees of Freedom Wave Energy Converters with Non-Ideal Power Take-Off. *J. Mar. Sci. Eng.* **2021**, *9*, 890. [CrossRef]
11. Gonzalez, T.D.; Parker, G.G.; Anderlini, E.; Weaver, W.W. Sliding Mode Control of a Nonlinear Wave Energy Converter Model. *J. Mar. Sci. Eng.* **2021**, *9*, 951. [CrossRef]

Journal of
Marine Science and Engineering

MDPI

Article

Techno-Economic Optimisation for a Wave Energy Converter via Genetic Algorithm

Sergej Antonello Sirigu *, Ludovico Foglietta, Giuseppe Giorgi, Mauro Bonfanti , Giulia Cervelli, Giovanni Bracco and Giuliana Mattiazzo

Department of Mechanical and Aerospace Engineering, Politecnico di Torino, 10129 Turin, Italy; ludovico.foglietta@studenti.polito.it (L.F.); giuseppe.giorgi@polito.it (G.G.); mauro.bonfanti@polito.it (M.B.); giulia.cervelli@polito.it (G.C.); giovanni.bracco@polito.it (G.B.); giuliana.mattiazzo@polito.it (G.M.)
* Correspondence: sergej.sirigu@polito.it

Received: 9 June 2020; Accepted: 24 June 2020; Published: 30 June 2020

Abstract: Although sea and ocean waves have been widely acknowledged to have the potential of providing sustainable and renewable energy, the emergence of a self-sufficient and mature industry is still lacking. An essential condition for reaching economic viability is to minimise the cost of electricity, as opposed to simply maximising the converted energy at the early design stages. One of the tools empowering developers to follow such a virtuous design pathway is the techno-economic optimisation. The purpose of this paper is to perform a holistic optimisation of the PeWEC (pendulum wave energy converter), which is a pitching platform converting energy from the oscillation of a pendulum contained in a sealed hull. Optimised parameters comprise shape; dimensions; mass properties and ballast; power take-off control torque and constraints; number and characteristics of the pendulum; and other subcomponents. Cost functions are included and the objective function is the ratio between the delivered power and the capital expenditure. Due to its ability to effectively deal with a large multi-dimensional design space, a genetic algorithm is implemented, with a specific modification to handle unfeasible design candidate and improve convergence. Results show that the device minimising the cost of energy and the one maximising the capture width ratio are substantially different, so the economically-oriented metric should be preferred.

Keywords: wave energy; wave energy converter; PeWEC; techno-economic optimisation; genetic algorithm; cost of energy; CaPex; CWR

1. Introduction

Based on the gradual depletion of conventional fossil fuels, and most importantly, the established awareness of their destructive impact on the environment, recent years have witnessed a compelling momentum towards the energy transition and decarbonisation, shared by industry, governmental bodies and policy-makers. A condition for effective and reliable energy procurement is diversification, especially concerning renewable sources, which are usually more variable and volatile. Ocean energy, wave energy in particular, can play a major role in the overall energy mix, thanks to its high power density and availability [1]. Despite its potential, wave energy still remains substantially untapped since several challenges, hindering commercialisation at industrial scale, remain to be overcome. Wave energy conversion is yet to reach economic viability and is not competitive with other renewable energy technologies, due to an excessive LCOE (levelised cost Of energy) at the current stage of development.

From a high-level perspective, one of the main reasons for the unsuccessful development of effective technologies is that typical development pathways prefer to rapidly increase readiness levels before an acceptable performance is achieved [2]. Considering a matrix composed of technology readiness level (TRL) and the technology performance level (TPL), deficient development pathways tend to increase TRL first, at low TPL; conversely, optimal trajectories should increase TPL first, at low TRL,

and then increase TRL towards commercialisation [3]. Although is it challenging to perform an accurate estimation of some performance aspects at low TRL, due to inherent limitations of small-scale devices and subsystems, techno-economic aspects should be taken into account. Changing such a development paradigm involves adopting better design practices, since common approaches are inherently suboptimal. In particular, often, design is performed in sequential fashion, considering different parts of the power conversion chain independently. A representative example is the optimisation of the hydrodynamics and power absorption of an uncontrolled device, followed by a design of an optimal controller, followed by the inclusion of technical constraints and efficiency, finally reaching the stage of cost evaluation and reduction. Although such an incremental approach is justified by the complexity of the system, neglecting mutual interaction typically leads to a suboptimal solution.

An effective design requires one to follow a holistic approach, based on representative wave-to-wire mathematical models [4], including some energy-maximising control strategy [5,6] considering technological constraints [7,8] and costs [9], since all of such aspects are tightly interrelated. Representative hydrodynamic models are advisable, since a controlled device may be affected by strong nonlinearities with major negative effects on power production [10]. Furthermore, unconstrained linear or partially-linear models may predict unrealistic behaviour under the action of an optimal controller [11], which is also sensitive to modelling errors [12,13]. Note that it is essential to include an energy-maximising control strategy, since it has the ability to significantly increase power-production performance over the operational sea states. Moreover, the control strategy has a great influence on the dynamic characteristic of the response of the device [14], making the power-wise optimal solutions for uncontrolled and controlled conditions significantly different [15]. However, the ability of the controller to optimise power absorption is highly dependent on physical constraints, mainly on displacement, speed and force/torque [16]. Such constraints depend on the electrical and mechanical subcomponents characteristics, and ultimately, cost. On the other hand, the hydrodynamic behaviour of the device mainly depends on its shape and dimensions, which entail volume and mass, which are main drivers of capital cost.

A practical implementation of an all-encompassing design optimisation is challenging, mainly due to the vast multi-dimensional search space which cannot be tackled with conventional global optimisation approaches due to computational limitations. Moreover, often there is no analytical representation of the relationship between input and output variables, due to hydrodynamic curves defined by points through panel-based simulations (BEM) and implicit nonlinearities requiring simulation via time-advancing schemes [17], or in some conditions, harmonic balance [18]. Therefore, both cost function and constraints usually behave as grey or black boxes. For such problems, genetic algorithms are among the most common choice, since they can handle design spaces of high dimensionality and complex cost functions and constraints, without relying on the knowledge of their mathematical structure [19]. Genetic algorithms are metaheuristic optimisation codes based on the evolutionary theory, relying on the survival-of-the-fittest principle. Thanks to their stochastic approach, they favour the identification of the global optimum, reducing the risk of convergence to a local minimum. Furthermore, they impose no specific requirement on the system to be optimised, since it is treated as a black box. Genetic algorithms are used in this paper based on previous experience of the authors, although other metaheuristic approaches exist, able to handle a large parameter space, such as covariance matrix adaptation, differential evolution and particle swarm algorithms [20].

Following their use in the general marine engineering field [21], genetic algorithms recently gained popularity in the wave energy field, but are mainly used for the optimisation of the array layout of several wave energy converters (WECs) [22,23]. Although scarce, some single WEC design optimisations via genetic algorithm are found in the literature. Reference [24] optimised the radius and draft of an archetypal cylinder, maximising the absorbed power and bandwidth. The design space is bi-dimensional; the geometry is idealised; and the power take-off (PTO) is a simple linear damper with a frequency-independent damping coefficient. Since power is not an effective single-objective function for practical design, Ref. [25] introduces proxies for costs, structural loads and PTO rating loads into the objective function. Costs are assumed to be proportional to the submerged surface and

the maximum reaction force. While [25] considered fixed-axis devices of conventional shape, Ref. [26] attempted to generalise the geometry as much as possible, using B-splines to describe wetted surfaces of arbitrary shapes. Moreover, frequency-dependent energy-maximising control is introduced, also including constraints to limit unrealistically large amplitudes of motion that follow. As a proxy for costs, length and displaced volumes are considered in the cost functions. Finally, Ref. [27] proposes a thorough optimisation of the SEAREV device, attempting to maximise the produced power while minimising the device mass (as a crude proxy for costs), including various constraints and latching-declutching control.

This paper proposes a comprehensive techno-economic optimisation of the PeWEC (pendulum wave energy converter), which is a self-reacting WEC extracting energy from the oscillation of a pendulum sealed in a floating hull [28]. Several novelties, with respect to other design optimisation of WECs, are included. First and foremost, similar only to [27], a high level of detail of a realistic device is considered, as opposed to archetypal or generic geometries. However, a wide design space with high dimensionality is investigated, counting up to 13 design variables, comprising shape and dimensions of the floater; ballast and inertial properties; pendulum properties and numerosity; PTO rated torque; velocity and power; and gearbox speed conversion ratio. Moreover, realistic geometrical, technical and structural constraints are implemented, based on subcomponents characteristics. No idealised proxy is used for estimating costs, which are directly computed based on the cost of different material used for construction and different PTOs from a catalogue. Finally, a simple but realistic energy-maximising control strategy is implemented, including explicit constraint handling, in order to perform a control-informed optimisation. Due to the high-dimensionality and mutual dependence of design variables, a stochastic optimisation approach, treating different variables as independent and random, encounters a high level of unfeasible combinations, which may potentially hinder the success of the optimisation. In order to deal with unfeasible solutions, a tournament-based genetic algorithm is implemented, reducing the impact of mortality rate on the convergence rate. The objective function, which the genetic algorithm tries to minimise, is the ratio between capital cost and annual energy production (AEP). However, in order to highlight the impact of the performance index and to generate a Pareto front, the capture width ratio is also considered as an additional objective. It is shown that hydrodynamic efficiency and cost of energy are contrasting objectives; therefore, this paper provides evidence that challenges the common practice of optimising the hydrodynamic performance during early-stage development, suggesting companies should pursue economic performance instead.

The remainder of the paper is organised as follows: Section 2 describes the technology while Section 3 presents its parametrisation for the optimisation algorithm, also focusing on constraints, cost functions and different objective functions. Finally, Section 4 provides main significant results with a critical discussion. Some final remarks are given in Section 5. Appendix A provides full general details about the genetic algorithm that effectively deals with discrete multi-variate problems with high mortality rate.

2. Technology

The system under consideration in this optimisation study is the PeWEC, an acronym of pendulum wave energy converter. PeWEC is a self-referenced inertial-based floating WEC, composed of a sealed hull enclosing a pendulum and the power take-off (PTO). There are notional similarities between PeWEC and the SEAREV device [29], both based on an inertial-activated body contained in a floating hull; however, while SEAREV is designed for ocean applications, PeWEC is initially aiming at lower energetic closed seas with lower-period waves (e.g., the Mediterranean Sea). The device is anchored to the seabed by means of a 3-line-3-segment mooring system, with each line composed of a jumper (riser) and a clump-weight [30]. When the device is moved by the waves, a relative motion between the hull and the internal pendulum is obtained, mostly due to the pitching motion. The kinetic energy related to this movement is converted into electrical energy by the PTO connected to the pendulum's hinge. A control law is implemented in the PTO driver to adjust the pendulum dynamics to the instantaneous

sea conditions, with the purpose of maximising the output energy. A schematic of the PeWEC system is shown in Figure 1.

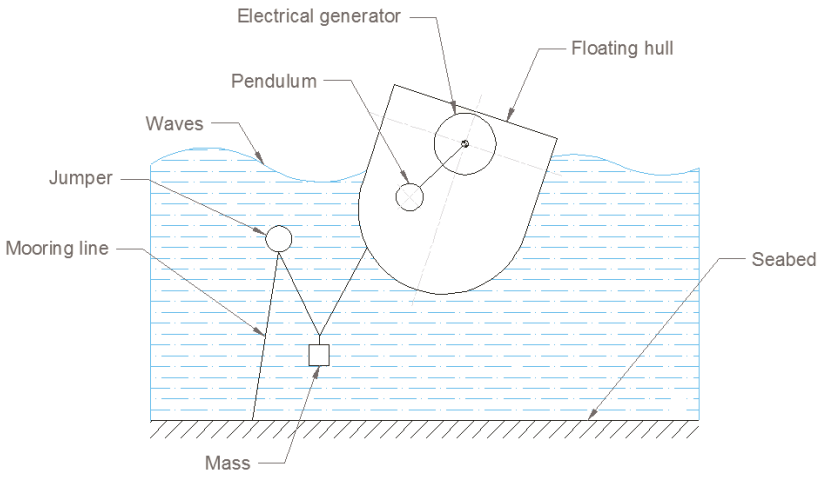

Figure 1. Schematic of the PeWEC working principle. Incoming waves excite the floating hull in pitch, transferring energy to the oscillation of an inner pendulum, whose motion is damped by a PTO. Three 3-segment mooring system, composed of a jumper and a clump-weight, keeps the system in place.

The hull is a sealed steel structure composed of a curved keel, two side walls and a flat topping; three internal sand ballasts (on the keel, stern and bow) ensure the mass distribution necessary to guarantee the required inertial properties, while a trellis structure is used to support the pendulum and the electronic equipment. The pendulum is composed of a cylindrical steel oscillating mass and a shaft, which is connected to the PTO system through a gearbox that ensures an appropriate coupling between the pendulum oscillation velocity and the PTO nominal speed. In order to extract energy from the pendulum movement, the PTO generates a reaction torque, which is adjusted by the driver's control system. Such constructive and technical features, based on early-development of the device, are here optimised via genetic algorithm. The technology has already been proven to be effective and promising, mainly thanks to wave tank tests at 1:45 and 1:12 scales [31]. Figure 2 shows a 3D digital model of the 1:45 prototype while Figure 3 shows a photo of the 1:12 prototype in the testing wave tank.

The concept of PeWEC germinated from the ISWEC (inertial sea wave energy converter), which generates the inertial coupling between PTO and the hull by means of the gyroscopic effect of a spinning flywheel [32]. While ISWEC requires power to keep the flywheel in rotation and create the self-reaction force [33], PeWEC is entirely passive, hence reducing explicit power loss sources. Further technological improvements are being explored for both the PeWEC and the ISWEC in order to increase the overall power conversion efficiency, such as resonant U-tanks [34], advanced control techniques [35], estimation and forecasting [36]. Moreover, the mooring system is under development, since it can affect the device performance [37]. However, this paper deals with a more fundamental early holistic optimisation of the PeWEC device shape, geometry and subcomponents, as further discussed in Section 3. The mathematical model, used to predict motion and loads of a given device, is presented in Section 2.1. The strategy to parametrically define multiple devices that the genetic algorithm can automatically optimise is presented in Section 3.

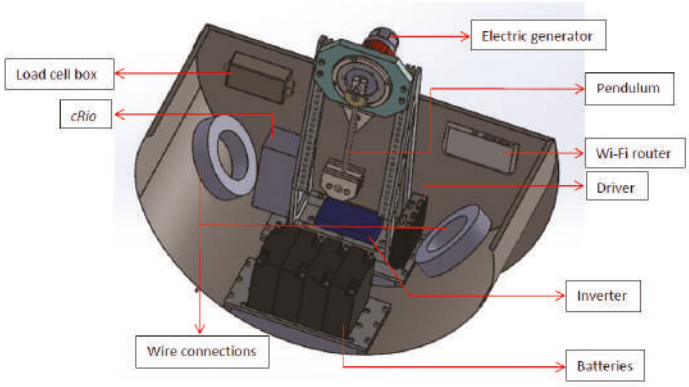

Figure 2. Digital representation of the 1:45 PeWEC prototype and its subcomponents.

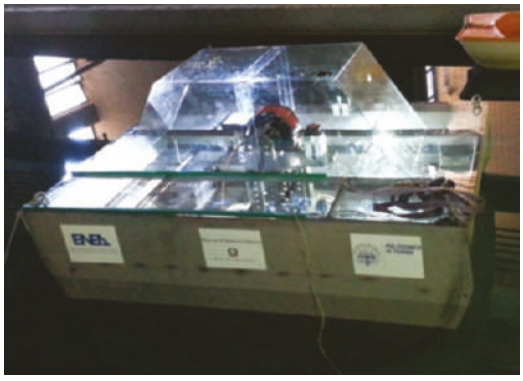

Figure 3. Photo of the 1:12 PeWEC prototype tested a wave tank [31].

2.1. Mathematical Model

The optimisation software relies on a mathematical model to evaluate the objective function which, in this paper, depends on the response of the device to incoming waves. An essential requirement for such a mathematical model is low computational speed, since a high number of individuals (order of tens of thousands) have to be assessed in a reasonable time. Therefore, a fully-linear model based on linear potential flow is implemented in frequency domain, thanks to its computational convenience. However, in order to avoid unrealistic motion that a linear model would predict under controlled conditions, various constraints are included, as further discussed in Section 3.2. Potential-flow-based models are conceptually divided into two phases: Firstly, the linear hydrodynamic curves, namely, excitation coefficients ($\mathbf{F}_w$), added mass ($\mathbf{A}$) and radiation damping ($\mathbf{B}$), are evaluated at a representative set of frequencies by means of a boundary element method (BEM) software, such as NEMOH [38] (this must be automatised in the genetic algorithm). Secondly, the dynamic response of the device is evaluated for a comprehensive set of sea states, characteristic of the designed installation site, taking care of determining appropriate energy-maximising control parameters. Although the run time of BEM codes depends on the number of simulated frequencies and on the discretised geometry, it is of the order of magnitude of 10^2 s, on average. Since shape and dimensions of the hull are among the optimisation parameters, a detailed description is provided in Section 3.1. On the other hand, the structure of the dynamic response simulator is invariant:

$$[\mathbf{M} + \mathbf{A}(\omega)]\,\ddot{\mathbf{X}} + \mathbf{B}(\omega)\dot{\mathbf{X}} + (\mathbf{K}_h + \mathbf{K}_p)\mathbf{X} = A_w(\omega)\mathbf{F}_w(\omega) + \mathbf{T}_{PTO} \tag{1}$$

where $\mathbf{M}$ is the mass matrix, $\mathbf{K}_h$ is the hydrostatic stiffness, $\mathbf{K}_p$ the restoring force of the pendulum, A_w is the wave amplitude, $\mathbf{T}_{PTO}$ is the PTO action and $\mathbf{X}$ is the state vector. Under the assumption of mono-directional waves aligned with the longitudinal axis of the hull, a planar motion of the hull can be assumed, namely, in surge (x), heave (z) and pitch (δ). Including the pendulum oscillation (ε), the state vector has four dimensions:

$$\mathbf{X} = \begin{bmatrix} x \\ z \\ \delta \\ \varepsilon \end{bmatrix} \tag{2}$$

The PTO acts on the rotational degree of freedom of the pendulum, applying active and reactive power, proportional to displacement and velocity with constant coefficients, k_{PTO} and c_{PTO}, respectively:

$$\mathbf{T}_{PTO} = \begin{bmatrix} 0 \\ 0 \\ 0 \\ -k_{PTO}\varepsilon - c_{PTO}\dot{\varepsilon} \end{bmatrix} \tag{3}$$

Coupling between the pendulum and the hull is provided by the restoring force of the pendulum and inertial reaction forces, which are expressed in $\mathbf{K}_p$ and $\mathbf{M}$, respectively. After linearisation [39]:

$$\mathbf{K}_p = \begin{bmatrix} 0 & 0 & 0 & 0 \\ 0 & 0 & 0 & 0 \\ 0 & 0 & -gm_p(d-l) & gm_pl \\ 0 & 0 & gm_pl & gm_pl \end{bmatrix} \tag{4}$$

$$\mathbf{M} = \begin{bmatrix} (M + m_p + m_b) & 0 & m_p(d-l) & -m_pl \\ 0 & (M + m_p + m_b) & 0 & 0 \\ m_p(d-l) & 0 & I_y + I_p + I_b + m_p(d-l)^2 & I_p + m_pl^2 - m_pdl \\ -m_pl & 0 & I_p + m_pl^2 - m_pdl & I_p + m_pl^2 \end{bmatrix} \tag{5}$$

where M is the mass of the hull; I_y is the hull moment of inertia; g is the acceleration of gravity; d is the distance between the device centre of gravity (CoG) and the pendulum fulcrum; l is the pendulum length; m_p and m_b are the masses of the pendulum and the bar holding the pendulum, respectively, and I_p and I_b are their moments of inertia, respectively.

In order to maintain the model linear, mooring effects are neglected, as are mean drift forces and second order effects. Moreover, viscous effects are neglected, since they would require specific tuning for each device [40]. However, the linearised model has been validated through an experimental campaign [39], ensuring appropriate accuracy and representativeness for global design optimisation problems [41]. Nevertheless, it is worth noticing that these assumptions (planar waves and motion, and absence of a mooring system) are simplifications, since real waves may be short-crested, inducing complex motion in 6 degrees of freedom, which is also possible due to parametric instabilities and nonlinear coupling [42], and the mooring system may significantly affect the dynamics of the system [37].

The fully-linear model can be efficiently solved in the frequency domain with a very low computational time. For each wave, the optimal k_{PTO} and c_{PTO} are sought by means of a multi-variate simplex algorithm [43], respecting global constraints on loads and displacements, as discussed in Section 3.2.

It is worth remarking that the optimal control (performed by the simplex algorithm for each device) is completely independent of the design optimisation (performed by the genetic algorithm modifying geometrical and technical characteristics of the device). For each individual, the response to each irregular wave (modelled according to a Jonswap spectrum), comprising the simplex optimisation, requires about one second of computation. The productivity is computed over a scatter diagram densely described by 128 waves, accounting for about 100–150 seconds of computation. The targeted installation site is near Pantelleria island, in the Mediterranean Sea. The set of representative waves is chosen in order to adequately cover areas of the scatter diagram with non-negligible occurrence, as shown in Figure 4.

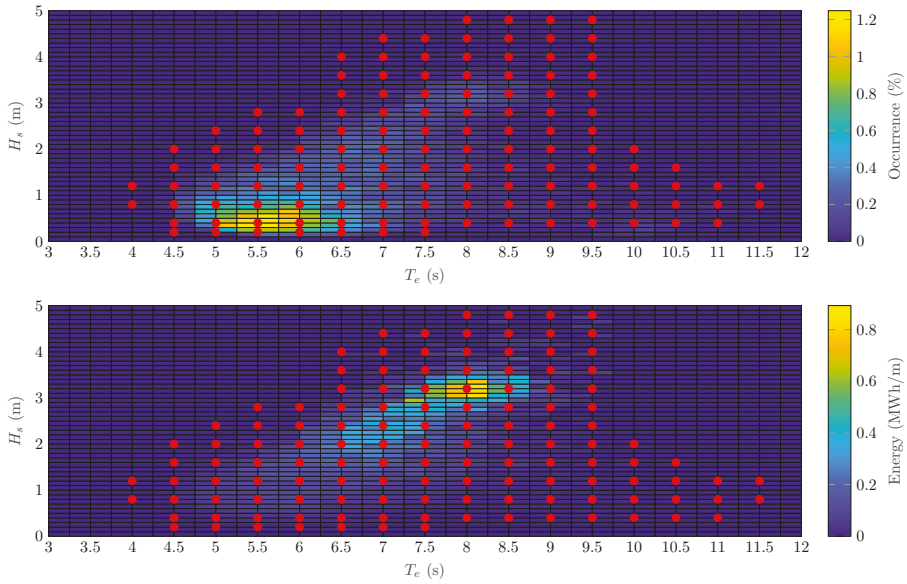

Figure 4. Occurrences and energy scatter diagrams for the installation site close to Pantelleria island, Italy; 128 representative waves were selected for the productivity estimation, shown by the red markers, where the occurrence percentage is not negligible.

3. Optimisation Software

The implementation of the optimisation software, as presented in Figure A1 and discussed in Appendix A, requires the definition of the design variables, the objective function and the tuning parameters of the genetic algorithm. The system, presented in Section 2, has virtually an infinite number of design variables that define its hydrodynamic behaviour, inertial properties and power absorption/conversion characteristics. Therefore, making some assumptions on the geometry and subcomponents is mandatory. Moreover, a parametric definition is required, allowing the software to fully define the system without direct human intervention. Section 3.1 details such a parametric representation, univocally identifying a device by its shape, dimensions, mass, inertia, ballast's distribution, pendulum and PTO characteristics. Starting from the shape of the hull, a BEM code automatically computes hydrodynamic curves, used to predict the device response to waves. However, techno-economic considerations should be included in the optimisation process, as extensively discussed in Section 1. Section 3.2 provides all functions that are used to estimate the cost of material and components. Moreover, constraints are imposed on displacements, velocities and loads, in accordance to the characteristics (and costs) of subcomponents. Finally, Section 3.3 presents tuning parameters of the genetic algorithm and the definitions of different performance indexes that the software aims at optimising.

3.1. Parametric Definition

In this work, 13 parameters are chosen to describe the device, summarised in Table 1 and hereafter discussed in detail: six for the hull, five for the pendulum and two for the PTO.

The shape of the hull is based on previous experience matured during the development of the PeWEC devices. For both manufacturability and hydrodynamic performance, the hull profile is assumed to be composed of a bottom circumference, tangential to two circumferences in the bow/stern sections, as shown in Figure 5, while the transversal section is assumed to be constant. The floater is symmetric with respect to the y-z and x-z planes and it results from the extrusion of the floater profile shape along the y-axis. The x-axis coincides with the floater deck and the z-axis goes from the deck of the floater upwards. The smooth surface with large radius of curvature is easier and cheaper to manufacture [44]. Moreover, the absence of sharp edges in the hull profile guarantee a low impact of vortex shedding and viscous drag losses [41]. Finally, the absence of re-entrant angles significantly reduces the risk of slamming events [27].

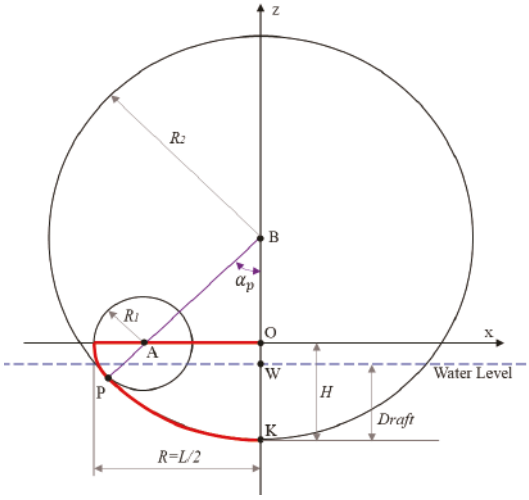

Figure 5. Parametric definition of the cross sectional of the floater.

The following relevant parameters, with respect to Figure 5, characterise the hull's profile:

- R: semi-length of the floater;
- H: overall height of the hull—i.e., the distance between the keel and the deck;
- D: draft of the hull;
- R_1: radius of circumference C_1;
- (x_A, z_A): x- and z-coordinates of the centre of C_1, respectively, with $z_A = 0$;
- R_2: radius of circumference C_2;
- (x_B, z_B): x- and z-coordinates of the centre of C_2, respectively, with $x_B = 0$;
- $\alpha_P = \angle$PBO.

A subset of six independent geometrical and inertial parameters is defined, which are used as design parameters in the genetic algorithm:

- L: length of the floater;
- W: width of the floater;
- $h = x_A/R$: bow/stern circumference ratio;

- $k = H/R$: height ratio;
- $j = D/H$: draft ratio;
- BFR: ballast filling ratio, defined as the ratio of ballast located in aft/fore ballast tanks over the total ballast (BFR = 1: all the ballast is stored in aft/fore ballast tanks; BFR = 0: all the ballast is stored in bottom ballast tank).

Figure 6 shows four examples of the effects of the geometric parameters h and k. Figure 7 shows examples of draft and ballast allocation; namely, j and BFR. Note that the amount of ballast required (M_{bal}) is univocally defined by the mass of the displaced volume of water (M_{tot}), the mass of the hull structure (M_h) and the mass of the pendulum-PTO units. The allocation of M_{bal} between bow/stern and keel compartments determines the total moment of inertia of the system, which is an important parameter to conveniently change the resonant period in pitch. The ballast material is assumed to be sand, with density (ρ_{bal}) of 1400 kg m^{-3}, which is considered to be an appropriate compromise between cost and specific weight. Filling of the ballast compartments is assumed from the extremities inwards, providing higher inertia and being easier from a practical point of view.

The hull is made out of standard naval carpentry steel, with a density (ρ_h) of 7800 kg m^{-3}. Based on previous experience with prototyping of the PeWEC device, M_h is assumed to be 90 times the total volume of the floater. Consequently, assuming the walls of the floater as thin plates, an equivalent thickness is computed from the lateral surface of the floater and M_h, making the computation of inertial properties of the hull possible.

On the hull's centreline, multiple pendulums can be placed, and their number (N_p) is one of the design parameters of the genetic algorithm. Each pendulum is composed of an oscillating cylindrical steel-made mass and a steel shaft. A trellis structure envelopes and supports the pendulum, a gearbox and the PTO; the ensemble of these components is referred to as unit, and its mass, inertia and volume are parametrically estimated starting from the pendulum's properties. The mass and inertia of the entire unit are 20% and 30% higher than the mass and inertia of the pendulum, respectively. The extension of the unit in the y-direction is 2 m longer than the pendulum dimension, in order to account for the required space for machinery and technical operators during assembly and maintenance. The overall mass of the device depends on the submerged volume, defined by j, k and L. Since the mass of the hull is proportional to its total volume, the remaining part has to be composed of the ballast and units. A design parameter (β_U) is defined so that the mass of each unit is:

$$M_{unit} = \frac{\beta_U \left(M_{tot} - M_h\right)}{N_p} \tag{6}$$

Consequently, the ballast mass is the complementary fraction of β_U.

Each pendulum is composed of a cylinder with axis parallel to the y-direction, swinging around a fulcrum. The volume of the cylinder is computed from its mass and density ($\rho_p = 7800$ kg m^{-3}). Known volume, radius and height are defined by a shape factor (σ_p), which is a free design parameter deciding if the pendulum is large and short ($\sigma_p = 0$) or small and long ($\sigma_p = 10$), with respect to the available space. Once the geometry is defined, the length of the swinging arm of the pendulum is defined by a design ratio γ_p, which takes the available space in the hull into account. Finally, the height of the fulcrum is defined by a further design parameter λ_p. Note that the relative geometry of the hull and the pendulum allow for full rotation of the swinging mass around the fulcrum.

Note that not all possible combinations of geometric and pendulum property parameters are feasible due to volume and weight physical restrictions. Consequently, during the optimisation, unfeasible individuals are discarded and the death penalty function is computed, contributing to increase the mortality rate of the genetic algorithm.

Finally, the actual conversion stage is performed by a permanent magnet syncronous motor (PMSM), one for each pendulum, combined with a planetary gearbox that is well suited for high torque and low speed applications. The gearbox ratio r_g is a further design parameter. Finally, different PTO systems are

used (ID_{PTO}), with different combinations of nominal speed (n_{PTO}) and nominal torques (T_{PTO}), hence the costs, as shown in Figure 8.

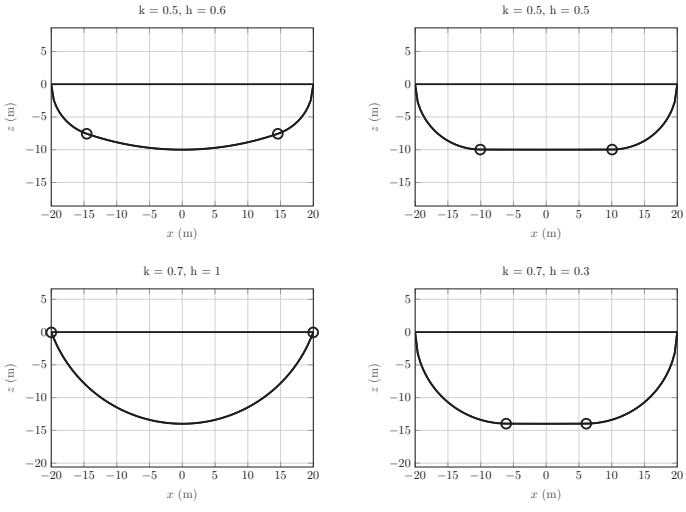

Figure 6. Examples of the effects of the *h* and *k* geometric design parameters.

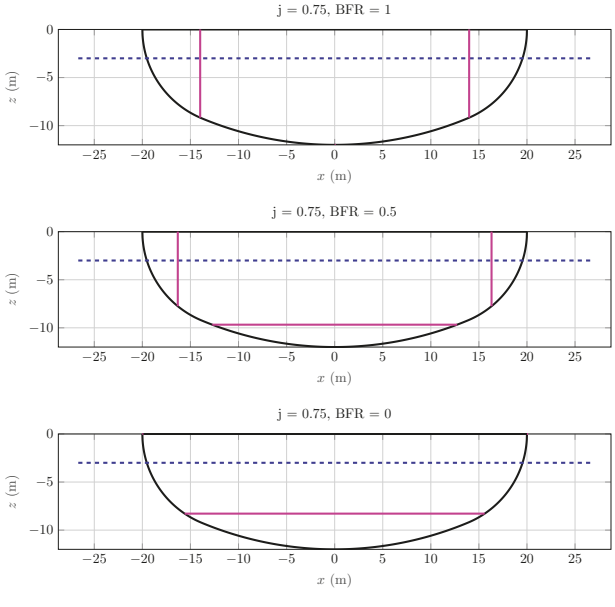

Figure 7. Examples of the effects of the *j* and ballast filling ratio (BFR) design parameters.

A summarising table of the 13 design parameters is provided in Table 1, including lower and upper bounds, and number of equally spaced steps. Bounds and step sizes are based on the authors' experience in developing the technology and running the model, ensuring that the minimum allowed variations of the design parameters produce small but relevant variations in the device performance. In this way, the algorithm is forced to consider only substantially different individuals, preventing the risk of simulating almost-equal devices. Although this objective could be achieved with a continuous

parameter space by applying appropriate tolerances and checks on parameter variations, the authors believe that a gridded approach is more convenient, since it is easier to inspect and implement.

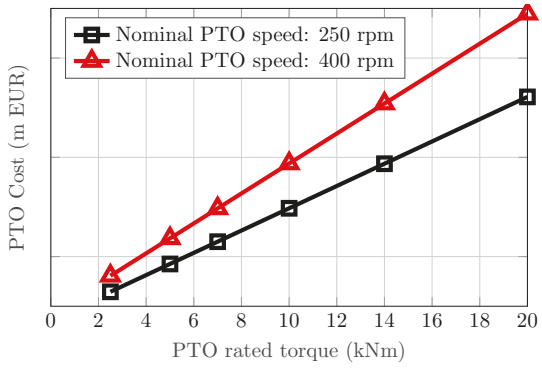

Figure 8. Cost of each power take-off, linearly proportional to the rated torque, with slope depending on the nominal speed.

Table 1. Thirteen design parameters used by the genetic algorithm to univocally define an individual, as discussed in Section 3.1. Discrete values with constant spacing are used, with lower and upper bounds.

Design Parameter	Symbol	Units	Lower Bound	Upper Bound	# Discretisation
Hull length	L	(m)	8	30	23
Hull width	W	(m)	5	30	26
Bow/stern circumference ratio	h	(-)	0.5	1	6
Height ratio	k	(-)	0.5	1	6
Draft ratio	j	(-)	0.65	0.8	4
Ballast filling ratio	BFR	(-)	0.5	1	6
Number of pendulum/PTO	N_p	(-)	1	15	15
Unit mass ratio	β_U	(-)	0.05	0.95	18
Pendulum shape factor	σ_p	(-)	0.05	0.95	10
Pendulum arm factor	γ_p	(-)	0.1	1	10
Pendulum fulcrum factor	λ_p	(-)	0.1	1	10
Gearbox ratio	r_g	(-)	10	30	3
PTO ID	$\mathrm{ID_{PTO}}$	(-)	1	11	11

3.2. Techno-Economic Definitions and Constraints

The definition of the fitness index beholds primary importance in the identification of an optimal device: the genetic algorithm, similarly to other optimisation codes, iteratively tests several devices to find the one that minimises the objective function. In this work, three different fitness functions are used in three independent optimisation cycles, in order to have a deeper understanding of the phenomenon by building the Pareto front. In fact, multi-objective algorithms are usually performed as several single-objective optimisations where the performance index is computed as a weighted average of the multiple objectives [45].

The first objective is to minimise the capital expenditure (CapEx) over productivity (CoP) ratio, computed as the ratio between the overall capital expenditure (CapEx) and the produced energy over the lifetime of the plant (N_y, assumed 25 years for PeWEC):

$$\mathrm{CoP} = \frac{\mathrm{CapEx}}{N_y\,\mathrm{AEP}} \tag{7}$$

where the annual energy production (AEP) is computed considering net power, affected by efficiencies and baseload: the gearbox is assumed to have a 0.95 mechanical efficiency; the PTO conversion system is considered to have a conversion efficiency of 0.95; the baseload considers all the electrical machinery input energy necessary for their correct operation: 500 W for each pendulum. Power losses from the bearings have been neglected, since the pendulum rotates at low speed [39].

The overall cost considers the device's capital expenditures to be classified in three main terms: hull's materials and construction, units' materials and construction, PTO. The mooring system is not considered, since its layout and cost are device-specific and no clear automatic parametrisation could be tackled in such an early design stage. Similarly, operational and maintenance expenditure (OpEx) is not considered in this work: on the one hand, its assessment requires extensive experience and a mature technology; on the other hand, in sealed WECs such as PeWEC but also ISWEC and SEAREV, OpEx is usually negligible compared to CapEx, since there are no moving parts subject to hostile marine environment (salty water, dust and debris). In fact, for common WECs presenting moving parts in hostile environment, it is estimated that the CapEx accounts for up to 35% only [46]. However, for the SEAREV device (with all moving parts enclosed in a sealed hull, as the PeWEC) it is estimated that OpEx is about 2% of the overall expenses [27]. Moreover, in such conditions, the levelised cost of energy (LCOE) is shown to be mainly sensitive to AEP and CaPex, while Opex, inflation rate, lifetime and expected internal rate of return are less impactful [27].

Several PTO models are considered in this analysis; each of them is characterised by its own maximum and nominal values in torque and speed. PTO costs are assumed to be significantly proportional to the nominal torque, with slope proportional to the nominal velocity, as shown in Figure 8. The PTO costs comprise those of the generator, the gearbox and various power electronic ancillary systems. However, the explicit costs of PTOs have been hidden for confidentiality. Note that a larger PTO provides higher freedom to the controller and is able to convert more energy. However, such a flexibility requires higher investments. The optimisation algorithm attempts to find a suitable compromise, also taking into account technical constraints on speed, torque and power of the PTO.

Material and manufacturing costs of the hull (C_h) and the pendulums (C_p) are estimated to be proportional to their respective mass, with the specific cost of the pendulums being almost twice the specific cost of the hull. Although simplified, all cost functions (PTO, hull construction and pendulum construction) are notionally based on the experience of the authors in the development and deployment of actual small and full-scale devices.

As discussed in Section 1, it is advisable to optimise the overall CoP, since it takes into account the compromise between techno-economic performance and hydrodynamic performance. However, a popular approach in the literature is to optimise the AEP or the hydrodynamic absorption abilities, regardless of the cost and/or technical characteristics and the limitations of the subcomponents required to achieve such a high conversion efficiency. In order to highlight substantial differences in convergence direction and the obtained optimal device, a second objective is considered: the capture width ratio (CWR), which is a common measure of energy conversion ability, defined as ratio between AEP and annual energy available in the resource (E_w):

$$\mathrm{CWR} = \frac{\mathrm{AEP}}{E_w} \tag{8}$$

Note that the correspondent performance index (to be minimised) is defined as -CWR, since CWR should be maximised. For each sea state, the incoming wave power on the device is defined as:

$$P_w = \frac{\rho g^2}{64\pi} H_s^2 T_e W \tag{9}$$

where ρ is the water density, H_s the significant wave height and T_e the energy period. Equation (9) shows how the incoming available energy is proportional to the width, which is one of the main design parameters in the optimisation. In practice, while maximising AEP will likely maximise (W) in order

to have access to larger power, maximising CWR seeks to increase the portion of the converted energy from the wave to the grid, regardless of price of conversion. Finally, maximising CoP focuses on the cost of the conversion, regardless of its efficiency.

Since there are two competing objectives (minimising CoP and maximising CWR), a multi-objective optimisation approach is adopted. By means of a scalarisation technique [47], the two different objectives are aggregated into a unique objective by means of a weighted average, using a pair of weights (w_1, w_2). Through the choice of different weights, it is possible to build the Pareto-optimal set. Three pairs of weights have been considered, as shown in Table 2. Effectively, sets (1) and (3) are single-objective optimisations, while set (2) is a proper multi-objective one. However, by aggregating the results of the three optimisations, a Pareto front can be constructed.

Table 2. Multi-objective weights.

Weight Set ID	Explanation	CoP-Weight (w_1)	CWR-Weight (w_2)
(1)	CoP-driven	1	0
(2)	Weight-driven	0.5	0.5
(3)	CWR-driven	0	1

Technological constraints are applied to all three optimisations. For each sea state, the optimal control parameters are chosen in order fulfil constraints tabulated in Table 3. Note that velocity and torque constraints depend on the particular PTO and the gearbox installed, and hence on the design parameters $\mathrm{ID}_{\mathrm{PTO}}$ and r_g, respectively.

Table 3. Technological constraints, fulfilled by tuning the control parameters.

Constrained Variable	Units	Constrained Value
$\mathrm{rms}(\delta)$	(°)	15
$\mathrm{rms}(\varepsilon)$	(°)	40
$\max(\dot{\varepsilon})$	(rpm)	$n_{PTO}^{\max}/r_g$
$\max(T_{PTO})$	(kNm)	$T_{PTO}^{\max} r_g$

3.3. Genetic Algorithm

In Appendix A, a detailed description of the genetic algorithm is provided. Considering the specific problem, presented in Section 3.1, the tuning factors of the algorithm in Table 4 were chosen. The MATLAB built-in implementation of the genetic algorithm has been used, along with its default tuning parameters, which are considered to be suitable. Although beyond of the scope of this paper, a throughout sensitivity analysis can potentially improve the convergence rate of the algorithm.

Table 4. Tuning parameters of the genetic algorithm, described in Appendixes A.1–A.6 and shown in red in the flow chart in Figure A1.

Name	Symbol	Value
Population size	N	150
Maximum generation count	M	200
Maximum stall generation	M_Δ	50
Convergence threshold	Δ	1.00×10^{-6}
Elitism percentage	ϵ	5%
Tournament size	k	4

4. Results

The MI-LXPM genetic algorithm has been chosen since it can effectively handle integer optimisation problems with potentially high number of unfeasible solutions. Figure 9 shows the development of the mortality rate through generations for the example of the CoP-driven optimisation. The first population has a significant number of unfeasible solutions, since it results from a purely stochastic process. However, the mortality rapidly drops to an average value (excluding the first two generations) of 25.5% with a standard deviation of 4.3%. Furthermore, note that there are 118 generations, meaning that the algorithm met convergence criteria before the maximum generation count of 200.

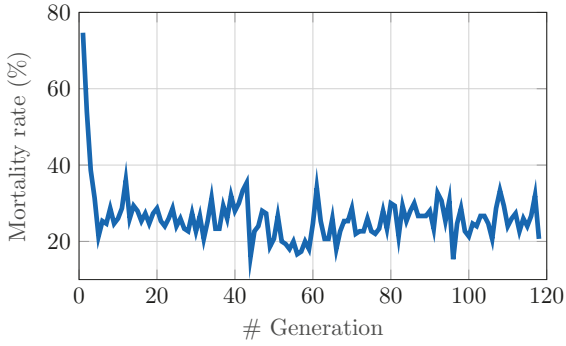

Figure 9. Mortality rate for the capital expenditure (CapEx) over productivity (CoP)-driven optimisation. Excluding the first two generations, the average is 25.5% and the standard deviation is 4.3%.

Note that two different seeds for the randomisation of the initial population of each optimisation have been used, reaching consistent results, hereafter discussed. The overall development of the algorithm is shown in Figure 10 for the example of the CoP-driven optimisation. The generic objective function f^* to be minimised is on the vertical axis. For each generation, individuals are sorted according to f^*, so that the Nth individual has the highest f^*. Unfeasible individuals are missing markers at lowest individual count. The colour code is in accordance with the generation count, showing the evolution of the population. The final population count is 118, as also shown in Figure 9. Therefore, since the maximum stall generation criterion is 50 (see Table 4), improvements of the overall-optimum are found until generation 68. The cloud of points is also projected onto the vertical planes, highlighting relevant trends. The projection on the vertical right plane has the purpose of showing the potentially significant change of theslope as generations advance; i.e., if the ratio of fit individuals over the whole population changes. The fact that such a projection preserves about the same shape shows that the overall distribution of fit individuals remains about constant, apart from early generations. This is also shown in the projection on the vertical left plane: the minimum of f^* decreases as generations progress, as expected and desired; however, the improvement is abrupt in early generations (until generation 40) and slows down afterwards (until generation 68). Furthermore, the number of devices at a low f^* is relatively scarce, with a rarefied gap between the fittest individuals and the rest of the population. This suggests that the degradation of performance is quite sensitive to the choice and combination of design parameters. Moreover, the presence of about 20% of unfeasible devices may have an impact on the uniform improvement of the whole population. An alternative, smoother definition of the performance index, a finer parameter grid and different cross-over/mutation strength may smooth the convergence and increase the convergence rate. Moreover, the definition of the design parameters may be appropriately revised in order to structurally reduce the likelihood of unfeasible individuals. However, although such an extensive sensitivity analysis is an interesting topic for future investigation, it is believed that the current setup provides appropriate convergence and satisfactory results to discuss techno-economic aspects of the PeWEC device optimisation.

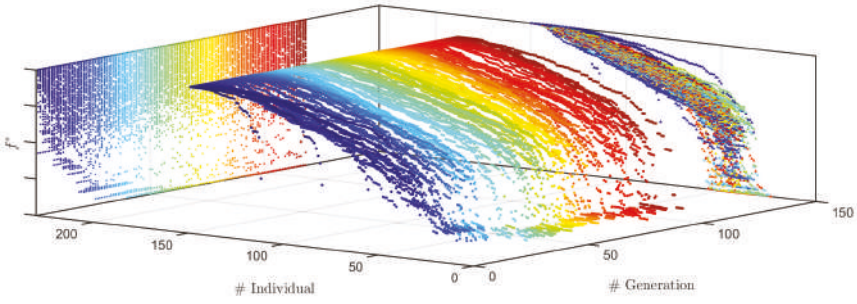

Figure 10. CoP-driven optimisation results: for each generation, individuals are sorted according to the objective function (f^*) to be minimised. The cloud of points is projected onto the vertical planes. The colour code corresponds to the generation count.

Three different optimisations have been performed, pursuing different objective functions in order to generate a Pareto front, as discussed in Section 3.2. Figure 11 shows the ensemble of all individuals generated from the three separate optimisations aggregated, plotting on the productivity versus the device cost, with the colour code being proportional to the CoP (left) and CWR (right). Elliptical annotations on the graphs indicated the most convenient region according to the respective metric (low CoP and high CWR, respectively). As expected, the optimal device changes with the optimality metric. In fact the highest AEP, the highest CWR and the lowest CoP are achieved by three significantly different individuals. In particular, it is evident that the increase in AEP is slower than the required increase in cost, so that the lowest CoP is found in the low cost region, in spite of a lower AEP. Moreover, low-CoP devices have also low CWRs, demonstrating the fact that the main driver is the device cost. Conversely, achieving high CWR and/or high AEP typically requires such an increase in device cost that the overall conversion becomes economically unfavourable.

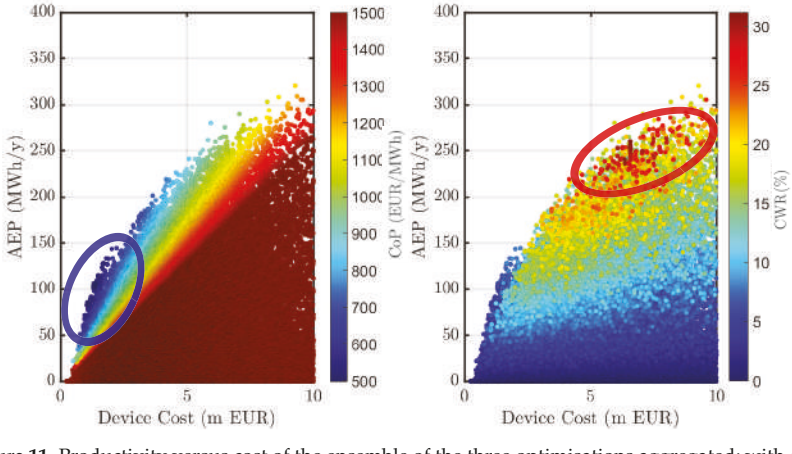

Figure 11. Productivity versus cost of the ensemble of the three optimisations aggregated; with each marker (individual), colour is proportional to the CoP (left) and capture width ratio (CWR) (right). The elliptical annotation highlight the most convenient region according to the evaluation metric (low CoP and high CWR).

It is interesting to analyse the direction that each optimisation tries to follow in order to improve performance index. Figure 12 shows a map of CWR versus COE, with three shaded areas encompassing individuals generated according to the three optimisation objectives. Individuals are also represented by markers of the same colour of the respective shaded area. As expected, the COE-driven area

is attracted towards the bottom CoP-axis and achieves the overall minimum CoP. Similarly the CWR-driven optimisation extends the furthest along the CWR-axis, while obtaining higher CoP. In between, the weighted optimisation reaches good compromises of the two metrics.

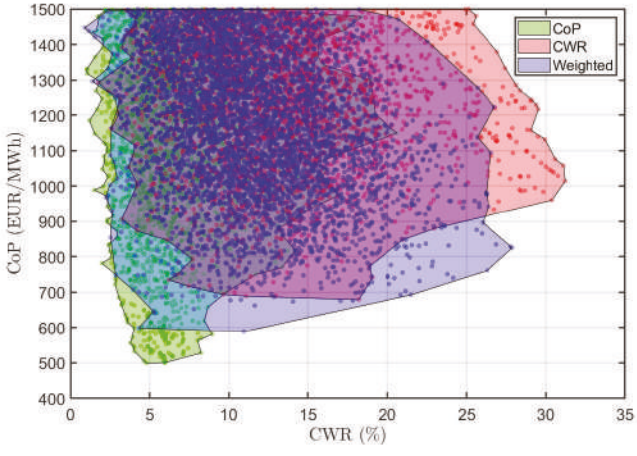

Figure 12. Ensemble of the three optimisations (CoP-driven, CWR-driven and weighted), with shaded areas encompassing each one of the three populations.

Overall, it is important to remark that the CWR-driven optimum has a significantly high CoP, twice the overall minimum CoP. Similarly, also the device with lowest CoP from the CWR-driven optimisation has a high CoP, compared to the entire populations. Conversely, the lowest CoP is obtained by a device with a CWR 6 times smaller than the highest-overall CWR.

From Figure 12 it is possible to extract the Pareto front, shown in Figure 13. Moreover, it is interesting to highlight the evolution of the Pareto front as the algorithm advances through generations. Five different stages of progression are shown, equally spaced from 0% to 100% progression. It is evident that an abrupt improvement is achieved in early stages of the optimisation. Afterwards, although the improvement slows down, the Pareto front is gradually improved, moving downwards and rightwards, namely, to lower CoP and higher CWR.

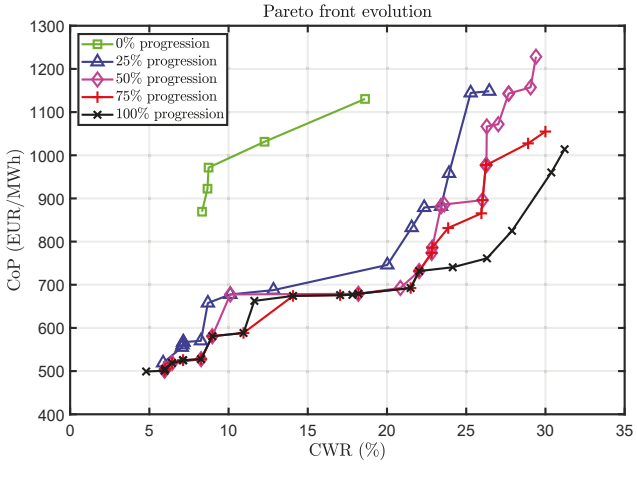

Figure 13. Evolution of the Pareto front, from 0% to 100% progression.

4.1. CoP and CWR Optima

The characteristics of the optimum devices according to different objective functions are hereafter discussed. Figures 14 and 15 show the cross-section and the top-view, respectively, of the optimal devices according to the three optimisations; namely, the CoP-driven optimum, the weight-driven optimum and the CWR-driven optimum. The same axis scale and dimension are used in order to highlight differences in size. Moreover, position, size and number of pendulums are shown.

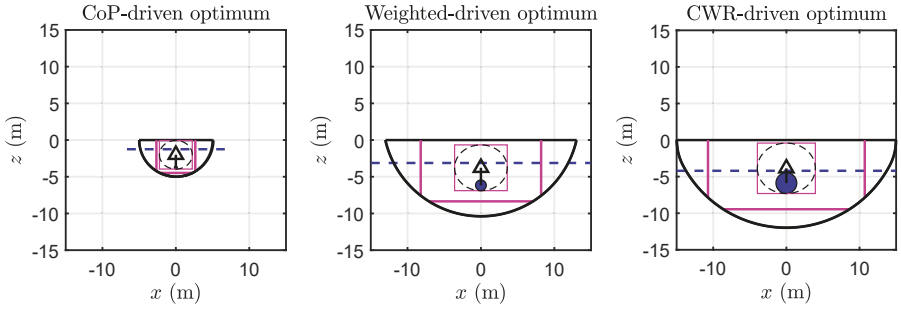

Figure 14. Cross-section of the CoP-driven, the weight-driven and the CWR-driven optima, with common scale and axis dimensions. The pink rectangles represents the ballast compartments and the bulk of the unit. The blue circle is the cross-section of the pendulum mass. The triangular marker represents the fulcrum. The blue dashed line is the still water level.

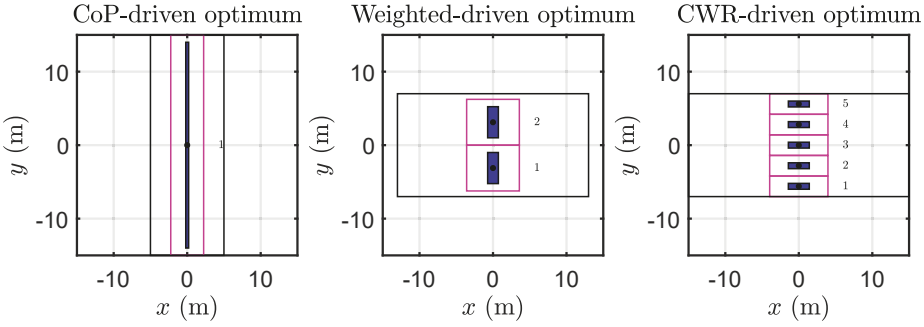

Figure 15. Top view of the CoP-driven, the weight-driven and the CWR-driven optima, with common scale and axis dimensions. The pink rectangles represents the bulk of the unit. The blue rectangle is the pendulum mass.

Clearly, dimensions in the $x - z$ plane increase from left (CoP-driven) to right (CWR-driven), suggesting that a long and high hull is more hydrodynamically efficient for the considered installation site. However, the CoP-optimum is wider than the CWR-optimum, intercepting more wave-crest, hence the high amount of incoming energy. This suggests that increasing the width requires a lower increment in cost than the consequent increase in AEP, hence lowering the resulting CoP. Moreover, the number of pendulums (and PTOs) increases from left to right, hinting that the cost of the PTO is a limiting constraint in the CoP-driven optimisation. Conversely, higher CWR requires more pendulums with larger cross sectional areas and smaller radius/length ratios.

Figure 16 shows the response amplitude operator (RAO) of the CoP-optimum (left) and CWR-optimum (right), for the pitch (RAO_{55}, top) and pendulum oscillation (RAO_{77}, bottom) degrees of freedom. The PTO-free RAO is shown in solid lines and square markers, showing that the natural attitudes of the devices differ according to the pursued objective. In particular, maximising

the CWR leads to a higher natural period (about 7 s) than optimising the CoP (about 5.4 s), so that it can be inferred that converting lower energetic waves (lower period) is more economically convenient. Furthermore, Figure 16 also shows RAOs, including optimal control parameters, shown in Figure 17, which significantly modify the dynamics of the system in order to maximise the performance, while remaining compliant with technical constraints. Since the PTO acts directly on the pendulum (under-actuated system), RAO_{77} is more affected by the control, with significant increases in amplitude and bandwidth. Conversely, the RAO_{55} is damped out, due to the inertial coupling between the hull and the pendulum. Overall, the control increases the energy flux from the hull to the pendulum, and ultimately, the PTO.

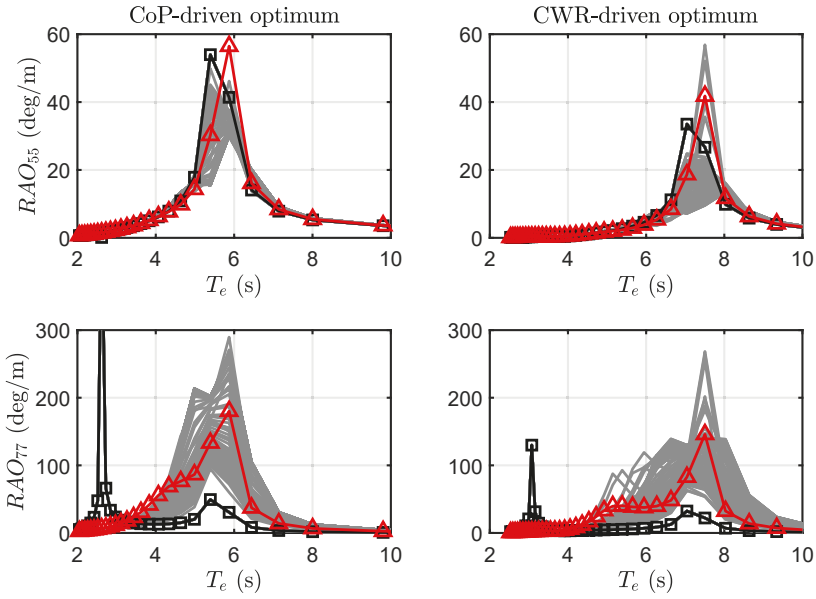

Figure 16. Response amplitude operator of the CoP-optimum (left) and CWR-optimum (right), for the pitch (RAO_{55}, top) and pendulum oscillation (RAO_{77}, bottom) degrees of freedom. The black solid line with square markers is for the PTO-free condition. The set of grey RAO lines is for the various controlled conditions, shown in Figure 17, among which a representative example is the red solid line with triangular markers, referring to c_{PTO} and k_{PTO} weighted over the occurrences matrix.

Overall, Figure 16 highlights the importance of a controlled-informed optimisation. In fact, the algorithm selects a device that is structurally apt to perform well when controlled, as opposed to select a performing uncontrolled device, and then applies a control.

Figure 17, in accordance with Figure 16, shows that the peak of conversion efficiency, i.e., CWR, is around lower wave periods for the CoP-optimum than the CWR-optimum. The control parameters maps show that c_{PTO} is higher for the CWR-driven optimum, since it has to apply a higher damping torque to convert power in higher-energetic sea states. The reactive term of the PTO control, i.e., k_{PTO}, is negative almost across the whole scatter in order to obtain the resonant period of the pendulum T_{res}, shown in the last row of Figure 17. The natural period of the pendulum can be affected by the properties of the pendulum (mass, inertia and length) and k_{pto}. However, the inertial properties of the pendulum also affect the coupling between hull and pendulum, as shown in the off-diagonal terms of (5) and (4), while k_{pto} only affects the diagonal term of the pendulum. Therefore, it appears that the control-informed optimisation algorithm favours lighter pendulums with negative k_{PTO} rather than heavier pendulums and higher k_{PTO}.

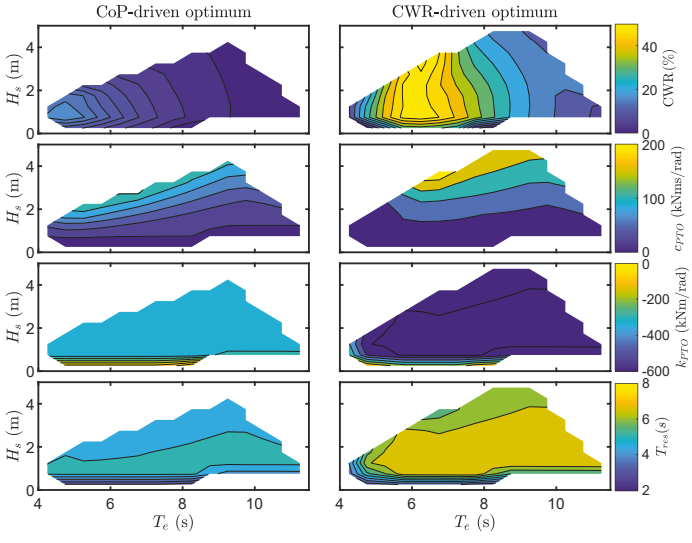

Figure 17. Capture width ratio, reactive control parameters and resonant period of the pendulum for the CoP-driven and CRW-driven optima. The same colour bar is used for each row, in order to favour comparison.

4.2. Techno-Economic Trends and Considerations

It is important to remark that Figures 14 and 15, although representative, are just three examples. Moreover, comments so far have no general or absolute validity, since many interrelated parameters comes into play. In order to investigate significant and more informative trends, Figures 18–21 show relevant results and design parameters for a selection of 28 devices, chosen in order to be representative of the fittest individuals in the whole population, according to the two evaluation metrics considered (CWR and CoP). In practice, the range of CWR from 0% to 30% is equally divided into 14 bins, and the individual with highest CWR of each bin is selected. Likewise, the range of CoP from 500 EUR/MWh to 1000 EUR/MWh is equally divided into 14 bins, and the individual with lowest CoP of each bin is selected. In order to highlight the most convenient individual, according to each metric, bars colour is proportional to CWR and 1/CoP, for the left and right graphs, respectively, so that best devices are represented by blue bars, while worst devices are in red.

The first row of Figure 18 highlights that high CWRs consistently result in high CoPs and vice versa, remarking that conversion efficiency and economic ability can be contrasting objective. It follows that the best devices in the CWR sense (blue bars in the left column) have high CoP. Conversely, the best devices in the CoP sense (blue bars in the right column) are economically performant in spite of their low CWR. In fact, the second and third rows of Figure 18 show that high AEPs come at high device costs and their ratio is more convenient at low AEP.

Figure 19 explores variations in the hull dimensions, which are the main drivers of hydrodynamic performance, and consequent mass, which is proportional to the hull cost. On the one hand, while CWR consistently increases with the hull length, longer hulls generate high CoP. Conversely, the device width is about constant for all CWR and CoP bins, with strong variations just around the second and third bins of the CWR and CoP scales, respectively. Finally, mainly as a consequence of length and width trends, the hull mass increases for increasing CWR and CoP. In particular, low CoP devices require lighter and cheaper hulls.

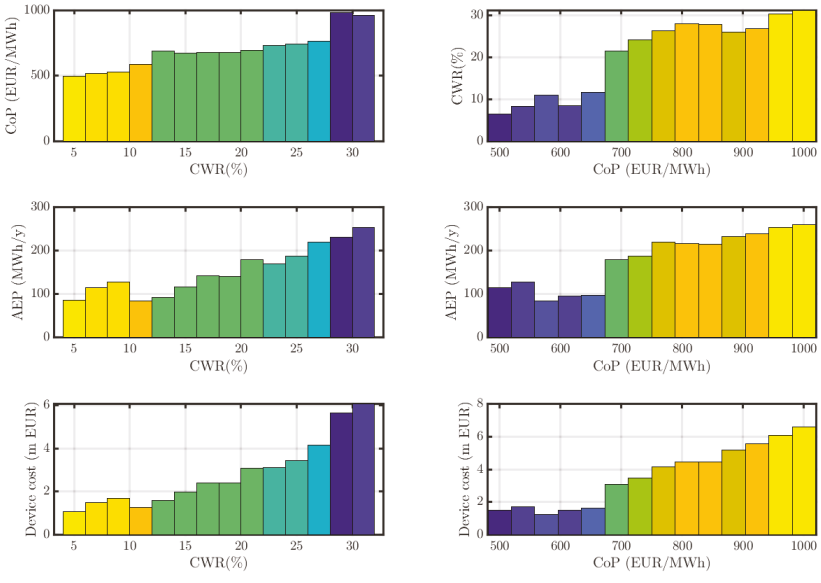

Figure 18. On the left: 14 individuals with the highest CWRs for each CWR-bin, with bars coloured proportionally to CWR. On the right: 14 individuals with the lowest CoPs for each CoP-bin, with bars coloured proportionally to 1/CoP.

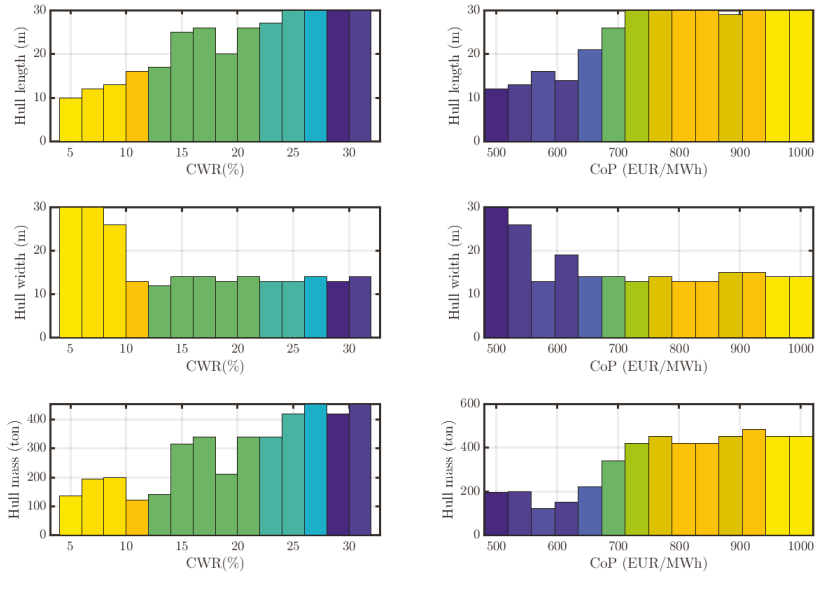

Figure 19. On the left: 14 individuals with highest CWR for each CWR-bin, with bars coloured proportionally to CWR. On the right: 14 individuals with lowest CoP for each CoP-bin, with bars coloured proportionally to 1/CoP.

Figure 20 shows the total pendulum mass, the geometry ratio and the number of pendulums. The cost of the unit is proportional to the total masses of pendulums and their numbers, since there is one PTO attached to each pendulum. Figure 20 shows that more and overall heavier pendulums

increase the CWR but also the CoP, in a similar trend found for the hull dimension and mass, confirming that the incremental investment required to produce more energy is not cost-effective. However, since the pendulums mass and number of pendulums follow the same trend, the single pendulum has about a constant mass in all bins. The geometry ratio σ_p defines how slender the pendulum is, considering the available space. Overall, although no strong correlation is found, it seems that once the masses and number of pendulums are defined, the algorithm leads to cylinders as long and slim as possible (high σ_p).

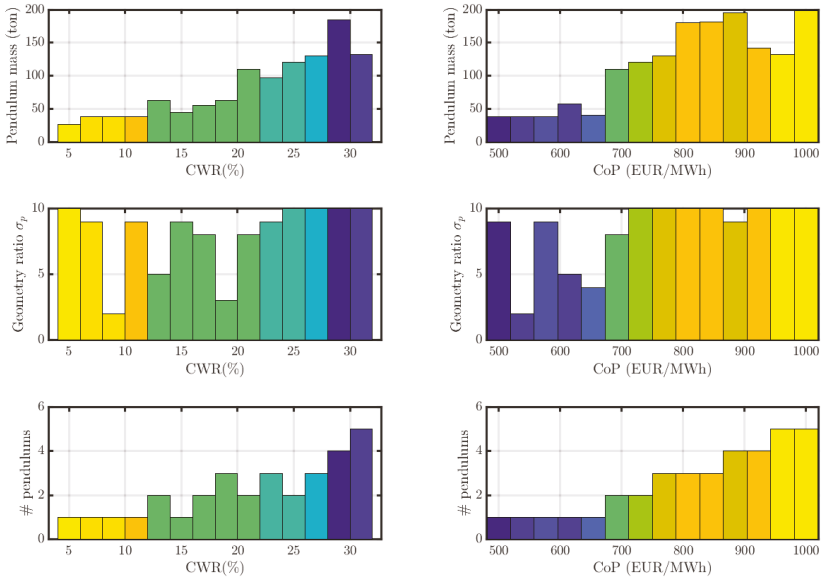

Figure 20. On the left: 14 individuals with the highest CWRs for each CWR-bin, with bars coloured proportionally to CWR. On the right: 14 individuals with the lowest CoPs for each CoP-bin, with bars coloured proportionally to 1/CoP.

Figure 21 shows that CWR and CoP are not particularly sensitive to the single-PTO parameters. In fact, the gearbox ratio is almost always the highest available, while the highest rated torque is often selected, despite the absence of a clear trend, especially in the CWR bins. Similarly, the rated torque is about equally split across both CWR and CoP bins, without any significant pattern. Consequently, the PTOs affect the performance mainly by means of their number, since there is an equal number of PTOs and pendulums: as the optimisation seeks more torque to increase the power conversion, since the largest PTO is already used, the number of pendulum units is increased. Likewise, it seems more cost effective to have fewer pendulums with the largest PTOs than more pendulums with small-medium PTOs.

Finally, Figure 22 shows the total and percentage costs, divided in the hull, pendulum and PTO subcomponents. On the one hand, the absolute cost of each subcomponent tends to increase with both CWR and CoP. On the other hand, the rates of increase seem to be different, since the hull tends to become less relevant in favour of the pendulum/PTO unit. Although the mass (and cost) of the hull increases (from 300 tons to 450 tons), as shown in Figure 19, the number (and cost) of pendulums/PTOs increases at a higher rate (from 1 to 5), as shown in Figure 20. Therefore, Figure 22 shows that the proportional increase of pendulum units has a higher impact than the increase of hull dimension and mass. Alternatively, it can be inferred that the optimisation algorithm reduces the number of

pendulum units in order to reduce the CoP. Conversely, in order to increase the CWR, regardless of subcomponents cost, there must be a higher number of conversion units.

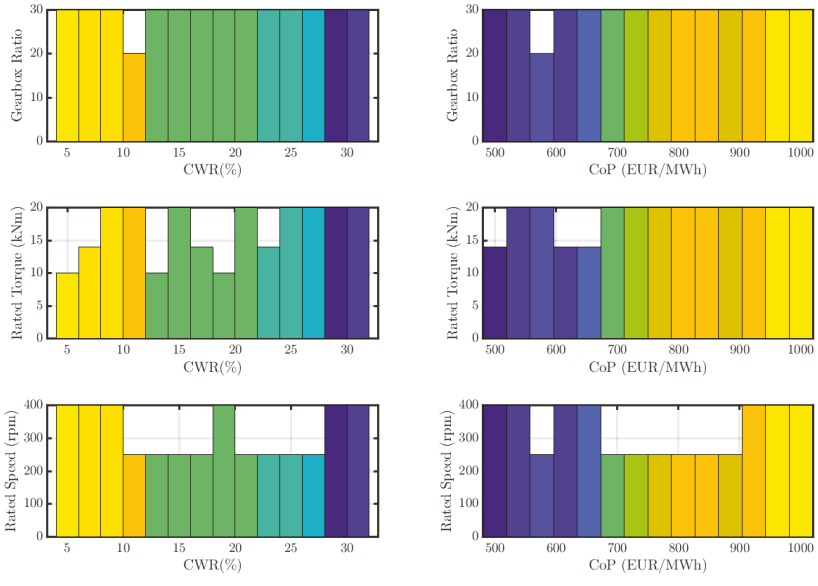

Figure 21. On the left: 14 individuals with the highest CWRs for each CWR-bin, with bars coloured proportionally to CWR. On the right: 14 individuals with lowest the CoPs for each CoP-bin, with bars coloured proportionally to 1/CoP.

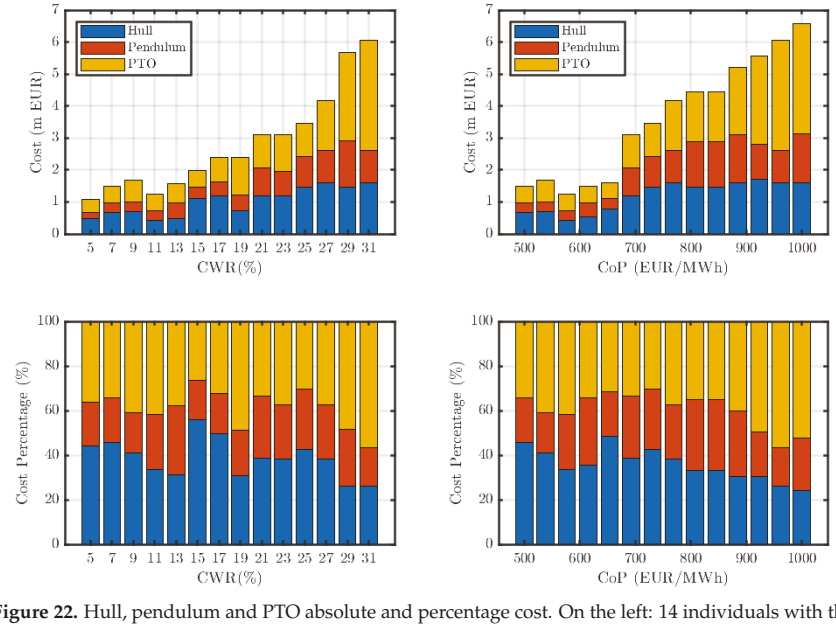

Figure 22. Hull, pendulum and PTO absolute and percentage cost. On the left: 14 individuals with the highest CWRs for each CWR-bin. On the right: 14 individuals with the lowest CoPs for each CoP-bin.

The results discussed so far highlight a limitation of the current concept, which is also an opportunity for substantial improvement. In particular, CWR and CoP are partially competing objectives, due to intrinsic limitations and assumptions. In all configurations, while the largest PTO and gearbox ratio possible are selected, the numbers of pendulum/PTO units are mainly selected in order to either maximise CWR or minimise CoP. Therefore, if the total cost of the PTO system could be decreased while maintaining the same conversion ability, both CWR and CoP would benefit. This can be achieved by connecting each PTO to more than one pendulum. However, since this solution implies requiring an even higher PTO torque, electrical generators become ill-suited. Conversely, hydraulic PTOs work better with high loads at low speed, so the gearbox could also be removed. Moreover, virtually, just one hydraulic PTO could be connected to all pendulums by means of an appropriate hydraulic system. Although the hydraulic PTO system introduces more power losses, the overall cost benefits could lead to a significantly lower CoP.

5. Conclusions

The present paper tackles a comprehensive techno-economic optimisation of a floating wave energy converter via genetic algorithm, considering a wide multi-variate design space, including shape and dimensions of the floater, and subcomponent configuration and characteristics. It is crucial to consider both power conversion ability and total cost of the device, taking physical constraints and control into account for a realistic assessment of the overall performance. Results herein presented are preliminary and not meant to have general validity since they are the consequence of specific techno-economic assumptions and hypotheses on the working principle and configuration. However, there is general validity in stating that the optimisation objective has a great influence on the optimised design, so it should be carefully chosen to be as close as possible to the actual intended target. In this paper it is shown that *efficient* conversion does not necessary imply *economical* conversion. On the contrary, for the specific case analysed, it resulted that increasing conversion efficiency required an excessive increase in costs, so that the most convenient solution in the economic sense had a relatively low conversion efficiency. Moreover, specific and detailed techno-economic considerations at an early design optimisation stage can lead to substantial conceptual modifications of the system, impossible at a mature development stage, which may be key for the success of such technology.

Author Contributions: Conceptualisation, L.F., S.A.S., G.G., M.B., G.C., G.B. and G.M.; methodology, L.F., S.A.S., G.G., M.B., G.C., G.B. and G.M.; software, L.F., S.A.S., G.G., M.B.; validation, L.F., S.A.S., G.G., M.B.; formal analysis, L.F., S.A.S., G.G., M.B.; investigation, L.F., S.A.S., G.G., M.B., and G.C.; resources, G.G., G.B. and G.M.; data curation, L.F., S.A.S.; writing—original draft preparation, L.F., S.A.S. and G.G.; writing—review and editing, L.F., S.A.S., G.G. and G.C.; visualisation, L.F., S.A.S., G.G. and G.C.; supervision, G.B. and G.M.; project administration, G.B. and G.M.; funding acquisition, G.G., G.B. and G.M. All authors have read and agreed to the published version of the manuscript.

Funding: This research has received funding from the Italian National Agency for New Technologies, Energy and Sustainable Economic Development (ENEA), under the project PTR-PTR_19_21_ENEA_PRG_7. Furthermore, this research was also partially funded by the European Research Executive Agency (REA) under the European Union's Horizon 2020 research and innovation programme under grant agreement No 832140.

Acknowledgments: Computational resources provided by hpc@polito (http://hpc.polito.it).

Conflicts of Interest: The authors declare no conflict of interest. The funders had no role in the design of the study; in the collection, analyses, or interpretation of data; in the writing of the manuscript, or in the decision to publish the results.

Appendix A. Genetic Algorithm

Genetic algorithms find their best applications in complex and multi-dimensional optimisation problems, especially those with no analytical formulation of cost and constraint functions. The usual way to handle constraints is via penalty functions, worsening the fitness value in order to avoid unfeasible individuals to proceed in the optimisation. However, in approaches implementing multi-level [48] or dynamic [49] penalty functions, deciding on the penalty parameter is challenging. Moreover, since there

is no direct analytical formulation of the constraints based on the input variables, specific constraint handling based on the knowledge of the mathematical structure (such as the cutting plane method, reduced gradient method or gradient projection method) is not applicable. On the other hand, since genetic algorithms are population based, pair-wise comparison tournament selection is possible [19]. In a tournament, no penalty parameter is required, but only a one-to-one comparison of the severity of the constraint violation. The design optimisation problem presents real variables, which can be handled more efficiently than binary variables, also avoiding the Hamming-Cliff effect [50]. Moreover, in order to improve the convergence rate, variables are defined in a discrete way through integers. The size of each step for each variable is decided by the engineer, based on common sense and previous experience. In this way, the number of possible combinations is reduced, and only significant variations of control parameters are allowed.

Based on previous consideration, the MI-LXPM genetic algorithm has been chosen; it is schematically shown in Figure A1, where:

- **MI**: mixed-integer [51];
- **LX**: Laplace crossover [52];
- **PM**: power mutation [53].

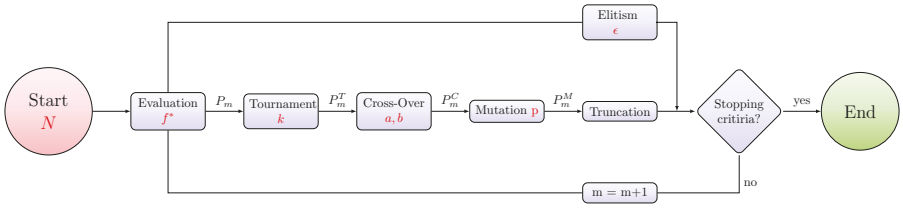

Figure A1. Flowchart of the MI-LXPM genetic algorithm. All phases are described in detail in Appendixes A.1–A.6. Major tuning parameters of the genetic algorithm are shown in red in the flow chart, and summarised in Table 4.

Appendix A.1. Optimisation Problem

The optimisation problem under study can be framed as the minimisation of a generic scalar function $f(\boldsymbol{x})$ of a vector $\boldsymbol{x}$, subject to various scalar constraints $g_i(\boldsymbol{x})$. Note that functions f and g_i present a notional dependence on $\boldsymbol{x}$, which does not necessary require an explicit mathematical formulation, since they can be evaluated via numerical simulation. Furthermore, each element $\boldsymbol{x}(j)$ of the input vector $\boldsymbol{x}$ is bounded, with $\boldsymbol{x}^L(j)$ being the lower bound and $\boldsymbol{x}^L(j)$ being the upper bound. Finally, note that all elements of $\boldsymbol{x}$ have discrete variations, defined as integer times appropriate steps. Therefore, the optimisation problem can be presented as follows:

$$\begin{aligned} \min_{\boldsymbol{x}} \quad & f(\boldsymbol{x}) \\ \text{subject to} \quad & g_i(\boldsymbol{x}) \geq 0 && \forall i, \\ & \boldsymbol{x}^L(j) \leq \boldsymbol{x}(j) \leq \boldsymbol{x}^U(j) && \forall j. \end{aligned} \tag{A1}$$

Constraints are enforced by applying a parameter-free penalty to the objective function when there is a constraint violation. As a condition, constraint functions $g_i(\boldsymbol{x})$ should also express the severity of the constraint violation, so that ranking between unfeasible position is possible. Therefore, the following fitness index (f^*) is defined:

$$f^*(\boldsymbol{x}) = \begin{cases} f(\boldsymbol{x}) & \text{if } g_i(\boldsymbol{x}) \geq 0 \ \ \forall i, \\ f_{\text{death}} + \frac{\Delta_C}{C} & \text{otherwise} \end{cases} \tag{A2}$$

where f_{death} is a death penalty and $\frac{\Delta_C}{C}$ represents the distance from of the unfeasible point to the violated constraint, normalised by the constraint itself, as shown in Figure A2. Note that, if f is bounded, f_{death} should be higher than the upper boundary. If f has no upper-boundary, then f_{death} can be iteratively updated with the maximum f until the current generation. Such a formulation, advantageous in handling feasibility and high mortality rates, requires and is made possible by a tournament-type selection of the fittest individuals, as explained in Appendix A.3.

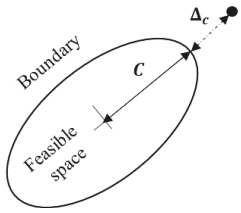

Figure A2. Schematic representation of the constraint violation handling, with reference to (A2).

Appendix A.2. Initial Population and Stopping Criteria

The algorithm starts from an initial population of N individuals, randomly chosen in the design space. The success and computational requirements of the optimisation depend, among other things, on N, which should be large enough to ensure diversification of the genetic code, but not excessively large, which would demand longer simulation time tp progress through generations.

In each iteration m of the algorithm, with $m = 1$ at the start, the population P_m goes through a tournament stage, a crossover stage, a mutation stage, and a truncation stage, described in Appendixes A.3–A.6, respectively. In this process, the population is appropriately modified in order to eventually reach a global optimum. However, according to the elitism principle, at each iteration there is a small percentage (ϵ) of the current population which by-passes the mixing-scheme without modifying its genetic information. Such an elite group is formed by the best individuals, whose genetic information should be passed down to the next generation.

The algorithm iterates until one of the two following stopping criteria is met:

(a) The relative variation of the best fitness index ($f^*_{\min}$) over the previous M_Δ generations is less than a threshold tolerance Δ;
(b) The generation count m reaches the allowed limit (M).

Satisfying criterion (a) represents a successful convergence to a minimum. If the population is large enough and with appropriate genetic algorithm parameters (see following sections), such a minimum can be confidently assumed to be also the absolute minimum within given boundaries. On the contrary, if the exit condition is (b), either Δ is overly strict, or the algorithm did not converge, so the tuning parameters of the algorithm should be adjusted.

Appendix A.3. Tournament

The tournament stage implements the survival-of-the-fittest principle by creating an appropriate mating pool P^T_m, where P^T_m stands for the m-population P_m after the tournament phase (T). In each tournament, there are k individuals competing, where k is the tournament size. The winner of each tournament is copied in the mating pool and can continue competing. Every individual takes part to exactly k tournaments so that $(1-\epsilon)N$ tournaments are played, and in turn, the mating pool is finally populated by $(1-\epsilon)N$ individuals. It is worth noting that the best-overall individual wins all matches, hence sending k copies of itself into the mating pool and ensuring higher chances to pass their genes over to the next generation. Conversely, the worst-overall individual loses all matches and disappear from the population. In each tournament, the k individuals are compared in pairs until the one that

wins all comparisons is found.. If both individuals are feasible, the one with lowest fitness value wins. If only one is feasible, it survives. If both individuals are unfeasible, the one with lowest constraint violation wins.

Appendix A.4. Laplace Crossover

The crossover phase aims at appropriately mixing genetic information of two parents, randomly taken within the mating pool P_m^T, hence generating a set of off-springs, two from each parents, in order to preserve the total number of individuals. The population of off-springs is called P_m^C, which refers to the m-population P_m after crossover (C). The mixing of information should be a compromise between the need to preserve optimal characteristics of the parents and introducing variability in the genetic code.

Let us consider two arbitrary individuals n_1 and n_2 from the m-population mating pool, namely $\left(\boldsymbol{x}_{n_1}^T, \boldsymbol{x}_{n_2}^T\right) \in P_m^T$. Two off-springs are generated, namely $\left(\boldsymbol{x}_{n_1}^C, \boldsymbol{x}_{n_2}^C\right) \in P_m^C$, in the following manner:

$$\boldsymbol{x}_n^C(j) = \boldsymbol{x}_n^T(j) + \beta_j \left|\boldsymbol{x}_{n_1}^T(j) - \boldsymbol{x}_{n_2}^T(j)\right| \ , \ \forall j \ \text{ and } \ n \in [n_1, n_2] \tag{A3}$$

where β_j satisfies the Laplace distribution thanks to the following formulation:

$$\beta_j = \begin{cases} a - b\log\left(u_j\right), & \text{if } \ r_j \leq \frac{1}{2} \\ a + b\log\left(u_j\right), & \text{if } \ r_j > \frac{1}{2} \end{cases} \tag{A4}$$

with u_j and r_j uniform random numbers between 0 and 1, a the location parameter (usually set to 0) and $b > 0$ the scaling parameter. From (A3) and (A4), it is clear that the scaling parameter determines how far the off-springs fall from the parents, hence affecting the convergence rate and success.

Appendix A.5. Power Mutation

Once off-springs are generated, it is necessary to add random variations in the population in order to appropriately investigate the whole design space and avoid the risk of convergence to a local but not global minimum. This is the objective of the mutation phase, generating the P_m^M population, referring to the m-population P_m after mutation (M). A power-distribution mutation scheme is adopted, creating a new individual $\boldsymbol{x}_n^M$ in the proximity of $\boldsymbol{x}_n^C$ as follows:

$$\boldsymbol{x}_n^M(j) = \begin{cases} \boldsymbol{x}_n^C(j) - s_j^p\left(\boldsymbol{x}_n^C(j) - \boldsymbol{x}^L(j)\right), & \text{if } \ t_j < r_j \\ \boldsymbol{x}_n^C(j) + s_j^p\left(\boldsymbol{x}^U(j) - \boldsymbol{x}_n^C(j)\right), & \text{if } \ t_j \geq r_j \end{cases} \ , \ \forall j \tag{A5}$$

with

$$t_j = \frac{\boldsymbol{x}_n^C(j) - \boldsymbol{x}^L(j)}{\boldsymbol{x}^U(j) - \boldsymbol{x}_n^C(j)} \tag{A6}$$

and s_j and r_j uniform random numbers between 0 and 1, and p is the index of mutation, determining the strength of the perturbation induced by the power mutation. It follows that, if $p < 1$, s_j^p is statistically closer to 1, amplifying the mutation; conversely, if $p > 1$, s_j^p is statistically closer to 0, attenuating the mutation [51].

Appendix A.6. Truncation

In general, after crossover and mutation, design variables are real values different from the discrete set in the problem definition, shown in (A1). Therefore, for each individual, each element is randomly approximated to either the discretised input variable right below or above, with equal probability. Such an approach ensures to keep the optimisation problem discrete, while adding further randomness in the process.

References

1. Gunn, K.; Stock-Williams, C. Quantifying the global wave power resource. *Renew. Energy* **2012**, *44*, 296–304. [CrossRef]
2. Weber, J. WEC Technology Readiness and Performance Matrix—Finding the best research technology development trajectory. In Proceedings of the 4th International Conference on Ocean Energy (ICOE), Dublin, Ireland, 17–19 October 2012; pp. 1–10.
3. Weber, J.; Roberts, J. Cost, time and risk assessment of different wave energy converter technology development trajectories. In Proceedings of the Twelfth European Wave and Tidal Energy Conference, Cork, Ireland, 27 August–1 September 2017.
4. Penalba, M.; Ringwood, J.V. A high-fidelity wave-to-wire model for wave energy converters. *Renew. Energy* **2019**, *134*, 367–378. [CrossRef]
5. Genuardi, L.; Bracco, G.; Sirigu, S.A.; Bonfanti, M.; Paduano, B.; Dafnakis, P.; Mattiazzo, G. An application of model predictive control logic to inertial sea wave energy converter. In *Mechanisms and Machine Science*; Springer Nature: Heidelberg, Germany, 2019; Volume 73, pp. 3561–3571. [CrossRef]
6. Bracco, G.; Casassa, M.; Giorcelli, E.; Giorgi, G.; Martini, M.; Mattiazzo, G.; Passione, B.; Raffero, M.; Vissio, G. Application of sub-optimal control techniques to a gyroscopic Wave Energy Converter. *Renew. Energ. Offshore* **2014**, *1*, 265–269.
7. Sirigu, A.S.; Gallizio, F.; Giorgi, G.; Bonfanti, M.; Bracco, G.; Mattiazzo, G. Numerical and Experimental Identification of the Aerodynamic Power Losses of the ISWEC. *J. Mar. Sci. Eng.* **2020**, *8*, 49. [CrossRef]
8. de Andres, A.; Maillet, J.; Todalshaug, J.H.; Möller, P.; Bould, D.; Jeffrey, H. Techno-economic related metrics for a wave energy converters feasibility assessment. *Sustainability* **2016**, *8*, 1109. [CrossRef]
9. Farrell, N.; Donoghue, C.; Morrissey, K. Quantifying the uncertainty of wave energy conversion device cost for policy appraisal: An Irish case study. *Energy Policy* **2015**, *78*, 62–77. [CrossRef]
10. Giorgi, G.; Ringwood, J.V. Analytical formulation of nonlinear Froude-Krylov forces for surging-heaving-pitching point absorbers. In Proceedings of the ASME 2018 37th International Conference on Ocean, Offshore and Arctic Engineering, Madrid, Spain, 17–22 June 2018.
11. Giorgi, G.; Ringwood, J.V. Articulating parametric nonlinearities in computationally efficient hydrodynamic models. In Proceedings of the 11th IFAC Conference on Control Applications in Marine Systems, Robotics, and Vehicles, Opatija, Croatia, 10–12 September 2018.
12. Ringwood, J.V.; Merigaud, A.; Faedo, N.; Fusco, F. Wave Energy Control Systems: Robustness Issues. In Proceedings of the IFAC Conference on Control Aplications in Marine Systems, Robotics, and Vehicles, Opatija, Croatia, 10–12 September 2018.
13. Ringwood, J.V.; Merigaud, A.; Faedo, N.; Fusco, F. An Analytical and Numerical Sensitivity and Robustness Analysis of Wave Energy Control Systems. *IEEE Trans. Control Syst. Technol.* **2019**, *28*, 1337–1348. [CrossRef]
14. Giorgi, G.; Ringwood, J.V. Parametric motion detection for an oscillating water column spar buoy. In Proceedings of the 3rd International Conference on Renewable Energies Offshore RENEW, Lisbon, Portugal, 8–10 October 2018.
15. Gilloteaux, J.C.; Ringwood, J.V. Control-informed geometric optimisation of wave energy converters. *IFAC Proc. Vol. (IFAC-PapersOnline)* **2010**, *43*, 366–371. [CrossRef]
16. Garcia-Rosa, P.; Bacelli, G.; Ringwood, J. Control-Informed Geometric Optimization of Wave Energy Converters: The Impact of Device Motion and Force Constraints. *Energies* **2015**, *8*, 13672–13687. [CrossRef]
17. Giorgi, G.; Ringwood, J.V. Articulating parametric resonance for an OWC spar buoy in regular and irregular waves. *J. Ocean Eng. Mar. Energy* **2018**, *4*, 311–322. [CrossRef]
18. Novo, R.; Bracco, G.; Sirigu, S.; Mattiazzo, G.; Merigaud, A.; Ringwood, J. Non-linear simulation of a wave energy converter with multiple degrees of freedom using a harmonic balance method. In Proceedings of the International Conference on Offshore Mechanics and Arctic Engineering (OMAE), Madrid, Spain, 17–22 June 2018; Volume 10. [CrossRef]
19. Deb, K. An efficient constraint handling method for genetic algorithms. *Comput. Methods Appl. Mech. Eng.* **2000**, *186*, 311–338. [CrossRef]
20. Göteman, M.; Giassi, M.; Engström, J.; Isberg, J. Advances and Challenges in Wave Energy Park Optimization—A Review. *Front. Energy Res.* **2020**, *8*, 26. [CrossRef]
21. Birk, L. Application of constrained multi-objective optimization to the design of offshore structure hulls. *J. Offshore Mech. Arct. Eng.* **2009**, *131*, 011301. [CrossRef]

22. Sharp, C.; DuPont, B. Wave energy converter array optimization: A genetic algorithm approach and minimum separation distance study. *Ocean Eng.* **2018**, *163*, 148–156. [CrossRef]
23. Giassi, M.; Göteman, M. Layout design of wave energy parks by a genetic algorithm. *Ocean Eng.* **2018**, *154*, 252–261. [CrossRef]
24. Shadman, M.; Estefen, S.F.; Rodriguez, C.A.; Nogueira, I.C. A geometrical optimization method applied to a heaving point absorber wave energy converter. *Renew. Energy* **2018**, *115*, 533–546. [CrossRef]
25. Kurniawan, A.; Moan, T. Optimal geometries for wave absorbers oscillating about a fixed axis. *IEEE J. Ocean. Eng.* **2013**, *38*, 117–130. [CrossRef]
26. McCabe, A.P. Constrained optimization of the shape of a wave energy collector by genetic algorithm. *Renew. Energy* **2013**, *51*, 274–284. [CrossRef]
27. Cordonnier, J.; Gorintin, F.; De Cagny, A.; Clément, A.H.; Babarit, A. SEAREV: Case study of the development of a wave energy converter. *Renew. Energy* **2015**, *80*, 40–52. [CrossRef]
28. Pozzi, N.; Bonetto, A.; Bonfanti, M.; Bracco, G.; Dafnakis, P.; Giorcelli, E.; Passione, B.; Sirigu, S.; Mattiazzo, G. PeWEC: Preliminary design of a full-scale plant for the mediterranean sea. In Proceedings of the NAV International Conference on Ship and Shipping Research, Trieste, Italy, 20–22 June 2018; pp. 504–514. [CrossRef]
29. Ruellan, M.; Benahmed, H.; Multon, B.; Josset, C.; Babarit, A.; Clement, A. Design methodology for a SEAREV wave energy converter. *IEEE Trans. Energy Convers.* **2010**, *25*, 760–767. [CrossRef]
30. Sirigu, S.A.; Bonfanti, M.; Begovic, E.; Bertorello, C.; Dafnakis, P.; Bracco, G.; Mattiazzo, G. Experimental Investigation of Mooring System on a Wave Energy Converter in Operating and Extreme Wave Conditions. *J. Mar. Sci. Eng.* **2020**, *8*, 180. [CrossRef]
31. Pozzi, N.; Bracco, G.; Passione, B.; Sirigu Sergej, A.; Vissio, G.; Mattiazzo, G.; Sannino, G. Wave Tank Testing of a Pendulum Wave Energy Converter 1:12 Scale Model. *Int. J. Appl. Mech.* **2017**, *9*, 1750024. [CrossRef]
32. Sirigu, S.A.; Bonfanti, M.; Passione, B.; Begovic, E.; Bertorello, C.; Dafnakis, P.; Bracco, G.; Giorcelli, E.; Mattiazzo, G. Experimental investigation of the hydrodynamic performance of the ISWEC 1:20 scaled device. In Proceedings of the NAV International Conference on Ship and Shipping Research, Trieste, Italy, 20–22 June 2018; pp. 551–560. [CrossRef]
33. Pozzi, N. Numerical Modeling and Experimental Testing of a Pendulum Wave Energy Converter (PeWEC). Ph.D. Thesis, Polytechnic of Turin, Torino, Italy, 2018. [CrossRef]
34. Sirigu, S.; Bonfanti, M.; Dafnakis, P.; Bracco, G.; Mattiazzo, G.; Brizzolara, S. Pitch Resonance Tuning Tanks: A novel technology for more efficient wave energy harvesting. In Proceedings of the OCEANS 2018 MTS/IEEE Charleston (OCEAN 2018), Charleston, SC, USA, 22–25 October 2019. [CrossRef]
35. Bonfanti, M.; Bracco, G.; Dafnakis, P.; Giorcelli, E.; Passione, B.; Pozzi, N.; Sirigu, S.; Mattiazzo, G. Application of a passive control technique to the ISWEC: Experimental tests on a 1:8 test rig. In Proceedings of the NAV International Conference on Ship and Shipping Research,Trieste, Italy, 20–22 June 2018; pp. 60–70. [CrossRef]
36. Sirigu, S.A.; Bracco, G.; Bonfanti, M.; Dafnakis, P.; Mattiazzo, G. On-board sea state estimation method validation based on measured floater motion. *IFAC-PapersOnLine* **2018**, *51*, 68–73. [CrossRef]
37. Giorgi, G.; Gomes, R.P.F.; Bracco, G.; Mattiazzo, G. The effect of mooring line parameters in inducing parametric resonance on the Spar-buoy oscillating water column wave energy converter. *J. Mar. Sci. Eng.* **2020**, *8*, 29. [CrossRef]
38. Babarit, A.; Delhommeau, G. Theoretical and numerical aspects of the open source BEM solver NEMOH. In Proceedings of the 11th European Wave and Tidal Energy Conference, Nantes, France, 6–11 September 2015; pp. 1–12.
39. Pozzi, N.; Bracco, G.; Passione, B.; Sirigu, S.A.; Mattiazzo, G. PeWEC: Experimental validation of wave to PTO numerical model. *Ocean Eng.* **2018**, *167*, 114–129. [CrossRef]
40. Fontana, M.; Casalone, P.; Sirigu, S.A.; Giorgi, G. Viscous Damping Identification for a Wave Energy Converter Using CFD-URANS Simulations. *J. Mar. Sci. Eng.* **2020**, *8*, 355. [CrossRef]
41. Penalba, M.; Giorgi, G.; Ringwood, J.V. Mathematical modelling of wave energy converters: A review of nonlinear approaches. *Renew. Sustain. Energy Rev.* **2017**, *78*, 1188–1207. [CrossRef]
42. Giorgi, G.; Gomes, R.P.F.; Bracco, G.; Mattiazzo, G. Numerical investigation of parametric resonance due to hydrodynamic coupling in a realistic wave energy converter. *Nonlinear Dyn.* **2020**. [CrossRef]
43. Lagarias, J.C.; Reeds, J.A.; Wright, M.H.; Wright, P.E. Convergence properties of the nelder–mead simplex method in low dimensions. *SIAM J. Optim.* **1998**, *9*, 112–147. [CrossRef]

44. Garcia-Teruel, A.; Forehand, D.I.; Jeffrey, H. Wave Energy Converter hull design for manufacturability and reduced LCOE. In Proceedings of the 7th International Conference on Ocean Energy (ICOE), Cherbourg, Normandy, France, 12–13 June 2018; pp. 1–9.
45. Emmerich, M.T.; Deutz, A.H. A tutorial on multiobjective optimization: Fundamentals and evolutionary methods. *Nat. Comput.* **2018**, *17*, 585–609. [CrossRef]
46. Astariz, S.; Iglesias, G. Enhancing Wave Energy Competitiveness through Co-Located Wind and Wave Energy Farms. A Review on the Shadow Effect. *Energies* **2015**, *8*, 7344–7366. [CrossRef]
47. Miettinen, K. *Nonlinear Multiobjective Optimization*, 1st ed.; Springer: Boston, MA, USA, 1998; p. 298. [CrossRef]
48. Homaifar, A.; Qi, C.X.; Lai, S.H. Constrained Optimization Via Genetic Algorithms. *Simulation* **1994**, *62*, 242–253. [CrossRef]
49. Joines, J.A.; Houck, C.R. On the use of non-stationary penalty functions to solve nonlinear constrained optimization problems with GA's. In Proceedings of the First IEEE Conference on Evolutionary Computation (IEEE World Congress on Computational Intelligence), Orlando, FL, USA, 27–29 June 1994; pp. 579–584. [CrossRef]
50. Cheung, B.K.; Langevin, A.; Delmaire, H. Coupling Genetic Algorithm with a grid search method to solve Mixed Integer Nonlinear Programming problems. *Comput. Math. Appl.* **1997**, *34*, 13–23. [CrossRef]
51. Deep, K.; Singh, K.P.; Kansal, M.L.; Mohan, C. A real coded genetic algorithm for solving integer and mixed integer optimization problems. *Appl. Math. Comput.* **2009**, *212*, 505–518. [CrossRef]
52. Deep, K.; Thakur, M. A new crossover operator for real coded genetic algorithms. *Appl. Math. Comput.* **2007**, *188*, 895–911. [CrossRef]
53. Deep, K.; Thakur, M. A new mutation operator for real coded genetic algorithms. *Appl. Math. Comput.* **2007**, *193*, 211–230. [CrossRef]

© 2020 by the authors. Licensee MDPI, Basel, Switzerland. This article is an open access article distributed under the terms and conditions of the Creative Commons Attribution (CC BY) license (http://creativecommons.org/licenses/by/4.0/).

Journal of
Marine Science and Engineering

MDPI

Article

Comparison of Wave Energy Park Layouts by Experimental and Numerical Methods

Marianna Giassi *, Jens Engström, Jan Isberg and Malin Göteman

Department of Electrical Engineering, Uppsala University, Ångströmlaboratoriet, Box 65, 75103 Uppsala, Sweden; jens.engstrom@angstrom.uu.se (J.E.); jan.isberg@angstrom.uu.se (J.I.); malin.goteman@angstrom.uu.se (M.G.)

* Correspondence: marianna.giassi@angstrom.uu.se

Received: 11 September 2020; Accepted: 23 September 2020; Published: 26 September 2020

Abstract: An experimental campaign of arrays with direct-driven wave energy converters of point-absorbing type is presented. The arrays consist of six identical floats, moving in six degrees of freedom, and six rotating power take-off systems, based on the design developed at Uppsala University. The goals of the work were to study and compare the performances of three different array layouts under several regular and irregular long-crested waves, and in addition, to determine whether the numerical predictions of the best performing array layouts were confirmed by experimental data. The simulations were executed with a frequency domain model restricted to heave, which is a computationally fast approach that was merged into a genetic algorithm optimization routine and used to find optimal array configurations. The results show that good agreement between experiments and simulations is achieved when the test conditions do not induce phenomena of parametric resonance, slack line and wave breaking. Specific non-linear dynamics or extensive sway motion are not captured by the used model, and in such cases the simulation predictions are not accurate, but can nevertheless be used to get an estimate of the power output.

Keywords: wave energy; arrays; experiments; wave tank; scale test; point absorber; array optimization

1. Introduction

Within ocean waves, an incredibly huge amount of energy is stored which can potentially be extracted and transformed into electricity. An efficient way to produce power in the MW range and to reduce the power fluctuations and the overall costs, is to construct and deploy parks of wave energy converters (WECs). As wave energy technologies are now facing the challenge of early stage commercialization, it is crucial to have access to accurate hydrodynamic and optimization simulation tools for such arrays of converters.

However, analytical and numerical modeling is always connected with some approximations and uncertainties, and physical experiments are required to validate the numerical results. Experiments of wave energy arrays are both expensive and complex to carry out, and it is only in recent years that several large-scale physical experiments have been conducted and their results published [1]. Nevertheless, experimental data are required to validate the numerical models, allowing for an understanding of the levels of uncertainty of the tools commonly used in the design process. In particular, due to the high computational cost, optimization of WEC arrays is typically carried out using simplified models based on assumptions such as restricted degrees of freedom, linear equations that can be solved in the frequency domain, unidirectional waves, etc. There has been little published work comparing these models to the experimental data of arrays and evaluating their validity.

Only a few physical experiments on arrays of point-absorbing WECs have been carried out during the past few years. Konispoliatis and Mavrakos [2] experimentally studied three floating oscillating water column (OWC) devices and compared the results with a semi-analytical multiple scattering

method. Experimental results from a three spar-buoy type OWC in scale 1:32 were presented in da Fonseca et al. [3] and compared to the case of an isolated device. The interaction factor in an array of OWC was measured by Magagna et al. [4]. Wolgamot et al. [5] studied trapped modes within an array of eight fixed truncated cylinders, and Ji et al. [6] observed near-trapping in an array of fixed cylinders in short-crested waves. da Fonseca et al. [3] studied a triangular array of three spar-buoy WECs in scale 1:32, and it was observed that the interaction factor was larger than 1 in wave climates with large energy periods. Five fixed OWCs deployed in two different layouts (chosen based on earlier layout optimization) were studied experimentally and numerically by Bosma et al. [7], both in regular and irregular waves: a maximal power increase of 12% was found between the non-optimal and the optimal layout. In Mackay et al. [8], an array consisting of four Wavebob models at scale 1:19 was studied experimentally and compared to a numerical time-domain model. Mercadé Ruiz et al. [9] presented results from numerical simulations and experiments for five WaveStar devices at scale 1:20. Mackay et al. [8] and Mercadé Ruiz et al. [9] studied one array layout, typically a staggered park geometry or WECs in line. On the other hand, Troch et al. [10], Stratigaki et al. [11,12] studied several array layouts with up to 25 heaving point-absorber buoys connected to friction-damping power take-off systems (PTO). In these studies it was found that the wave height was reduced by up to 18% due to park effects. Similarly, Child and Weywada [13] presented results from an analogous experimental set-up with different array layouts of 24 heaving buoys; it was found that the park could experience up to 26% energy loss due to park interactions. Experimental measurements of the responses of an array of five heaving floats in regular waves were compared to numerical predictions in Thomas et al. [14], and in irregular waves by Weller et al. [15]. Nader et al. [16] and Thomas et al. [17] performed array experiments of up to four point-absorber WECs moving in six degrees of freedom. The former experiment, performed at the Australian Maritime College, measured the interaction factor for 1 or 2 floats moving in heave and surge, by tracking the surface elevation with videogrammic measurements. The latter consisted of testing both a linear damping and an advanced control algorithm based on machine learning and artificial neural networks [18]. The energy absorption of three array layouts of WECs with linear damping was compared for six devices in Giassi et al. [19].

Uppsala University (UU) has developed a wave energy converter concept consisting of a buoy and a linear generator (LG) [20]. The buoy transmits the movement of the waves to the translator of the LG on the sea bed and is free to move in six degrees of freedom (DoF). Permanent magnets are mounted on the translator and, during the vertical movement of the translator, electricity is induced in the coils located in the stator, according to Faraday's law of induction.

This paper presents results from an experimental campaign of wave energy converter arrays. The work was carried out in the COAST Lab at Plymouth University, UK: three different arrays of six devices have been tested under several regular and irregular wave conditions. The model represents a 1:10 scaled prototype of an array of point absorbers, based on the WEC concept developed at Uppsala University. The experimental set-up consisted of six identical ellipsoidal floats free to move in six degrees of freedom and connected via ropes and pulleys to six power take-off systems (PTO) located on a gantry above the water. The PTO was performed by passive damping using a rotatory system appositely designed for the wave tank experiment, described in detail in [21]. To the knowledge of the authors, this experiment represents the first one on point absorbing WEC arrays moving in six degrees of freedom published so far.

The goals of the work are multiple: to provide a set of data for validation of the array model, to study the performances of different array layouts under several wave conditions and to understand whether the genetic algorithm's optimization tool developed for the specific UU WEC technology [22] can predict optimal layouts in realistic situations. In fact, if the objective function of the optimization is the maximization of the power output, different possible solutions (i.e., array layouts) must be ranked according to their hydrodynamic performance. This experiment intended to clarify whether the predictions of the simulations of the best performing array layouts would be confirmed by experimental data.

In [23] we published the results obtained with a single device in isolation. In [19] the physical set-up was described and some preliminary results in terms of measurements of the wave elevation in the tank and energy absorption for three different array configurations are presented. Here, we present results in terms of array power absorption for different sea states, and for each buoy within the arrays. Through the calculation of the interaction factor (q-factor), the results have been compared to the prediction of the model.

This paper is organized as follows: the numerical model used for the simulation is described in Section 2. Section 3 describes the physical experiments, including the set-up, the array layouts and the tests that were carried out. In Section 4 we describe the parameters used in the array simulations. In Section 5, results of the modeling and experiment are presented and discussed. Further conclusions are drawn in Section 6.

2. Theory and Numerical Model

Mathematical Model

A semi-analytical frequency domain model based on linear potential flow theory and implemented in MATLAB has been used to model the array of converters. We consider a park of n_b WECs labelled by $i = 1, \ldots, n_b$. Each WEC consists of a float, which is a truncated cylinder with individual radius R^i and draft d^i, and the generator is characterized by individual power take-off constants γ^i. The model's equation of motion is restricted to heave motion and unlimited stroke length is assumed. The float and the generator are assumed to be connected by a stiff line, so that one single coupled equation of motion can be written for the float-translator system

$$m\ddot{z}^i(t) = F^i_{\text{exc}}(t) + F^i_{\text{rad}}(t) + F^i_{\text{PTO}}(t) + F^i_{\text{stat}}(t) \tag{1}$$

where $m = m_b + m_t$ is the total mass of the float and the translator, F^i_{exc} and F^i_{rad} are the hydrodynamic excitation and radiation forces, respectively, $F^i_{\text{PTO}}(t) = -\gamma^i \dot{z}^i(t)$ is the power take-off force and $F^i_{\text{stat}}(t) = \rho g \pi {R^i}^2 (d^i - z^i(t))$ is the hydrostatic restoring force.

By Fourier transformation, the problem can be considered in the frequency domain, in which the equation of motion (1) takes the form

$$\left[-\omega^2(m^i + m^i_{\text{add}}(\omega)) - i\omega(B^i(\omega) + \gamma^i) - \rho g \pi {R^i}^2\right] z^i(\omega) = f^i_{\text{exc}}(\omega)\eta^i(\omega) \tag{2}$$

where the radiation force has been divided into added mass (m_{add}) and radiation damping (B) as $F^i_{\text{rad}}(\omega) = [\omega^2 m^i_{\text{add}}(\omega) + i\omega B^i(\omega)]z^i$ and $f^i_{\text{exc}}(\omega)$ and $\eta^i(\omega)$ are the frequency domain amplitudes of the excitation force and of the incident waves, respectively. The hydrodynamic forces are computed as surface integrals over the wetted surfaces of the buoys, $\bar{F} = i\omega\rho \iint_S \phi \, d\bar{S}$, where ϕ represents the fluid velocity potential that satisfies the Laplace equation in the fluid domain and which is a superposition of incident, scattered and radiated waves, $\phi = \phi_I + \phi_S + \phi_R$. To evaluate the velocity potential in the fluid domain, a semi-analytical hydrodynamic model based on the multiple scattering method has been used, as previously presented in [24,25].

After computation of the forces, the dynamics of each WEC are determined in the time domain by inverse Fourier transform of the solution to the equation of motion (2), and the instantaneous power absorption computed as

$$P^{\text{i}}_{\text{SIM}}(t) = \gamma \cdot [\dot{z}^i(t)]^2. \tag{3}$$

The power output of the park will be the sum of all n_b converters:

$$P_{\text{SIM}}(t) = \sum_{i=1}^{n_b} P^i_{\text{SIM}}(t). \tag{4}$$

The frequency domain model has been coupled with an optimization model based on a genetic algorithm in previous works [22,26]. One of the goals of the present study was to verify the feasibility of optimizing parks of the Uppsala University WEC with such tools. The optimization routine aims to find the best array layout (i.e., set of coordinates of the WECs) which maximizes the power absorption. The genetic algorithm optimization was inspired by Charles Darwin's theory of evolution and iteratively follows these evolutionary steps: *natural selection*, *pairing*, *mating* or *crossover* and *mutation*. Each chromosome in the evolution represents a wave power park, and contains a number of genes equal to the number of WECs in the park. Each gene contains a couple of coordinates for each WEC. The optimization algorithm is described in detail in [22] and it was validated against a parameter sweep optimization for a single WEC, with excellent agreement.

3. Physical Experiments

3.1. Wave Tank

The experimental campaign was carried out in the COAST Lab at the University of Plymouth, UK. The Ocean basin is 35 m long and 15.5 m wide, with a moveable floor set to operate at a depth of 2.5 m. The waves are produced by 24 flap wave makers of 2.0 m hinge depth. At the end of the wave basin a parabolic beach provides energy dissipation and minimizes reflected waves.

A set of ten twin-wire resistance wave gauges have been used to measure the wave elevation at different locations around the basin. To avoid interference with the optical system for motion capture, all the probes are located on the right side of the tank (following the direction of the waves). Their position within the wave tank is shown in Figure 1a (G1 to G10), and was decided in order to enable measurement of the wave elevation at each line of the arrays, and the incoming and outgoing waves. The results of these data have been studied in [19]. On the basin floor floor, connection points for the WECs were installed in a 2 × 2 m grid (Figure 1b).

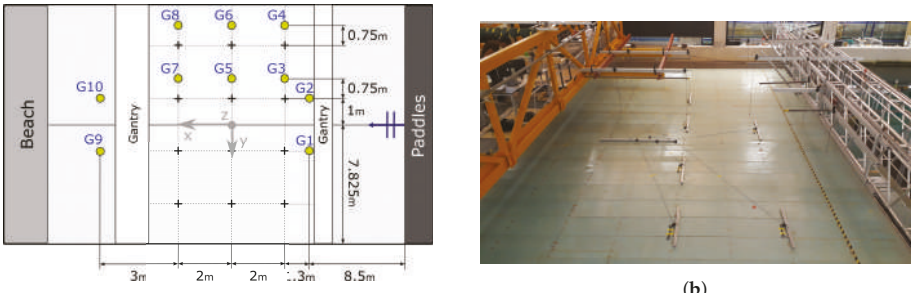

(**a**) (**b**)

Figure 1. (**a**) Schematic top view of the COAST wave basin and location of the the attachment grid (+) with respect to the paddles and the beach. G1–G10 show the locations of the ten wave gauges installed during the experiment. (**b**) Picture of the attachment bars on the basin floor.

3.2. Experimental Set-Up

The set-up used for this experiment is based on the one introduced in [21,23]. The wave energy converter model tested is a 1:10 scaled prototype based on the point-absorber wave energy concept developed at Uppsala University [20]. In the full-scale device, a buoy is connected via a rope to a linear generator positioned on the sea floor; the motion of the waves induces the motion of the buoy and of the sub-surface generator, inducing electricity in the coils of the stator.

Differently from the work carried out in [23], six devices have been tested simultaneously, forming a park of wave energy converters. Six identical ellipsoidal floating buoys made of polyethylene (0.488 m in diameter and 0.280 m in height; total mass 4378 g) have been used, connected via a system of highly stiff ropes (100% Dyneema, 3 mm) and pulleys (Harken, 57 mm) to the power take-off systems

located on the main gantry (Figure 2). Each float was equipped with five reflective markers for motion capture, which were tracked by a set of eight Qualisys six DoF cameras.

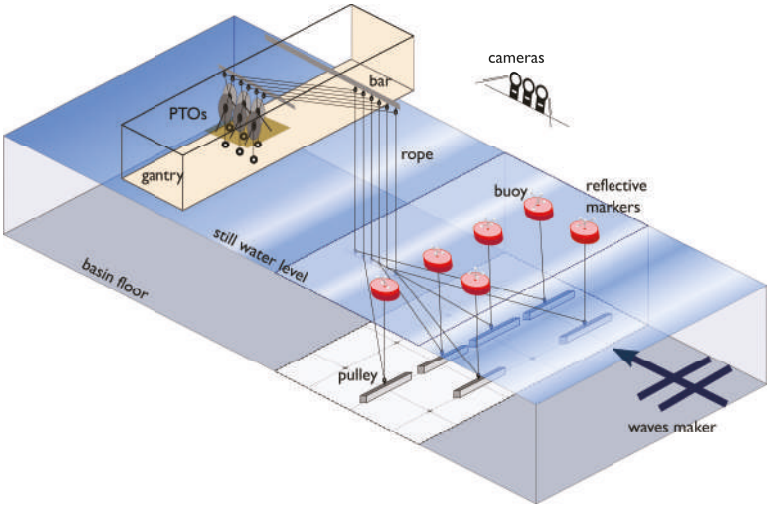

Figure 2. Sketch of the set-up's components.

The PTO is a rotatory system consisting of a table securely holding a bicycle truing stand (Tacx T3175) with a bicycle front hub (Shimano XT HB-M756) and a vice (Clarke CSV4E 100mm). On one external side of the bicycle hub, which has a low friction ball bearing, an aluminum disc (2 mm thickness × 40 mm diameter) was mounted, and on the internal part two ropes were wound in opposite directions. One line went towards the upper part through the pulley system to the float; the other line went downwards and held a 5 kg mass. On the vice's moveable clamps a set of magnets (5 × Neodymium N42 20 × 20 × 10 mm) were positioned. The damping γ of the PTO was changed by changing the air gap between the magnets and the aluminum disc, which changed the magnetic flux inside the disc. An inertia measurement unit (IMU, Intel Curie SoC) positioned on the disc recorded its rotational speed ω_d^i and accelerations in the disc plane. The experimental power output of each converter was then obtained as

$$P_{\mathrm{PTO}}^i(t) = \gamma \cdot [r\omega_d^i(t)]^2, \tag{5}$$

where $\omega_d^i(t)$ is the angular velocity of the i-*th* disc and r is the distance between the IMU and the center of the disc. Different damping values were achieved by varying the magnetic flux inside the disc, i.e., by manually changing the distance between the magnets and the aluminum disc. The damping was evaluated by measuring the achieved speed at steady-state with a known mass. In these experiments, a constant damping value of 306 Ns/m for all the converters was used. A more detailed discussion on the PTO and its damping can be found in [21].

3.3. Tests

Table 1 reports the characteristics of the sea states used in the experiment, together with the duration of each test (100 wave periods for regular waves tests and 20 min full scale for irregular wave tests). Waves were long-crested (unidirectional) and propagating along the positive x-axis direction in Figure 1a.

Five regular and five irregular sea states were studied for each layout, defined such that they had the same energy per ocean area and energy transport per meter wave crest. The significant wave

height was $H_s = 0.175$ m (scaled value), and the wave (energy) periods spanned the range 1.11–2.37 s. The time series of the irregular waves were obtained from the Bretschneider spectrum.

Table 1. Sea states tested in the wave tank. Top: regular waves, bottom: irregular waves. Scaled values (1:10) (left) and full scale values (right).

Regular Waves						
	Scale 1:10			Full scale		
Wave ID	H_{rms} [m]	T [s]	Run time [min]	H_{rms} [m]	T [s]	Run time [min]
RW1	0.124	1.11	1.8	1.24	3.5	5.8
RW2	0.124	1.42	2.4	1.24	4.5	7.5
RW3	0.124	1.74	2.9	1.24	5.5	9.2
RW4	0.124	2.06	3.4	1.24	6.5	10.8
RW5	0.124	2.37	4.0	1.24	7.5	12.5
Irregular Waves						
	Scale 1:10			Full scale		
Wave ID	H_s [m]	T_e [s]	Run time [min]	H_s [m]	T_e [s]	Run time [min]
IW1	0.175	1.11	6	1.75	3.5	20
IW2	0.175	1.42	6	1.75	4.5	20
IW3	0.175	1.74	6	1.75	5.5	20
IW4	0.175	2.06	6	1.75	6.5	20
IW5	0.175	2.37	6	1.75	7.5	20

3.4. Array Layouts

The basin floor was prepared to test three different array layouts, under the ten wave conditions specified in Table 1. All the array configurations were obtained by positioning the floats over a fixed grid of 2×2 m wide cells, over a total area of 4×6 m^2. The locations of the buoys within the three layouts are shown in Figures 3–5, and referred to as array 1 (A1), array 2 (A2) and array 3 (A3), respectively. Each buoy, and corresponding PTO, is identified by a letter (A, B, C, D, E, F).

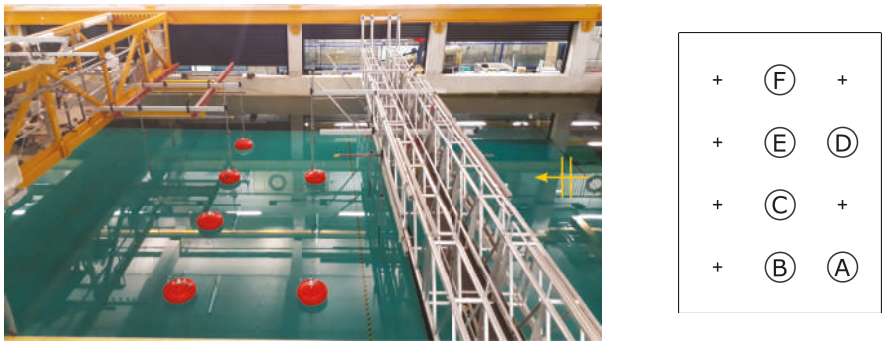

Figure 3. Layout A1.

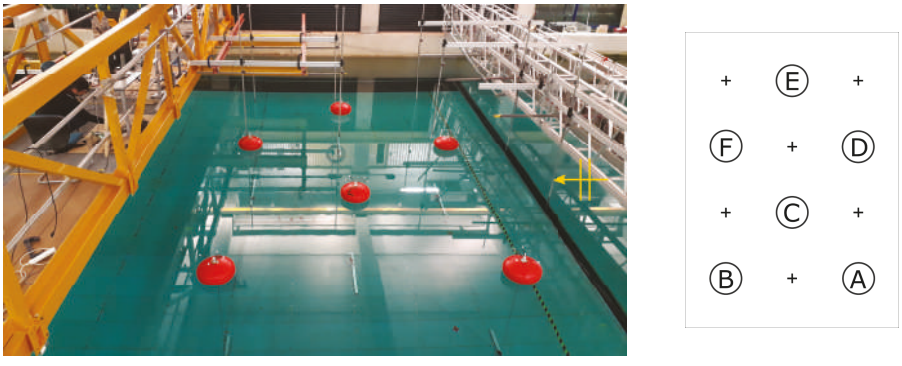

Figure 4. Layout A2.

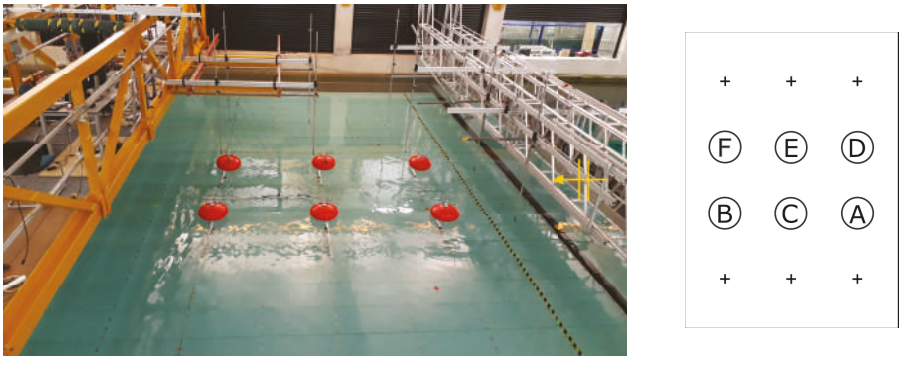

Figure 5. Layout A3.

A1 consisted of a two-line array with a complete line on the back and a line filled every second spot in the front; A2 consisted of a classical three-line staggered configuration; and A3 was a three-line aligned array. Each array's upstream line was located 9.8 m from the wave makers. Layout A1 has been tested twice on two different days, while layout A2 and A3 have been tested once.

4. Simulations

As in [23], the float's geometry has been simulated in two ways: as identical equivalent cylinders of 0.244 m radius and 0.0501 m draft, which correspond to the same submerged volume and radius as the physical elliptical buoy, and as identical equivalent cylinders of 0.178 m radius and 0.0948 m draft, which correspond to the same submerged volume and draft of the physical elliptical buoys. The results corresponding to these two geometries are referred to as frequency domain simulations R1 and R2, respectively. This is due to a restriction of the semi-analytical hydrodynamical model, which can only handle cylinder-shaped floats or cylinders with moon-pool. In the equation of motion an extra rotational inertia of the PTO of 48 kg was added, together with an additional damping of 63.2 Ns/m to account for the friction of the ropes and pulley movement inside the water [21,23].

5. Results and Discussion

In order to analyze the motion data acquired with the Qualisys optical system and understand the results shown in the upcoming section, the authors would like to make the following clarification. Let us consider a cylindrical buoy i moving in three translational degrees of freedom (neglecting the rotational motion for simplicity), $\left[x^i(t), y^i(t), z^i(t)\right]$ (surge, sway and heave, respectively) and the

translator moving only vertically, $\zeta^i(t)$. From the geometry of the problem (Figure 6), the vertical position of the translator is given in terms of the buoy position as

$$\zeta^i \approx \Delta L^i = \sqrt{\left({x^i}^2 + {y^i}^2 + (L + {z^i}^2\right)} - L \approx z^i + \frac{1}{2L}({x^i}^2 + {y^i}^2) \tag{6}$$

where L is the length of the line connecting the translator and buoy; ΔL^i is the vertical PTO position variation; and the approximation holds up to second order in the small parameter $\varepsilon = \sqrt{{x^i}^2 + {y^i}^2}/L$. Here, the case of a slack line is neglected. This approach has been used to estimate the translator position from the float's motion data.

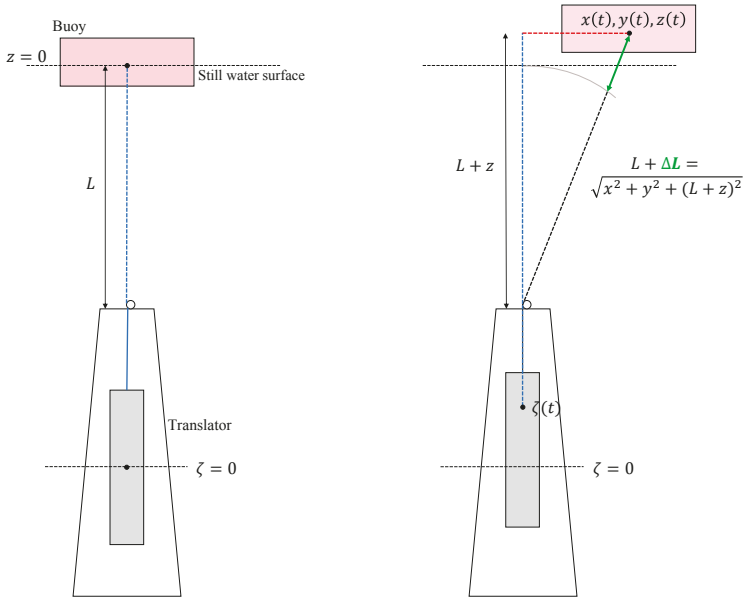

Figure 6. The wave energy converter (WEC) developed at Uppsala University at equilibrium and with waves, respectively. The translator is situated in a sealed generator hull. The distance L is measured from the top of the generator hull to the water's surface at equilibrium. In the experimental tests, the distance L was measured from the water's surface at equilibrium to the pulley on the seabed beneath the buoy. Reproduced from [23].

In the results section the power computed numerically is referred to as P_{SIM}, computed from the buoy displacement $z(t)$, which is assumed to be equal to the translator displacement $\zeta(t)$ (Equations (3) and (4)). From the experimental results, we display the power absorption measured from the power take-off system P_{PTO} (Equation (5)) and the power absorption computed from the buoy motion $P_{\Delta L}$, computed analogously to Equation (3) where z is replaced with ΔL. In other words, $P_{\Delta L}$ is calculated considering all the three translational DoFs of the floats. This latter is called virtual power of the buoy, as it does not represent the actual motion of the PTO, from which power is absorbed. In fact, the buoy motion along the connection line ΔL would correspond to the position of the translator ζ only assuming a stiff connection between them, which is assumed in the numerical model, but is not realistic in the physical experiment.

5.1. Power Output

Figure 7 shows the results in terms of average power output over the time window tested, including both experimental and simulation results, for all the three layouts. Simulations are shown for the two buoy geometries mentioned in Section 4.

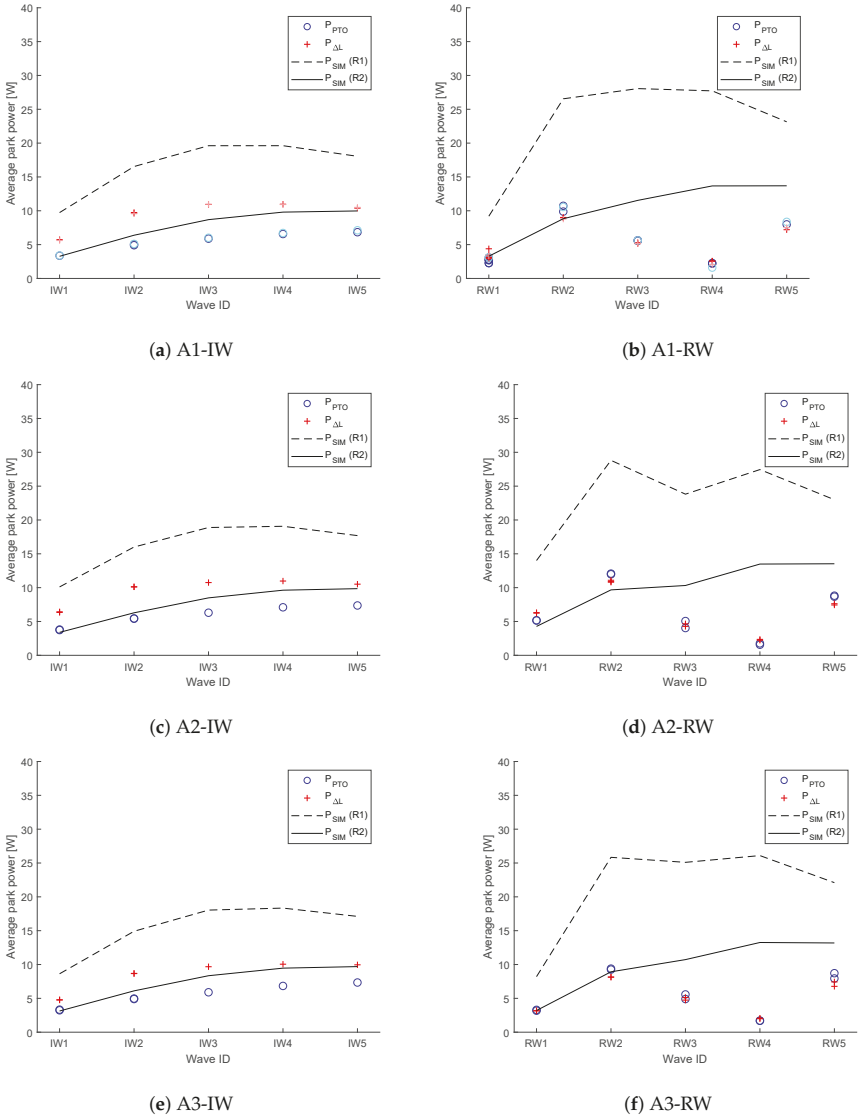

(**a**) A1-IW (**b**) A1-RW

(**c**) A2-IW (**d**) A2-RW

(**e**) A3-IW (**f**) A3-RW

Figure 7. Average power absorbed by the park. (**a**,**b**) Layout A1. (**c**,**d**) Layout A2. (**e**,**f**) Layout A3. Results from irregular waves are shown in (**a**,**c**,**e**) and regular waves in (**b**,**d**,**f**).

In irregular waves (Figure 7a,c,e), the simulations reproduced the power behavior quite well, even though the error between simulations and experiments increased with increasing energy period. In the case of float geometry R1 the power was overestimated, while in the case of R2

the one-DoF-restricted, simplified simulation fit the experimental data quite well. Within the goals of the present work, it was important to reproduce the qualitative behavior of the power output; i.e., the results obtained with R1 are still useful if the goal is the park optimization by relative comparison between layouts.

The wave height is constant for all wave conditions and the (energy) period increases linearly. The energy flux incident on the buoy thus increases linearly with the wave conditions. As can be seen from Figure 7, the absorbed power increases with the period, but not linearly. The increase is largest for the lowest periods, after which the increase is only small. This can be explained from the fact that the natural period is $T_{\text{nat}} = 1.36$ s, i.e., it lies just below wave condition 2. Hence, the WECs will absorb most power relative to the incident energy in the wave conditions with period around wave condition 2.

From the experimental data, it can be observed that the power computed from the power take-off system (P_{PTO}) differs from the power computed from the optical system of the float ($P_{\Delta L}$). This means that the connection line does not behave as a stiff connection, as is the case here. In fact, the intermittent nature of the irregular waves make the float be exposed to sudden and quick changes of its motion, which is not synchronously followed by the rotating PTO, due also to the pulley system and PTO inner inertia. This does not happen in the regular waves, where the motion of the PTO follows the motion of the buoy more easily, at least for the PTO damping used. As we showed in [23], for other damping values, the buoy and PTO motion could differ also in regular waves.

However, in the regular wave results, the experimentally obtained power undergoes a significant reduction in RW3 and RW4, while a lesser reduction is observed in RW5. This can be explained by referring to the results obtained in [23]; a single WEC in isolation was studied in terms of the Mathieu-type instability. Results have shown that in RW3 and RW4 the buoy is affected by a high transverse instability, due to the coupling between heave and sway, resulting in a high sway motion. RW5 displayed only little sway instability. As for the irregular waves, the simulations with geometry R1 overestimated the power (including stable waves); however, in this case we did not expect agreement between the heave model and the experiments that displayed Mathieu instabilities.

An example of results of the buoys' power output within array A1 is shown in Figure 8, while for array A2 and A3 the data are reported in the Appendices (Figures A1 and A2). The power output of the buoys within the same layout is strongly dependent on the wave condition (regular, irregular) and the wave period. In the regular tests the maximum power is achieved by different buoys according to the wave period; in irregular waves the relative level of power output is more or less kept even over different waves periods; an example for layout A2 is shown in Figure 9. As noted before, the two-body dynamics of the UU WEC are noticeable, especially in irregular waves, from the difference between P_{PTO} and $P_{\Delta L}$ measured for each buoy.

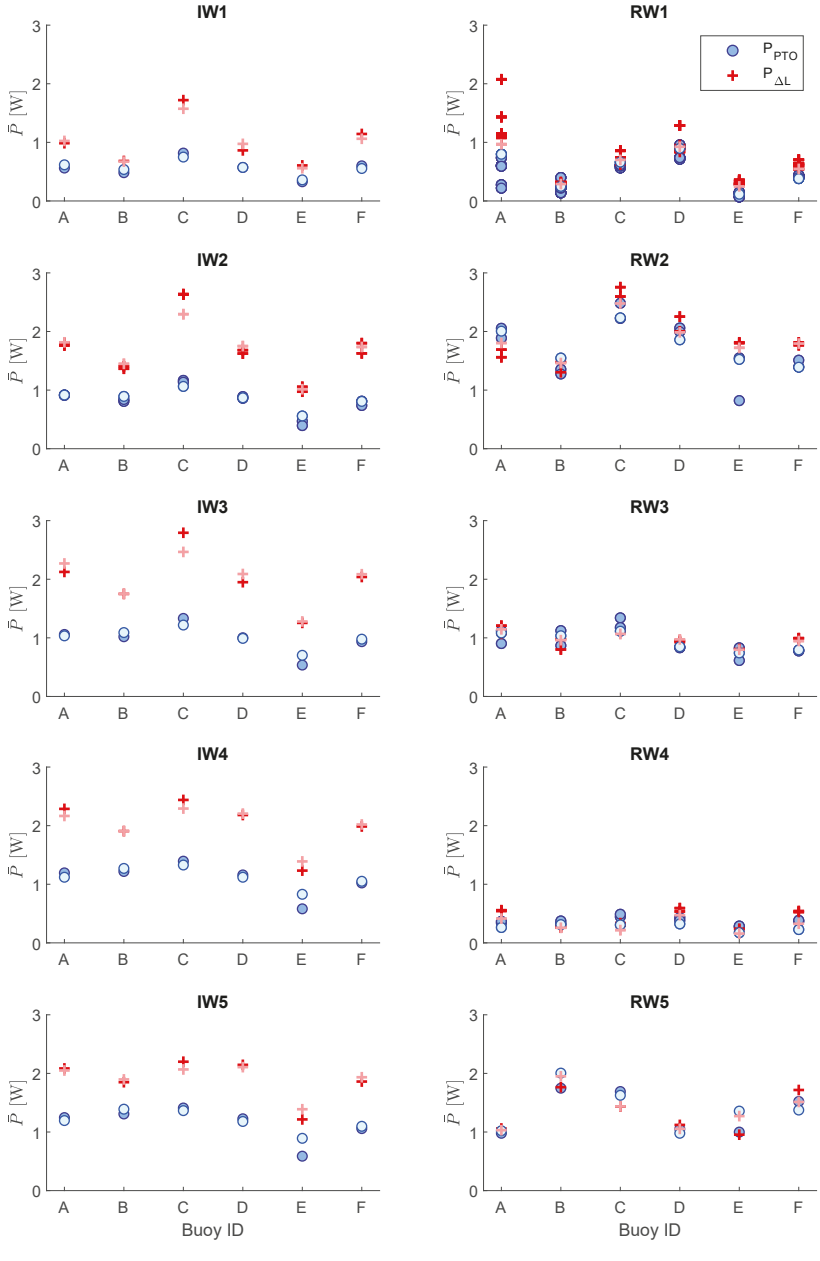

Figure 8. Average power of each buoy for layout A1 in all the tested sea states. Comparison between $P^i_{\Delta L}$ obtained from the Qualisys data (+) and P^i_{PTO} obtained from the PTO data (o). Multiple markers refer to repeated tests. Light blue and light red markers refer to layout A1 tested for the second time. The left column shows results in irregular waves, the right column shows results in regular waves.

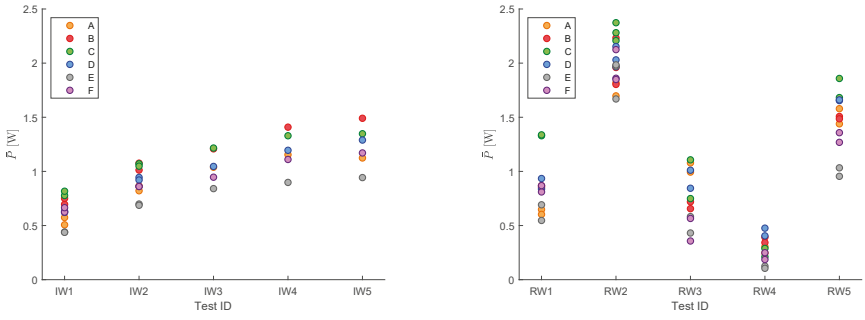

(**a**) IW (**b**) RW

Figure 9. Average power output (P^i_{PTO}) of the buoys in layout A2. (**a**) irregular waves; (**b**) regular waves.

The experimental testing of layout A1 performed at two different occasions has shown consistent results (Figures 7a,b and 8).

Layouts A1 and A2 are not symmetric with respect to the center of the tank, whereas A3 is symmetric with respect to the center of the tank and the lateral walls. However, due to disturbances in the wave tank and high sway motion, there was no symmetry in the experimental results (Figures 8, A1 and A2). The buoys moved in heave, surge and sway in the experiment (if we neglect rotations), and therefore the shadowing effect was minimized. We can notice that on several occasions, the WECs that should have been shadowed produced higher power output than the non-shadowed ones.

5.2. q-Factor

Different layouts have been compared in terms of the interaction factor (or q-factor), defined as:

$$q = \frac{P}{n_b \cdot P^i_{IS}}. \tag{7}$$

P represents the total power of the array and n_b is the number of WECs in the park. P^i_{IS} is the power of the device in isolation, obtained from the previous work for the isolated system in [23]. The experimental q-factor has been compared to the simulated one in Figure 10, for the three layouts. The q-factor values of the WECs within the three layouts are reported in the Appendices (Figures A3–A5).

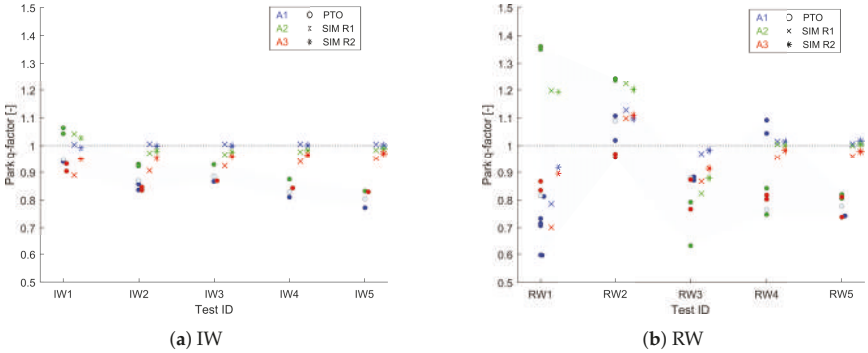

(**a**) IW (**b**) RW

Figure 10. Comparison of the park q-factor values of layouts A1, A2 and A3, in all the tested sea states, calculated from PTO experimental data (o), from simulations with R1 (x) and from simulations with R2 (*). (**a**) Irregular waves; (**b**) regular waves.

The experimental results of Figure 10 show that the best layout was A2 for all the irregular wave conditions and for regular wave conditions RW1, RW2 and RW5. In RW3 and RW4 the best layout was A1.

The best performing layout according to the simulations was A2 in IW1, RW1, RW2 and A1 in IW2, IW3, IW4, IW5, RW3, RW4 and RW5; however, the difference between A1 and A2 was very small.

The shadowed layout, i.e., A3, should have been the worst performing layout for all the wave conditions according to the simulations, but this was not always the case in the experiment. This could be explained by the fact that the experimental WECs were moving in sway, interfering with the expected hydrodynamical interaction and the shadowing effects. In fact, rear devices did experience complete shadowing in the simulations, but not in the wave tank experiment. On the other hand, in the simulations, perfectly heaving devices influenced the hydrodynamic interaction in a different way.

For realistic optimization, we should take into account WECs with at least three DoFs, or better, six DoFs, and waves coming from different directions (multi-directional waves), which would lead to less influence in the shadowing of WECs during the simulations.

The experimental conditions are more controlled in IW1 and IW2, where waves are less energetic and we have less phenomena of slack line and breaking. In these cases we see better agreement of the arrays' q-factor values with the experimental results. The same is valid for RW1 and RW2, in which the devices do not present parametric resonance. However, there is still some ambiguity between the simulations performed with R1 vs R2.

Both in experiments and simulations, the difference between the arrays in terms of q-factor is small in most of the cases, in particular for all the irregular waves. When we have non-linear dynamics, the discussed uncertainties in the experimental data imply that the modeling is not so accurate as to capture such small variations among layouts. Nevertheless, although the WEC dynamics and the hydrodynamic model is limited by constrained heave motion, the stiff connection between buoys and PTOs and linear dynamics, the q-factor estimation is rather good, and the results are close to the experimental region (gray zone in Figure 10).

In general, we expect the hydrodynamic interaction to be larger in larger parks (i.e., parks with more units) [24], resulting in a larger difference between best and worst layouts. In such cases, the model can be expected to better capture such discrepancies. The present study was based on a trade-off between a feasible experimental campaign and simulation work. A larger layout would have given more accurate information, but would also have been difficult to test.

It is worth mentioning that the sources of uncertainty in an experimental campaign were multiple: reflection of waves against the walls of the tank, possibly unbalanced buoys due to the optical markers, uncertainty in the damping and friction estimation, varying damping due to unbalanced discs, elasticity of the connection line and friction in the pulley system. Whereas the optical markers are not expected to influence the dynamics to a relevant degree, the other uncertainties might affect the results. In [21], the friction and line elasticity for the system were evaluated, and it was found that adding a slight elasticity better reproduced the experimental results, and the friction was measured qualitatively. In this paper, friction has been included in the simulations as an additional damping term. Other potential error sources in wave tank testing, highlighted in [27], are: the spatial variation of the wave-field within the wave basin; the temporal variation of the wave-field from one repeat to another; the repeatability of a model's response for any single individual WEC; the reproducibility of a model's response for various identical WECs. In [19] the spatial variation of the wave field around the basin was studied and the results showed that, in irregular waves, the expected significant wave height was always under-reproduced. Moreover, it was found that the discrepancies are larger in relation to shorter periods. To partially asses these problems, repeated tests were executed, when possible, and measurements of the wave field in the empty tank were conducted and used as inputs series in the simulations for the irregular waves. The results from the repeated tests show good agreement, which increases the trustworthiness of the results.

6. Conclusions

The work presented an experimental campaign conducted with six point-absorber WECs moving in six DoFs. The goals were to (a) study the performances of different array layouts under several wave conditions and to (b) understand whether the simulation optimization predictions of best performing array layouts would be confirmed by experimental data. The experimental campaign represents a unique example of array testing with a point-absorber moving in six degrees of freedom. The simulations have been carried out by a frequency domain model restricted to heave, with unlimited stroke length and stiff connection between the float and the generator, so that each WEC is considered as a single body.

6.1. Performances of Different Array Layouts under Several Wave Conditions

Although there is a vast literature on numerical simulations on wave energy parks, there is very little published material on experimental data. The paper is the first publication of experimental data of several array layouts of WECs moving in six DoFs, subjected to both regular and irregular waves.

In both the simulations and the experimental data, arrays A1 and A2 were the best performing layouts in most wave conditions. However, although the numerical simulations predicted that the array A3 should be the worst performing layout in all wave conditions due to the shadowing effect, in the experiments this did not always happen. This can be understood from the fact that in reality, the floats moved also in sway, reducing the shadowing effect. It is worth mentioning that the differences between the best and worst layouts were quite small in irregular waves, both in the simulations and experiments (within 14% in the experiments and within 15.5% and 8% in simulations with R1 and R2, respectively). For larger parks, the shadowing effect would be larger and be present also in realistic conditions, and we would expect both a bigger difference between the layouts and a closer agreement between the simulations and the experimental results. In addition, short-crested waves can decrease the shadowing effect, and thus experiments and simulations using short-crested waves would probably agree to a larger extent.

The power absorption of the array in irregular waves increases with increased energy flux up to an optimum energy period, after which the power is constant or decreases slightly. This behavior is shown both in the simulations and experimental data. Since the natural period of the device is $T_{\text{nat}} = 1.36$ s, i.e., it lies between just below wave condition 2, the WECs will absorb most power relative to the incident energy in the wave conditions with a period around wave condition 2.

The highest q-factor was obtained for the staggered array A2 in the irregular waves with the shortest energy period, in both the experiments ($q = 1.04$, $q = 1.06$) and simulations ($q = 1.03, 1.04$). In the simulations, the q-factor was close to 1 in all irregular sea states, whereas it decreased with increasing energy period in the experiments, down to a minimum of $q = 0.77$. In the regular waves, the range of the q-factor obtained in different wave conditions and for different arrays was much larger, both in the simulations and experiments. Additionally, in the regular waves, the highest q-factor was obtained for the staggered array A2 in the waves with the shortest energy period, both in the simulations and in the experiments.

6.2. Comparison of Simulation Optimization Predictions with Experimental Data

The paper gives several important insights into common assumptions and models used for wave energy park optimization. In most of the modeling works of wave energy parks, in particular in array optimization studies, a stiff connection between the float and the PTO is assumed, and the numerical model of the float is restricted to heave, although the physical float is free to move in six DoFs. Do these two assumptions hold in realistic conditions?

- The experimental data show that in regular waves and for the PTO damping used, the power obtained from the float and the PTO motion is the same, so the assumption of a stiff line is valid. In the irregular waves, however, the WEC shows clear two-body dynamics with different displacement of the float and the PTO due to slack and elasticity in the connection line. As a result, the power obtained from the float and the PTO can differ significantly, and the assumption no longer holds. The virtual power obtained from the float's motion is in this case higher than the actual power obtained from the PTO; in other words, if a stiff connection between the float and the PTO were to be assumed, the predicted power would be higher than the one that will be obtained in reality. This is confirmed by comparing the power computed in the simulations (which assume a stiff line) with the experimental data: the simulations generally overestimate the absorbed power by the PTO. This conclusion holds both for the total power of the park (Figure 7) and for the power absorbed by the individual buoys (Figure 8).
- The results from the simple one-DoF simulation model are able to reproduce the qualitative behavior of the absorbed power at least to an approximate degree (Figures 7 and 10), as long as non-linear dynamics such as Mathieu instabilities are not present. In the experiments, Mathieu instabilities mostly occurred in some of the regular wave cases; hence, in realistic, irregular waves, the simulations can give an estimation of the power output of the UU WEC. In summary, in the wave conditions wherein we neither observe extensive sway nor non-linear behavior, the results of the optimization are reliable. However, when non-linear dynamics or motions in multiple degrees of freedom are present, then the optimization routine does not provide accurate results. In other words, the discrepancy between the experimental and numerical results is mostly due to either slack line condition (mostly in irregular waves) or Mathieu-type instability (mostly in regular waves). In addition, losses, friction and reflections in the wave tank, and other sources of uncertainty in the experimental set-up, also play roles in the outcome of the present study.

In order to improve the output of the presented model, an array hydrodynamical model with six DoFs and multi-directional waves could be implemented in the optimization routine. To capture the non-linear effects and two-body dynamics, a non-linear time-domain model would be required. However, the computational costs of such a model would probably be too high to enable large-scale optimization.

Author Contributions: Conceptualization, M.G. (Marianna Giassi), J.E., J.I. and M.G. (Malin Göteman); data curation, M.G. (Marianna Giassi); formal analysis, M.G. (Marianna Giassi); funding acquisition, J.E., J.I. and M.G. (Malin Göteman); investigation, M.G. (Marianna Giassi) and M.G. (Malin Göteman); project administration, J.E., J.I. and M.G. (Malin Göteman); supervision, J.E. and M.G. (Malin Göteman); writing—original draft, M.G. (Marianna Giassi); writing—review and editing, J.E., J.I. and M.G. (Malin Göteman). All authors have read and agreed to the published version of the manuscript.

Funding: This research is supported by the the Swedish Research Council (VR, grant number 2015-04657), the Swedish Energy Agency (project number 40421-1), StandUp for Energy, the Lundström-Åman foundation and Miljöfonden.

Acknowledgments: The authors would like to thank Martyn Hann and Edward Ransley for discussions and input provided; and Kieran Monk and Tom Tosdevin for the technical support and help in the COAST Lab ocean basin.

Conflicts of Interest: The authors declare no conflict of interest.

Nomenclature

Numerical model:

x^i	buoy position in surge
y^i	buoy position in sway
z^i	buoy position in heave
ζ^i	PTO position
γ	PTO damping
P^i_{SIM}	WEC power output (i^{th} WEC)
P_{SIM}	park power output

Experimental data:

X^i	buoy position in surge measured by the optical system
Y^i	buoy position in sway measured by the optical system
Z^i	buoy position in heave measured by the optical system
ΔL^i	buoy position along the connection line calculated from the optical measurements
γ	PTO damping
P^i_{PTO}	WEC experimental PTO power output
P_{PTO}	park experimental PTO power output
$P^i_{\Delta L}$	WEC experimental virtual power output computed from the buoy motion along the connection line
$P_{\Delta L}$	park experimental virtual power output computed from the buoy motion along the connection line

Abbreviations

The following abbreviations are used in this manuscript:

DoF	Degrees of freedom
IW	Irregular wave
LG	Linear generator
PTO	Power take-off
RW	Regular wave
UU	Uppsala University
WEC	Wave energy converter

Appendix A

Appendix A.1. WEC's Power Output

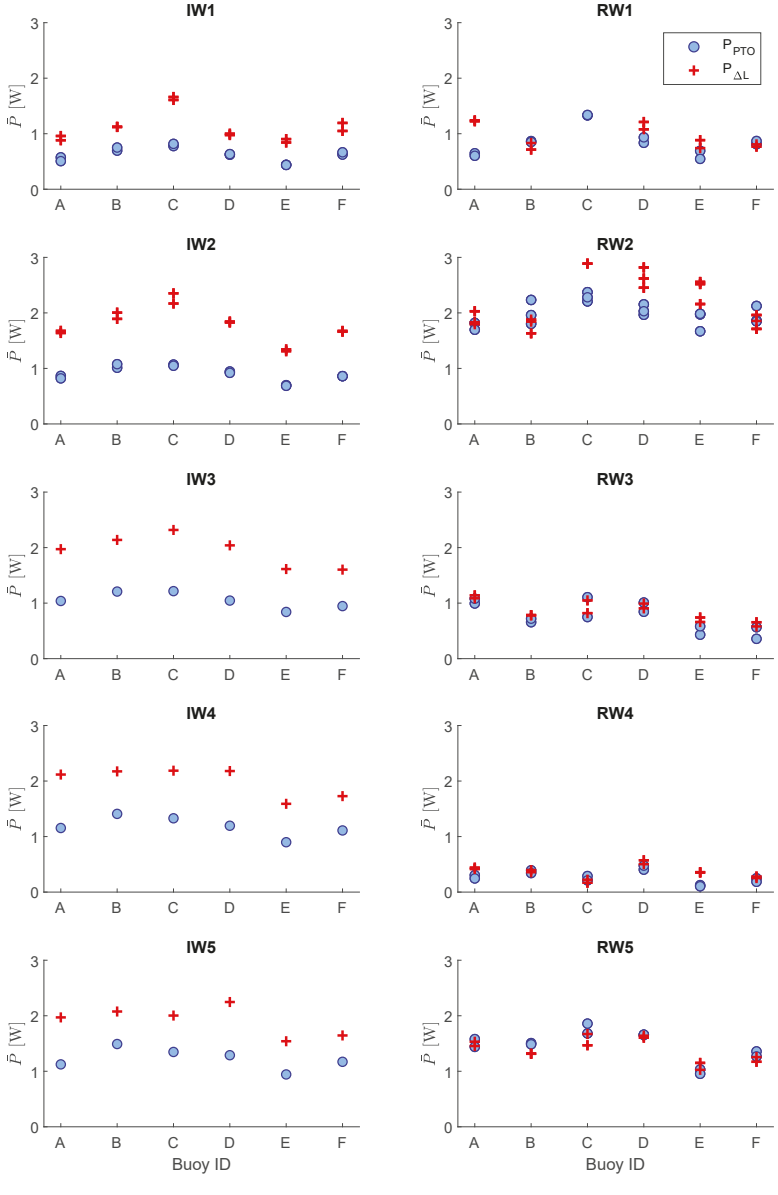

Figure A1. Average power of each buoy for Layout A2 in all the tested sea states. Comparison between $P^i_{\Delta L}$ obtained from the Qualisys data (+) and P^i_{PTO} obtained from the PTO data (o). Multiple markers refer to repeated tests. Left column shows results in irregular waves, right column in regular waves.

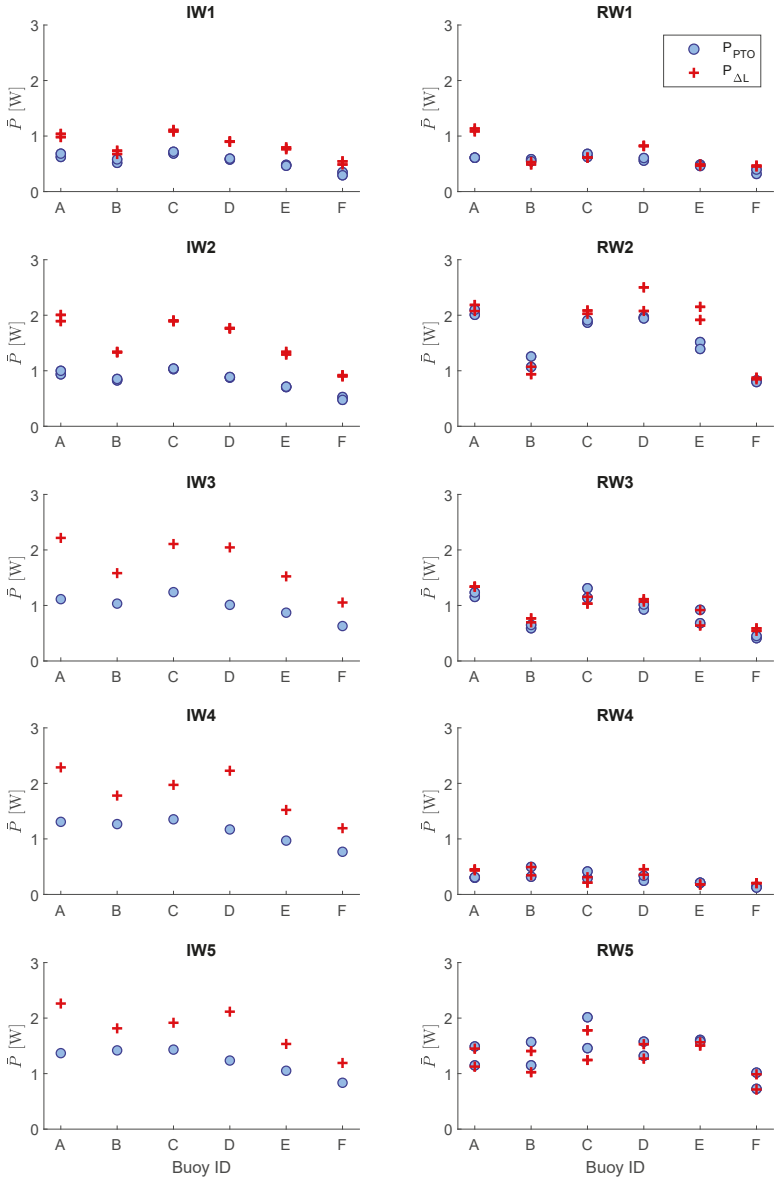

Figure A2. Average power of each buoy for Layout A3 in all the tested sea states. Comparison between $P^i_{\Delta L}$ obtained from the Qualisys data (+) and P^i_{PTO} obtained from the PTO data (o). Multiple markers refer to repeated tests. Left column shows results in irregular waves, right column in regular waves.

Appendix A.2. WEC's q-Factor

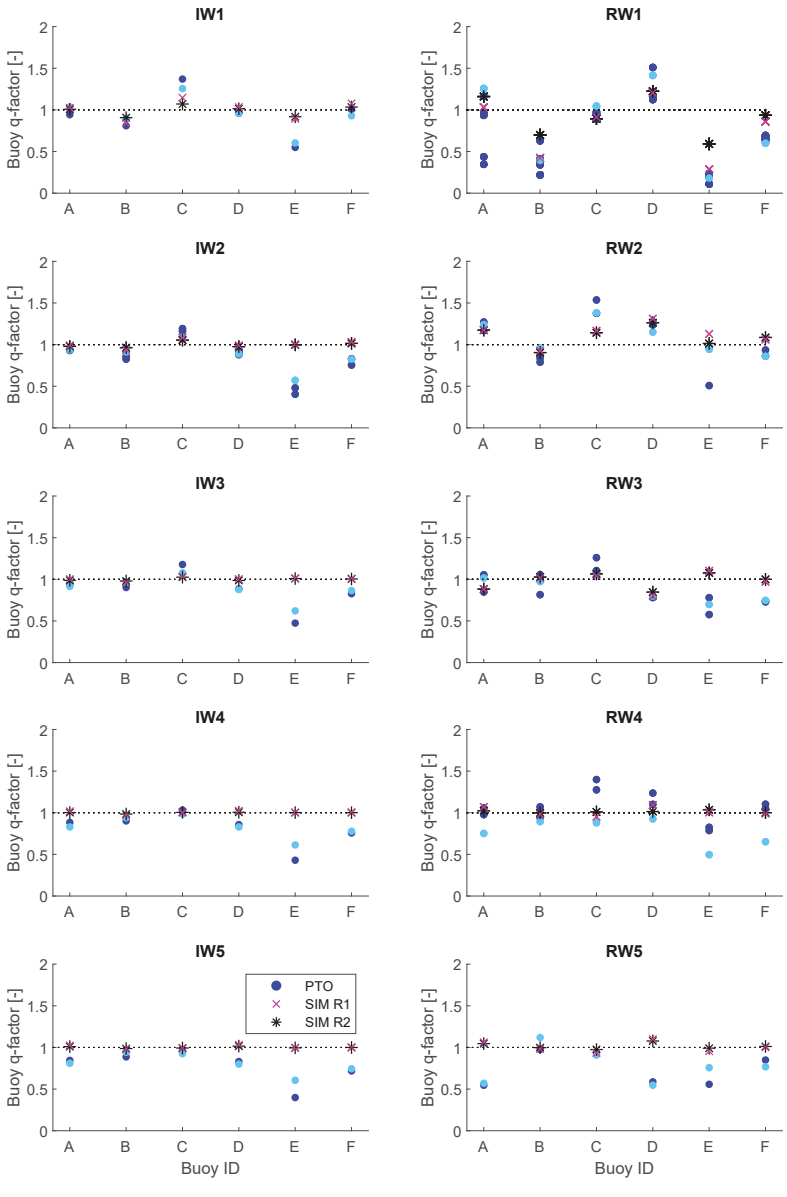

Figure A3. The buoys' *q*-factor for layout A1 computed from PTO experimental data and simulations. Left column shows results in irregular waves, right column in regular waves.

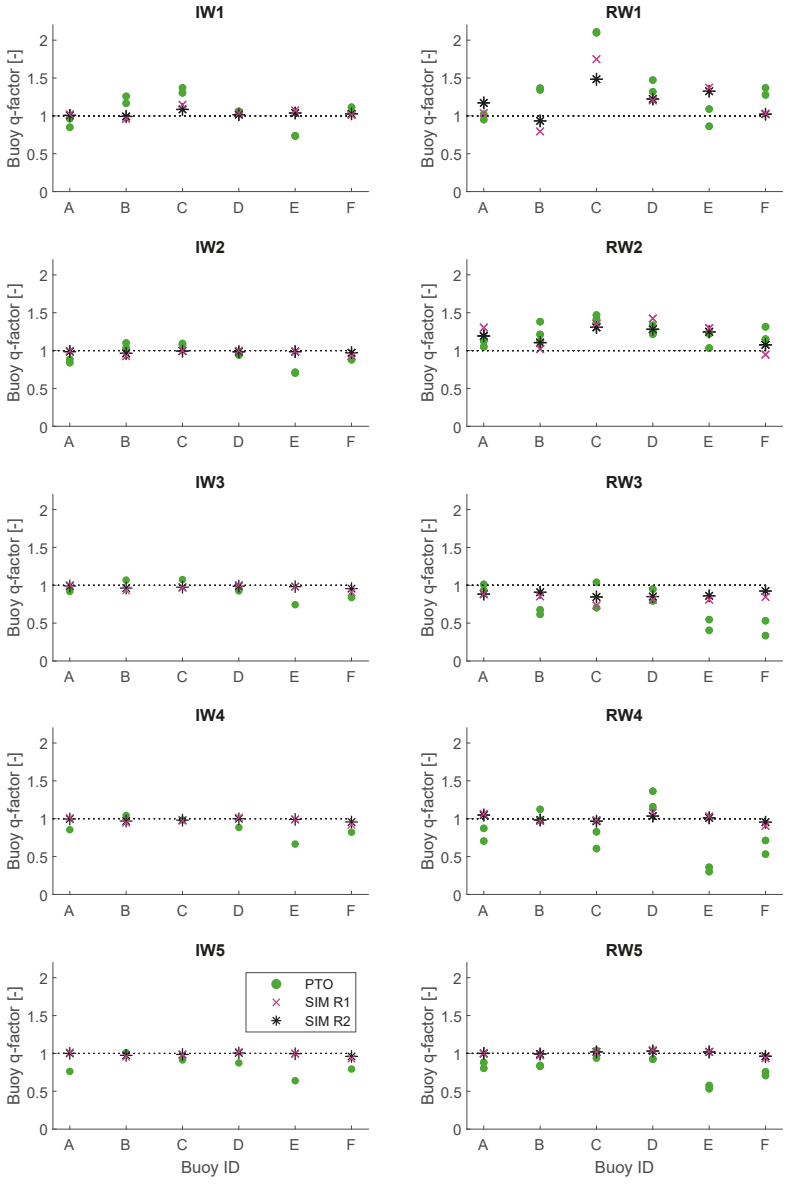

Figure A4. The buoys' q-factor for layout A2 computed from PTO experimental data and simulations. Left column shows results in irregular waves, right column in regular waves.

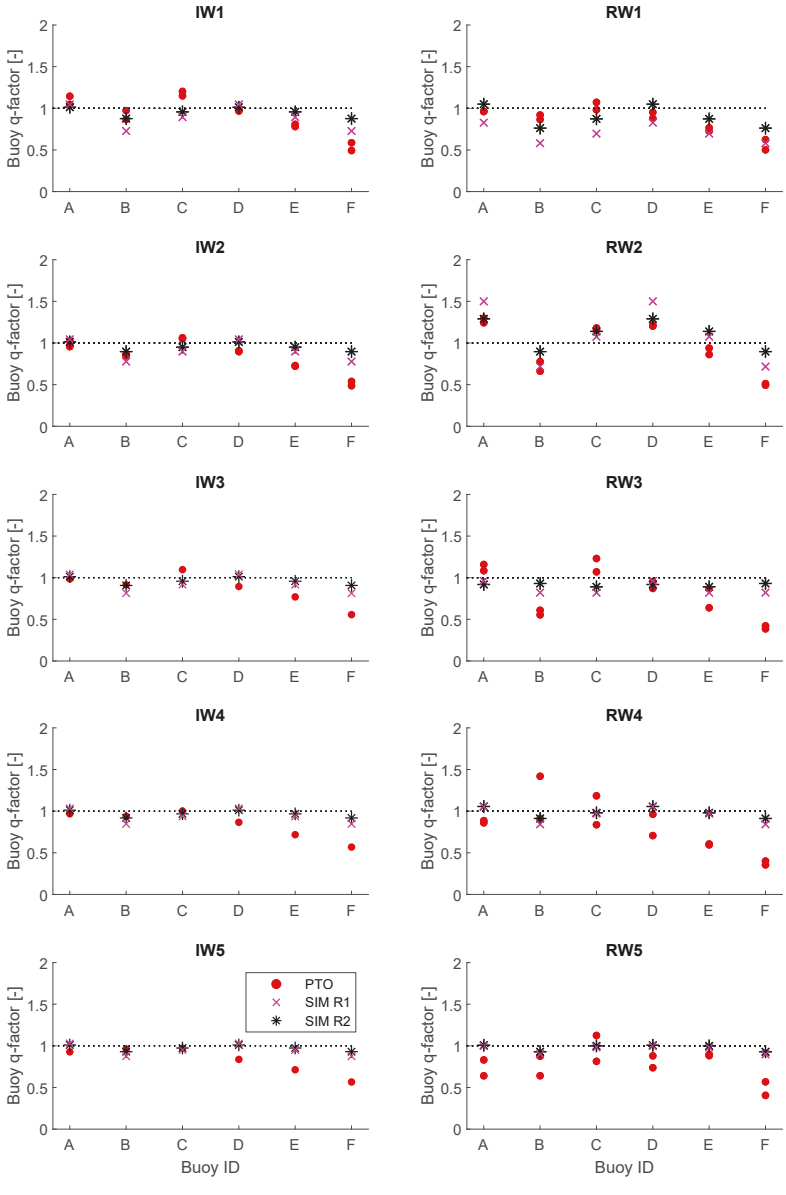

Figure A5. The buoys' q-factor for layout A3 computed from PTO experimental data and simulations. Left column shows results in irregular waves, right column in regular waves.

References

1. Göteman, M.; Giassi, M.; Engström, J.; Isberg, J. Advances and Challenges in Wave Energy Park Optimization—A Review. *Front. Energy Res.* **2020**, *8*, 26. doi:10.3389/fenrg.2020.00026. [CrossRef]
2. Konispoliatis, D.; Mavrakos, S. Mean drift loads on arrays of free floating OWC devices consisting of concentric cylinders. In Proceedings of the 29th International Workshop on Water Waves and Floating Bodies (IWWWFB2014), Osaka, Japan, 30 March– 2 April 2014.

3. Da Fonseca, F.; Gomes, R.; Henriques, J.; Gato, L.; Falcao, A. Model testing of an oscillating water column spar-buoy wave energy converter isolated and in array: Motions and mooring forces. *Energy* **2016**, *112*, 1207–1218. [CrossRef]
4. Magagna, D.; Carr, D.; Stagonas, D.; Mcnabola, A.; Gill, L.; Muller, G. Experimental Evaluation of the Performances of an Array of Multiple Oscillating Water Columns. In Proceedings of the 9th European Wave and Tidal Energy Conference (EWTEC), Southampton, UK, 5–9 September 2011.
5. Wolgamot, H.; Taylor, P.; Eatock Taylor, R.; Van Den Bremer, T.; Raby, A.; Whittaker, C. Experimental observation of a near-motion-trapped mode: Free motion in heave with negligible radiation. *J. Fluid Mech.* **2016**, *786*. [CrossRef]
6. Ji, X.; Liu, S.; Bingham, H.; Li, J. Multi-directional random wave interaction with an array of cylinders. *Ocean. Eng.* **2015**, *110*, 62–77. [CrossRef]
7. Bosma, B.; Brekken, T.; Lomonaco, P.; DuPont, B.; Sharp, C.; Batten, B. Array modeling and testing of fixed OWC type Wave Energy Converters. In Proceedings of the 13th European Wave and Tidal Conference (EWTEC), Napoli, Italy, 1–6 September 2019
8. Mackay, E.; Cruz, J.; Livingstone, M.; Arnold, P. Validation of a Time-Domain Modelling Tool for Wave Energy Converter Arrays. In Proceedings of the 10th European Wave and Tidal Energy Conference, Alborg, Denmark, 2–5 September 2013.
9. Mercadé Ruiz, P.; Ferri, F.; Kofoed, J. Experimental validation of a wave energy converter array hydrodynamics tool. *Sustainability* **2017**, *9*, 115. [CrossRef]
10. Troch, P.; Stratigaki, V.; Stallard, T.; Forehand, D.; Folley, M.; Kofoed, J.; Benoit, M.; Babarit, A.; Sánchez, D.; De Bosscher, L.; et al. Physical modelling of an array of 25 heaving wave energy converters to quantify variation of response and wave conditions. In Proceedings of the 10th European Wave and Tidal Energy Conference Series (EWTEC), Aalborg, Denmark, 2–5 September 2013; pp. 2–5.
11. Stratigaki, V.; Troch, P.; Stallard, T.; Forehand, D.; Kofoed, J.; Folley, M.; Benoit, M.; Babarit, A.; Kirkegaard, J. Wave basin experiments with large wave energy converter arrays to study interactions between the converters and effects on other users in the sea and the coastal area. *Energies* **2014**, *7*, 701–734. [CrossRef]
12. Stratigaki, V.; Troch, P.; Stallard, T.; Forehand, D.; Folley, M.; Kofoed, J.; Benoit, M.; Babarit, A.; Vantorre, M.; Kirkegaard, J. Sea-state modification and heaving float interaction factors from physical modelling of arrays of wave energy converters. *J. Renew. Sustain. Energy* **2015**, *7*, 061705. [CrossRef]
13. Child, B.; Weywada, P. Verification and validation of a wave farm planning tool. In Proceedings of the 10th European Wave and Tidal Energy Conference (EWTEC) conference, Aalborg, Denmark, 2–5 September 2013; pp. 2–5.
14. Thomas, S.; Weller, S.; Stallard, T. Float response within an array: Numerical and experimental comparison. In Proceedings of the 2nd International Conference on Ocean Energy (ICOE), Brest, France, 15–17 October 2008; Volume 1517.
15. Weller, S.; Stallard, T.; Stansby, P. Interaction factors for a rectangular array of heaving floats in irregular waves. *IET Renew. Power Gener.* **2010**, *4*, 628–637. [CrossRef]
16. Nader, J.; Fleming, A.; Macfarlane, G.; Penesis, I.; Manasseh, R. Novel experimental modelling of the hydrodynamic interactions of arrays of wave energy converters. *Int. J. Mar. Energy* **2017**, *20*, 109–124. [CrossRef]
17. Thomas, S.; Eriksson, M.; Göteman, M.; Hann, M.; Isberg, J.; Engström, J. Experimental and numerical collaborative latching control of wave energy converter arrays. *Energies* **2018**, *11*, 3036. [CrossRef]
18. Thomas, S.; Giassi, M.; Eriksson, M.; Göteman, M.; Isberg, J.; Ransley, E.; Hann, M.; Engström, J. A model free control based on machine learning for energy converters in an array. *Big Data Cogn. Comput.* **2018**, *2*, 36. [CrossRef]
19. Giassi, M.; Thomas, S.; Shahroozi, Z.; Engström, J.; Isberg, J.; Tosdevin, T.; Hann, M.; Göteman, M. Preliminary results from a scaled test of arrays of point-absorbers with 6 DOF. In Proceedings of the 13th European Wave and Tidal Conference (EWTEC), Napoli, Italy, 1–6 September 2019.
20. Leijon, M.; Waters, R.; Rahm, M.; Svensson, O.; Boström, C.; Strömstedt, E.; Engström, J.; Tyrberg, S.; Savin, A.; Gravråkmo, H.; et al. Catch the wave to electricity. *IEEE Power Energy Mag.* **2009**, *7*, 50–54. [CrossRef]

21. Thomas, S.; Giassi, M.; Göteman, M.; Hann, M.; Ransley, E.; Isberg, J.; Engström, J. Performance of a Direct-Driven Wave Energy Point Absorber with High Inertia Rotatory Power Take-off. *Energies* **2018**, *11*, 2332. [CrossRef]
22. Giassi, M.; Göteman, M. Layout design of wave energy parks by a genetic algorithm. *Ocean. Eng.* **2018**, *154*, 252–261. [CrossRef]
23. Giassi, M.; Thomas, S.; Tosdevin, T.; Engström, J.; Hann, M.; Isberg, J.; Göteman, M. Capturing the experimental behaviour of a point-absorber WEC by simplified numerical models. *J. Fluids Struct.* **2020**, (accepted).
24. Göteman, M.; Engström, J.; Eriksson, M.; Isberg, J. Fast modeling of large wave energy farms using interaction distance cut-off. *Energies* **2015**, *8*, 13741–13757. [CrossRef]
25. Göteman, M. Wave energy parks with point-absorbers of different dimensions. *J. Fluids Struct.* **2017**, *74*, 142–157. [CrossRef]
26. Giassi, M.; Castellucci, V.; Göteman, M. Economical layout optimization of wave energy parks clustered in electrical subsystems. *Appl. Ocean. Res.* **2020**, *101*, 102274. [CrossRef]
27. Lamont-Kane, P.; Folley, M.; Whittaker, T. Investigating Uncertainties in Physical Testing of Wave Energy Converter Arrays. In Proceedings of the 10th European Wave and Tidal Energy Conference (EWTEC), Aalborg, Denmark, 2–5 September 2013.

© 2020 by the authors. Licensee MDPI, Basel, Switzerland. This article is an open access article distributed under the terms and conditions of the Creative Commons Attribution (CC BY) license (http://creativecommons.org/licenses/by/4.0/).

Journal of
Marine Science and Engineering

MDPI

Article

Simple Controllers for Wave Energy Devices Compared

Demián García-Violini [1,*], Nicolás Faedo [2], Fernando Jaramillo-Lopez [2] and John V. Ringwood [2]

[1] Departamento de Ciencia y Tecnología, Universidad Nacional de Quilmes, Roque Saenz Peña 352, Bernal B1876, Argentina
[2] Centre for Ocean Energy Research, Maynooth University, W23 F2K8 Co. Kildare, Ireland; nicolas.faedo@mu.ie (N.F.); fernando.jaramillolopez@mu.ie (F.J.-L.); john.ringwood@mu.ie (J.V.R.)
* Correspondence: ddgv83@gmail.com

Received: 11 September 2020; Accepted: 1 October 2020; Published: 13 October 2020

Abstract: The design of controllers for wave energy devices has evolved from early monochromatic impedance-matching methods to complex numerical algorithms that can handle panchromatic seas, constraints, and nonlinearity. However, the potential high performance of such numerical controller comes at a computational cost, with some algorithms struggling to implement in real-time, and issues surround convergence of numerical optimisers. Within the broader area of control engineering, practitioners have always displayed a fondness for simple and intuitive controllers, as evidenced by the continued popularity of the ubiquitous PID controller. Recently, a number of energy-maximising wave energy controllers have been developed based on relatively simple strategies, stemming from the fundamentals behind impedance-matching. This paper documents this set of (5) controllers, which have been developed over the period 2010–2020, and compares and contrasts their characteristics, in terms of energy-maximising performance, the handling of physical constraints, and computational complexity. The comparison is carried out both analytically and numerically, including a detailed case study, when considering a state-of-the-art CorPower-like device.

Keywords: wave energy; wave energy converter; energy-maximising control; optimal control; impedance-matching; renewable energy systems

1. Introduction

Despite being a vast resource, wave energy conversion technology has not yet reached economic commercialisation. The main reason for the lack of proliferation of wave energy can be attributed to the fact that harnessing the irregular reciprocating motion of the sea is not as straightforward as, for example, extracting energy from the wind. This is clearly reflected in the striking absence of clear technology convergence, with over a thousand different concepts and patents proposed over the years (see, for instance, [1]).

Dynamic analysis and control system technology can impact many aspects of wave energy converter (WEC) design and operation, including device sizing and configuration, maximising energy extraction from waves, and optimising energy conversion in the power take-off (PTO) system. As a matter of fact, it is already clear (and well-established) that appropriate control technology has the capability to greatly enhance energy extraction from WECs [2,3]. In particular, the control input, supplied by means of the PTO system, and effectively realising the mechanical load on the device, plays a key role in the optimisation of the operation of wave energy devices: Ultimately, energy conversion must be performed as economically as possible, to minimise the delivered energy cost, while also maintaining the structural integrity of the device, minimising wear on WEC components, and operating across a wide range of sea conditions. This is virtually always written in terms of an

energy-maximising criterion, so that the control problem for WECs can be informally posed [2] as depicted in Table 1:

Table 1. Control problem for WECs.

Design the PTO Force (Control Input) Such That:	
Maximises	Energy absorption from incoming waves.
Subject to	WEC dynamics. Device and actuator physical limitations.

In recent years, wave energy control researchers applied optimal control methods, where the energy-maximisation design is written in terms of an appropriate optimal control problem (OCP), and well-developed techniques (mainly originated within the theory of calculus of variations [4]) can be considered. In particular, direct optimal control techniques are often adopted [5], which discretise the variables involved in the WEC OCP, and attempt to maximise the resulting nonlinear program (NP) directly. This NP has to be solved while using numerical optimisation routines, whose complexity (both analytical and computational) depends upon a number of factors, including the specific discretisation method selected. This family of optimisation-based controllers is optimal by design, facilitated by a suitable definition of the energy-maximising control objective in the corresponding OCP. In addition, device safety can be directly addressed by adding a (feasible) set of constraints (i.e., device and actuator limitations) to the optimisation problem.

Although optimal by design, these optimisation-based controllers have their specific drawbacks, which can limit their application in 'real-world' scenarios. In particular, depending on the discretisation utilised, optimisation-based controllers may or may not be suitable for real-time implementation; the complexity of the associated NP, and the numerical routines that are required to approximate its solution, can preclude real-time operation, often especially true if nonlinearities are considered in the WEC dynamical model [6]. In addition, these controllers often lack of any 'intuitive' interpretation, given the mathematical complexity behind their derivation. In other words, very specific expertise is often required to design, synthesise, and calibrate these controllers, which is relatively unappealing for industrial practitioners.

Aiming to find simple and intuitive solutions, a number of researchers attempt to solve the WEC OCP while using fundamental theory behind maximum power transfer: the so-called impedance-matching principle [7]. In particular, this family of simple controllers attempts to provide a (physically implementable) realisation of the impedance-matching condition for maximum power transfer, by proposing simple systems, mostly characterised by well-known techniques from linear time-invariant theory. These techniques have mild computational requirements, and their implementation can be performed in real-time with almost any physical hardware platform, including commercial low-cost microcontrollers.

Naturally, this simplicity comes at a certain cost: altough simple to implement, the performance of these controllers is inherently suboptimal, leading to a drop in energy absorption when compared to optimisation-based techniques. In addition, and since the impedance-matching condition does not consider any physical limitations (i.e., device and actuator limits), constraint handling is virtually always performed by means of simple mechanisms, which do not take into account optimality with respect to power absorption. In other words, the limitation mechanisms are designed independently from the energy-maximising objective, effectively providing constrained optimal solutions, rather than optimal constrained solutions. This naturally implies a loss of energy absorption under constrained conditions.

Nonetheless, despite their suboptimal performance, the main advantage of these controllers relies on their simplicity of implementation, and intuitive design, synthesis, and calibration, which makes this family of strategies highly appealing for practical applications. Additionally, it is worth noting that, when considering the simplicity of controllers based on the impedance-matching principle, this family

of controllers can be implemented in almost any physical hardware platform, such as commercial low cost microcontrollers while using traditional discrete-time recursive routines, which represents one of the main features of these controllers. Motivated by the potential that is offered by this set of techniques in real-world scenarios, this paper documents a critical comparison between five (5) different controllers, developed over the period 2010–2020. It is important to note that, even though the origins of impedance-matching control originate in the 1970s [8], practical algorithms dealing with panchromatic operation and system constraints were only developed within the past decade, hence the focus on the period post 2010′. In particular, this study compares and contrasts their characteristics, in terms of energy-maximising performance, the handling of physical constraints, and computational load. The comparison is carried out both analytically and numerically, with special attention paid to the stability issue that can arise in the implementation of each selected strategy. These controllers are those published in [9–13], listed, in chronological order, in Table 2.

Table 2. Set of five (5) simple controllers compared in this study.

Reference	Controller Name	Shorthand Notation
[9]	*Suboptimal causal reactive controller*	C1
[10]	*Simple and effective real-time controller*	C2
[11]	*Multi resonant feedback controller*	C3
[12]	*Feedback resonating controller*	C4
[13]	*LiTe-Con*	C5

Note that, in Table 2, the column 'Controller name', is defined while using the title of each corresponding reference. It should be noted that, in terms of operation and performance of this set of controller under real conditions in open waters, the control algorithms reviewed in this paper are designed to operate only in the power production region of sea states and devices; under extreme wave conditions, a supervisory control system will put the system into a safe configuration, under which no power is produced.

The remainder of this paper is organised as follows. Section 1.1 introduces the mathematical notation used throughout this study. Section 2 presents the fundamentals behind control-oriented modelling of WECs, while Section 3 provides a detailed description of the fundamental principle of impedance-matching, highlighting each of its features. Section 4 outlines the theory behind the design and synthesis of each of the five (5) simple controllers that are listed in Table 2, in chronological order of publication. Section 5 presents a case study based on a full-scale CorPower-like device, where the set of selected simple controllers is assessed in terms of a number of indicators, including energy-maximising performance, constraint handling, computational complexity, and stability features. Section 6 provides a detailed discussion on the results that are presented in Section 5, specifically providing insight into each of the strenghts and weaknesses of each simple controller. Finally, Section 7 encompasses the main conclusions of this study.

1.1. Notation

Standard notation is considered throughout this paper, most of which is defined in this section. $\mathbb{R}^+$ ($\mathbb{R}^-$) denotes-* the set of non-negative (non-positive) real numbers. The notation $\mathbb{N}_q$ indicates the set of all positive natural numbers up to q, i.e., $\mathbb{N}_q = \{1, 2, \ldots, q\}$. The symbol 0 stands for any zero element, dimensioned according to the context. The notation $A^\star$, with $A \in \mathbb{C}^{n\times n}$, denote the Hermitian transpose of the matrix A. The notation $\mathbb{R}\mathrm{e}\{z\}$ and $\mathbb{I}\mathrm{m}\{z\}$, with $z \in \mathbb{C}$, stands for the real-part and the imaginary-part of z, respectively. The convolution between two functions f and g, with $\{f, g\} \subset L^2(\mathbb{R})$, over the set $\mathbb{R}$, i.e., $\int_{\mathbb{R}} f(\tau)g(t-\tau)d\tau$ is denoted as $f * g$, and where $L^2(\mathbb{R}) = \{f : \mathbb{R} \to \mathbb{R} \mid \int_{\mathbb{R}} |f(\tau)|^2 d\tau < +\infty\}$ is the Hilbert space of square-integrable functions in $\mathbb{R}$. The Laplace transform of a function f (provided if exists), is denoted as $F(s)$, $s \in \mathbb{C}$. With some

abuse of notation[1], the same is used for the Fourier transform of f, written as $F(\omega)$, $\omega \in \mathbb{R}$. Finally, the expression $\deg\{p\}$ is used to denote the degree of the polynomial p, defined over the field $\mathbb{R}$.

2. Control-Oriented Modelling of WECs

This section begins by recalling well-known theory behind control-oriented linear WEC modelling (see, for instance, [8]), for a one-degree-of-freedom (DoF) wave energy device[2]. In particular, under linear potential flow theory, the equation of motion for such a WEC is generally written in terms of a dynamical system Σ, for $t \in \mathbb{R}^+$, given by the set of equations

$$\Sigma : \begin{cases} \ddot{x} = \mathcal{M}\left(f_r + f_{re} + f_{ex} - f_u\right), \\ y = \dot{x} = v, \end{cases} \tag{1}$$

where $x : \mathbb{R}^+ \to \mathbb{R}$, $t \mapsto x(t)$ is the device excursion (displacement), $v : \mathbb{R}^+ \to \mathbb{R}$ is the device velocity, $f_{ex} : \mathbb{R}^+ \to \mathbb{R}$, $t \mapsto f_{ex}(t)$ the wave excitation force (external uncontrollable input due to the incoming wave field), f_{re} the linearised hydrostatic restoring force, f_r the radiation force, and $\mathcal{M} \in \mathbb{R}^+/0$ is the inverse of the generalised mass matrix of the device (see [8]). Finally, the notation $f_u : \mathbb{R}^+ \to \mathbb{R}$, $t \mapsto f_u(t)$, is used for the control input, being supplied by means of a power take-off (PTO) system. As previously discussed in Section 1, the mapping f_u plays a key role in the optimisation of the operation of wave energy devices: ultimately, energy conversion must be performed as economically as possible, in order to minimise the delivered energy cost, while also maintaining the structural integrity of the device, minimising wear on WEC components, and operating across a wide range of sea conditions.

Continuing with the description of Equation (1), the linearised hydrostatic force can be written as $f_{re}(t) = -s_{\mathrm{h}} x(t)$, where s_{h} denotes the hydrostatic stiffness, which depends upon the device geometry. The radiation force f_r is modelled based on linear potential theory and, using the well-known Cummins' equation [14], can be written, for $t \in \mathbb{R}^+$, using the expression

$$f_r(t) = -m_\infty \ddot{x}(t) - \int_{\mathbb{R}^+} h_r(\tau) v(t-\tau) d\tau, \tag{2}$$

with $h_r : \mathbb{R}^+ \to \mathbb{R}^+$, $h_r \in L^2(\mathbb{R})$, the (causal) radiation impulse response function containing the memory effect of the fluid response, and $m_\infty = \lim_{\omega \to +\infty} A_r(\omega) \in \mathbb{R}$, where $A_r : \mathbb{R} \to \mathbb{R}$ is the radiation added-mass, defined as

$$A_r(\omega) = m_\infty - \frac{1}{\omega} \int_{\mathbb{R}^+} h_r(t) \sin(\omega t) dt. \tag{3}$$

The non-parametric term $A_r(\omega)$, together with the so-called radiation damping $B_r : \mathbb{R} \to \mathbb{R}$, given by

$$B_r(\omega) = \int_{\mathbb{R}^+} h_r(t) \cos(\omega t) dt, \tag{4}$$

fully characterise the (well-defined) Fourier transform of h_r, i.e., we can write $H_r : \mathbb{R} \to \mathbb{C}$ as

$$H_r(\omega) = B_r(\omega) + j\omega \left[A_r(\omega) - m_\infty\right]. \tag{5}$$

In particular, radiation damping describes the dissipative effect of the energy transmitted from the oscillating body in the form of waves (i.e., radiated waves propagate away from the body).

---

1 The use of the capitalised letter for Laplace or Fourier transforms is always clear from the context.
2 Note that all five controllers listed in Table 2 assume a one-DoF device in each corresponding analytical formulation.

The radiation added-mass represents the additional inertial effect due to the acceleration of the water, which moves together with the body. Equations (3) and (4) are commonly referred to as Ogilvie's relations [15], and they stem from the definition of the Fourier transform. Furthermore, note that the impulse response function h_r completely characterises an LTI system Σ_r, describing the dynamics of radiation effects.

Finally, the equation of motion of the WEC is given by

$$\Sigma : \begin{cases} \ddot{x} = \mathcal{M}\left(-h_r * v - s_{\mathrm{h}} x + f_{ex} - f_u\right), \\ y = v. \end{cases} \tag{6}$$

3. Fundamentals of WEC Control: The Impedance-Matching Principle

One of the first and fundamental results applied within the wave energy control literature relies on a direct approach to the energy-maximising problem, inspired by impedance matching in electrical circuits, where device and actuator constraints are neglected. In particular, this principle, which is effectively utilised by the five controllers compared in this study, heavily relies on a frequency-domain analysis of the WEC dynamics, and it is detailed and discussed in the following paragraphs.

Consider the linear Cummins' formulation, as defined in Equation (6). A direct application of the Fourier transform, together with the radiation force frequency-domain equivalent introduced in Equation (5), yields

$$j\omega(M + m_\infty)V(\omega) + H_r(\omega)V(\omega) + \frac{s_h}{j\omega}V(\omega) = F_{ex}(\omega) - F_u(\omega), \tag{7}$$

where the mappings $V : \mathbb{R} \to \mathbb{C}$ and $F_u : \mathbb{R} \to \mathbb{C}$ represent the Fourier transform of the device velocity v and controller input f_u, respectively. From (7), it directly follows that

$$V(\omega) = \frac{1}{I(\omega)}\left[F_{ex}(\omega) - F_u(\omega)\right], \tag{8}$$

where the mapping $I : \mathbb{R} \to \mathbb{C}, \omega \mapsto I(\omega)$, defined as

$$I(\omega) = B_r(\omega) + j\omega\left[A_r(\omega) + M - \frac{s_h}{\omega^2}\right], \tag{9}$$

denotes the equivalent (intrinsic) impedance of the WEC. Naturally, Equation (8) resembles well-known representations in the field of electrical/electronic engineering and circuits theory: the WEC dynamics (7) can be equivalently represented by the analogue circuit that is depicted in Figure 1a.

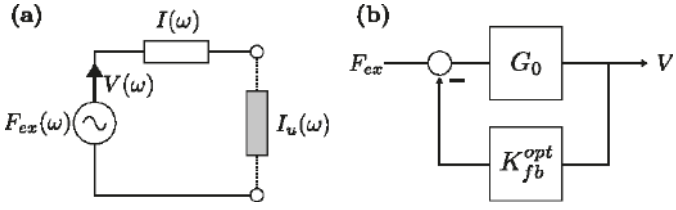

Figure 1. Impedance-matching principle. (**a**) Equivalent circuit for the frequency-domain analysis of Cummins' Equation (7). (**b**) Closed-loop impedance-matching formulation.

In other words, the control input $F_u(\omega)$ can be considered as a load, which has to be designed, so that maximum power transfer is achieved from the source, i.e., the wave excitation input $F_{ex}(\omega)$. From this particular point of view, this problem can be directly addressed using the so-called *impedance-matching* (or *maximum power transfer*) theorem [7], which is a well-established

result within the electrical/electronic engineering community. This theorem states that the *load* impedance, I_u, should be designed, for alternating (a.c.) circuits, such that it exactly coincides with the complex-conjugate of the *source* impedance, I. In other words, the control input that maximises power transfer, for the WEC case, is given by

$$F_u(\omega) = I_u(\omega)V(\omega) = I^\star(\omega)V(\omega) = K_{fb}^{opt}(\omega)V(\omega), \tag{10}$$

where the notation K_{fb}^{opt} is used to denote that the 'controller' in (10) is of a feedback-type. The result that is posed in (10) is indeed appealing, mainly due to its intrinsic simplicity, and its direct link to fundamental and well-established theory in the field of analogue circuits. Nevertheless, there are several issues that are associated with the control specifications given in (10), which prohibits the smooth application of what could potentially be an extremely appealing principle. These are listed and discussed in the following paragraphs.

To begin this discussion, note that the Laplace-transform analogue of Equation (7), when considering zero initial conditions, directly yields,

$$V(s) = G_0(s)\left[F_{ex}(s) - F_u(s)\right], \tag{11}$$

where the mapping $G_0 : \mathbb{C} \to \mathbb{C}$, defining the input-output dynamics $f_{ex} - f_u \mapsto v$, is given by

$$G_0(s) = \frac{H_r^D(s)s}{(M + m_\infty)H_r^D(s)s^2 + H_r^N(s)s + H_r^D(s)s_h}, \tag{12}$$

where the Laplace transform of the radiation impulse response, H_r, has been written, without any loss of generality, as $H_r(s) = H_r^N(s)/H_r^D(s)$. Given the causality property of the radiation force system Σ_r (see, for instance, [16]), and the fact that Σ_r is always strictly proper [8], the following relation

$$\deg\left\{H_r^N(s)\right\} < \deg\left\{H_r^D(s)\right\}, \tag{13}$$

holds. Direct observation of Equations (8) and (11) yields that, in the frequency-domain, the relation $I(\omega) = 1/G_0(\omega)$, holds. In other words, the dynamical system that is associated with the frequency-response $I(\omega)$ is inherently non-causal, as a direct consequence of the fact that the transfer function $G_0(s)$ is strictly proper (see Equation (13)). This poses a major issue with respect to the applicability of result (10): the dynamical system that is associated with the control law (10) cannot be practically implemented, due to its intrinsic non-causality. In addition to this non-causality issue, the following additional implications that are associated with the matching-principle can be identified:

- The optimal control law (10) implies a different matching-condition for each input-frequency ω.
- Neither device nor actuator limitations are observed by the matching condition (10). As a matter of fact, this control strategy often requires unrealistic displacement, velocity, and control input values to successfully achieve maximum power absorption. This is a direct product of the linearising assumptions under which Equation (6) is derived.
- The stability, sensitivity, and robustness properties of the control loop associated with the impedance-matching principle of (10), depicted in Figure 1b, have been recently questioned in [17]. In particular, [17] shows that radiation damping modelling errors can be particularly detrimental in the impedance-matching condition, given that a very specific zero-pole cancellation takes place when f_u is selected, as in (10).

Note that the force-to-motion (force-to-velocity in this case) frequency-response mapping, under impedance-matching condition (10), can be readily computed as

$$V(\omega) = \frac{G_0(\omega)}{1 + G_0(\omega)K_{fb}^{opt}(\omega)}F_{ex}(\omega) = \frac{1}{2B_r(\omega)}F_{ex}(\omega), \tag{14}$$

where B_r is the radiation damping, as defined in Section 2. In particular, there exists an optimal real-valued scaling function $T^{opt} : \mathbb{R} \to \mathbb{R}^+$, which is given by

$$T^{opt}(\omega) = \frac{1}{2B_r(\omega)}. \tag{15}$$

Note that the image of T^{opt} is effectively contained in $\mathbb{R}^+$, as a consequence of the passivity property of the radiation force, i.e., $B_r(\omega) > 0, \forall \omega \in \mathbb{R}/0$.

Although impedance-matching, as in (10), has some difficulties in practical application (for the reasons discussed above), it effectively describes the underlying dynamics behind maximum energy absorption, in an intuitive way. As a matter of fact, this principle underpins the family of simple controllers analysed in this study (see Table 2), which effectively attempt to provide implementable approximations of the control law derived in (10). The methodologies, which were employed by each of these five (5) controllers to approximate the impedance-matching condition (10), are discussed in detail in Section 4.

4. Simple WEC Controllers (in Chronological Order)

This section outlines the fundamentals behind each of the simple energy-maximising control strategies listed in Table 2, which are inherently based on the impedance-matching principle (as described in Section 3), proposed during the period between 2010–2020. In particular, the five (5) control strategies originally presented in [9–13], are recalled (in chronological order) in Sections 4.1–4.5, respectively. From now on, the shorthand notation introduced in Table 2 is used to refer to each specific strategy.

Note that this section does not simply recall results, but it also provides a critical analysis of each controller with respect to their potential success in a practical implementation, from a system dynamics perspective. In particular, the presented discussion aims to highlight the underlying simplicity of each presented controller, in terms of its applicability in the widest possible range of hardware platforms, including, for instance, low-cost microcontrollers. In the light of this, properties, such as nature of the control structure (i.e., linear, nonlinear, time-varying, etc.), as well as order, stability, and constraint handling capabilities (if any), are explicitly discussed, for each of the controllers that are listed in Table 2.

4.1. Suboptimal Causal Reactive Control (2011, C1)

This energy-maximising control strategy is essentially based on a velocity-profile tracking-loop (typical of approximate velocity tracking (AVT) WEC controllers [18]), schematically depicted in Figure 2, where $\hat{f}_{ex}(t)$ indicates the estimation of the wave excitation force $f_{ex}(t)$. Using the fundamental impedance-matching principle and the optimal mapping $T^{opt}(\omega)$, as described in Equation (15), the control methodology presented in [9], although being suboptimal, represents a suitable methodology for real-time application, considering that only linear time-invariant (LTI) systems are involved in the control design procedure (further discussed in the following paragraphs). It should be noted that, even though this control methodology requires the estimation of the wave excitation force (to effectively compute the velocity profile v_{ref}), such an estimate can be obtained by means of standard unknown-input observers. This includes, for instance, Kalman-based estimators, in combination with a harmonic description of the wave excitation input [19].

Essentially, this control technique approximates the optimal mapping $T^{opt}(\omega)$ as follows:

$$T^{opt}(\omega) = \frac{1}{2B_r(\omega)} \approx \frac{1}{2\hat{H}}, \tag{16}$$

where $\hat{H} \in \mathbb{R}^+$. In particular, the study that is presented in [9] computes the constant gain $\hat{H}$ using a second order approximation of the force-to-velocity WEC model:

$$G_0(\omega) \approx \tilde{G}_0(\omega), \tag{17}$$

where $\tilde{G}_0 : \mathbb{R} \to \mathbb{C}$ represents the frequency-response mapping of a second-order system, obtained by means of a model reduction routine that is based on Hankel singular values (see, for instance, [20]). Thus, if $G_0(\omega) \approx \tilde{G}_0(\omega)$, then the authors of the C1 controller rely on the following relation

$$B_r(\omega) \approx \tilde{B}_r = \hat{H}, \tag{18}$$

with $\tilde{B}_r \in \mathbb{R}^+/0$, being the approximation in Equation (18) valid (i.e., accurate) for a certain range of ω.

Note that, in order to obtain a system $\tilde{G}_0(\omega)$ that satisfies Equation (18), while preserving the band-pass nature of the force-to-velocity mapping of a WEC system, a zero at the origin can be forced in the determination of $\tilde{G}_0(\omega)$. Nevertheless, only the order (number of eigenvalues) and stability of the approximating system can be handled using model reduction routines that are based on Hankel singular values. Note that, when the zero at the origin is guaranteed, and $\tilde{G}_0(s)$ consequently represents a band-pass structure, then:

$$\tilde{B}_r = \mathbb{R}\mathrm{e}\left\{\frac{1}{\tilde{G}_0(\omega)}\right\}, \tag{19}$$

where $\tilde{G}_0(\omega)$ is, as a consequence of Equations (18) and (19), a passive system. However, in practical terms, the value of $\hat{H}$ can be determined, depending on, for example, the spectral content of the sea-states characterising the operating conditions of the specific device being controlled. In other words, one can select $\hat{H}$ merely as the radiation damping of the device, i.e., $B_r(\omega)$, evaluated at the frequency associated with the most energetic waves, in the total wave power spectrum.

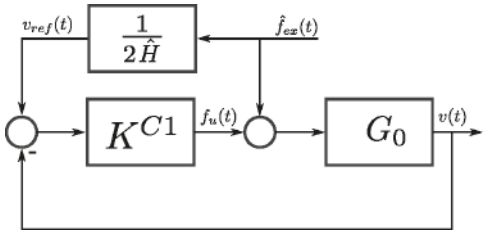

Figure 2. C1 control scheme presented in [9].

It should be noted that, depending on the operating conditions (i.e., sea-states under analysis), the optimal $\hat{H}$, which maximises the generated power for particular control specifications, can be potentially tuned while using a higher-order approximation of the WEC dynamics (rather than second-order, as per the original design behind the C1 controller). Furthermore, when considering that this control strategy can only interpolate the optimal condition at a finite number of frequencies[3], then only monochromatic (regular) sea-states can be efficiently addressed, in terms of maximum theoretical power production, with this energy maximising control technique.

Concerning the stability of the C1 controller, note that the system $1/2\hat{H}$ is an open-loop static mapping, and the definition of $\hat{H}$ does not affect the stability of the complete control loop;

[3] Take into account that with this control strategy the optimal condition is approximated using a constant value.

therefore, $1/2\hat{H}$ can be specifically tuned for different cases, considering a number of different design criteria, driven by the operating conditions.

On the other hand, under certain assumptions, which, when considering the passivity of $G_0(s)$, are guaranteed for WEC systems, the tracking feedback controller K^{C1} (see Figure 2) can be synthesised, as suggested in [9], while using the Youla-Kučera parametrisation for stable systems [21], i.e.,

$$K^{C1}(s) = \frac{Q(s)}{1 - Q(s)G_0^{-1}(s)}, \tag{20}$$

where $Q(s) = F(s)G_0^{-1}(s)$ and, for example,

$$F(s) = \frac{\frac{\omega_c}{q_f}s}{s^2 + \frac{\omega_c}{q_f}s + \omega_c^2}, \tag{21}$$

which represents a classical band-pass filter, such that $F(\omega_c) = 1$, and where $q_f \in \mathbb{R}^+/0$ indicates the band-width of the filter. However, note that the design of the internal tracking controller K^{C1} can be performed using a wide variety of control techniques, including, for instance, $\mathcal{H}_\infty$-techniques, to cover system uncertainties, or sliding-modes methodologies, to tackle potential nonlinearities arising in the WEC dynamical system. From a stability perspective, which, as discussed in Section 3, represents a well-known issue in impedance-matching based controllers, this control strategy can be safely designed without compromising closed-loop stability.

Finally, note that this control strategy itself is purely based on LTI systems: both the computation of the reference velocity profile, v_{ref}, and the tracking controller, K^{C1}, involve LTI systems. Regarding the order of the C1 controller when the above Youla-Kučera parametrisation technique is considered, i.e., Equations (20) and (21), the order of the controller $K^{C1}(s)$ is given by $n + 1$, where n denotes the order of the WEC model $G_0(s)$.

4.2. Simple and Effective Real-Time Controller (2013, C2)

The C2 controller, as schematically depicted in Figure 3, has one particular appealing feature: It not only provides a simple a approximation of the impedance-matching principle, but also incorporates a constraint handling mechanism. This controller, together with the C5 (see Section 4.5), are the only two simple controllers presented in the literature which are capable of handling physical constraints as part of their design.

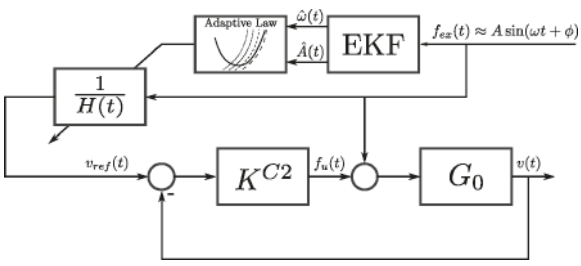

Figure 3. C2 control scheme presented in [10].

The C2 controller arises as an extension of the controller presented in [9], as detailed here in Section 4.1. In particular, the wave excitation force, as considered for this control strategy, is approximated using a monochromatic sinusoidal process, i.e.,

$$f_{ex}(t) \approx A(t)\sin(\omega(t)t + \phi(t)), \tag{22}$$

with parameters $\{A, \omega, \phi\} \subset \mathbb{R}$, which can vary with time. Similarly to the C1 controller, the C2 is essentially based on a velocity-profile tracking-loop (AVT controller). Unlike its predecessor, the C2 strategy features an adaptive process, where the velocity reference profile is updated in real time by means of an Extended Kalman filter (EKF), which provides an instantaneous estimate of the set of parameters $\{A, \omega, \phi\}$, fully characterising the excitation force as in (22). Such an estimation is motivated by two clear objectives, as detailed in the following. Firstly, knowledge of these estimates is used to improve the block $\frac{1}{2\hat{H}}$ that is proposed in the C1 controller (as shown in Figure 2), by means of a continuous-time adaptation procedure, aiming to approach the optimal condition $T^{opt}(\omega)$, stated by the impedance-matching principle. Secondly, the information provided by the estimation is used to normalise the wave excitation force estimate and compute a suitable velocity profile, according to pre-defined constraint specifications. To be precise, the information provided by the EKF is explicitly employed in the computation of the following time-varying scaling function:

$$\frac{1}{H(t)} = \begin{cases} \frac{1}{2B_r(\hat{\omega}(t))}, & \text{if} \quad \frac{\hat{\omega}(t)X_{lim}}{\hat{A}(t)} > \frac{1}{2B_r(\hat{\omega}(t))}, \\ \frac{\hat{\omega}(t)X_{lim}}{\hat{A}(t)}, & \text{if} \quad \text{otherwise}, \end{cases} \tag{23}$$

where X_{lim} represents the maximum displacement limit. Such a mapping $H(t)$ is schematically shown in Figure 3, where $\hat{A}(t)$, $\hat{\omega}(t)$ represent the instantaneous estimates of amplitude A and frequency ω, both in Equation (22), respectively. Finally, the feedback tracking controller, denoted as K^{C2} in Figure 3, can be computed while using the Youla-Kučera parametrisation, as per the case of the C1 controller, described in Section 4.1. To be precise, the controller K^{C2} can be designed following the expressions provided in Equations (20) and (21). It is important to highlight that, although the estimation process in the C2 controller is performed in terms of an EKF, a wide variety of estimation techniques could be potentially employed to provide instantaneous estimates of A and ω (see, for instance, [19]).

There are some aspects, both positive and negative, related to the C2 controller, and its applicability in realistic environments, which are worth mentioning. On the positive side, the C2 controller can effectively handle displacement limitations in terms of the design parameter X_{lim}. This is clearly fundamental in any practical application, where compliance with physical restrictions must be guaranteed by the energy-maximising control strategy, hence maximising energy absorption while minimising the risk of component damage. Nonetheless, on the negative side, and taking into account the challenge involved in the tuning of the corresponding estimator, and its sensitivity to design parameters [19], the inclusion of the EKF can potentially impact (negatively) on the resulting performance, as detailed in the following. In particular, when considering that the wave excitation force can be expressed as in Equation (22), methodologies that instantaneously estimate the amplitude A and frequency ω, virtually always assume that A is approximately constant. In addition, the computation of an estimate of the frequency ω, in Equation (22), inherently requires a non-linear estimation process [19]. The necessity of assuming a low variation rate for the amplitude modulation $A(t)$ (see [19]), and the fact that the design and calibration of the nonlinear estimation process that is required to compute the instantaneous input frequency is substantially challenging, can potentially degrade the quality of the approximating f_{ex} defined in (22). This naturally has a direct impact on the quality of the energy-maximising solution provided by the C2 controller (which explicitly uses this estimate in order to compute the corresponding control force), both in terms of performance, and satisfaction of physical limitations (i.e., constraints).

From a stability analysis point of view, this controller presents an advantage, directly related to the simple LTI velocity tracking controller K^{C2}: In other words, one can always guarantee stability in the C2 controller as long as the tracking loop is stable, and the EKF strategy converges towards a bounded wave excitation estimate. However, even though the reference tracking controller is based on a LTI system, this control methodology cannot be considered LTI altogether, due to the presence of the time-varying prefilter $1/H(t)$, which is involved in the computation of the velocity profile

v_{ref}. Regarding the feedback controller order, when the Youla-Kučera parametrisation is considered (i.e., as in Equations (20) and (21)), the order of $K^{C2}(s)$ is given by $n+1$, where n denotes the order of the WEC model $G_0(s)$. Finally, note that convergence of the EKF estimation, towards the real wave excitation force time-trace, cannot be generally guaranteed, mainly because such a force cannot be always expressed as in Equation (22). In other words, this controller inherently assumes that the device is subject to waves that arise from a narrowbanded sea-state, which is not always the case in practice.

4.3. Multi Resonant Feedback Control (2016, C3)

The controller that is presented in [11], i.e., the C3 controller, is strictly based on a feedback structure. It is important to note that, in contrast to the previously presented two controllers (Sections 4.1 and 4.2), the feedback structure does not require wave excitation force estimates, which positively impacts on its associated computational complexity. Aiming to address the energy-maximisation problem in a broadband sense, the design of the C3 controller is based on a specific approximation of the impedance-matching condition using a frequency-domain discretisation, i.e., considering a finite set of frequencies as,

$$\mathbf{\Omega} = \{\omega_1, \ldots, \omega_N\} \subset \mathbb{R}^+. \tag{24}$$

To this end, and similarly to the case that is presented in Section 4.2, the wave excitation force is approximated as a finite sum of N purely sinusoidal processes, i.e.,

$$f_{ex}(t) \approx \sum_{i=1}^{N} A_i^{ex} \sin(\omega_i t + \phi_i^{ex}). \tag{25}$$

Subsequently, given the linearity associated with the WEC model $G_0(s)$, the device velocity can be consequently described as:

$$v(t) \approx \sum_{i=1}^{N} v_i(t) = \sum_{i=1}^{N} A_i \sin(\omega_i t + \phi_i). \tag{26}$$

Note that the C3 control strategy, as presented in [11], uses position as the default output of the WEC system $G_0(s)$. However, aiming to be consistent with all the (other) controllers that are considered in this study, and without any loss of generality, the velocity is used in this study as the output of the WEC system. Figure 4 schematically depicts the C3 control strategy.

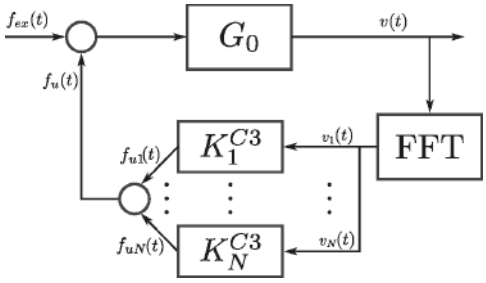

Figure 4. C3 control scheme presented in [11].

As a consequence of the assumption regarding the wave excitation force and velocity stated in Equations (25) and (26), the authors of [11] separate the system $G_0(s)$ into N second-order subsystems, i.e., $\{G_i(s)\}_{i=1}^{N}$, such that

$$G_0(\omega_i) = G_i(\omega_i), \tag{27}$$

for all $\omega_i \in \mathbf{\Omega}$, with $i \in \mathbb{N}_N$. The objective sought with the separation, as shown in Equation (27), is to deal with simpler individual systems $G_i(s)$ where, given the second-order nature of each subsystem $G_i(s)$, the following result

$$\mathbb{R}\mathrm{e}\left\{\frac{1}{G_i(\omega)}\right\} = B_r^i, \tag{28}$$

with $B_r^i \in \mathbb{R}^+$, for all $i \in \mathbb{N}_N$, holds. The relation that is posed in Equation (28) is a key factor in the definition of the optimal control condition exploited by the C3 controller: instead of solving the complete energy maximising control problem, i.e., considering the optimal frequency-domain impedance-matching condition for all $\omega \in \mathbb{R}$, the C3 control strategy aims to solve the impedance-matching problem for each subsystem $G_i(s)$, which is intrinsically related to each B_r^i, defined in Equation (28). In particular, the energy-maximising control problem is tackled while using a set $\mathbf{K}^{C3}$ of N proportional-integral (PI) controllers, i.e., $\mathbf{K}^{C3} = \left\{K_i^{C3}(s)\right\}_{i=1}^N$, with each K_i^{C3} defined as

$$K_i^{C3}(s) = \left(P_i^{C3} + \frac{I_i^{C3}}{s}\right), \tag{29}$$

where the set of parameters $\{P_i^{C3}, I_i^{C3}\}_{i=1}^N \subset \mathbb{R}$ is designed to approach the impedance-matching optimal condition for each subsystem $G_i(s)$.

Note that the control problem that is posed in [11] is stated as an optimisation problem, where the values A_i and ϕ_i, as expressed in Equation (26), are estimated in real-time. In other words, the determination of the instantaneous estimate of each A_i and ϕ_i, in Equation (25), plays a key role in this control strategy, and is addressed by the C3 in terms of an optimisation problem. In particular, the estimation required in [11] is tackled by means of a real-time implementation based on the fast Fourier transform (FFT), as shown in Figure 4. Note that different (time) window lengths are utilised in the case studies that are presented in [11], aiming to analyse their effect in the final energy-maximising performance.

From a general perspective, mainly concerning the applicability and the stability of this control strategy, some aspects are worth mentioning. Firstly, the use of a real-time FFT and the time window required for its implementation generates a time-delay between measurement and control actuation. It is important to highlight that time precision plays a decisive role in real-time implementation, and can intrinsically affect both the stability properties of the control loop, and its performance in terms of energy capture. By the way of example, and in order to highlight the importance of having good timing in realistic control implementations, the use of a real-time operating system (RTOS), such as, for example real-time LabView, Matlab xPC Target, RTOSs for the microcontroller architecture, or even FPGA-based systems, is a common practice for realistic control implementation. This effectively reduces the time-delay between measurement and control actuation (i.e., latency or jitter). Note that the FFT procedure can be potentially replaced by suitable recursive least square (RLS) routines, such as those that are described in [22][4]. This allows for a potentially more computationally efficient implementation than its FFT counterpart, which would be appealing for real-time applications. Secondly, the methodology that is employed in [11] to define $G_i(s)$ is not clearly stated. Note that there exists an infinite number of possible second-order systems $G_i(s)$ fulfilling Equation (27), which can lead to different control scenarios. In addition, even though a stability analysis is performed in [11] while using the classical Routh–Hurwitz criterion (see, for instance, [23]) for each controller-plant pair (K_i^{C3}, G_i), it is not clear how the stability of the complete interconnection, i.e., $(\mathbf{K}^{C3}, G_0)$, can be guaranteed. Furthermore, the authors of [11] do not

[4] As a matter of fact, using RLS algorithms effectively resembles optimisation-based spectral techniques based on trigonometric basis functions (see, for instance, [22]).

take into account the estimation of each A_i and ϕ_i in the closed-loop stability analysis, which further increases the degree of uncertainty behind the practicality of this solution. Note that such an estimation process depends upon a time-dependent optimisation routine, which automatically renders the control loop as time-varying, commonly requiring converse Lyapunov theory (see, for instance, [24]) to guarantee uniform stability, which intrinsically complicates the nature of the problem.

Finally, note that this controller cannot be considered a LTI system, due to the optimisation process that is involved in the feedback path. In addition, regarding the order of the set of controllers $\mathbf{K}^{C3}$, when considering the PI structure presented in Equation (29), the total order always matches the number of elements considered in the frequency set $\mathbf{\Omega}$, i.e., there is one PI (first-order) controller for each element of the set $\mathbf{\Omega}$.

4.4. Feedback Resonating Control (2019, C4)

As in the case detailed in Section 4.3, the energy maximising control strategy presented in [12], denoted here as C4, is essentially based on a classical feedback control structure, as depicted in Figure 5. Thus, as for the C3 controller, knowledge of the wave excitation force is not required to implement the C4 control strategy, which significantly reduces the controller complexity and simplifies its implementation, as well as contributing to improving the resulting performance, as long as some guarantee of closed-loop stability can be provided.

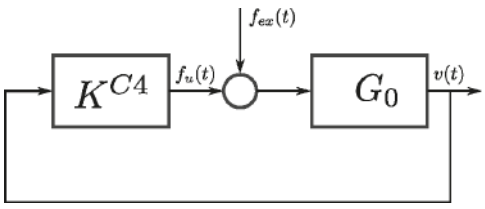

Figure 5. The C4 control scheme presented in [12].

In the energy-maximising control strategy proposed in [12], the controller is synthesised while using system identification algorithms, aiming to approximate the frequency-domain feedback optimal control condition, i.e., Equation (10). The control strategy is schematically depicted in Figure 5. In particular, the proposed controller has a fixed rational polynomial structure, as follows

$$K^{C4}(s) = \frac{b_2 s^2 + b_1 s + b_0}{s^2 + a_1 s + a_0}, \tag{30}$$

which structurally considers two poles and two zeros, with $\{b_0, b_1, b_2, a_0, a_1\} \subset \mathbb{R}$. Subsequently, in order to approximate the impedance-matching optimal condition over a certain frequency range, the system in Equation (30) is designed to satisfy the following relation:

$$K^{C4}(\omega) \approx K_{fb}^{opt}(\omega). \tag{31}$$

with $K_{fb}^{opt}(\omega)$ defined in Equation (10). Given that input-output stability can be generally set as a requirement in the majority of standard identification approaches available in the literature [25], the stability of the controller can be straightforwardly satisfied, which is recommended for any realistic control system implementation. However, this does not necessarily guarantee closed-loop stability for the system that is depicted in Figure 5; additional requirements need to be imposed on the structure in (30) in order to secure stable closed-loop behaviour, such as, for instance, passivity.

In addition, the simplicity of the controller structure, given its second-order nature, is worth highlighting. Furthermore, recalling that stability represents a key issue for controllers that are based on the impedance-matching principle, the C4 control methodology can be relatively easily designed in

order to guarantee both controller and, more important, closed-loop, stability, although the latter is not theoretically addressed in [12]. Nevertheless, the lack of a constraint handling mechanism can render the C4 controller unsuitable for realistic implementations.

From a dynamical systems perspective, this controller is based on a single LTI system. In addition, considering the fixed structure that is presented in Equation (30), the controller order is always set to 2.

4.5. LiTe-Con (2020, C5)

Similarly to the case that is presented in Section 4.4, the so-called LiTe-Con [13] (referred to here as C5), is synthesised using system identification algorithms, aiming to approximate the frequency-domain energy-maximising optimal condition. In particular, based on the impedance-matching feedback law (10), in order to provide an alternative energy maximising control solution that is capable of dealing with the stability issues detailed in Section 1, the authors of [13] recast the controller solution into an equivalent feedforward structure, i.e.,

$$K_{ff}^{opt}(\omega) = \frac{\mathbb{R}\mathrm{e}\left\{G_0(\omega)\right\} + \jmath\mathbb{I}\mathrm{m}\left\{G_0(\omega)\right\}}{2\mathbb{R}\mathrm{e}\left\{G_0(\omega)\right\}}, \tag{32}$$

where the mapping $f_{ex} \mapsto v$, corresponding with the feedforward structure (32), is equivalent to that presented in Equation (15). Note that, in contrast to C4, which does not require estimation of the wave excitation force, the feedforward control structure requires the estimation of the excitation force of the wave. Thus, the requirement of having an estimate of $f_{ex}(t)$, can negatively impact on the resulting performance [26]. The aspect that is related to the requirement of having an estimate of the wave excitation force can be considered as the essence of the distinction between C4 and C5. The non-parametric frequency-response mapping K_{ff}^{opt} is then approximated by means of black-box system identification techniques, as further discussed in the upcoming paragraphs.

Given the inherent feedforward structure of the C5 controller, estimation of the wave excitation force is required. The control structure C5, as presented in [13], is schematically depicted in Figure 6, where $\hat{f}_{ex}$ denotes the estimate of the wave excitation force f_{ex}, and K^{C5} is the C5 controller. Note that a constraint handling mechanism is proposed in C5, extending its applicability range to realistic environments.

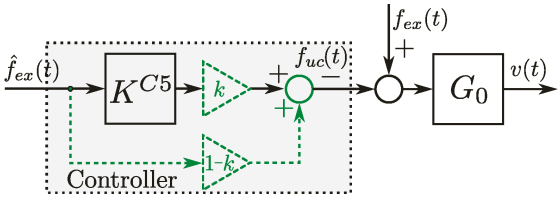

Figure 6. C5 control scheme presented in [13]. The constraint handling mechanism of the C5 is indicated using a shadowed-grey box, using dashed-green line to represent the internal block interconnections.

The controller methodology that is presented in [13] proposes the approximation of the optimal impedance-matching controller K_{ff}^{opt}, as defined in Equation (32), with a LTI-stable and implementable dynamical system K^{C5}, such that

$$K^{C5}(s)\Big|_{s=jw} \approx K_{ff}^{opt}(\omega), \tag{33}$$

where $K^{C5}(s)$ is obtained using frequency-domain system identification algorithms, such as subspace [25] or moment-matching-based [27] system identification techniques. Subsequently, the resulting control force (in the frequency domain) is expressed as:

$$F_u(\omega) = K^{C5}(\omega)\hat{F}_{ex}(\omega). \tag{34}$$

In order to implement the synthesised C5 controller in a realistic environment, a constraint handling mechanism is essential to prevent inflicting damage on the mechanical system. In particular, [13] proposes a constraint handling mechanism, using a constant value $k \in [0, 1]$, so that the control force F_u in Equation (34) is redefined as:

$$F_{uc}(\omega) = \underbrace{\left[kK^{C5}(\omega) + (1-k)\right]}_{\text{Controller}} \hat{F}_{ex}(\omega), \tag{35}$$

where it is straightforward to check that $F_{uc}(\omega) = F_u(\omega)$ when $k = 1$. Assuming perfect matching in Equation (33), the optimal mapping in Equation (15) can be defined as:

$$T^{C4}(\omega) = k\left(\frac{\mathbb{Re}\left\{G_o(\omega)\right\}^2 + \mathbb{Im}\left\{G_o(\omega)\right\}^2}{2\mathbb{Re}\left\{G_o(\omega)\right\}}\right). \tag{36}$$

Note that, if $k = 1$ in Equation (36), then the optimal condition in Equation (15) is obtained, i.e., $T^{C4}(\omega) = T^{opt}(\omega)$. On the other hand, if $k = 0$, then $T^{C4}(\omega) = 0$. In other words, the inclusion of the term k allows for a simple implementation of position and velocity constraints, effectively constraining the position and velocity between zero and their theoretical maxima. The constraint handling mechanism of the C5 is indicated in Figure 6 using a dotted-grey box, while dashed-green lines are used to represent the internal block interconnections.

Some comments that are related to this control strategy and its applicability, particularly focusing on stability features, can be mentioned. On the positive side, the feedforward nature of the C5 controller requires a simple and relatively effortless implementation in real-world applications, while also effectively taking into account device limitations in terms of a simple constraint mechanism. Nonetheless, the C5 controller requires an estimate of the wave excitation force, which can potentially have a negative impact on the energy-maximising performance of the controller [28] and computational complexity. However, in contrast to, for instance, the C2 controller (which uses requires an EKF structure), the estimation that is required by the C5 can be addressed while using relatively standard wave excitation force estimation techniques. In particular, a LTI Kalman filter[5], featuring a harmonic description for ocean waves, is considered in [28]. As demonstrated in [19], this observer provides good overall estimation quality, while inherently handling measurement noise (in an optimal sense). From a stability perspective, the complete control structure stability (WEC system, excitation force estimator, and controller) is guaranteed as long as each individual component (WEC model, estimator, and controller) is stable, i.e., under the separability principle [23].

Finally, note that this control strategy is purely based on LTI systems (even taking into account the required estimation process for the wave excitation force). Regarding the order of the controller, it directly depends upon the system identification process that is employed to compute K^{C5}. For instance, using a moment-based identification approach [27], where the user can select a number of interpolation frequencies (or points) to preserve steady-state response characteristics (see Section 5.1.5), the order of the controller K^{C5} is twice the number of matching points.

5. Results

This section presents a case study, where the performance obtained with the set of five (5) controllers presented in Section 4, i.e., C1, C2, C3, C4, and C5, is assessed. Aiming to provide a set of benchmark cases in terms of maximum achievable absorbed energy, two reference measures are considered. Firstly, for the unconstrained case, the performance that is obtained with each controller is compared with the corresponding theoretical maximum, which is analytically computed while

[5] Infinite horizon version [23].

using Equation (15). Such a benchmark case is denoted here as CR1. Secondly, in the constrained case, where, unlike its unconstrained counterpart, there is not an explicit analytical formulation for the maximum achievable performance, an optimisation-based controller is considered. Even though the resulting performance that is obtained with optimisation-based formulations is not a theoretical maximum per-se (due to any potential errors arising from the intrinsic necessity of discretisation and use of numerical routines), it is considered here as a surrogate reference for maximum achievable performance in a constrained scenario. In particular, a moment-based controller [29], denoted in this study as CR2, is considered in this application case for the performance comparison in the constrained case, analogously to the performance assessment that is presented in [13]. It is important to note that, for the constrained case, only the C2 and C5 control methodologies can be considered for the performance assessment presented in this section: the controllers C1, C3, and C4 do not provide any constraint handling mechanism at all, which directly compromises their application in realistic scenarios. This is further discussed in the following paragraphs.

The control strategies are applied to a state-of-the-art full-scale CorPower-like device oscillating in heave (translational motion) [30]. This type of device is often considered throughout the WEC literature, being one of the most well-established WEC system within the wave energy field (see, for example, [31] or [32]), and it is illustrated in Figure 7 with its corresponding physical dimensions specified in meters. To perform the simulations and analysis shown in this section, the considered the WEC model, as in Figure 7, is described using an seventh-order LTI state-space representation, which is denoted in the frequency-domain as $G_0(\omega)$.

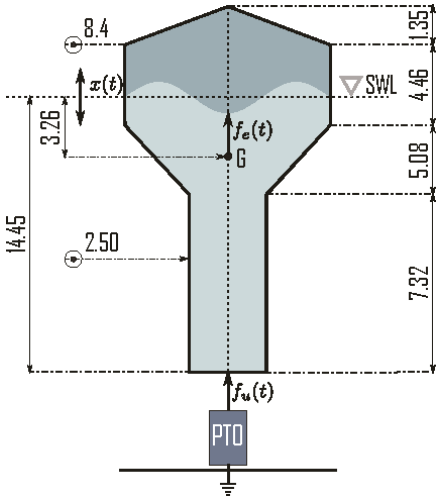

Figure 7. Full-scale CorPower-like device considered in this case study. Dimensions are in metres. The acronym SWL stands for still water level and the letter G is used to denote the center of gravity of the device. The lower side of the power take-off is anchored to the sea bed, which provides an absolute reference for device motion. The displacement of the device is denoted by $x(t)$.

In this application case, the time-trace of the wave excitation force, $f_{ex}(t)$, considering irregular waves, is determined from the so-called free-surface elevation, $\eta(t)$, based on a JONSWAP spectrum $S_\eta(\omega)$ [33]. The corresponding sea-state parameters, which characterise the nature of the mapping S_η, are as follows: Peak period in the interval $T_p \in [5.0, 12.0]$ s, significant wave height $H_s = 2.0$ m, and a peak-enhancement factor $\gamma = 3.3$. In Figure 8, $S_\eta(\omega)$ is depicted for $T_p = \{5, 6.4, 7.8, 9.2, 10.6, 12\}$ s, where $T_p = 5$ s and $T_p = 12$ s indicate the extremes of the considered range for T_p.

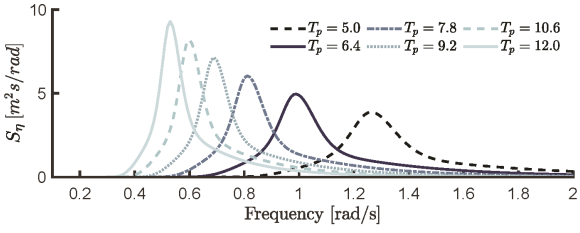

Figure 8. $S_\eta(\omega)$ for $T_p = \{5, 6.4, 7.8, 9.2, 10.6, 12\}$ s.

The power spectral density of the excitation force is given by the relation $|F_{ex}(\omega)| = |G_\eta(\omega)||S_\eta(\omega)|$, where $G_\eta(\omega)$, obtained using NEMOH [34], represents the frequency-response function associated with the mapping $\eta \mapsto f_{ex}$. The resulting performance is studied in both unconstrained, and constrained, scenarios, as detailed previously in this same section. In particular, in the constrained case, the maximum allowed displacement is set to $X_{max} = 1.5$ m. In this study, $\eta(t)$ is generated using a white noise signal, filtered according[6] to the spectrum $S_\eta(\omega)$ [35].

Throughout this section, performance is assessed in terms of the average absorbed power, which is evaluated as

$$P_{abs} = -\frac{1}{T}\int_0^T f_u(t)v(t)dt. \tag{37}$$

Note that, when considering the stochastic nature of the process involved, and to be statistically consistent, the results that are shown in this study are always representative average values, which are generated when considering 20 realisations of each specific sea-state.

Controllers C1, C2, and C5 require (potentially different) wave excitation force estimation procedures, as detailed throughout Section 4. For the case of C1 and C5, which rely upon an instantaneous estimate of the excitation force time-trace $f_{ex}(t)$, a linear Kalman filter is utilised, in combination with the internal model principle of control theory [36]. The design and synthesis procedure for such an observer, which is based upon a harmonic internal description of ocean waves, is well-established in the literature of WEC control, and it can be consulted elsewhere (see, for instance, [19]). Note that, in this study, the infinite-horizon Kalman gain is always utilised, i.e., the solution to the infinite-horizon algebraic Riccati equation, which directly implies that the associated estimator is LTI. The estimation requirements for controller C2 are different, and more 'sophisticated' methods than those associated with C1 and C5 are needed. In particular, this strategy relies upon having estimates of instantaneous amplitude $\hat{A}(t)$ and frequency $\omega(t)$, which, as previously discussed, inherently require a nonlinear estimation procedure, given the nature of the internal model used to describe the wave excitation force (see Equation (22)). As detailed in Section 4.2, an EKF is, as proposed in [10], considered to perform this task[7], which is designed and tuned following [10].

Although beyond the scope of this study, where 'idealised' conditions are assumed for simulation to guarantee a level playing field for the totality of the controllers studied, i.e., perfect knowledge of the WEC dynamics and noise-free measurements are considered, the reader is referred to, for instance, [17], for further detail on the impact of modelling mismatch in both feedback and feedforward structures, and [19,28], for potential performance deterioration caused by noisy measurements in wave excitation force estimators.

The remainder of this section is organised, as follows. Section 5.1 presents the design procedure of each controller recalled in Section 4. Sections 5.2.1 and 5.2.2 show the performance results for each

[6] For a detailed discussion about the synthesis of stochastic processes, the interested reader is referred to [35].
[7] An alternative to the use of an EKF can be found in [37], where estimates of $\hat{A}$ and $\hat{\omega}$ are computed based on the Hilbert–Huang transform [38].

controller, in both unconstrained, and constrained scenarios, respectively, while Section 5.3 discusses the time-domain behaviour obtained with each controller.

5.1. Design Procedures

This section outlines the design procedure of each controller presented in Section 4. Throughout the following paragraphs, detailed comments and insight, with respect to design process, are also included, when appropriate.

5.1.1. C1

The design procedure for the C1 controller, as presented in Section 4.1, can be separated into two clear stages. Firstly, the constant function $1/2\hat{H}$ has to be designed, so that a suitable velocity reference v_{ref} is generated. The second stage involves the design and synthesis of a closed-loop controller, which is able to track such a velocity reference profile.

To approximate the optimal mapping $T^{opt}(\omega)$, in terms of $1/2\hat{H}$, note that the waves that are considered in this study are generated using a stochastic description with peak period $T_p \in [5, 12]$ s, i.e., waves with significant energy components in a frequency range of approximately $[0.3, 2]$ rad/s (see Figure 8). Motivated by this, the value of $\hat{H}$ is determined to be as representative as possible in such a frequency range, as depicted in Figure 9. In particular, the obtained $1/2\hat{H}$ is shown using a dashed line, while the optimal mapping $T^{opt}(\omega)$ is depicted with solid line.

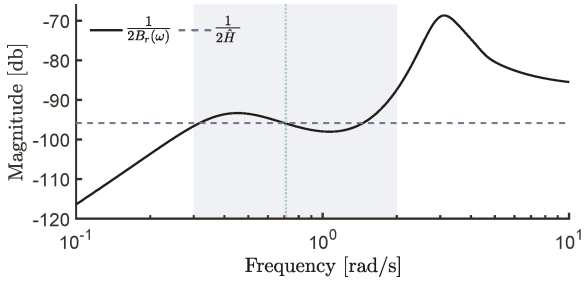

Figure 9. C1 design process.The optimal mapping, $T^{opt}(\omega) = 1/2B_r(\omega)$, and the obtained approximation, $1/2\hat{H}$, are depicted while using solid and dashed lines, respectively.

Note that, in Figure 9, the mean period $T_p = 8.5$ s (which is obtained as the average between the extreme of the complete range) is depicted using a dotted line. Additionally, the corresponding frequency range, i.e., $\approx [0.3, 2]$ rad/s, is depicted with a grey box. By the direct observation of Figure 9, one can appreciate that the best approximation of this optimal mapping $T^{opt}(\omega)$, provided by the constant gain $\hat{H}$, happens precisely at $2\pi/8.5$ rad/s, i.e., the C1 controller interpolates $T^{opt}(\omega)$ at $T_p = 8.5$ s.

As can be directly recalled from Section 4.1, the design procedure that is associated with the reference tracking loop is addressed while using a standard Youla-Kučera parametrisation for stable systems, which can be directly considered for the WEC case due to its passive and non-minimum phase nature [8]. To be precise, the velocity tracking loop, as depicted in Figure 2, can be synthesised using the following structure:

$$K^{C1}(s) = \frac{Q(s)}{1 - Q(s)G_0(s)^{-1}}, \tag{38}$$

where $Q(s) = F(s)G_0(s)^{-1}$ and

$$F(s) = \frac{\frac{\omega_c}{q_f}s}{s^2 + \frac{\omega_c}{q_f}s + \omega_c^2}, \tag{39}$$

with $\omega_c = 2\pi/8.5$ and $q_f = 0.1$. Thus, a LTI feedback controller K^{C1}, with order 8, is obtained. Figure 10 depicts the resulting mapping $v_{ref} \mapsto v$, i.e., the closed-loop frequency-response from the reference velocity, to the actual velocity of the CorPower-like device. A flat 0 dB response (both in terms of magnitude and phase) is achieved in the frequency range of interest, effectively indicating that the design criteria are being met, i.e., the output velocity is approximately following the input reference velocity, according to the spectral description of the ocean waves that are considered in this study.

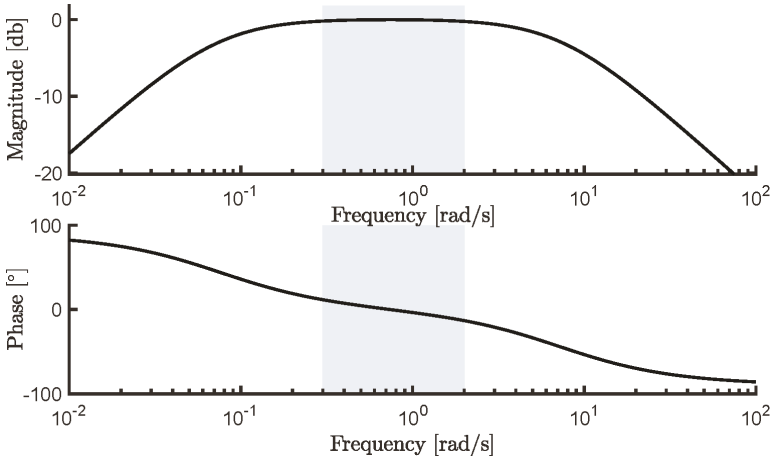

Figure 10. Obtained mapping between the reference velocity, and the actual velocity of the CorPower-like device, for the C1 and C2 controllers.

5.1.2. C2

This section describes the design procedure that is required by the C2 controller, schematically depicted in Figure 3. Similarly, as in the case presented in Section 5.1.1 for the C1 strategy, the design of the C2 controller can also be separated into two clearly distinctive stages: A velocity reference generation procedure, followed by a suitable closed-loop tracking mechanism. The reference tracking loop required by this control strategy can be analogously designed to that presented for the C1 controller in Equations (38) and (39), so the same tracking controller is utilised for the C2 controller, exhibiting the input-output behaviour previously illustrated (and described) in Figure 10, i.e., $K^{C2}(s) = K^{C1}(s)$.

The main difference between the C2 controller and its predecessor (i.e., the C1 controller) lies in the generation of the velocity profile, and its subsequent impact in final energy absorption. In the case of the C2 controller, the reference profile is generated in terms of instantaneous estimates of frequency and amplitude of the wave excitation force signal, computed by means of an EKF strategy. By way of example, Figure 11 shows estimation results for instantaneous amplitude $\hat{A}(t)$ (left axis—dashed) and frequency $\hat{\omega}(t)$ (right axis—dotted), for a particular sea-state realisation (left axis—solid), with $T_p = 8.5$ s.

Note that the sea states that are selected for this case study (see Figure 8) are based on a JONSWAP description with a peak enhancement factor of $\gamma = 3.3$, i.e., they are relatively narrowbanded. C2 generally performs better in narrowbanded seas, where a dominant frequency is present, as discussed in Section 4.2. However, and beyond the scope of this case study, the reader is reminded that this assumption might not always be fulfilled in a practical scenario. See Section 4.2 for further discussion.

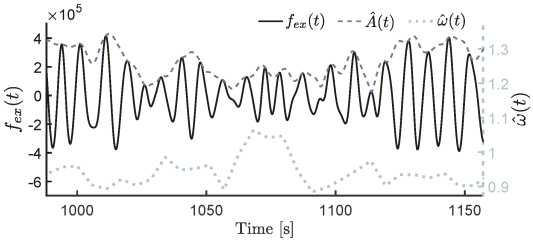

Figure 11. C2 design procedure. The wave excitation force and its amplitude and frequency estimation are shown with solid, dashed, and dotted lines, respectively.

5.1.3. C3

The design of this feedback controller begins with the definition of a finite set of frequencies $\mathbf{\Omega}$, as detailed in Equation (24), which allows for the computation of an approximation of the device velocity in terms of a finite set of frequency components (see Equation (26)). Such a set $\mathbf{\Omega}$ can be empirically defined, by explicitly using the frequency-domain characterisation of the stochastic process describing the different sea-states under analysis. In other words, the set $\mathbf{\Omega}$ is generated in order to guarantee a suitable representation of excitation forces with significant frequency components in the range corresponding with $[0.3, 2]$ rad/s, i.e.,

$$\mathbf{\Omega} = \left\{ \omega_k \in \mathbb{R}^+ \,\middle|\, \omega_k = \frac{\pi}{10} + \frac{\left(\frac{\pi}{2} - \frac{\pi}{10}\right)}{63} k,\ k \in \{0, \ldots, 63\} \right\}, \tag{40}$$

which represents a set with a cardinality of 64.

Subsequently, to determine estimates of each A_i and ϕ_i, in Equation (26), different FFT windows lengths, which are empirically determined using an exhaustive search methodology, are used for each different considered sea-state. In addition, each controller $K_i^{C3}(s)$ (see Equation (29)) is tuned, so that energy-maximisation is achieved, at each ω_i, while bearing in mind closed-loop stability. Thus, from a dynamical systems point of view, the resulting set $\mathbf{K}^{C3}$, considering the cardinality of the set $\mathbf{\Omega}$, represents a diagonal system of order 64.

By way of example, when considering the assumption expressed in Equation (25), which essentially inspires this control strategy, Figure 12a illustrates the approximation $\hat{f}_{ex}(t)$ (dashed line) obtained with the associated set of finite frequencies that are described in (40), for one particular realisation of the excitation force $f_{ex}(t)$ (solid line), computed according to a stochastic description with $T_p = 8.5$ s. Furthermore, Figure 12b provides the spectral representation of each of the excitation force time-traces, i.e., $\hat{f}_{ex}(t)$ and $f_{ex}(t)$, using dashed and solid lines, respectively.

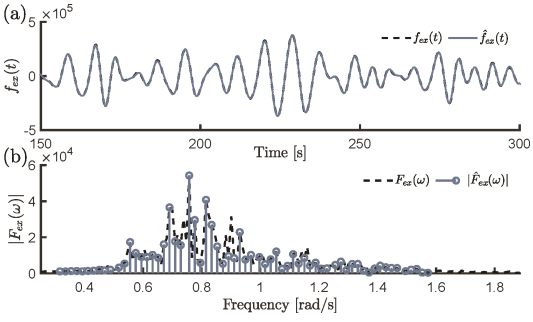

Figure 12. The approximated , $\hat{f}_{ex}(t)$, and the real excitation force, $f_{ex}(t)$, are shown using dashed and solid lines, respectively. In Figure 12 (**b**), the spectral representation of each time trace depicted in Figure 12 (**a**) is shown using the reference code employed for Figure 12a.

5.1.4. C4

The C4 control strategy, as depicted in Figure 5 and expressed in Equation (31), is essentially based on the application of system identification routines, considering a feedback control structure, as mentioned in Section 4.4. In order to satisfy Equation (31), frequency domain-based system identification routines are applied in this study. In particular, traditional least-mean-square error minimisation algorithms, for transfer function structures, are considered[8]. The identification process, required to compute K^{C4}, is performed using the data set defined for K_{fb}^{opt} in Equation (10), which is essentially based on the WEC frequency-response mapping G_0. The resulting controller, for the CorPower-like device that was considered in this case study, is given by the expression

$$K^{C4}(s) = \frac{-1.195 \times 10^6 s^2 + 5.883 \times 10^4 s - 5.244 \times 10^6}{s^2 + 9.800s + 0.216}. \tag{41}$$

Note that the focus of the frequency-domain identification algorithm is on ensuring the controller approximation in the frequency range characterising the wave inputs, i.e., $[0.3, 2]$ rad/s. To be precise, the following relation

$$K^{C4}(\omega) \approx K_{fb}^{opt}(\omega), \quad \forall \omega \in [0.3,\, 2]\,, \tag{42}$$

holds. This can be clearly appreciated in Figure 13, where the frequency-response mappings, which are associated with the control-loop featuring the approximating structure K^{C4}, are explicitly shown. In particular, the left column of Figure 13 shows $K^{C4}(\omega)$, together with the frequency-response associated with the (theoretical) optimal feedback controller K_{fb}^{opt}. In addition, the right column of Figure 13 depicts the input-output frequency-response mapping when the approximating feedback controller K^{C4} is considered, i.e., $T^{C4}(\omega)$, along with the corresponding (theoretical) optimal input-output frequency-response $T^{opt}(\omega)$.

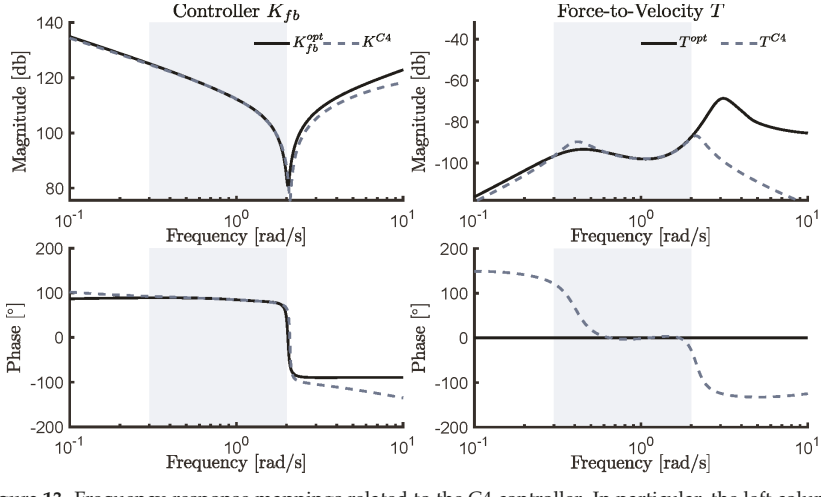

Figure 13. Frequency-response mappings related to the C4 controller. In particular, the left column illustrates $K^{C4}(\omega)$ (dashed line), together with the optimal feedback mapping $K_{fb}^{opt}(\omega)$ (solid line). The right column depicts the force-to-velocity mapping associated with the C4 controller, i.e., $T^{C4}(\omega)$ (dashed line), along with the optimal force-to-velocity frequency response $T^{opt}(\omega)$ (solid line).

[8] The interested reader is referred to [25] for a detailed discussion regarding classical system identification approaches.

5.1.5. C5

The C5 control strategy, as outlined in Section 4.5, is similar to that of the C4 controller, in the sense that both strategies are essentially based on performing system identification routines, aiming to approximate pre-defined optimal frequency-response mappings. However, there is one fundamental difference: While the C4 control methodology approximates a feedback structure, the C5 control strategy proposes a feedforward equivalent, which allows for constraint handling to be accommodated in a relatively straightforward manner. In particular, the C5 controller K^{C5} aims to approximate the impedance-matching condition that is expressed in Equation (33), i.e.,

$$K^{C5}(\omega) \approx K_{ff}^{opt}(\omega), \quad \forall \omega \in [0.3, 2], \tag{43}$$

where, once again, the focus for the frequency-domain identification algorithm is put on the frequency range characterising the wave inputs. The identification of the feedforward structure K_{ff}^{opt} is performed using a moment-matching-based identification approach, in order to ensure perfect frequency-response matching at a set of user-selected frequencies, as considered by the authors in [13]. Note that the definition of these matching points is designed to improve the fit between K^{C5} and K_{ff}^{opt}, within the target bandwidth defined in Equation (43). According to moment-matching-based identification theory [16], the order of the resulting controller is twice the number of matching points. In this study, seven matching points are considered, selected as

$$\omega_M = \left\{0.42, \quad 0.92, \quad 1.49, \quad 1.65, \quad 1.74, \quad 2.29, \quad 2.86\right\}, \tag{44}$$

generating an approximating structure K^{C5} of order 14. Figure 14 shows the set of frequency-response mappings that are related to the C5 controller. In particular, the left column of Figure 14 illustrates $K^{C5}(\omega)$, together with the optimal feedforward mapping $K_{ff}^{opt}(\omega)$. The right column of Figure 14 depicts the force-to-velocity mapping associated with the C5 controller, i.e., $T^{C5}(\omega)$, along with the optimal force-to-velocity frequency response $T^{opt}(\omega)$. Note that both the left and right columns also show the effect of varying the constant gain k, used to handle physical limitations, on each respective frequency-response profile. In particular, values for k in the set $\{0.5000, 0.2500, 0.1250, 0.065\}$ are considered, while using an arrow to indicate a decrease in k. Finally, the matching points, chosen to achieve moment-matching within the system identification procedure (i.e., the elements of the set (44)), are indicated using circular markers.

Regarding the tuning of the constraint handling mechanism, for this application case, the value of the constant k (as described in Equations (35) and (36)) is determined using exhaustive (simulation-based) search, depending on each particular sea-state considered. Figure 15 shows the resulting k, for each $T_p \in [5, 12]$ s.

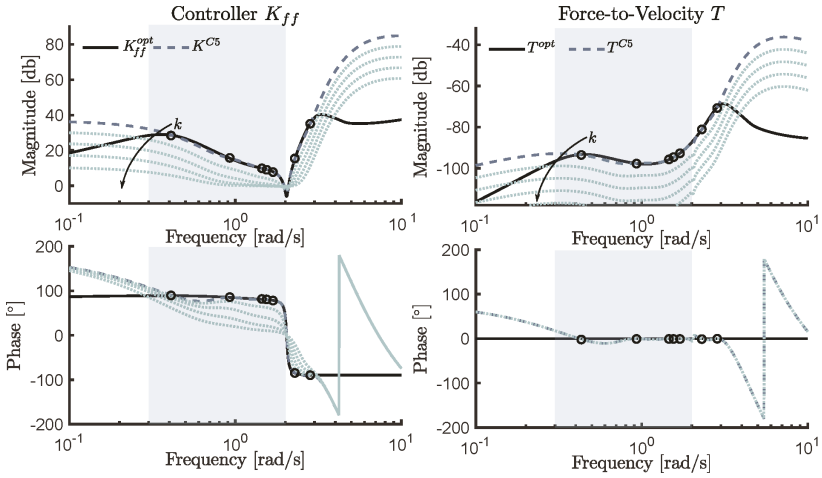

Figure 14. Frequency-response mappings related to the C5 controller. In particular, the left column illustrates $K^{C5}(\omega)$ (dashed line), together with the optimal feedforward mapping $K_{ff}^{opt}(\omega)$ (solid line). The right column depicts the force-to-velocity mapping associated with the C5 controller, i.e., $T^{C5}(\omega)$ (dashed line), along with the optimal force-to-velocity frequency response $T^{opt}(\omega)$ (solid line). The effect of the constraint handling mechanism for k in the set $\{0.5000, 0.2500, 0.1250, 0.065\}$, is depicted with dotted lines. The matching points (used in the moment-based identification process) are depicted while using circular markers.

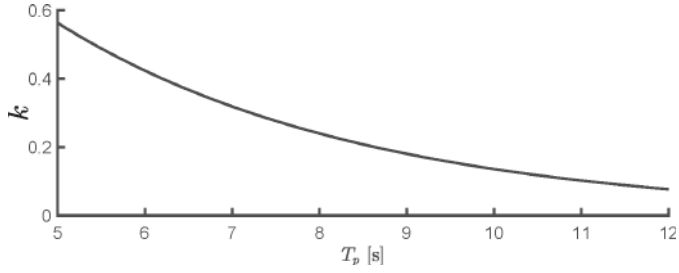

Figure 15. Optimised k for each $T_p \in [5, 12]$ employed for the constraint handling mechanism of the C5 controller.

5.2. Performance Analysis: Energy Absorption

In this section, the resulting performance that is obtained which each controller presented in Section 4 is analysed and discussed, for both unconstrained and constrained scenarios. Two performance benchmarks are considered here, as mentioned in the introductory paragraph of Section 5. For the unconstrained case, the theoretical maximum absorbed energy (computed analytically, as in, for instance, [8]), denoted CR1, is considered as a reference measure. In contrast, for the constrained scenario, the performance obtained with an optimisation-based controller, denoted here as CR2, is considered as a surrogate performance reference.

Throughout this section, the performance results for each controller are shown in terms of relative values with respect to each corresponding benchmark case, i.e.,

$$\mathrm{RGP} = \frac{P^C}{P^R}, \tag{45}$$

where RGP denotes the relative absorbed power, P^C represents the power generated with the controller C, i.e., C1, C2, C3, C4, or C5, and P^R denotes the power that is generated with the reference controller R, i.e., CR1 (unconstrained case) or CR2 (constrained case).

5.2.1. Unconstrained Control

Figure 16 shows performance results in terms of RGP, for the unconstrained case. Note that Figure 16 also includes the maximum relative RGP (dashed-black line), defined as the maximum theoretical achievable energy absorption, i.e., CR1. The RGP values that were obtained with the C1, C2, C3, C4, and C5 strategies, are denoted in Figure 16 using diamond, circle, square, triangular, and dot markers, respectively. It is important to note that, from an overall analysis, it is clear that the C2, C4, and C5 control methods obtain a high performance level, which, in practical terms, is comparable with the maximum achievable RGP. This is especially noteworthy for the case of the C4 controller, which is essentially a simple second-order system. The lowest performance level is obtained with the C3, which achieves its maximum for the central range of T_p. However, significant performance degradation can be observed for both lower and higher peak periods.

Note that a significant difference in terms of performance can be appreciated for the only two feedback structures analysed in this study, i.e., C3 and C4. In particular, the C4 controller significantly outperforms the C3 controller, in both terms of power absorption and controller simplicity (i.e., LTI second-order system vs. time-varying control system).

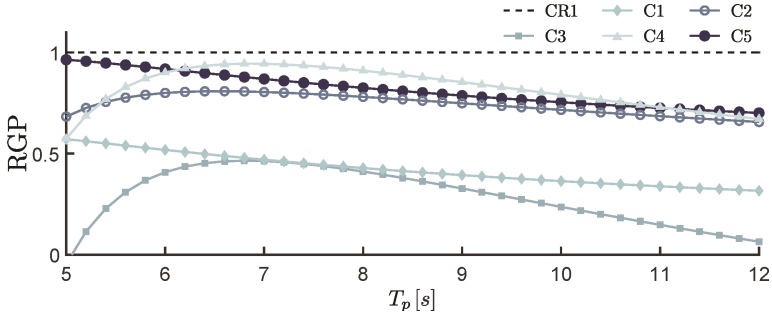

Figure 16. Relative generated power for the unconstrained case.

5.2.2. Constrained Control

In accordance with the unconstrained case, as described in Section 5.2.1, the resulting generated power for the constrained scenario is depicted in Figure 17. Analogously to Figure 16, Figure 17 also illustrates the maximum achievable performance, obtained via the surrogate reference measure CR2 (dashed-black line). Note that only the C2 and C5 control methodologies can be considered for performance assessment in the constrained case, since the other control strategies that are presented in Section 4, i.e., C1, C3, and C4, do not provide constraint handling mechanisms. The RGP obtained with the C2 and C5 strategies, is denoted using circle and dot markers, respectively. From an overall analysis, it can noted that, in general, the C5 controller performs better than the C2, for the totality of the analysed peak wave periods. In addition, both of the controllers show decreasing performance with increasing period T_p.

In particular, both of the controllers achieve their best performance when short T_p values are considered, i.e., $T_p \approx 5$, since the oscillation amplitude of the considered waves decreases along with T_p (according to the spectrum considered) and, consequently, the displacement constraint is not active. Further discussion on this topic can be found in [32].

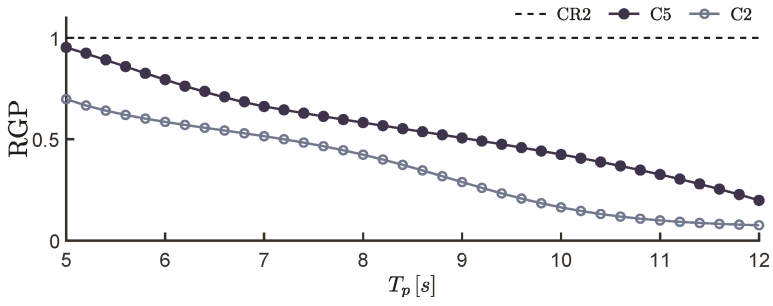

Figure 17. Relative generated power for the constrained case.

5.3. Time-Domain Response

Figure 18 illustrate a particular set of time-traces obtained with each control strategy studied, for a JONSWAP sea-state (as described in Section 5), with a peak period of $T_p = 8.5$ s, for both constrained (a) and unconstrained (b) cases. The results related to each controller, i.e., C1, C2, C3, C4, and C5, are denoted using thick-solid black, dashed, dash-dotted, thick-dotted, and solid-grey lines, respectively. In addition, unconstrained and constrained benchmark references, i.e., CR1 and CR2, are indicated with thin-dotted lines, in Figure 18a,b, respectively.

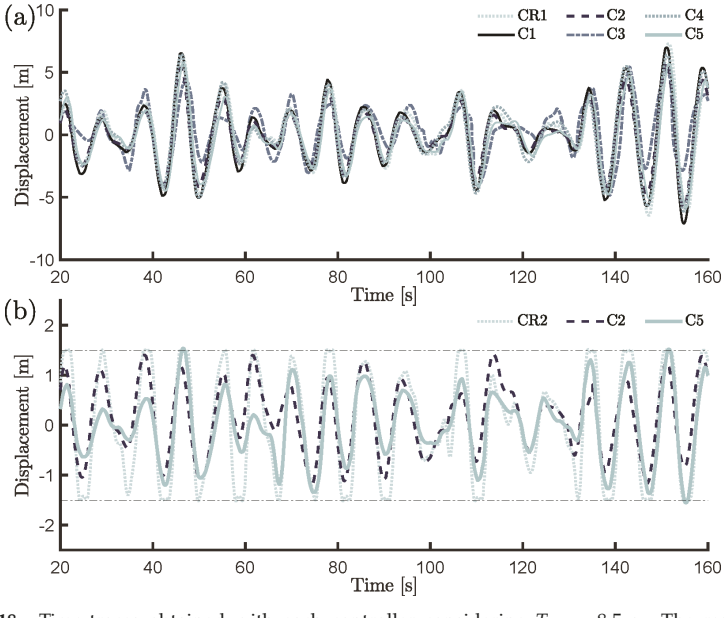

Figure 18. Time-traces obtained with each controller considering $T_p = 8.5$ s. The results for unconstrained and constrained cases are shown in (**a**,**b**), respectively. Note that the constraints are explicitly dealt with only the C2 and C5 controllers.

In the unconstrained case, as shown in Figure 18a, a large deviation with respect to the reference CR1 can be noted for the C3 controller, both in terms of instantaneous amplitude and phase. Note that, the effects that were observed in each corresponding time-domain behaviour, directly support the performance results (in terms of generated power) presented in Figure 16. Finally, in the constrained case, as depicted in Figure 18b, the C5 controller exploits the allowed displacement region more

effectively than the C2 controller, which is directly translated into an increase in power production, supporting the results that are presented in Figure 17.

6. Discussion

This section presents a general discussion on the overall controller design procedure, while taking into account both capabilities and energy-maximising performance of each simple control strategy. To this end, this section provides a critical comparison between methods, using four distinguishing features (or categories): (1) computational simplicity; (2) stability; (3) constraint handling capability; and, (4) performance. In particular, a rating system is proposed, aiming to assign a score to each of the above categories, with such a score taking values between 0 (minimum) and 1 (maximum), for each controller analysed in this paper. The underlying principles behind each of this features, and its associated scoring system, are described in the following paragraphs.

- **Computational Simplicity.** With the aim of analysing computational simplicity, Table 3 presents controller *normalised run-time* (denoted as t_R), i.e., ratio between the time required to compute the control signal for each controller, and the length of the simulation itself (in seconds). The computations are performed using Matlab® R2019a, running on a PC comprising an Intel® Core™i3-2120 CPU @ 3.30 GHz processor with 16 GB of RAM operated by a Windows 10 Pro 64 bits version 2004 compilation OS 19041.450. Table 3 also presents the corresponding scoring that is assigned to each of the analysed controllers, based on the relation described in the following. Note that, given the wide range of normalised run-times calculated (see Table 3), a normalised logarithmic scale is used for scoring the computational simplicity. Let $t_R^{\min}$ and $t_R^{\max}$ be the minimum and maximum normalised run-times among the set of five controllers. The scoring $S : \mathbb{R} \to [0, 1]$, $t_R \mapsto S(t_R)$, for each controller is defined via:

$$S(t_R) = 1 - \frac{\log_{10}\left[\frac{t_R}{t_R^{min}}\right]}{\log_{10}\left[\frac{t_R^{max}}{t_R^{min}}\right]}. \tag{46}$$

  It is straightforward to note that $S(t_R^{\min}) = 1$ and $S(t_R^{\max}) = 0$, i.e., in terms of run-time, the slowest controller is rated with 0 (minimum score), while the fastest is scored with 1 (maximum score).
- **Stability.** It is well-know that stability is a classical issue in controllers based on the energy-maximising impedance-matching principle, as mentioned in Section 4. When considering the discussion provided in Section 4 related to the stability of each controller, this category is rated, as follows :

  1. If the stability of the control loop can be fully guaranteed, the controller is rated with 1,
  2. if the stability of the control loop cannot be fully guaranteed, the controller is rated with 0.
- **Constraint Handling Capability.** This category analyses the capabilities of each controller in handling physical limitations, i.e., constraints. In particular, this category is rated as follows:

  1. If a controller provides a constraint handling mechanism, the controller is rated with 1,
  2. if a controller does not provide a constraint handling mechanism, the controller is rated with 0.
- **Performance.** Using the performance results that are presented for the unconstrained case (since constrained performance metrics are not available for all controllers), presented in Figure 16, this category measures the total energy-maximising performance with respect to the RGP (defined in Equation (45)), as follows:

$$\frac{1}{7}\int_5^{12} \mathrm{RGP}\, dT_p \tag{47}$$

where the denominator of the quotient, i.e., 7, arises from computing the length (in seconds) of the range of peak periods that are considered to generate the wave inputs. Note that, if the reference measure CR1 is considered, then the expression in Equation (47) is effectively 1.

Table 3. Normalised run-time and computational simplicity scoring for each controller.

Controller	Run-Time t_R	Scoring $S(t_R)$
C1	0.2×10^{-3}	1.00
C2	9.8×10^{-3}	0.46
C3	303×10^{-3}	0.00
C4	2.5×10^{-3}	0.65
C5	28×10^{-3}	0.32

The results of evaluating each control strategy, following the set of features that are defined above, can be found in both Table 4, and the four-dimensional spider plot presented in Figure 19.

Table 4. Score assigned to each controller considering each category.

Controller	Computational Simplicity	Stability	Constraint Handling	Performance
C1	1.00	1	0	0.42
C2	0.46	1	1	0.75
C3	0.00	0	0	0.30
C4	0.65	1	0	0.82
C5	0.32	1	1	0.81

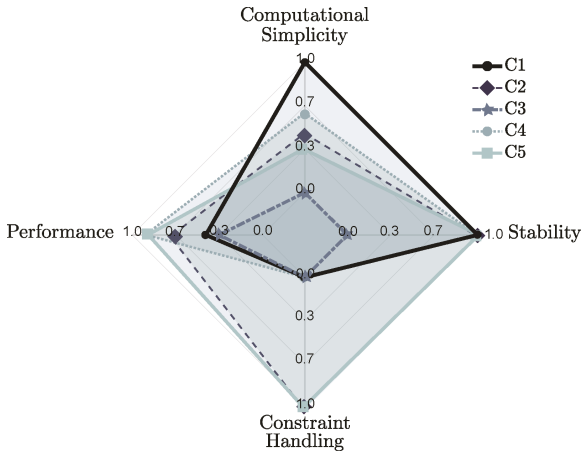

Figure 19. Graphical representation of the results shown in Table 4.

From the observation of Table 4, Figure 19, and the discussion in Sections 4 and 5, some comments, related to the status and perspectives of energy-maximising WEC controllers based on the impedance-matching principle, are worth highlighting. Firstly, a strong trade-off between the estimation of wave excitation forces, and capabilities of managing constraints, can be mentioned. In addition, it is noteworthy that, even with a simple feedback structure, high performance levels can be reached, as demonstrated by the C4 controller, which features a second-order LTI system. Nonetheless, the lack of a constraint handling mechanism renders the C4 controller unsuitable for realistic applications, in which large (and potentially unrealistic) displacements may be induced in unconstrained control conditions. This fact, which is also discussed here in Section 3, can be directly appreciated in Figure 18a.

From the analysis of Table 4 and Figure 19, it can be noted that the C5 controller provides a framework in which physical constraints are considered, while, at the same time, good performance levels are effectively achieved. Note that the C2 controller also provides a constraint handling mechanism, via a suitable modification of the feedforward velocity reference generation, although such a mechanism depends upon a nonlinear estimation process. In other words, constraint handling in the C2 has an inherently higher computational (and analytical) complexity than the C5 controller.

The results that are presented in Table 4 and Figure 19 give some clear directions and perspectives for future research and the development of simple controllers for wave energy systems. In particular, there is a clear lack of LTI feedback strategies that are capable of handling physical limitations. Such a scenario, if achievable, would provide controllers capable of optimising energy-absorption by using motion measurements only, dropping any requirement of wave excitation force estimation, while being able to successfully handle constraints. This would be, effectively, an ideal simple controller for WEC systems, completely covering essential requirements for WEC energy maximising controllers.

7. Conclusions and Future Directions

This paper documents a set of (5) controllers, all based on the impedance-matching principle, which have been developed over the period 2010–2020, and compares and contrasts their characteristics, in terms of performance, the handling of physical constraints, dynamical features, and computational load. The comparison is carried out both analytically and numerically, focusing on issues, such as stability, which can arise in the implementation of panchromatic resonant control, and the availability of suitable constraint handling mechanisms, given that the unrealistic motion often required by the impedance-matching condition. The holistic performance of the controllers is assessed under irregular waves in unconstrained, and constrained (where possible), scenarios. The assessment is carried out in terms of relative absorbed power, including a set of benchmark reference performance metrics for each case, and relative computational load.

A scoring system, which considers four specific features, is proposed in this study, aiming to perform a fair comparison between the five controllers. In particular, computational simplicity, stability, constraint handling, and resulting performance, are explicitly taken into account. From this analysis, a number generic limitations can be identified. In particular, as shown and summarised in Section 6, there is an intrinsic link between feedback-based controllers and an inability to handle constraints, while feedforward controllers, able to handle physical constraints, inevitably require wave excitation force estimates, bringing extra computational load and potential sensitivity to excitation force estimation errors.

While this study has some limitations, for example, the relative sensitivity of controllers to modelling error and measurement noise, etc. has not been considered (though the interested reader is referred to [17] in relation to the relative sensitivity of feedforward and feedback controllers), it shows that, for the unconstrained case, low-order LTI controllers can achieve almost theoretical performance levels, in realistic irregular waves. However, to date, there is not a control methodology that provides an estimator-free, low-order structure (i.e. demanding low hardware requirements), while, at the same time, being able to handle physical constraints. This points to an important potential future research direction: the development of an alternative simple, estimator-free, feedback controller, incorporating a suitable constraint handling mechanism. Whether such a controller is possible, given the generic limitations of the set of controllers studies in this paper, remains an open question.

Author Contributions: Conceptualization, D.G.-V., N.F., and J.V.R.; methodology, D.G.-V., N.F., and J.V.R.; formal analysis, D.G.-V., N.F., F.J.-L. and J.V.R.; writing–original draft preparation, D.G.-V. and N.F.; writing–review and editing, D.G.-V., N.F., F.J.-L. and J.V.R.; supervision, J.V.R.; project administration, J.V.R.; funding acquisition, J.V.R.. All authors have read and agreed to the published version of the manuscript.

Funding: This research was funded by Science Foundation Ireland under grant number SFI/13/IA/1886 and Grant No. 12/RC/2302 for the Marine Renewable Ireland (MaREI) centre.

Conflicts of Interest: Three of the controllers studied in this paper have been proposed by various authors of this manuscript. However, every attempt has been made to ensure a fair comparison, while no special coding attention has been given to any of the controllers/estimators in relation to computation time. The funders had no role in the design of the study; the collection, analyses, or interpretation of data; in the writing of the manuscript, or in the decision to publish the results.

References

1. Drew, B.; Plummer, A.R.; Sahinkaya, M.N. A review of wave energy converter technology. *Proc. Inst. Mech. Eng. Part A J. Power Energy* **2009**, *223*, 887–902. [CrossRef]
2. Ringwood, J.V.; Bacelli, G.; Fusco, F. Energy-maximizing control of wave-energy converters: The development of control system technology to optimize their operation. *IEEE Control Syst.* **2014**, *34*, 30–55.
3. Korde, U.A.; Ringwood, J.V. *Hydrodynamic Control of Wave Energy Devices*; Cambridge University Press: Cambridge, UK, 2016.
4. Liberzon, D. *Calculus of Variations and Optimal Control Theory: A Concise Introduction*; Princeton University Press: Princeton, NJ, USA, 2011.
5. Faedo, N.; Olaya, S.; Ringwood, J.V. Optimal control, MPC and MPC-like Algorithms for Wave Energy Systems: An Overview. *IFAC J. Syst. Control* **2017**, *1*, 37–56. [CrossRef]
6. Faedo, N. Optimal Control and Model Reduction for Wave Energy Systems: A Moment-Based Approach. Ph.D. Thesis, Department of Electronic Engineering, Maynooth University, Kildare, Ireland, 2020.
7. Floyd, T.L.; Pownell, E. *Principles of Electric Circuits*; Prentice Hall: Upper Saddle River, NJ, USA, 2000.
8. Falnes, J. *Ocean Waves and Oscillating Systems: Linear Interactions Including Wave-Energy Extraction*; Cambridge University Press: Cambridge, UK, 2002.
9. Fusco, F.; Ringwood, J. Suboptimal causal reactive control of wave energy converters using a second order system model. In Proceedings of the 21st 2011 International Offshore and Polar Engineering Conference. International Society of Offshore and Polar Engineers (ISOPE), Maui, HI, USA, 19–24 June 2011; pp. 687–694.
10. Fusco, F.; Ringwood, J.V. A simple and effective real-time controller for wave energy converters. *IEEE Trans. Sustain. Energy* **2013**, *4*, 21–30. [CrossRef]
11. Song, J.; Abdelkhalik, O.; Robinett, R.; Bacelli, G.; Wilson, D.; Korde, U. Multi-resonant feedback control of heave wave energy converters. *Ocean Eng.* **2016**, *127*, 269–278. [CrossRef]
12. Bacelli, G.; Nevarez, V.; Coe, R.G.; Wilson, D.G. Feedback Resonating Control for a Wave Energy Converter. *IEEE Trans. Ind. Appl.* **2019**, *56*, 1862–1868. [CrossRef]
13. García-Violini, D.; Peña-Sanchez, Y.; Faedo, N.; Ringwood, J.V. An Energy-Maximising Linear Time Invariant Controller (LiTe-Con) for Wave Energy Devices. *Trans. Sustain. Energy* **2020**, *11*, 2713–2721. [CrossRef]
14. Cummins, W.E. The impulse Response Function and Ship Motions. *Schiffstechnik* **1962**, *47*, 101–109.
15. Ogilvie, T.F. Recent progress toward the understanding and prediction of ship motions. In Proceedings of the 5th Symposium on Naval Hydrodynamics, Bergen, Norway, 10–12 September 1964; Volume 1, pp. 2–5.
16. Peña-Sanchez, Y.; Faedo, N.; Ringwood, J.V. Moment-based parametric identification of arrays of wave energy converters. In Proceedings of the 2019 American Control Conference, Philadelphia, PA, USA, 10–12 July 2019.
17. Ringwood, J.V.; Mérigaud, A.; Faedo, N.; Fusco, F. An Analytical and Numerical Sensitivity and Robustness Analysis of Wave Energy Control Systems. *IEEE Trans. Control Syst. Technol.* **2019**, *28*, 1337–1348. [CrossRef]
18. Hals, J.; Falnes, J.; Moan, T. A comparison of selected strategies for adaptive control of wave energy converters. *J. Offshore Mech. Arct. Eng.* **2011**, *133*, 031101–031113. [CrossRef]
19. Peña-Sanchez, Y.; Windt, C.; Josh, D.; Ringwood, J.V. A Critical Comparison of Excitation Force Estimators for Wave Energy Devices. *IEEE Trans. Control Syst. Technol.* **2019**, *28*, 2263–2275. [CrossRef]
20. Antoulas, A.C. *Approximation of Large-Scale Dynamical Systems*; SIAM: Philadelphia, PA, USA, 2005.
21. Sánchez-Peña, R.S.; Sznaier, M. *Robust Systems Theory and Applications*; Wiley: New York, NY, USA, 1998.
22. Astrom, K.J.; Wittenmark, B. *Adaptive Control*, 2nd ed.; Addison-Wesley Publishing Company: Boston, MA, USA, 1994.
23. Goodwin, G.C.; Graebe, S.F.; Salgado, M.E. *Control System Design*; Prentice Hall: Upper Saddle River, NJ, USA, 2001; Volume 240.
24. Khalil, H.K.; Grizzle, J.W. *Nonlinear Systems*; Prentice Hall: Upper Saddle River, NJ, USA, 2002; Volume 3.
25. Ljung, L. *System Identification—Theory for the User*; Prentice Hall: Upper Saddle River, NJ, USA, 1999.

26. Fusco, F.; Ringwood, J. A model for the sensitivity of non-causal control of wave energy converters to wave excitation force prediction errors. In Proceedings of the 9th European Wave and Tidal Energy Conference (EWTEC), Southampton, UK, 5–9 September 2011; School of Civil Engineering and the Environment, University of Southampton: Southampton, UK, 2011.
27. Faedo, N.; Peña-Sanchez, Y.; Ringwood, J.V. Finite-Order Hydrodynamic Model Determination for Wave Energy Applications Using Moment-Matching. *Ocean Eng.* **2018**, *163*, 251–263. [CrossRef]
28. García-Violini, D.; Peña-Sanchez, Y.; Faedo, N.; Windt, C.; Ringwood, J.V. Experimental implementation and validation of a broadband LTI energy-maximising control strategy for the Wavestar device. *IEEE Trans. Control Syst. Technol.* **2020**, response to reviewers submitted.
29. Faedo, N.; Scarciotti, G.; Astolfi, A.; Ringwood, J.V. Energy-maximising control of wave energy converters using a moment-domain representation. *Control Eng. Pract.* **2018**, *81*, 85–96. [CrossRef]
30. Todalshaug, J.H.; Ásgeirsson, G.S.; Hjálmarsson, E.; Maillet, J.; Möller, P.; Pires, P.; Guérinel, M.; Lopes, M. Tank testing of an inherently phase-controlled wave energy converter. *Int. J. Mar. Energy* **2016**, *15*, 68–84. [CrossRef]
31. Giorgi, G.; Ringwood, J.V. Analytical representation of nonlinear Froude-Krylov forces for 3-DoF point absorbing wave energy devices. *Ocean Eng.* **2018**, *164*, 749–759. [CrossRef]
32. Faedo, N.; García-Violini, D.; Peña-Sanchez, Y.; Ringwood, J.V. Optimisation-vs. non-optimisation-based energy-maximising control for wave energy converters: A case study. In Proceedings of the 2020 European Control Conference (ECC), Saint Petersburg, Russia, 12–15 May 2020; pp. 843–848.
33. Hasselmann, K. Measurements of wind wave growth and swell decay during the Joint North Sea Wave Project (JONSWAP). *Deutches Hydrogr. Inst.* **1973**, *8*, 95.
34. LHEEA, NEMOH-Presentation. Laboratoire de Recherche en Hydrodynamique Énergetique et Environnement Atmospherique. 2017. Available online: https://goo.gl/yX8nFu (accessed on 1 August 2019).
35. Papoulis, A. *Probability, Random Variables and Stochastic Processes*; McGraw-Hill: New York, NY, USA, 1991.
36. Francis, B.A.; Wonham, W.M. The internal model principle of control theory. *Automatica* **1976**, *12*, 457–465. [CrossRef]
37. Garcia-Rosa, P.B.; Kulia, G.; Ringwood, J.V.; Molinas, M. Real-time passive control of wave energy converters using the Hilbert-Huang transform. *IFAC-PapersOnLine* **2017**, *50*, 14705–14710. [CrossRef]
38. Huang, N.E.; Shen, Z.; Long, S.R.; Wu, M.C.; Shih, H.H.; Zheng, Q.; Yen, N.C.; Tung, C.C.; Liu, H.H. The empirical mode decomposition and the Hilbert spectrum for nonlinear and non-stationary time series analysis. *Proc. R. Soc. Lond. Ser. A Math. Phys. Eng. Sci.* **1998**, *454*, 903–995. [CrossRef]

© 2020 by the authors. Licensee MDPI, Basel, Switzerland. This article is an open access article distributed under the terms and conditions of the Creative Commons Attribution (CC BY) license (http://creativecommons.org/licenses/by/4.0/).

Journal of
Marine Science and Engineering

MDPI

Article

A Real-Time Detection System for the Onset of Parametric Resonance in Wave Energy Converters

Josh Davidson * and Tamás Kalmár-Nagy

Department of Fluid Mechanics, Faculty of Mechanical Engineering, Budapest Univeristy of Technology and Economics, 1111 Budapest, Hungary; kalmarnagy@ara.bme.hu
* Correspondence: davidson@ara.bme.hu

Received: 10 September 2020; Accepted: 13 October 2020; Published: 20 October 2020

Abstract: Parametric resonance is a dynamic instability due to the internal transfer of energy between degrees of freedom. Parametric resonance is known to cause large unstable pitch and/or roll motions in floating bodies, and has been observed in wave energy converters (WECs). The occurrence of parametric resonance can be highly detrimental to the performance of a WEC, since the energy in the primary mode of motion is parasitically transferred into other modes, reducing the available energy for conversion. In addition, the large unstable oscillations produce increased loading on the WEC structure and mooring system, accelerating fatigue and damage to the system. To remedy the negative effects of parametric resonance on WECs, control systems can be designed to mitigate the onset of parametric resonance. A key element of such a control system is a real-time detection system, which can provide an early warning of the likely occurrence of parametric resonance, enabling the control system sufficient time to respond and take action to avert the impending exponential increase in oscillation amplitude. This paper presents the first application of a real-time detection system for the onset of parametric resonance in WECs. The method is based on periodically assessing the stability of a mathematical model for the WEC dynamics, whose parameters are adapted online, via a recursive least squares algorithm, based on online measurements of the WEC motion. The performance of the detection system is demonstrated through a case study, considering a generic cylinder type spar-buoy, a representative of a heaving point absorber WEC, in both monochromatic and polychromatic sea states. The detection system achieved 95% accuracy across nearly 7000 sea states, producing 0.4% false negatives and 4.6% false positives. For the monochromatic waves more than 99% of the detections occurred while the pitch amplitude was less than 1/6 of its maximum amplitude, whereas for the polychromatic waves 63% of the detections occurred while the pitch amplitude was less than 1/6 of its maximum amplitude and 91% while it was less than 1/3 of its maximum amplitude.

Keywords: paramertic resonance; wave energy conversion; real-time detection; recursive least squares

1. Introduction

Parametric resonance is an instability phenomenon caused by the time-varying parameters of a system [1]. Whereas normal resonance causes oscillations in a system to grow linearly with time, parametric resonance causes an exponential increase in the oscillation amplitude. This phenomena was first identified by Faraday [2], who observed the generation of surface waves when a liquid-filled container was oscillated vertically, thereby varying the restoring force usually provided by the constant gravitational acceleration only. The time-varying wetted surface of a floating body subject to incident waves can produce temporal variations in the system's parameters and thus trigger parametric resonance. The first noted observation of parametric resonance in floating bodies dates back to Froude in the 19th century [3], who described that large roll motions occur when the natural period of a ship's roll is twice the natural period of the heave or pitch modes of motion. This parametric coupling

between heave, pitch and roll degrees of freedom (DoFs) has been investigated in offshore engineering fields, such as shipping (see, for example, [4,5] and the references therein) and in offshore spar-type structures [6–10].

The large unstable motions which accompany the occurrence of parametric resonance can be extremely hazardous for the safe operation of marine structures and vessels. For example, container ships have lost cargo overboard due to large parametric roll motions. Research in the marine engineering field has therefore investigated control methods for the suppression and stabilisation of parametric pitch/roll [11,12]. Similarly to ships and other offshore floating structures, the large amplitude unstable motions—due to parametric resonance—have been observed in wave energy converters (WECs). As such, there is motivation to design control systems to mitigate the onset of parametric resonance in WECs.

1.1. Parametric Resonance in WECs

The concept of resonance is very well known in the study of wave energy conversion, since a WEC is usually designed to resonate with the incident waves for maximum power extraction. By comparison, parametric resonance has received far less attention. A major barrier in studying parametric resonance is the complexity of the mathematical models required to capture this nonlinear phenomenon, compared to the computationally efficient linear/frequency domain hydrodynamic models traditionally utilised in WEC research and analysis. Therefore, the first reported observations of parametric resonance in WECs stem from physical scale model wave tank testing, dating back to work on the frog in the late 1980s by Bracewell [13]. Numerous further observations of parametric resonance were subsequently reported from physical scale model wave tank testing of WECs [14–26], which in many cases was unanticipated when first observed, since the occurrence of parametric resonance was not predicted by the simple numerical modelling results that preceded the wave tank experiments.

Therefore, over the past decade, in line with the availability of computationally efficient, nonlinear hydrodynamic models [27], increased attention towards numerical modelling of parametric resonance in WECs can be noted. The first publication in this direction was at the end of the 2000s by Babarit et al. [28], which investigated the use of a nonlinear hydrodynamic model to capture the parametric roll resonance in the SeaREV, observed during the earlier experimental tests in Durand et al. [14]. The nonlinear hydrodynamic model calculates the Froude–Krylov force on the exact wetted surface of the WEC at each time step, rather than using the time-invariant mean wetted surface (as is the case for linear hydrodynamic models). This type of nonlinear Froude–Kylov force model has subsequently been used in [29–34] to investigate parametric resonance in WECs. Other nonlinear hydrodynamic modelling approaches include only modelling the restoring force nonlinearly, rather than the entire Froude–Krylov force [35–40]. Modelling parametric resonance has also been explored through high-fidelity CFD simulations [41].

In some circumstances, the parametric excitation can arise due to the effect of the mooring system on the overall WEC dynamics. Therefore, several modelling approaches have been employed to capture this mooring induced effect. For the case of a taut moored WEC, Nicoll et al. [42] utilised the pendulum equation to model the parametric excitation, whereas Orszagova et al. [21,25,43] utilised a 2nd order Taylor series for the mooring system dynamics to successfully capture the parametric resonance phenomenon.

1.2. Suppression Control Methods for Parametric Resonance in WECs

The various control methods designed to suppress the occurrence of parametric resonance in WECs can be broadly classified into two main categories: passive and active control. The passive control approaches typically utilise fins or strakes to increase the hydrodynamic damping in the pitch/roll DoFs, which has been shown to reduce the occurrence of parametric resonance in offshore spar platforms [44]. This type of passive control method was first investigated for a WaveBob-like, two-body heaving point absorber in Beatty et al. [20] using numerical simulations, which confirmed

the ability of the strakes to reduce pitch and roll amplitudes, allowing increased WEC power output. Follow-up work by Ortiz [45] investigated an alternative passive control approach, which utilises the mooring dynamics to reduce the occurrence of parametric resonance. The use of fins has been investigated experimentally for the stabilisation of the OWC Spar Buoy in Gomes et al. [46]. The wave flume experiments on a scale model device confirmed the ability of the fins to reduce, though not eliminate, the amplitude of the pitch and roll oscillations due to the occurrence of parametric resonance. A different passive control approach is shown in Cordonnier et al. [47] and Gomes et al. [48], based on the optimisation of the initial WEC design. A procedure to identify the frequency and amplitude ranges in which parametric resonance will occur is included into the numerical optimisation routines for the design of the geometry and mass distributions. A penalty is then added in the optimisation routine to the configurations where parametric resonance occurs due to the decreased performance. Cordonnier et al. [47] showed that the optimal geometry when taking parametric resonance into consideration has a larger width than the original geometry, which does not consider parametric resonance during the design optimisation.

The active control approaches involve a mechanism to influence the WEC dynamics and mitigate the onset of parametric resonance. Villegas and van der Schaaf [49] proposed an active control system for the WaveBob, after parametric pitch and roll were detected in physical experiments and were observed to hinder the performance of the WEC. The control system acts on the WEC dynamics, through the effect of the power take-off (PTO) force between the outer torus and inner spar of the WaveBob. The PTO force couples the motion of the two bodies, influencing the resonant peaks in the frequency responses of the heave, pitch and roll DoFs. The active control system proposed by Villegas and van der Schaaf applies a notch filter, designed to eliminate any PTO forces at the frequencies for which parametric resonance occurs. Experimental results for a model scale device in a wave tank validate the effectiveness of this approach in [49]. Maloney [50] also considered a WaveBob-like WEC, but proposed including an internal, elastically supported reaction mass within the inner spar, which can be utilised to control the natural frequency of the spar through the use of a variable inertia system. They term this three-body system the VISWECand utilise the variable inertia system to eliminate parametric excitation in roll, in addition to its primary function of tuning the response of the spar to increase the output power.

Looking forward, more advanced active control mechanisms may switch on only when required and remain inactive during normal operation. A key component for such a system is a monitoring and detection system, to give an early warning. Such early warning systems have already been developed for ships [51–57], enabling the crew to take corrective measures such as speed and/or course changes to avoid the occurrence of parametric roll. However, to date, no such early warning system has been developed for a WEC.

1.3. Objectives and Outline of the Paper

The objective of the present paper is to provide the first implementation of a real-time detection system for the onset of parametric resonance in WECs, capable of providing an early warning for a control system to take preventive measures. The details of the proposed detection system are introduced in Section 2. Next, the performance of the detection system is assessed in an illustrative test case. The details of the test case and the implementation of the detection system are presented in Section 3. The test case results are presented in Section 4 and the performance of the detection system is evaluated and discussed. Finally, a number of conclusions are drawn in Section 5.

2. A Real-Time Detection System for Early Warning of Parametric Resonance in WECs

The proposed monitoring and detection system is based on a method developed for the detection of parametric roll in ships, presented in Holden et al. [51]. The method works by performing real-time parameter identification of a linear time-varying model, based on the onboard measurements of the angular displacement and velocity of the ship's roll. The detection system regularly assesses the

stability of the identified model by monitoring the eigenvalues of the model system, giving a warning that roll resonance is probable when the model becomes unstable.

Owing to the simplicity of this detection method, it was selected for our investigation as the first real-time detection system for the onset of parametric resonance in WECs. The details of the linear time-varying model are given in Section 2.1, the real-time parameter identification in Section 2.2 and then the detection criteria in Section 2.3.

2.1. The Linear Time-Varying Model

Since the detection system is based on real-time measurements from the WEC, the system requires a discrete time model, taking as input the discrete measured signals at each sampling instant. The discrete time model employed here for the evolution of the displacement z_1 and velocity z_2, subject to an external forcing $\mathbf{u}$, can be expressed as:

$$\begin{gathered}\mathbf{z}_{k+1} = \mathbf{A}_k \mathbf{z}_k + \mathbf{u}_k, \\ \begin{bmatrix} z_{1,k+1} \\ z_{2,k+1} \end{bmatrix} = \begin{bmatrix} A_{1,k} & A_{2,k} \\ A_{3,k} & A_{4,k} \end{bmatrix} \begin{bmatrix} z_{1,k} \\ z_{2,k} \end{bmatrix} + \begin{bmatrix} u_{1,k} \\ u_{2,k} \end{bmatrix},\end{gathered} \tag{1}$$

where the parameters of the matrix $\mathbf{A}$ are unknown and time-varying.

2.2. Real-Time Parameter Identification

A recursive least-squares algorithm is employed to regularly update the parameter values of $\mathbf{A}$, based on the real-time measurements of z_1 and z_2. Recursive least squares is employed in [51] to identify the roll dynamics of a ship and has also been used for online identification of the model parameters for the WEC dynamics in an adaptive controller [58,59]. The recursive least squares algorithm in [58,59] assumes that the excitation force is known a priori, which requires the use of a robust estimation algorithm to be used in conjunction with the adaptive controller (see Pena et al. [60] for a critical comparison of excitation force estimators for WECs). However, the approach used in [51], which is followed in the present study, makes the assumption that the external forcing parameters in Equation (1), u_1 and u_2, are independent, zero-mean, Gaussian white noise processes. Under this assumption the recursive least squares identification takes the form

$$\theta_{i,k} = \theta_{i,k-1} + P_{i,k}\Phi_{i,k-1}e_{i,k}, \tag{2}$$

$$P_{i,k}^{-1} = P_{i,k-1}^{-1} + \Phi_{i,k-1}^2, \tag{3}$$

where $i \in \{1,2\}$ and

$$\begin{bmatrix} \theta_{1,k} \\ \theta_{2,k} \end{bmatrix} = \begin{bmatrix} -(A_{1,k} + A_{4,k}) \\ A_{1,k}A_{4,k} - A_{2,k}A_{3,k} \end{bmatrix}, \tag{4}$$

$$\Phi_{i,k} = -z_{i,k} - z_{i,k-1}, \tag{5}$$

$$e_{i,k} = -z_{i,k} - \Phi_{i,k-1}\theta_{i,k-1}. \tag{6}$$

2.3. Detecting Instability

The detection algorithm monitors the eigenvalues of $\mathbf{A}$ to identify whether the system is possibly becoming unstable. For a discrete-time, linear time-invariant system, if the eigenvalues of the matrix $\mathbf{A}$ lie outside of the unit circle, then the system is unstable. However, for a discrete-time, linear time-varying system, such as Equation (1), instability cannot be concluded when the eigenvalues lie outside of the unit circle. Therefore, by monitoring when the eigenvalues of $\mathbf{A}$ moving outside of the of the unit circle, the present detection system provides an early warning for the probable occurrence

of parametric resonance (the analytical conditions for the stability/instability of a discrete system are given in, for example, [61]). The eigenvalues λ_k are determined by solving

$$\lambda_k^2 + \theta_{1,k}\lambda_k + \theta_{2,k} = 0. \tag{7}$$

3. Test Case

The test case considers evaluating the proposed detection system in a numerical simulation of a generic heaving point-absorber-type WEC. The performance of the proposed detection system is assessed with the following two main criteria:

- Correctly warning when parametric resonance occurs (correct positive) and not giving a false warning when parametric resonance does not occur (correct negative).
- How early the system detects the onset of parametric resonance and sends a warning.

The specific device considered in this test case is introduced in Section 3.1. The range of input waves in which the device was tested is detailed in Section 3.2. The details of the numerical model are presented in Section 3.3. The simulation details and the implementation of the early warning system are provided in Section 3.4. The results are then presented in Section 4.

3.1. The Device

The device in this study is a cylindrical spar-buoy, providing a generic representation of a heaving point absorber WEC. The selection of this type of WEC stems from the numerous reports of parametric pitch/roll for axisymmetric heaving point absorbers [17–20,29–34,39,41,45,46,48–50]. The particular geometry used in this study is a representation of a classic spar platform from the literature [62–65], comprising a simple vertical cylinder whose natural period of pitch motion is about twice the heave resonant period. The 2:1 ratio of heave to pitch natural frequency makes the floating cylinder prone to parametric excitation in pitch. The simple geometry was selected in order for the test case to remain generic. Likewise, no power take-off mechanisms or wave enengy extraction capability are considered on the device, with the focus of the tests being on the ability of the detection system to give an early warning of the onset of parametric resonance from measurements of the pitch motion. Hong et al. [62] tested the floating cylinder at model scale, under various regular wave conditions in the Samsung Ship Model Basin. A numerical model of the cylinder was used by Jingrui et al. [63] to study the combination resonance response. Gavasoni et al. [64] employed a numerical model for the investigation of nonlinear vibration modes and instability. Giorgi et al. [65] demonstrated the potential yaw instability which may arise when including nonlinear kinematics in a nonlinear hydrodynamic model.

This particular spar-buoy was chosen since it is well known to exhibit parametric resonance and there exists a validated numerical model able to capture the existence of parametric resonance (see Section 3.3). However the spar-buoy's geometry is much larger than would be used in wave energy applications, with a heave natural period $T_{n,3} = 29$ s and pitch natural period $T_{n,5} = 57$ s. Thus the geometrical properties will be normalised in the analysis to provide insights for performance on smaller scale geometries, such as WECs, following the normalisation utilised in [65], where the frequencies are normalised against the pitch natural frequency $w_{n,5}$ and the wave heights are normalised against the metacentric height $\overline{GM}$.

3.2. Input Waves

The early warning detection system was evaluated in both monochromatic and polychromatic waves. For the monochromatic waves, a total of 4050 simulations were performed, spanning an array of 81 frequencies equally spaced between 1.6 and 2.4 times the natural pitch frequency $\omega_{n,5}$, and 50 wave heights from 2% to 100% of the metacentric height, $\overline{GM}$. For the polychromatic waves, the same number and range of wave heights were used; however, a larger frequency range was

employed. The wide bandwidth of the polychromatic wave spectra meant there was a broad range of peak frequency values for which significant energy was present in the expected frequency range where parametric resonance was likely to occur. Thus, the frequency range for the polychromatic waves spanned from $0.6\omega_{n,5}$ to $3.4\omega_{n,5}$, with a resolution of 0.05 $\omega_{n,5}$, resulting in 2800 simulations. The reason why more monochromatic simulations were performed than polychromatic (4050 compared to 2800) is that that the time taken for each polychromatic simulation was twice as long as for the monochromatic simulations.

For the monochromatic waves, each simulation was run for a time equal to 100 times the pitch natural period, $T_{n,5}$. The wave amplitude was linearly ramped up over the first $5T_{n,5}$ of the signal to reduce transient effects. An example of the monochromatic wave signal is shown in Figure 1a. The length of each simulation for the polychromatic waves was twice as long as for the monochromatic waves, i.e., $200T_{n,5}$, since parametric resonance may take longer to develop due to the irregular nature of the polychromatic waves. The polychromatic waves are based on a JONSWAP spectrum, defined by a significant wave height and peak frequency. Each spectrum comprises 100 frequencies ω_j, each with a randomly assigned phase ϕ_j uniformly distributed between 0 and 2π. The spectra have a frequency range from $0\omega_{n,5}$ to $9\omega_{n,5}$ with an average frequency resolution $\Delta\omega$ of $0.09\omega_{n,5}$. The frequencies are not equally spaced on harmonics (to avoid the time series being periodic and repeating itself, as demonstrated in [66]), with a random shift between $\pm\frac{\Delta\omega}{2}$ applied to each frequency. Note that the same set of random phases and frequency shifts is applied to each spectrum. Examples of the polychromatic wave signal and its power spectral density (PSD) are shown in Figure 1b,c, normalised against the metacentric height and pitch natural frequency respectively.

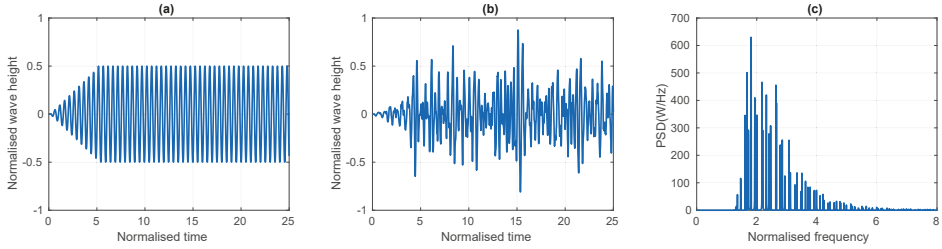

Figure 1. Example of the input waves: (**a**) monochromatic, (**b**) polychromatic, (**c**) power spectral density (PSD) of the polychomatic waves.

3.3. Numerical Model

The hydrodynamic model for the wave structure interaction follows the validated model for the same device from [62–64]. The model is able to articulate the occurrence of parametric resonance in the floating cylinder, through the coupled equations for heave x_3 and pitch x_5

$$F_{I,3}(\ddot{x}_3) + F_{D,3}(\dot{x}_5) + F_{R,3}(x_3, x_5, t) = F_{E,3}(t), \tag{8}$$

$$F_{I,5}(\ddot{x}_5) + F_{D,5}(\dot{x}_5) + F_{R,5}(x_3, x_5, t) = F_{E,5}(t), \tag{9}$$

where:

- $F_{I,i}$ is the inertia, detailed in Section 3.3.1.
- $F_{R,i}$ is the hydrostatic restoring force, detailed in Section 3.3.2.
- $F_{D,i}$ is the hydrodynamic damping force, detailed in Section 3.3.3.
- $F_{E,i}$ is the wave excitation force, detailed in Section 3.3.4.

The values for all of the parameters in the model are listed in Table 1 in Section 3.3.5.

3.3.1. Inertia

The inertial forces are given by the product of the inertia and acceleration:

$$F_{I,3} = (M + m_3)\ddot{x}_3, \tag{10}$$

$$F_{I,5} = (I_5 + m_5)\ddot{x}_5, \tag{11}$$

where M is the cylinder mass, m_3 is the hydrodynamic added mass in heave, I_5 is the pitch moment of inertia and m_5 is the hydrodynamic added moment of inertia in pitch.

3.3.2. Hydrostatic Restoring Force/Moment

The hydrodystatic restoring force and moment terms have time-varying parameters, which enables the existence of parametric resonance in the numerical model. In [63,64], the hydrodystatic restoring force and moment are given by

$$F_{R,3}\left(x_3, x_5, t\right) = \rho g A_C \left[x_3 - x_5^2 \frac{L_{MS}}{2}\right], \tag{12}$$

$$F_{R,5}\left(x_3, x_5, t\right) = \rho g A_C L_D \left[\overline{GM} x_5 - \frac{1}{2} x_3 x_5 + \frac{1}{2}\eta(t) x_5\right], \tag{13}$$

where ρ is the density of water, g is the gravitational constant, A_C is the WEC horizontal cross-sectional area, L_{MS} is distance from the WEC centre of mass to the still water level, L_D is the WEC draft, $\overline{GM}$ is the WEC metacentric height and $\eta(t)$ is the wave elevation.

3.3.3. Hydrodynamic Damping

Following [63,64], the hydrodynamic damping is measured from free decay experiments in [62] and is given by

$$F_{D,3}\left(\dot{x}_3\right) = C_3 \dot{x}_3, \tag{14}$$

$$F_{D,5}\left(\dot{x}_5\right) = C_5 \dot{x}_5, \tag{15}$$

where C_i are the damping coefficients identified from the experimental data.

3.3.4. Wave Excitation

For an input wave with amplitude A, frequency ω and phase ϕ, the wave elevation is

$$\eta(t) = A \sin\left(\omega t + \phi\right). \tag{16}$$

The excitation force is given by

$$F_{E,i}\left(t\right) = H_{E,i}(\omega) A \sin\left(\omega t + \phi + \phi_{E,i}(\omega)\right), \tag{17}$$

where $H_{E,i}(\omega)$ and $\phi_{E,i}(\omega)$ are the hydrodynamic excitation force coefficients for the amplitude gain and phase shift, respectively. The hydrodynamic excitation force coefficients are frequency dependent and their values for the given spar-buoy geometry are calculated using the open-source linear potential flow boundary element method software Nemoh [28]. The excitation force coefficient values, as a function of frequency, are displayed in Figure 2.

For the case of polychromatic waves, the excitation force comprises a linear superposition of the contributions from each of the 100 frequency components.

$$F_{E,i}\left(t\right) = \sum_{j=1}^{100} H_{E,i}(\omega_j) A_j \sin\left(\omega_j t + \phi_j + \phi_{E,i}(\omega_j)\right). \tag{18}$$

3.3.5. Model Parameters

The values for the parameters used in the model are listed in Table 1 following the values provided in [62–64] for the the validated model of the same device. Note again, the geometry is much larger than would likely be used for WECs, as detailed in Section 3.1. The values for the excitation force coefficients are plotted in Figure 2.

Table 1. Model parameter values used in the test case.

Parameter	Value	Parameter	Value	Parameter	Value
A_C	1087 m^2	ρ	1000 kg/m^3	M	2.15×10^8 kg
L_D	198.1 m	g	9.81 m/s^2	m_3	1.37×10^7 kg
$\overline{GM}$	10.1 m	C_3	1.19×10^6 kg/s	I_5	1.12×10^{12} kgm
L_{MS}	109.1 m	C_5	7.54×10^9 kgm/s	m_5	7.26×10^{11} kg

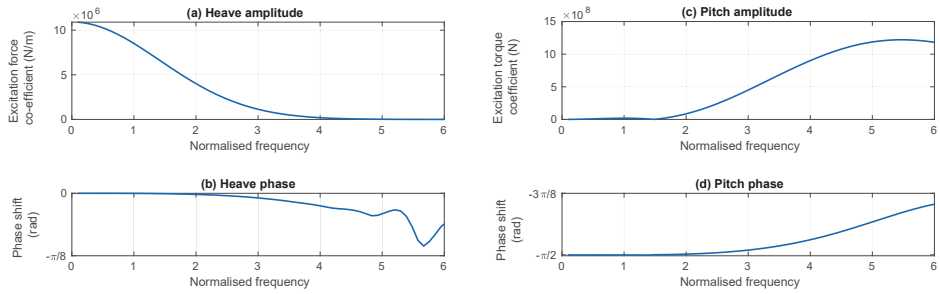

Figure 2. The excitation force coefficients (**a**) $H_{E,3}$, (**b**) $\phi_{E,3}$, (**c**) $H_{E,5}$ and (**d**) $\phi_{E,5}$.

3.4. Simulation Details and the Implementation of an Early Warning Detection System

3.4.1. Simulation Details

The model was implemented in MATLAB and Simulink. A Runge–Kutta 4th order solution scheme was employed, with a fixed time step dt equal to $0.01T_{n5}$. If the pitch angle exceeded 90°, the simulation was aborted and a maximum pitch angle of 90° was recorded.

3.4.2. Recursive Least Squares Implementation

The detection system monitors the pitch motion of the device; thus $z_1 = x_5$ and $z_2 = \dot{x}_5$. The recursive least squares algorithm is executed at each time step, after the ramping up of the input wave is completed, i.e., $t > T_{n,5}$ (see Section 3.2). The decision to postpone starting the detection until $t = 5T_{n,5}$ is to eliminate the possibility that the increase of pitch motion during this time, due to the ramping up of the wave amplitude, results in an increase of the eigenvalues which are calculated under the assumption of a Gaussian wave amplitude distribution. However, investigating this after the test cases were simulated reveals that the magnitudes of the eigenvalues oscillate less around their initial values during the ramping of the input wave amplitude, $t < 5T_{n,5}$, compared to when the wave amplitude is maximal.

The values of $\theta_{i,0}$ were initialised from the results of precursory trial runs, in numerous wave conditions where no parametric resonance was present. In all of these trial runs the values of both $\theta_{1,k}$ and $\theta_{2,k}$ were observed to converge to -0.5, regardless of the wave conditions (height, frequency, monochromatic/polychromatic) and of the initial values chosen. An illustrative subset of the precursory trial runs is shown in Figure 3, which plots the evolution of the $\theta_{i,k}$ values, demonstrating their convergence to -0.5 for different wave heights (Figure 3a), wave frequencies (Figure 3b) and initial conditions (Figure 3c). Therefore the values of $\theta_{1,0}$ and $\theta_{2,0}$ were both initialised to -0.5 for all

of the simulations in the case study. Note that from Equation (7), the initial values correspond to eigenvalues of $\lambda_1 = 1$ and $\lambda_2 = -0.5$.

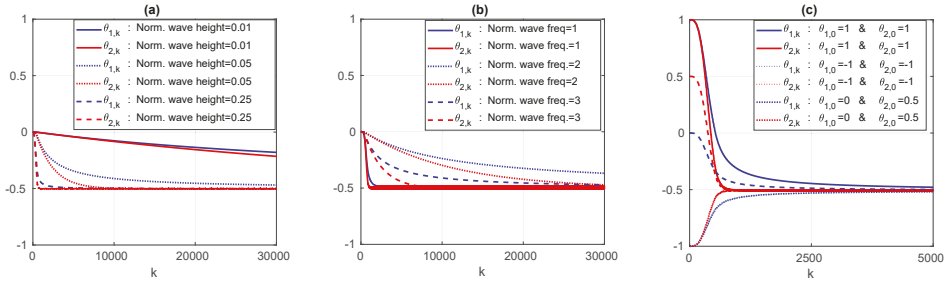

Figure 3. The online adaptation of $\theta_{i,k}$ using the recursive least squares algorithm. For monochromatic waves with: (**a**) a normalised wave frequency of 1.6 and varying wave height; (**b**) a normalised wave amplitude of 0.01 and varying wave frequency; and (**c**) a normalised wave frequency of 3, a normalised wave height of 0.1 and varying initial values.

3.4.3. Detection System Implementation

The principle of the detection system is to provide a warning of the probable onset of parametric resonance if one of the eigenvalues moves outside of the unit circle. Therefore, the absolute values of the eigenvalues are monitored at each time step and a warning is generated by the detection system when the following condition is met:

$$|\lambda_i| > 1 + \epsilon, \tag{19}$$

where ϵ is a user-specified threshold value. For the present test case, $\epsilon = 1$; thus, the detection system generates a warning if the magnitude of an eigenvalue exceeds 2. The pragmatic choice of $\epsilon = 1$ stemmed from the observations of the preliminary test runs, where small fluctations were present in the eigenvalues for normal operational conditions, $0.95 < \lambda_1 < 1.05$, but for the case where parametric resonance occurred, the eigenvalues rapidly diverged to values greater than 1000.

4. Results

The monochromatic waves are presented in Section 4.1 and then the polychromatic waves in Section 4.2. A brief discussion of the results and their implications is then provided in Section 4.3.

4.1. Monochromatic Waves

To evaluate the performance of the real-time early warning detection system, first each simulation had to be post-processed to determine the instances in which parametric resonance occurred (Section 4.1.1). Once the regions of parametric resonance were identified, then the performance of the early warning detection system could be assessed on its ability to correctly identify the onset of parametric resonance in a timely manner (Section 4.1.2).

4.1.1. Post Process Identification of Parametric Resonance

For normal operating conditions, in monochromatic waves, the frequencies of the pitch motion and the input waves are the same. However, when parametric resonance occurs, the frequency of the pitch motion becomes half of the input wave frequency. Therefore, the occurrence of parametric resonance in monochromatic waves can be easily identified during post processing by comparing the frequency of the pitch motion to the input wave frequency.

For each of the 4050 monochromatic wave simulations, a fast fourier Transform (FFT) was performed on the time series of the pitch displacement. If the peak amplitude of the PSD occurred

at a frequency less than 75% of the input wave frequency, then it is clear that parametric resonance occurred for that input wave condition. Figure 4 shows the wave frequencies and amplitudes for which parametric resonance occurs (the white region) and where it does not (the grey region). Three points are marked in red on Figure 4, which are subjected to the same wave height but with different frequencies, such that point A lays in the stable (no parametric resonance) region, point B on the border between the two regions and point C in the parametric resonance region. The pitch displacement time series and the PSD for points A, B and C are plotted in Figure 5A–C respectively. The pitch displacement for point A is seen to remain constant, with a small amplitude below 0.1 degrees and a frequency equal to the input wave frequency. For point B, the amplitude slowly grows throughout the simulation and the frequency has two peaks, one equal to the wave frequency and the other at half the wave frequency. For point C, the pitch displacement is seen to grow exponentially (to a value above 10°) and at a frequency equal to half the wave frequency.

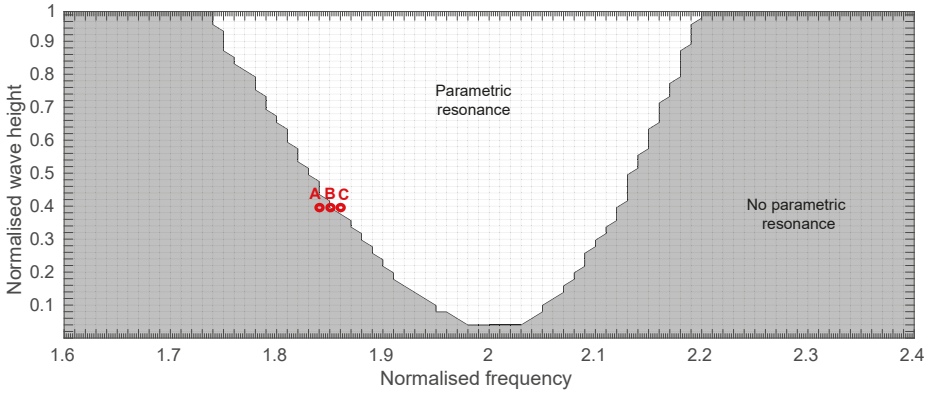

Figure 4. The amplitude and frequency range spanned by the monochromatic waves test cases. The white region denotes where parametric resonance was observed. Note the inclusion of grid lines in this figure to highlight the frequency and amplitude resolution, with a result simulated at every grid intersection. For reference, as discussed in Section 3.1, the wave height is normalised against $\overline{GM}$ and the wave frequency by $\omega_{n,5}$.

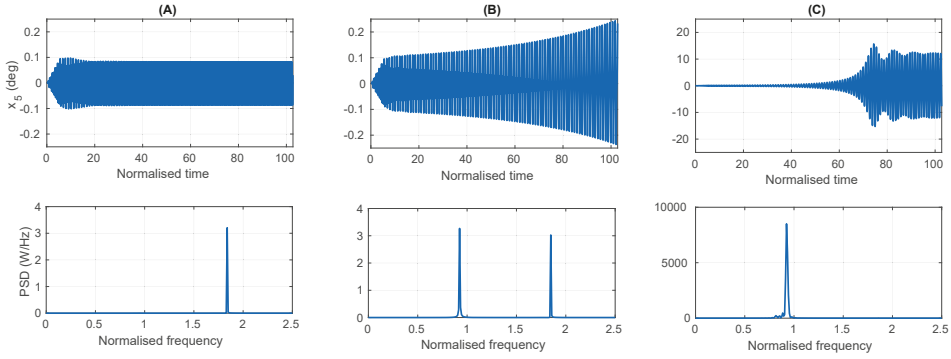

Figure 5. The pitch displacement time series and resulting PSD for the points (A) A, (B) B and (C) C in Figure 4.

4.1.2. Performance of the Early Warning Detection System

Figure 6 provides the results for the first assessment criteria: *correctly warning when parametric resonance occurs (correct positive) and not giving a false warning when parametric resonance does not occur*

(correct negative). Of the 4050 simulations, the detection system made 4 false negatives and 81 false positives. The false negatives all occurred on the border between the stable and parametric resonance regions, for low wave amplitudes, around twice the pitch natural frequency. The false positives occurred for large wave amplitudes at high frequencies, with three occurring on the border and the remainder occurring in a connected region in the corner of the graph with the highest wave amplitudes and frequencies. The behaviour of the false negatives is explored in Figure 7, which relates to the points A, B and C, marked in red on Figure 6, and the behaviour of the false positives is explored in Figure 8, which relates to the points D, E and F.

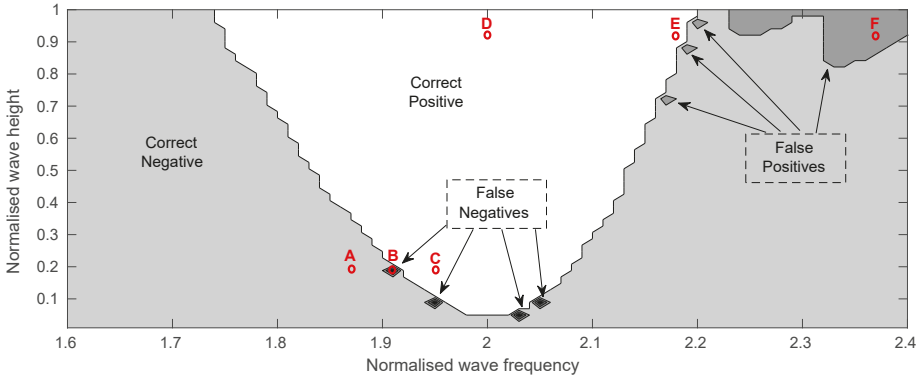

Figure 6. The performance of the early warning detection system in monochromatic waves; correct positives (white), correct negatives (grey), false positives (dark grey) and false negatives (black).

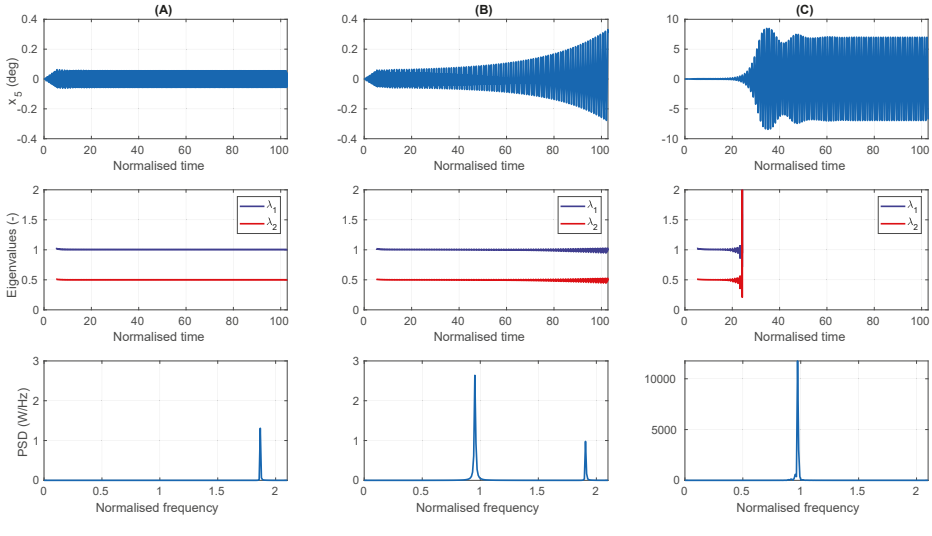

Figure 7. The pitch displacement time series (**top**), the magnitudes of the eigenvalues of the matrix **A** (**middle**) and the PSD of the pitch displacement (**bottom**), for the points (A) A, (B) B and (C) C in Figure 6.

Figure 7A relates to point A, which lies outside of the parametric resonance region. The top graph shows the pitch displacement is extremely small, about 0.05°, and the bottom graph shows that the pitch frequency is equal to the input wave frequency, as is expected for normal operating conditions with no parametric resonance. The magnitudes of the eigenvalues, in the middle graph, are seen

to remain constant and within the unit circle, signifying that the system is stable. For Figure 7C, since point C lies within the parametric resonance region, the bottom graph shows that the pitch frequency is now equal to half the input wave frequency. The top graph shows that the amplitude of the pitch displacement is approximately 100 times greater than for point A, even though the input wave amplitude is the same for at both points. The magnitudes of the eigenvalues in the middle graph are seen to diverge well outside of the unit complex circle at the same time as the amplitude of the pitch displacement starts to exponentially increase, highlighting the correct performance of the detection system. Since point B is near the border just inside the parametric resonance region, the exponential growth of the pitch displacement, seen in Figure 7B, occurs at a slower rate, only reaching a value of 0.2° by the end of the simulation. The frequency of the pitch displacement has a small peak at the wave frequency, but a larger one at half the wave frequency; thus this simulation is categorised in the parametric resonance region. The magnitudes of the eigenvalues are seen to increase slightly towards the end of the simulation, thus if the simulation ran for a longer time, then the eigenvalues would have likely diverged and the detection system would have correctly identified this case, rather than producing a false negative.

Points D, E and F correspond to the same large input wave amplitude and all trigger the parametric resonance warning system, although point F is a false positive. Figure 8D relates to point D, which is in the top middle of the parametric resonance region, resulting in the pitch motion becoming unstable and exceeding 90° (at which time the simulation is terminated) within approximately 20 wave periods. Figure 8E relates to point E, which is just within the boundary of the parametric resonance region, resulting in large pitch displacements of approximately 30 degrees at half the input wave frequency, which cause the eigenvalues to diverge out of the unit circle. For Figure 8F, which relates to the false positive at point F, the pitch displacement is stable throughout the simulation, with an amplitude less than 0.5° and a frequency equal to the wave frequency. However, although the magnitudes of the eigenvalues do not diverge, the largest eigenvalue has a magnitude of about 2.5, thereby triggering the parametric resonance detection system.

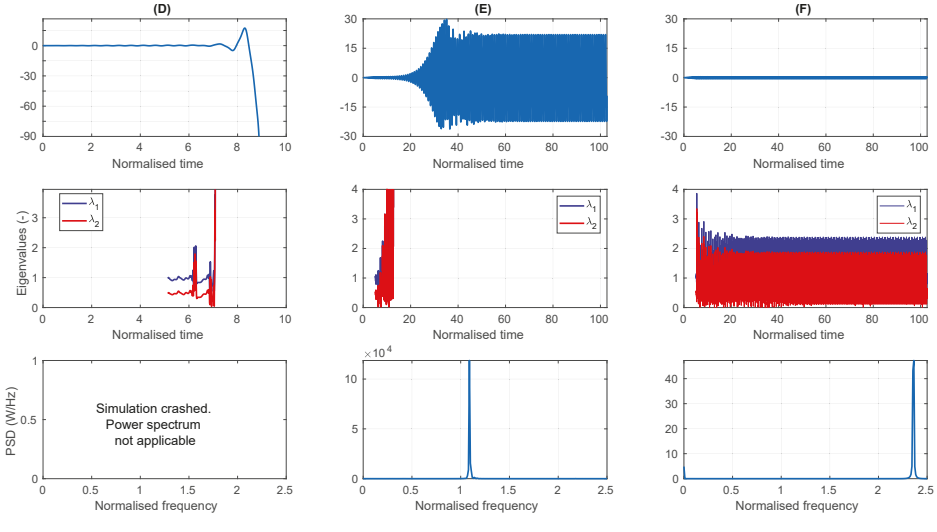

Figure 8. The pitch displacement time series (**top**), the magnitudes of the eigenvalues of the matrix **A** (**middle**) and the PSD of the pitch displacement (**bottom**), for the points (D) D, (E) E and (F) F in Figure 6.

Figure 9a–c highlights the performance of the detection system for the second criteria: *how early the system detects the onset of parametric resonance and sends a warning*. Figure 9a shows the amplitude

of the pitch displacement when the warning system detected parametric resonance, which for the majority of the cases occurred when the pitch displacement was less than 3°. While for some cases, the pitch amplitude was as high as 7° when the warning system detected parametric resonance, these cases correspond to extremely unstable conditions where the pitch displacement diverged within a few periods after the initial ramping of the input wave and exceeded 90° (such as in Figure 8D). The maximum amplitude of the pitch displacement when parametric resonance occurred is shown in Figure 9b[1]. A quantitative comparison of Figure 9a,b reveals that more that 99% of the detections occurred while the pitch amplitude was less than 1/6 of its maximum amplitude. Finally, Figure 9c shows the normalised time between when the warning system detects the onset of parametric resonance and when the pitch displacement reaches it maximum value. For the majority of cases, the parametric resonance was detected between 5 to $10T_{n5}$. For the extremely unstable regions in the top middle of the parametric resonance region, less warning time was available, with the detection occurring between 2 to $5T_{n5}$. On the border between the stable and parametric resonance regions, very early warning was given, more than $10T_{n5}$, due to the slower exponential growth rate of the pitch displacement amplitude (for example see Figure 8E).

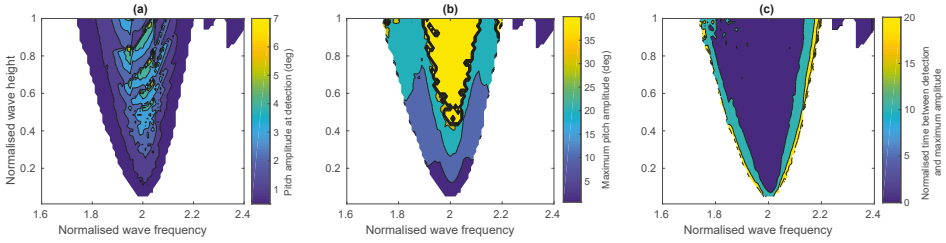

Figure 9. The performance of the early warning detection system in monochromatic waves. (**a**) The amplitude of the pitch displacement when the warning system detected parametric resonance. (**b**) The maximum amplitude of the pitch displacement when parametric resonance occurred (clipped at 40°, above which simulations always crashed). (**c**) The time between the when the warning system detected parametric resonance and when the maximum pitch displacement occurred.

4.2. Polychromatic

In this section, the performance of the real-time early warning detection system is evaluated for polychromatic input waves. Following the same layout as for the monochromatic waves, first each simulation was post-processed to determine the instances in which parametric resonance occurred (Section 4.2.1) and then the performance assessment was conducted (Section 4.2.2).

4.2.1. Post Process Identification of Parametric Resonance

Identifying the occurrence of parametric resonance in polychromatic waves is not as straightforward as for monochromatic waves. For a polychromatic wave spectrum, there is energy in the wave frequencies below the peak of the spectrum; thus, if there is pitch motion at half the peak frequency of the input waves, it can not be instantly identified whether this pitch motion response is due to parametric excitation or direct excitation from the spectral wave components at that lower frequency. Similarly, there is energy at wave frequencies above the peak of the spectrum, so once again it can not be instantly identified whether large pitch motion at low frequencies is due to direct excitation from the wave components at that frequency, or from parametric excitation caused by the

[1] Note: to limit the scale, the maximum amplitude is clipped at 40°, since for any simulation in which the amplitude exceeded this value, the pitch displacement grew to 90° and the simulation was terminated.

wave components at twice that frequency. Therefore, a different metric is applied for the polychromatic waves, based on the energy increase in the pitch motion observed during the simulation.

The energy in the pitch motion (calculated from the root mean square value of x_5), measured in the first $5T_{n5}$ after the input wave height is ramped to maximum amplitude (i.e., from $5T_{n5}$ to $10T_{n5}$), is compared to the energy in the last $5T_{n5}$ of the simulation (i.e., from $195T_{n5}$ to $200T_{n5}$). The energy increase in the pitch motion as a function of the normalised wave frequency and height is shown in the contour plot in Figure 10. The contour lines have a resolution of 0.25 and it can be seen that for low amplitude waves and for frequencies well away from $2\omega_{n,5}$, the energy is relatively constant over the length of the simulation, with the increase in energy laying between the 0.5 and 1.5 contour lines. However, for the region of larger amplitude waves centred around $2\omega_{n,5}$, where parametric resonance was expected, the increase in energy has a large positive gradient with respect to the wave height and frequency once the increase in energy values exceeds 1.5. Based on the results shown in Figure 10, if the energy increase from the start to the end of the simulation is more than 2, then the simulation is added to the parametric resonance region, as depicted in Figure 11.

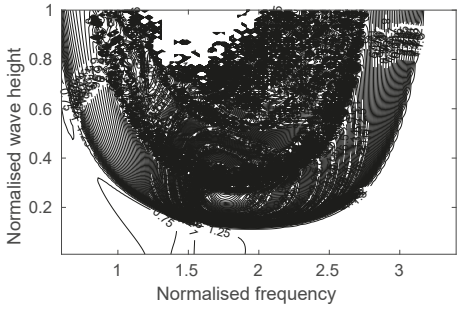

Figure 10. The energy increase in the pitch displacement from the start to the end of the simulation as a function of the normalised wave frequency and height. The contour lines have a resolution of 0.25.

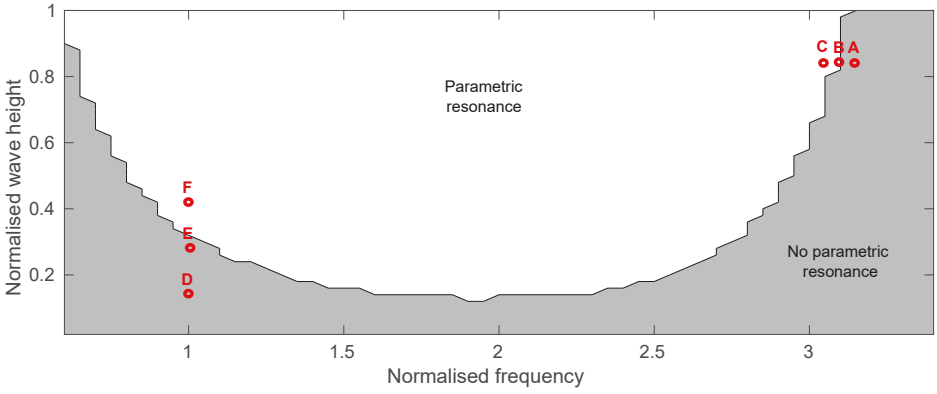

Figure 11. The amplitude and frequency range spanned by the polychromatic waves' test cases. The region in which parametric resonance was observed is shown in white.

As an example, three points marked in red, A, B and C, were selected, spanning the borderline between the stable and parametric resonance regions; their time series and PSD are plotted in Figure 12. Point A, which is just outside of the parametric resonance region, is seen to have a fairly constant pitch displacement amplitude, whose frequency components are predominantly in a spectrum which has a peak frequency equal to the peak frequency of the input wave spectrum. However, some frequency components exist, centred at half the peak frequency, whose amplitude is about half of the amplitude

at the peak frequency. For point B, just inside parametric resonance region, the pitch motion still contains a spectrum of frequency components with a peak frequency equal to the peak frequency of the input wave spectrum and whose amplitudes are approximately the same as for point A. However, the frequency component at half the peak frequency of the input wave spectrum has an amplitude more than 15 times greater than the amplitude at the peak wave frequency. For point C, only the frequency component at half the peak frequency of the input wave spectrum can be seen, whose amplitude is 90 times greater than the amplitude at the peak wave frequency.

To highlight the difference between the classification of normal resonance and parametric resonance, points D, E and F are selected at increasing wave heights on the pitch natural frequency, and their time series and PSD are plotted in Figure 13. The wave height is doubled between points D and E, which results in a doubling of the pitch motion, as is expected for normal resonance. However, between points D and F, the wave height is increased by a factor of three, but the pitch motion increases approximately tenfold, highlighting the nonlinear parametric resonant response.

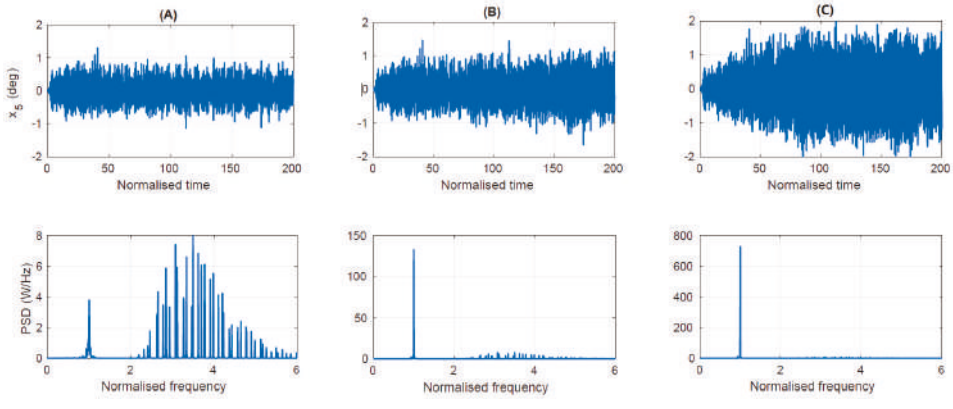

Figure 12. The pitch displacement time series and resulting PSD for the points (A) A, (B) B and (C) C in Figure 11.

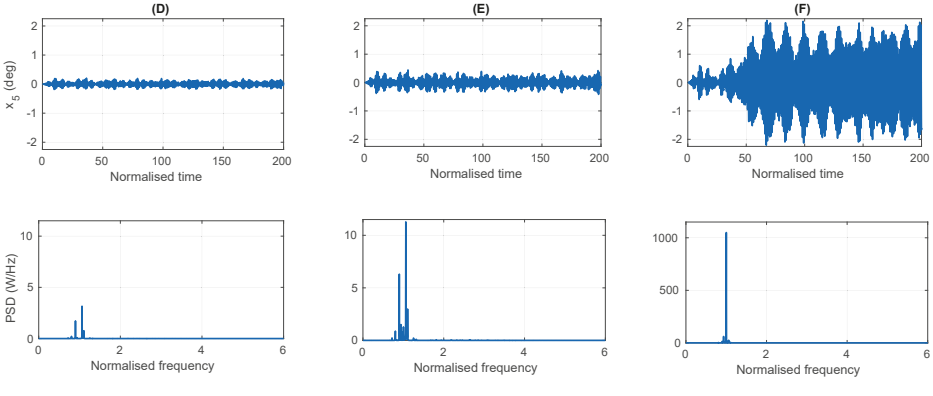

Figure 13. The pitch displacement time series and resulting PSD for the points (D) D, (E) E and (F) F in Figure 11.

4.2.2. Performance of the Early Warning Detection System

Figure 14 provides the results for the first assessment criteria: correctly warning when parametric resonance occurs (correct positive) and not giving a false warning when parametric resonance does not occur (correct negative). Of the 2800 simulations, the detection system had 25 false negatives and 235

false positives. The false negatives occurred along the border between the stable and the parametric resonance regions, for low wave amplitudes. The false positives, on the other hand, spanned an area from the border into the stable region, at large wave amplitudes, for both low and high frequencies.

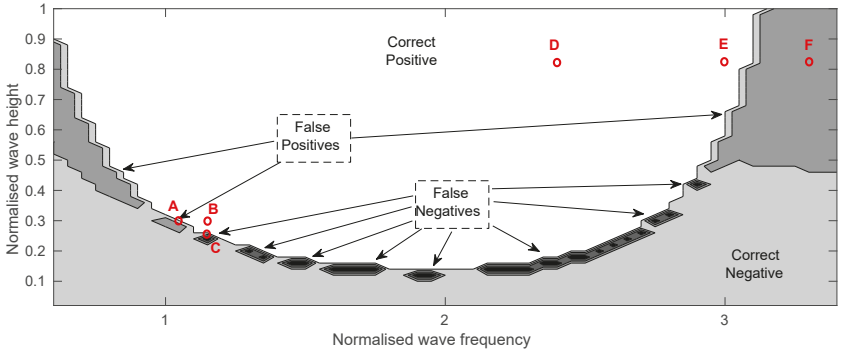

Figure 14. The performance of the early warning detection system in polychromatic waves; correct positives (white), correct negatives (grey), false positives (dark grey) and false negatives (black).

Figure 15A–C shows the time series of the pitch displacement and the magnitudes of the eigenvalues of the matrix **A**, along with the PSD of the pitch displacement, for points A–C, respectively. While point A corresponds to a false positive and point C corresponds to a false negative, their time series look quite similar. The increase of energy between the start and end of the simulation was 190% for point A and 232% for point B; thus, they both sit very close on either side of the selected threshold for which the parametric resonance region was defined in this study. At the ends of both simulations, large pitch oscillations occurred, with a maximum amplitude of 0.57° for point A, which caused the largest eigenvalue to grow to an absolute value of 264 and trigger the detection system. For point B, the pitch displacement amplitude only grew to 0.48° and the eigenvalues only grew to 1.44. For a comparison to the behaviour of these two points that sit on the borderline, point B sits just inside the parametric resonance region, with the same amplitude as point A and the same frequency as point C, but the energy increased by more than 800% from the start to the end of the simulation, and the maximum pitch displacement was about three times greater than for points A and C.

Yhe false positives at large wave amplitudes, Figure 16D–F, correspond to the points D–F, respectively, which are all subjected to an input spectrum with the same wave height. Point D is well within the parametric resonance region, point E is just inside the parametric resonance region and point F is in the stable region. Point D is seen to have an oscillatory, large amplitude pitch displacement, with rapid exponential growth and decay rates, and a single dominant frequency at half the peak frequency of the input wave spectrum. Point E also has a single dominant frequency at half the peak frequency of the input wave spectrum. However, the maximum amplitude of the pitch displacement is about 20% of the amplitude at point D and grows much slower and remains fairly constant once it reaches its maximum. For point F, the pitch displacement has a much smaller amplitude, which does not grow, and its frequency content is distributed in a spectrum with the same peak as the input waves. However, the magnitudes of the eigenvalues for point F are seen to diverge in much the same way as for points D and E.

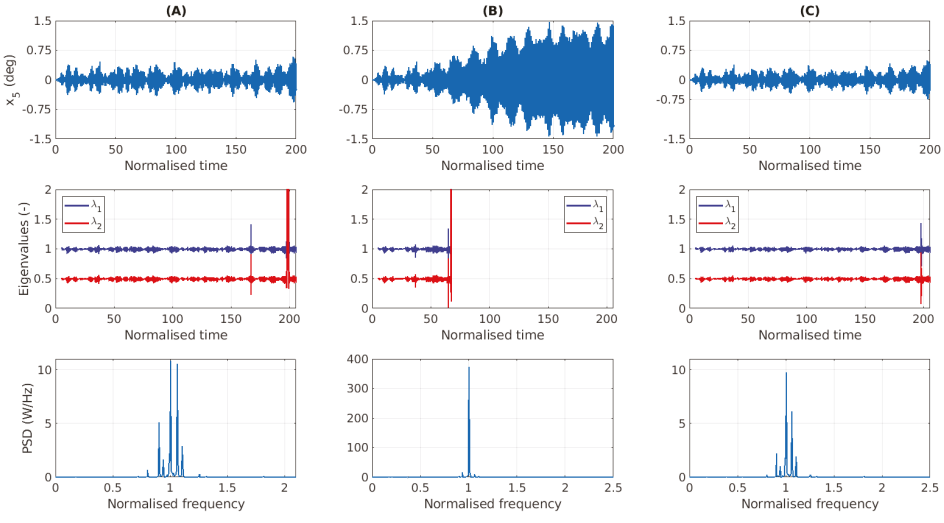

Figure 15. The time series for the pitch displacement (**top**), the magnitudes of the eigenvalues of the matrix **A** (**middle**) and the PSD of the pitch displacement (**bottom**), for the points (A) A, (B) B and (C) C in Figure 14.

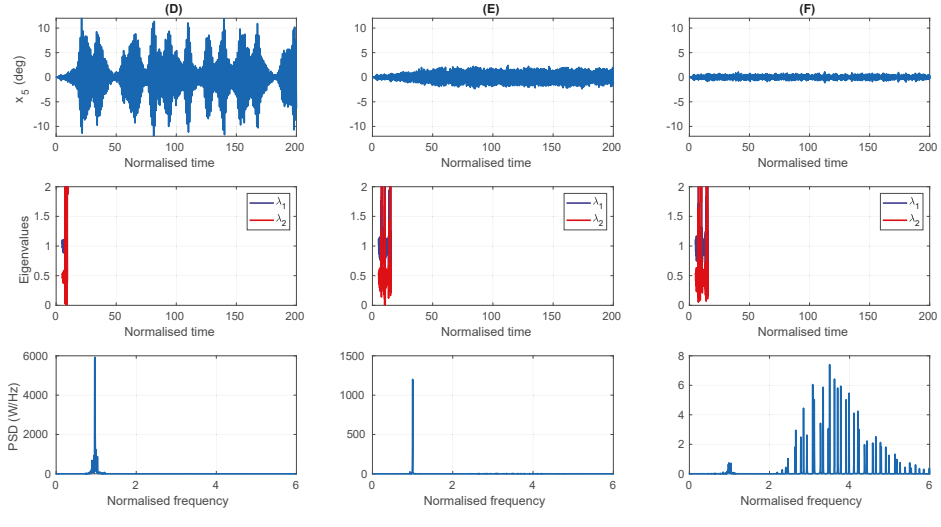

Figure 16. The time series for the pitch displacement (**top**), the magnitudes of the eigenvalues of the matrix **A** (**middle**) and the PSD of the pitch displacement (**bottom**), for the points (D) D, (E) E and (F) F in Figure 14.

Figure 17a–c highlights the performance of the detection system for the second criteria: how early the system detects the onset of parametric resonance and sends a warning. Figure 17a shows that for the majority of the cases, the detection system sends a warning when the pitch displacement amplitude is less than 1 degree, and in all cases before the amplitude reaches 2°. For the polychromatic waves, the maximum pitch amplitude is generally less than 20 degrees, except in a highly unstable region (normalised wave heights above 0.8 and normalised frequencies between 1.25 and 2) where the simulations are terminated at a pitch amplitude of 90°. Near the parametric resonance border and in

the region of false positives, the maximum displacement is less than 5°. A quantitative comparison of Figure 17a,b reveals that more that 91% of the detections occurred while the pitch amplitude was less than 1/3 of its maximum amplitude and 67% while the pitch amplitude was less than 1/6 of its maximum amplitude. Finally, Figure 17c shows the normalised time between detection and the maximum amplitude, which is in excess of $10T_{n5}$ for all cases within the parametric resonance region, and in many cases is more than $100T_{n5}$. The reason for the large times is that after the pitch amplitude grows larger, due to parametric resonance, it will then have a degree of variation around the new mean amplitude because of the irregular nature of the input waves. Therefore the maximum amplitude can occur at any time after the initial growth to the larger mean amplitude. For example, in Figure 16E, the pitch amplitude grows to a mean maximum level of about 2° within $60T_{n5}$; however, at $110T_{n5}$ the amplitude has a spike up to 2.4° which is the maximum value for the simulation.

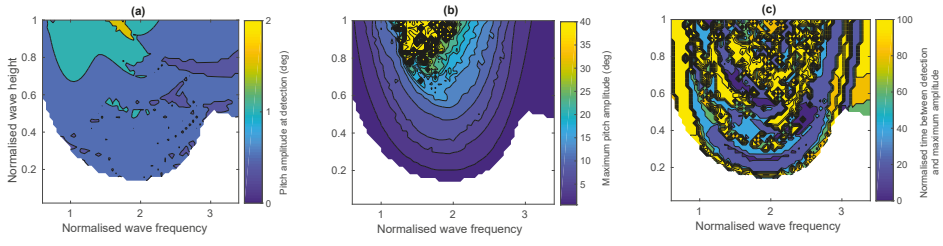

Figure 17. The performance of the early warning detection system in polychromatic waves. (**a**) The amplitude of the pitch displacement when the warning system detected parametric resonance. (**b**) The maximum amplitude of the pitch displacement when parametric resonance occurred (clipped at 40°, above which simulations always crashed). (**c**) The time between the when the warning system detected parametric resonance and when the maximum pitch displacement occurred.

4.3. Discussion

Overall, the results demonstrate the ability of the proposed system to effectively detect the onset of parametric resonance. The detection occurred in most cases while the pitch oscillations were small fractions of their maximum amplitudes, with many periods of early warning given for a control system to mitigate the impending growth of the pitch oscillations. For the extremely unstable conditions, much less warning time was available; however, these conditions occurred in the middle of the parametric resonance region. Thus, for such waves conditions to develop the sea state must first transition through the wave conditions in the border of the parametric resonance region, where ample warning for the potential instability of the pitch oscillations is provided.

The proposed system rarely failed to detect the occurrence of parametric resonance, with very few false negatives observed, especially for the monochromatic wave case. For the polychromatic wave case, the slightly higher percentage of false negatives might be attributed to the arbitrary classification of the parametric resonance region. As described in Section 4.2.1, if the energy of the pitch oscillations doubled from the start compared to the end of the simulation, then the simulation was classified as belonging to the parametric resonance region. From Figure 10, choosing a 2-fold increase in the energy of the pitch oscillations as the cut-off for the parametric resonance region seems like a reasonable choice, representing the knee of the curve, above which the pitch oscillation amplitude readily increases. However, choosing a slightly larger value around the knee of the curve, such as a 3-fold increase in the energy for example, could also be valid and might have resulted in a lower number of false negatives, but possibly at the cost of an increased number of false positives. Nevertheless, the false negatives produced by the detection system under the current classification system are not particularly troublesome, relating to pitch displacements of less than 1°.

The main advantages of the proposed system relate to its simplicity in terms of computational modelling and required inputs. The detection system does not require a complex, high-fidelity,

computationally expensive model. Instead, the simple black-box, linear model in Equation (1) has only four parameters that are adaptively tuned to any type of WEC system/geometry. This allows the detection system to be arbitrarily applied to different type of WECs, without requiring bespoke modelling to be tailored for each individual application, system and/or DoF. Indeed, another advantage of the detection system is its ability to treat each DoF independently, since it updates the parameters of a single DoF model using measurements of that single DoF. Thus, if multiple DoFs are to be considered, each DoF can be treated individually with its own detection system, independent of the other DoFs. However, the system requires that the dynamics of the DoF to be modelled can be approximated by a linear second-order differential equation, which is a reasonable assumption in most cases since the DoFs for which parametric resonance is to be monitored are not the primary mode of motion and amplitudes are relatively small in normal operating conditions. Future work will investigate different types of WECs and DoFs.

Perhaps the biggest advantage is the relatively simple and accessible set of inputs required by the detection system: the position and velocity of a single DoF. Measurement of these variables is relatively straightforward, using accelerometers, inclinometers, etc. However, the robustness of the detection system to noise and error in these measuring instruments should be investigated in future work. Nevertheless, the ability of the detection system to work without requiring more challenging inputs, such as prediction of the input waves or estimation of the excitation force, is a major advantage. The current inputs simplify the system requirements and remove the uncertainty/error involved with prediction and estimation methods.

Being a first implementation, for a real-time detection system for the onset of parametric resonance in WECs, the proposed system is not without its flaws and has room for improvement. The main disadvantage observed from the results was the number of false positives. For the monochromatic waves, the false positives occurred for the high frequency and large amplitude input waves, whereas for the polychromatic waves the false positives occurred for both high and low frequency input waves with large amplitudes.

One possible remedy to reduce the amount of false positives is to increase the detection threshold, i.e., the value of ϵ in Equation (19). For example, as seen in Figure 8F, increasing the value of ϵ from 1 to 3 would eliminate the false positive. Although increasing the detection threshold can in theory increase the number of false negatives, in practice when parametric resonance was detected the magnitudes of the eigenvalues typically diverged very rapidly to values exceeding 1000. For many false positives, the magnitudes of the eigenvalues were less than 10. Thus, it is unlikely that increasing the detection threshold to any single digit number would cause a currently correct positive detection to become a false negative. However, a false negative is more detrimental to the WEC system than a false positive, so prudently selecting the value of ϵ should be investigated on a case-by-case basis for different WEC systems and DoFs.

Alternatively, to reduce the nuumber of false positives, the underlying cause should be identified if possible and the detection algorithm improved accordingly. In particular, a possible explanation for the growth of the eigenvalues, which trigger the false detection, is due to the input excitation not being Gaussian white noise, as is assumed in Equation (1). The Gaussian white noise assumption stems from the original application of this detection method in [51], the roll motion of ships, for which in head seas there is no direct wave excitation to the roll DoF. In contrast, the present case study examined the pitch motion, which is directly excited by the input waves. Both the monochromatic and polychromatic waves were coloured, rather than a white spectrum; thus the assumption of a Gaussian white noise excitation was violated since the input spectrum was not flat, with equal amplitude across all frequencies. Therefore, future work will investigate a means to improve upon the assumption of Gaussian white noise input whilst hopefully maintaining the benefit of not explicitly requiring an estimation of the input waves/excitation force.

5. Conclusions

This paper demonstrated the first implementation of a real-time detection system for the early warning of the onset of parametric resonance in a WEC, by applying a method developed for the monitoring and detection of parametric roll motion in ships. The results from a test case, considering the parametric pitch motion in a heaving spar-buoy, show that the detection system performed very well, achieving 95% accuracy across a range of monochromatic and polychromatic sea states. In addition, the detection system provides an early warning while the pitch motion is a small fraction of its impending maximum amplitude. However, one potential shortcoming is the assumption of the external excitation to the system being described by Gaussian white noise, which is less valid for the pitch motion in a WEC compared to the roll motion in a ship. Assuming the input to be Gaussian white noise resulted in the system incorrectly detecting instability when the input waves were of large amplitudes and high frequencies, resulting in the warning system providing 10 times more false positives than false negatives. The practical implementation of the system imposes a low overhead, only requiring measurement of the position and velocity of the DoF to be monitored and enough computational resources to perform a recursive least squares algorithm for two time-varying parameters and then finding the roots of a quadratic equation.

Author Contributions: Conceptualization, J.D.; Formal analysis, J.D.; Investigation, J.D.; Supervision, T.K.-N.; Writing—original draft, J.D.; Writing—review & editing, T.K.-N. Both authors have read and agreed to the published version of the manuscript.

Funding: This project has received funding from the European Union's Horizon 2020 research and innovation programme under the Marie Sklodowska-Curie grant agreement number 867453. The research reported in this paper was supported by the BME Water Sciences and Disaster Prevention TKP2020 IE grant of NKFIH Hungary (BME IE-VIZ TKP2020) and by the BME NC TKP2020 grant of NKFIH Hungary.

Conflicts of Interest: The authors declare no conflict of interest.

References

1. Fossen, T.; Nijmeijer, H. *Parametric Resonance in Dynamical Systems*; Springer: New York, NY, USA, 2011.
2. Faraday, M. On a peculiar class of acoustical figures; and on certain forms assumed by groups of particles upon vibrating elastic surfaces. In *Philosophical Transactions of the Royal Society of London*; The Royal Society: London, UK, 1831; pp. 299–340.
3. Froude, W. *On the Rolling of Ships*; Institution of Naval Architects: London, UK, 1861.
4. Galeazzi, R. Autonomous Supervision and Control of Parametric Roll Resonance. Ph.D. Thesis, Department of Naval Architecture and Offshore Engineering, Technical University of Denmark, Lyngby, Denmark, 2009.
5. Shigunov, V.; El Moctar, O.; Rathje, H.; Germanischer Lloyd, A. Conditions of parametric rolling. In Proceedings of the 10th International Conference on Stability of Ships and Ocean Vehicles, St Petersberg, Russia, 22–26 June 2009.
6. Koo, B.; Kim, M.; Randall, R. Mathieu instability of a spar platform with mooring and risers. *Ocean Eng.* **2004**, *31*, 2175–2208. [CrossRef]
7. Neves, M.A.; Sphaier, S.H.; Mattoso, B.M.; Rodri´ guez, C.A.; Santos, A.L.; Vileti, V.L.; Torres, F.G. On the occurrence of Mathieu instabilities of vertical cylinders. In Proceedings of the 27th International Conference on Offshore Mechanics and Arctic Engineering, Estorill, Portugal, 15–20 June 2008.
8. Li, B.B.; Ou, J.P.; Teng, B. Numerical investigation of damping effects on coupled heave and pitch motion of an innovative deep draft multi-spar. *J. Mar. Sci. Technol.* **2011**, *19*, 231–244.
9. Yang, H.; Xu, P. Effect of hull geometry on parametric resonances of spar in irregular waves. *Ocean Eng.* **2015**, *99*, 14–22. [CrossRef]
10. Jang, H.; Kim, M. Mathieu instability of Arctic Spar by nonlinear time-domain simulations. *Ocean Eng.* **2019**, *176*, 31–45. [CrossRef]
11. Umeda, N.; Hashimoto, H.; Minegaki, S.; Matsuda, A. An investigation of different methods for the prevention of parametric rolling. *J. Mar. Sci. Technol.* **2008**, *13*, 16–23. [CrossRef]

12. Galeazzi, R.; Pettersen, K.Y. Parametric resonance in dynamical systems. In *Parametric Resonance in Dynamical Systems*; Chapter Controlling Parametric Resonance: Induction and Stabilization of Unstable Motions; Fossen, T.I., Nijmeijer, H., Eds.; Springer: New York, NY, USA, 2012; pp. 305–327.
13. Bracewell, R.H. Frog and PS Frog: A Study of Two Reactionless Ocean Wave Energy Converters. Ph.D. Thesis, University of Lancaster, Lancashire, UK, 1990.
14. Durand, M.; Babarit, A.; Pettinotti, B.; Quillard, O.; Toularastel, J.; Clément, A. Experimental validation of the performances of the SEAREV wave energy converter with real time latching control. In Proceedings of the 7th European Wave and Tidal Energy Conference, Porto, Portugal, 11–13 September 2007.
15. Payne, G.S.; Taylor, J.R.; Bruce, T.; Parkin, P. Assessment of boundary-element method for modelling a free-floating sloped wave energy device. Part 2: Experimental validation. *Ocean Eng.* **2008**, *35*, 342–357. [CrossRef]
16. Raftery, M.W. Harnessing Ocean Surface Wave Energy to Generate Electricity. Master's Thesis, Stevens Institute of Technology, Hoboken, NJ, USA, 2008.
17. Sheng, W.; Flannery, B.; Lewis, A.; Alcorn, R. Experimental studies of a floating cylindrical OWC WEC. In Proceedings of the 31st International Conference on Ocean, Offshore and Arctic Engineering, Rio de Janeiro, Brazil, 1–6 July 2012.
18. Gomes, R.; Henriques, J.; Gato, L.; Falcao, A. Testing of a small-scale floating OWC model in a wave flume. In Proceedings of the 4th International Conference on Ocean Energy, Dublin, Ireland, 17–19 October 2012.
19. Gomes, R.; Henriques, J.; Gato, L.; Falcão, A.d.O. Wave channel tests of a slack-moored floating oscillating water column in regular waves. In Proceedings of the 11th European Wave and Tidal Energy Conference, Nantes, France, 6–11 September 2015.
20. Beatty, S.J.; Roy, A.; Bubbar, K.; Ortiz, J.; Buckham, B.J.; Wild, P.; Stienke, D.; Nicoll, R. Experimental and numerical simulations of moored self-reacting point absorber wave energy converters. In Proceedings of the 25th International Ocean and Polar Engineering Conference, Kona, HI, USA, 25–30 June 2015.
21. Orszaghova, J.; Wolgamot, H.; Taylor, R.E.; Draper, S.; Rafiee, A.; Taylor, P. Simplified dynamics of a moored submerged buoy. In Proceedings of the 32nd International Workshop on Water Waves and Floating Bodies, Dalian, China, 23–26 April 2017.
22. Sergiienko, N.Y. Three-Tether Wave Energy Converter: Hydrodynamic Modelling, Performance Assessment and Control. Ph.D. Thesis, University Adelaide, Adelaide, Australia, 2018.
23. Gomes, R.; Henriques, J.; Gato, L.; Falcão, A. Experimental Tests of a 1: 16th-Scale Model of the Spar-Buoy OWC in a Large Scale Wave Flume in Regular Waves. In Proceedings of the 37th International Conference on Ocean, Offshore and Arctic Engineering, Madrid, Spain, 17–22 June 2018.
24. Kurniawan, A.; Grassow, M.; Ferri, F. Numerical modelling and wave tank testing of a self-reacting two-body wave energy device. *Ships Offshore Struct.* **2019**, *14*, 344–356. [CrossRef]
25. Orszaghova, J.; Wolgamot, H.; Draper, S.; Eatock Taylor, R.; Taylor, P.; Rafiee, A. Transverse motion instability of a submerged moored buoy. *Proc. R. Soc. A* **2019**, *475*, 20180459. [CrossRef]
26. Gomes, R.; Henriques, J.; Gato, L.; Falcão, A. Time-domain simulation of a slack-moored floating oscillating water column and validation with physical model tests. *Renew. Energy* **2020**, *149*, 165–180. [CrossRef]
27. Davidson, J.; Costello, R. Efficient Nonlinear Hydrodynamic Models for Wave Energy Converter Design—A Scoping Study. *J. Mar. Sci. Eng.* **2020**, *8*, 35. [CrossRef]
28. Babarit, A.; Mouslim, H.; Clément, A.; Laporte-Weywada, P. On the numerical modelling of the nonlinear behaviour of a wave energy converter. In Proceedings of the 28th International Conference on Offshore Mechanics & Arctic Engineering, Honolulu, HI, USA, 31 May–5 June 2009.
29. Tarrant, K.R. Numerical Modelling of Parametric Resonance of a Heaving Point Absorber Wave Energy Converter. Ph.D. Thesis, Trinity College Dublin, Dublin, Ireland, 2015.
30. Tarrant, K.; Meskell, C. Investigation on parametrically excited motions of point absorbers in regular waves. *Ocean Eng.* **2016**, *111*, 67–81. [CrossRef]
31. Giorgi, G.; Ringwood, J.V. A compact 6-DoF nonlinear wave energy device model for power assessment and control investigations. *IEEE Trans. Sustain. Energy* **2018**, *10*, 119–126. [CrossRef]
32. Giorgi, G.; Ringwood, J.V. Articulating Parametric Nonlinearities in Computationally Efficient Hydrodynamic Models. *IFAC-PapersOnLine* **2018**, *51*, 56–61. [CrossRef]

33. Giorgi, G.; Ringwood, J.V. Parametric motion detection for an oscillating water column spar buoy. In Proceedings of the 3rd International Conference on Renewable Energies Offshore, Lisbon, Portugal, 8–10 October 2018.
34. Giorgi, G.; Gomes, R.P.; Bracco, G.; Mattiazzo, G. The Effect of Mooring Line Parameters in Inducing Parametric Resonance on the Spar-Buoy Oscillating Water Column Wave Energy Converter. *J. Mar. Sci. Eng.* **2020**, *8*, 29. [CrossRef]
35. Zou, S.; Abdelkhalik, O.; Robinett, R.; Korde, U.; Bacelli, G.; Wilson, D.; Coe, R. Model Predictive Control of parametric excited pitch-surge modes in wave energy converters. *Int. J. Mar. Energy* **2017**, *19*, 32–46. [CrossRef]
36. Yerrapragada, K.; Ansari, M.; Karami, M.A. Enhancing power generation of floating wave power generators by utilization of nonlinear roll-pitch coupling. *Smart Mater. Struct.* **2017**, *26*, 094003. [CrossRef]
37. Abdelkhalik, O.; Zou, S. Time-varying linear quadratic gaussian optimal control for three-degree-of-freedom wave energy converters. In Proceedings of the 12th European Wave and Tidal Energy Conference, Cork, Ireland, 27 August–2 September 2017.
38. Abdelkhalik, O.; Zou, S.; Robinett, R.; Bacelli, G.; Wilson, D.; Coe, R. Control of three degrees-of-freedom wave energy converters using pseudo-spectral methods. *J. Dyn. Syst. Meas. Control* **2018**, *140*, 074501. [CrossRef]
39. Davidson, J.; Karimov, M.; Szelechman, A.; Windt, C.; Ringwood, J. Dynamic mesh motion in OpenFOAM for wave energy converter simulation. In Proceedings of the 14th OpenFOAM Workshop, Duisburg, Germany, 23–26 July 2019.
40. Zou, S.; Abdelkhalik, O. Time-varying linear quadratic Gaussian optimal control for three-degree-of-freedom wave energy converters. *Renew. Energy* **2020**, *149*, 217–225. [CrossRef]
41. Palm, J.; Bergdahl, L.; Eskilsson, C. Parametric excitation of moored wave energy converters using viscous and non-viscous CFD simulations. In *Advances in Renewable Energies Offshore*; Taylor & Francis Group: Abingdon, UK, 2019; pp. 455–462.
42. Nicoll, R.S.; Wood, C.F.; Roy, A.R. Comparison of physical model tests with a time domain simulation model of a wave energy converter. In Proceedings of the 31st International Conference on Ocean, Offshore and Arctic Engineering, Rio de Janeiro, Brazil, 1–6 July 2012.
43. Orszaghova, J.; Wolgamot, H.; Draper, S.; Taylor, P.H.; Rafiee, A. Onset and limiting amplitude of yaw instability of a submerged three-tethered buoy. *Proc. R. Soc. A* **2020**, *476*, 20190762. [CrossRef]
44. Rho, J.B.; Choi, H.S.; Shin, H.S.; Park, I.K. A study on Mathieu-type instability of conventional spar platform in regular waves. *Int. J. Offshore Polar Eng.* **2005**, *15*, 104–108.
45. Ortiz, J.P. The Influence of Mooring Dynamics on the Performance of Self Reacting Point Absorbers. Master's Thesis, University of Victoria, Victoria, BC, Canada, 2016.
46. Gomes, R.; Malvar Ferreira, J.; Ribeiro e Silva, S.; Henriques, J.; Gato, L. An experimental study on the reduction of the dynamic instability in the oscillating water column spar buoy. In Proceedings of the 12th European Wave and Tidal Energy Conference, Cork, Ireland, 27 August–2 September 2017.
47. Cordonnier, J.; Gorintin, F.; De Cagny, A.; Clément, A.; Babarit, A. SEAREV: Case study of the development of a wave energy converter. *Renew. Energy* **2015**, *80*, 40–52. [CrossRef]
48. Gomes, R.; Henriques, J.; Gato, L.; Falcao, A. An upgraded model for the design of spar-type floating oscillating water column devices. In Proceedings of the 13th European Wave and Tidal Energy Conference, Naples, Italy, 1–6 September 2019.
49. Villegas, C.; van der Schaaf, H. Implementation of a pitch stability control for a wave energy converter. In Proceedings of the 10th European Wave and Tidal Energy Conference, Southampton, UK, 5–9 September 2011.
50. Maloney, P. Performance Assessment of a 3-Body Self-Reacting Point Absorber Type Wave Energy Converter. Master's Thesis, University of Victoria, Victoria, BC, Canada, 2019.
51. Holden, C.; Perez, T.; Fossen, T.I. Frequency-motivated observer design for the prediction of parametric roll resonance. *IFAC Proc. Vol.* **2007**, *40*, 57–62. [CrossRef]
52. Shaw McCue, L.; Bulian, G. A numerical feasibility study of a parametric roll advance warning system. *J. Offshore Mech. Arct. Eng.* **2007**, *129*. [CrossRef]
53. Galeazzi, R.; Blanke, M.; Poulsen, N.K. Parametric roll resonance detection on ships from nonlinear energy flow indicator. *IFAC Proc. Vol.* **2009**, *42*, 348–353. [CrossRef]

54. Galeazzi, R.; Blanke, M.; Poulsen, N.K. Early detection of parametric roll resonance on container ships. *IEEE Trans. Control Syst. Technol.* **2012**, *21*, 489–503. [CrossRef]
55. Galeazzi, R.; Blanke, M.; Falkenberg, T.; Poulsen, N.K.; Violaris, N.; Storhaug, G.; Huss, M. Parametric roll resonance monitoring using signal-based detection. *Ocean Eng.* **2015**, *109*, 355–371. [CrossRef]
56. Caamaño, L.S.; González, M.M.; Casás, V.D. On the feasibility of a real time stability assessment for fishing vessels. *Ocean Eng.* **2018**, *159*, 76–87. [CrossRef]
57. Caamaño, L.S.; Galeazzi, R.; Nielsen, U.D.; González, M.M.; Casás, V.D. Real-time detection of transverse stability changes in fishing vessels. *Ocean Eng.* **2019**, *189*, 106369. [CrossRef]
58. Davidson, J.; Genest, R.; Ringwood, J. Adaptive control of a wave energy converter simulated in a numerical wave tank. In Proceedings of the 12th European Wave and Tidal Energy Conference, Cork, Ireland, 27 August–2 September 2017.
59. Genest, R.; Davidson, J.; Ringwood, J.V. Adaptive control of a wave energy converter. *IEEE Trans. Sustain. Energy* **2018**, *9*, 1588–1595.
60. Peña-Sanchez, Y.; Windt, C.; Davidson, J.; Ringwood, J.V. A Critical Comparison of Excitation Force Estimators for Wave-Energy Devices. *IEEE Trans. Control. Syst. Technol.* **2019**. [CrossRef]
61. Thompson, J.M.T.; Stewart, H.B. *Nonlinear Dynamics and Chaos*; John Wiley & Sons: Hoboken, NJ, USA, 2002.
62. Yong-Pyo, H.; Dong-Yeon, L.; Yong-Ho, C.; Sam-Kwon, H.; Se-Eun, K. An experimental study on the extreme motion responses of a spar platform in the heave resonant waves. In Proceedings of the 15th International Offshore and Polar Engineering Conference, Seol, Korea, 19–24 June 2005.
63. Zhao, J.; Tang, Y.; Shen, W. A study on the combination resonance response of a classic spar platform. *J. Vib. Control* **2010**, *16*, 2083–2107. [CrossRef]
64. Gavassoni, E.; Gonçalves, P.B.; Roehl, D.M. Nonlinear vibration modes and instability of a conceptual model of a spar platform. *Nonlinear Dyn.* **2014**, *76*, 809–826. [CrossRef]
65. Giorgi, G.; Davidson, J.; Habib, G.; Bracco, G.; Mattiazzo, G.; Kalmar-Nagy, T. Nonlinear Dynamic and Kinematic Model of a Spar-Buoy: Parametric Resonance and Yaw Numerical Instability. *Mar. Sci. Eng.* **2020**, *8*, 504. [CrossRef]
66. Wacher, A.; Nielsen, K. Mathematical and numerical modeling of the AquaBuOY wave energy converter. *Math. Case Stud.* **2010**, *2*, 16–33.

© 2020 by the authors. Licensee MDPI, Basel, Switzerland. This article is an open access article distributed under the terms and conditions of the Creative Commons Attribution (CC BY) license (http://creativecommons.org/licenses/by/4.0/).

Journal of
Marine Science and Engineering

MDPI

Article

Real-Time Wave Excitation Forces Estimation: An Application on the ISWEC Device

Mauro Bonfanti [1,*], Andrew Hillis [2], Sergej Antonello Sirigu [1], Panagiotis Dafnakis [1], Giovanni Bracco [1], Giuliana Mattiazzo [1] and Andrew Plummer [2]

[1] Marine Offshore Renewable Energy Lab (MOREnergy Lab), DIMEAS, Politecnico di Torino, Corso Duca degli Abruzzi 24, 10129 Turin, Italy; sergej.sirigu@polito.it (S.A.S.); panagiotis.dafnakis@polito.it (P.D.); giovanni.bracco@polito.it (G.B.); giuliana.mattiazzo@polito.it (G.M.)

[2] Department of Mechanical Engineering, University of Bath, Bath 44210, UK; a.j.hillis@bath.ac.uk (A.H.); A.R.Plummer@bath.ac.uk (A.P.)

* Correspondence: mauro.bonfanti@polito.it; Tel.: +39-01-1090-5921

Received: 3 October 2020; Accepted: 19 October 2020; Published: 21 October 2020

Abstract: Optimal control strategies represent a widespread solution to increase the extracted energy of a Wave Energy Converter (WEC). The aim is to bring the WEC into resonance enhancing the produced power without compromising its reliability and durability. Most of the control algorithms proposed in literature require for the knowledge of the Wave Excitation Force (WEF) generated from the incoming wave field. In practice, WEFs are unknown, and an estimate must be used. This paper investigates the WEF estimation of a non-linear WEC. A model-based and a model-free approach are proposed. First, a Kalman Filter (KF) is implemented considering the WEC linear model and the WEF modelled as an unknown state to be estimated. Second, a feedforward Neural Network (NN) is applied to map the WEC dynamics to the WEF by training the network through a supervised learning algorithm. Both methods are tested for a wide range of irregular sea-states showing promising results in terms of estimation accuracy. Sensitivity and robustness analyses are performed to investigate the estimation error in presence of un-modelled phenomena, model errors and measurement noise.

Keywords: Kalman Filter; Neural Network; wave excitation forces; estimation; Optimal Control; Wave Energy Converter

1. Introduction

Among the different renewable sources, ocean waves represent one of the most powerful and in the last few decades have been widely investigated. Despite this, wave energy remains a relatively untapped resource. The application of Wave Energy Converter (WEC) systems to such irregular sources requires a robust control logic capable of maximizing the extracted energy with acceptable efficiencies. At present, the Optimal Control problem represents an active area of research. The work of [1] reports a comprehensive review of the advances in Optimal Control, Model Predictive Control (MPC) and MPC-like techniques applied to the wave energy field. Within the context of Optimal Control, accurate knowledge about the future Wave Excitation Force (WEF) is essential to compute the optimal control signal. In literature, several approaches have been proposed to address the problem of the WEF estimation with promising results. An exhaustive classification and comparison of several estimation techniques is presented in the work of [2]. Some examples are cited hereafter. In [3,4] a Kalman Filter (KF) observer is employed on a linear Point-Absorber (PA) WEC. It is assumed that the WEF can be modelled as a linear superposition of fixed and finite harmonic components. Similarly, In [5] the wave force estimation and prediction problem for arrays of WECs is approached , comparing both global and independent estimators and forecasters. In the work of [6] two approaches are presented: the first approach is based on a KF coupled with a random-walk model of the WEF; the second performs a

receding horizon—unknown input estimation. In [7] a modified form of the well-known Fast Adaptive actuator Fault Estimation called Fast Adaptive Unknown Input Estimation (FAUIE) is applied to a non-linear PA. In [8] is studied a direct approach by measuring the pressures at discrete points on the buoy surface, in addition to the buoy heave position, to obtain the estimation of the WEF by an Extended Kalman Filter (EKF). Finally, In [9] studied the WEF estimation of WaveSub (by Marine Power Systems Ltd. (Swansea, England)), a multiple Degree of Freedom (DoF) non-linear WEC. The estimation problem is tackled with a stochastic and a periodic KF, using only quantities which are measurable in practice. A model-free approach is proposed by [10] emoploying a Neural Network (NN) framework to estimate the WEF on a PA. Similarly, In [11] is studied the estimation of the wave elevation using the measurements from a nearby buoy employing a Non-linear AutoRegressive with eXogenous input network (NARX). All the mentioned studies are promising in terms of estimation performances and robustness of the observer. However, most of the work cited refer to single Degree of Freedom (DoF) WECs and few studies on non-linear multiple DoF systems have been conduced so far.

The aim of this work is to estimate the WEFs on a non-linear three Degrees of Freedom (3-DoF) WEC using only readily measureable quantities to perform the estimation. The study is applied to the Inertial Sea Wave Energy Converter (ISWEC) device designed for the Mediterranean Sea. In this context, three different approaches have been applied to the ISWEC device in previous works. In [12] is built an unknown state observer with a second order augmented state space representation of the ISWEC for the estimation of the pitch excitation torque. The gain of the observer has been found with an LQR optimization. In [13] is presented a method to estimate the sea state Power Spectral Density (PSD) of the wave climate by using the device motion. The heave motion measurements are used to estimate the PSD of the incoming wave and the results compared with the wave PSD measured by a wave measurement system. Then, in [14] a feedforward NN is proposed to relate the ISWEC motion to the WEFs acting on surge, heave and pitch DoFs. In the current study two approaches are applied to the non-linear 3-DoF model of the ISWEC to estimate the WEFs acting on surge, heave and pitch DoFs:

1. Model-Based approach: a KF observer modelling the WEF as an unknown input with a harmonic nature. This estimation framework is studied in [3,4] and named Kalman Filter with Harmonic Oscillator (KFHO) in [2];
2. Model-Free approach: a feedforward NN to relate the ISWEC motion and gyroscopic reaction to the WEFs. The same approach reported in [14] is considered.

The main challenges lie in considering a non-linear 3-DoF model of the WEC and estimate the WEFs along three degrees of motion. In the KF context, tuning the system for the best performance in presence of measurement noise is crucial as well as identifying un-modelled phenomena and decoupling them from the signal to be estimated. Moreover, since the ISWEC device is slack-moored to the seabed, an accurate acquisition of the absolute displacements of the WEC is not trivial; in this context, measurement errors of the absolute diplacement could affect the estimation performances. For what concerns the NN, it is key to assess both the ability to estimate data that are not considered in the training process and the accuracy in presence of model uncertanities. The aim is to use the minimum amount of measurements to model the unknown exctitation forces in respect to the ISWEC kinematic. Outcomes of this investigation are the estimators performances in different irregular sea-states and different measurement frameworks in presence of sensors noises and plant uncertainties. The results of the 3-DoF KF estimator and the NN model are compared for different sensors framework in order to analyse the influence of the measurements available. Then, measurements noises and variations of the main plant parameters are introduced. Numerical simulations under different irregular sea conditions aim to compare the estimation results of the two approaches as well as the sensitivity to changes in the plant parameters relative to the case study presented. The novelty of this work is to perform an excitation force estimation for a 3-DoF non-linear WEC decoupling the mooring forces or, more in general, undesired phenomena that will appear in real operating condition. Moreover, the NN

represents a novel framework to address the wave extitation force estimation problem, able to handle strong non-linearities. In the NN context, there are very few examples of application to a multi-DOF non-linear WEC system in literature. Finally, investigating the influence of available sensors constitutes a key aspect of this work, which aims to highlight the importance of having reliable measurements in the context of WEF estimation.

This paper is organized as follows. First, in Section 2 the ISWEC architecture is described together with the non-linear 3-DoF time domain model. Second, Section 3 presents the linear 3-DoF ISWEC model in conjunction with the KF formulation used to estimate the WEFs. Section 4 describes the NN approach to estimate the WEFs as well as the network architecture. In Section 5 the parameters of both KF and NN are tuned considering the operating conditions of the ISWEC. Then, in Section 6, the numerical results are presented and discussed. Strengths and weaknesses of each method are compared and numerical experiments are used to assess estimation accuracy, robustness to different wave conditions, sensor noises and sensitivity to model errors. Finally, Section 7 presents conclusions and future works.

2. ISWEC Device

The ISWEC system has been considered as the case study in this paper. The first concept is dated 2005, conceived by the renewable group of the Department of Mechanical and Aerospace Engineering of the Politecnico di Torino (Italy). In 2012, a 1:8 prototype was realized and tested at INSEAN wave tank in Rome, crucial to draw the main guidelines for the ISWEC design. In 2012, the design of a 60 kW rated power ISWEC full-scale prototype (shown in Figure 1) started and the device has been installed in Pantelleria island (Sicily, Italy) in Summer 2015. The project aimed to evaluate the device energy production capabilities and efficiency. In 2018, a new collaboration with the Italian company Eni S.p.a. led to the construction of a second full-scale prototype in the early 2019, installed in the Adriatic Sea (Italy). This second full-scale prototype maintains the architecture and operating principle of the Pantelleria device. The development of more accurate numerical models together with ad hoc optimization algorithms validated and supported by the experimental data of the Pantelleria device enabled efficiency and reliability improvements to the overall device. In this section the device working principle and the non-linear 3-DoF numerical model refer to the prototype installed in Adriatic Sea.

(**a**) (**b**)

Figure 1. ISWEC device installed in Pantelleria island (Sicily, Italy): (**a**) ISWEC Pantelleria hull; (**b**) ISWEC Pantelleria gyroscope.

2.1. ISWEC Working Principle

The major disadvantage of PA-like devices is that they harness wave energy damping directly from the motion of an oscillating buoy, exploiting the relative motion of mechanical parts in contact with the harsh marine environment. The idea of the ISWEC is to harvest wave energy damping from the floater motion through a gyroscope system which is protected within the hull, reducing the risk of corrosion and biofouling, with consequent increase of reliability. Morevoer, also the power

conversion and conditioning systems are completely enclosed into the floater. The only part that have continuity from the inside out is the electric cable, following the idea of a "deploy and plug" device [15]. A schematic representation of the device concept is shown in Figure 2. It consists of a sealed hull carrying inside two gyroscopic units. The power conversion principle relies on the gyroscopic effect that converts the pitching angular motion of the hull into an inner precession oscillation of the gyroscopes. ISWEC is a directional WEC since, in normal working conditions, it is able to align itself with the wave direction. As shown in Figure 2b, the gyroscope is composed of a spinning flywheel that rotates around the z_1 axis with a speed $\dot{\varphi}$. The flywheel is supported by a frame that allows the rotation of the gyroscope around its precession axis x_1. The precession motion is excited through the dynamic coupling between the hull motion around the y_1 axis and the flywheel angular velocity around the z_1 axis. A mechanical gearbox and an electrical generator, connected to the gyroscopic frame, compose the electrical Power Take-Off (PTO). Two electrical generators extract electricity acting as a linear damper braking the precession motion of the gyroscope. Notwithstanding the energy required to keep the flywheel in rotation, the possibility to regulate its speed along with the tuning of the PTO torque allows the adaptation of the natural resonant frequency of the system to the incoming wave. An accurate description of the internal components and their working principle can be found in the works of [15–17].

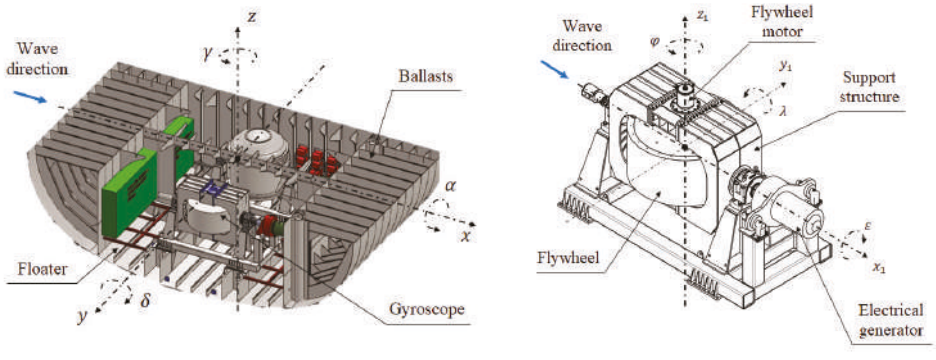

(a) (b)

Figure 2. ISWEC device: architectures. (**a**) ISWEC hull; (**b**) ISWEC gyroscope.

2.2. ISWEC Non-Linear Time Domain Model

The ISWEC mathematical model is obtained by coupling the hull hydrodynamics and the gyroscope dynamics. The non-linear system equations have been implemented in the MATLAB®/Simulink® environment employing the Simscape™ Multibody™ toolbox, which is particularly suitable for multi-physics system modelling. The derivation and the experimental validation of the model equations of the complete system is not within the scope of this work and details can be found in the studies of [18–21].

WEC modelling is the major area of interest within the field of Wave Energy. Multitudes of WEC models are proposed in literature with different levels of confidence and uncertainties [22,23]. In this work, the fluid-structure interaction model is based on linear potential flow theory under the assumptions of irrotational flow, inviscid and incompressible fluid, harmonic oscillations of the hull for each DoF and zero-forward-speed conditions [24]. Then, according to the well-known Cummins' equation [25], the dynamic behaviour of a floating body can be derived in the time domain. Some non-linear effects are considered: the non-linear viscous forces, the drift forces in the surge direction, the mooring action and the gyroscopic reaction on the hull. As stated in the previous paragraph, the ISWEC device extracts energy from the sea exploiting only the motion around the pitch axis. Moreover, the hull is symmetrical with respect to its longitudinal and transversal

plane. Under these assumptions, a planar 3-DoF model of the hull has been considered in this work. The reference plane is identified by the vertical gravity axis z and the horizontal direction of the incoming wave x as shown in Figure 2a. Let $X_f(t) \in \mathbb{R}^{n_D}$ be the vector containing the n_D DoFs of the hull:

$$X_f(t) = \begin{bmatrix} x(t) & z(t) & \delta(t) \end{bmatrix}^T \tag{1}$$

Then, $\dot{X}_f(t) \in \mathbb{R}^{n_D}$ and $\ddot{X}_f(t) \in \mathbb{R}^{n_D}$ are the first- and second-time derivative of X_f respectively. In a planar reference frame, $x(t)$ represents the surge motion, $z(t)$ the heave motion and $\delta(t)$ the pitch motion. Following the notation of Equation (1), the time-domain equation of the hull dynamics can be written as follows:

$$M\ddot{X}_f(t) + F_r(t) + F_\beta(t) + KX_f(t) = F_w(t) + F_d(t) + F_m(t) + F_g(t) \tag{2}$$

where $M \in \mathbb{R}^{n_D \times n_D}$ is the mass matrix including the added mass contribution evaluated for infinite oscillation frequency, $F_r(t) \in \mathbb{R}^{n_D}$ are the radiation forces, $F_\beta(t) \in \mathbb{R}^{n_D}$ the non-linear viscous forces, $K \in \mathbb{R}^{n_D \times n_D}$ the linear hydrostatic stiffness, $F_w(t) \in \mathbb{R}^{n_D}$ the wave exctitation forces, $F_d(t) \in \mathbb{R}^{n_D}$ the non-linear wave drift forces, $F_m(t) \in \mathbb{R}^{n_D}$ the mooring line actions and $F_g(t) \in \mathbb{R}^{n_D}$ the gyroscopic reactions on the hull. For the sake of clarity, the subscripts x, z and δ will be used in the next sections to specify the DoF to which the force or parameters refer and the subscript j to indicate the j-th DoF.

2.2.1. Radiation Convolution Term

The radiation forces arise from the motion of the hull through the water that results in inertia and friction components. These contributions can be obtained by solving the convolution integral of the impulse response function $h_r(t)$ [26]:

$$F_r(t) = \int_0^t h_r(t-\tau)\dot{X}_f(\tau)d\tau \tag{3}$$

As the computation of the convolution integral can be very time consuming, it is convenient to express this term with a state-space representation:

$$\begin{aligned} \dot{\zeta}(t) &= A_r\zeta(t) + B_r\dot{X}_f(t) \\ F_r(t) &= C_r\zeta(t) + D_r\dot{X}_f(t) \end{aligned} \tag{4}$$

The vector $\zeta(t) \in \mathbb{R}^{n_R}$ represents the state vector that approximates the radiation force contributions and n_R is the approximation order. The state space matrices $A_r \in \mathbb{R}^{n_R \times n_R}$, $B_r \in \mathbb{R}^{n_R \times n_D}$, $C_r \in \mathbb{R}^{n_D \times n_R}$ and $D_r \in \mathbb{R}^{n_D \times n_D}$ have been identified following the well-known Perez and Fossen and approach [26,27].

2.2.2. Non-Linear Viscous Forces

For evaluating the non-linear viscous forces F_β, [28] proposed a method for the identification of the viscous force for the pitch DoF:

$$F_{\beta\delta}(t) = \beta\dot{\delta}(t)|\dot{\delta}(t)| \tag{5}$$

The method relies on a full CFD approach through which a pitch free decay test is simulated. Once the time series is obtained, it is possible to identify the viscous damping coefficient β with two different methodologies: computing the viscous damping coefficients through the logarithmic decrement method and/or integrating the Cummins' equation of motion fitting the damping coefficients that minimize the difference with CFD results. In the surge direction, The work of [29] evaluated the viscous force according to the drag force contribution of the Morison equation, assuming the hypothesis of low forward speed:

$$F_{\beta x} = \frac{1}{2}\rho C_d A \dot{x}(t)|\dot{x}(t)| \tag{6}$$

In Equation (6), ρ represents the water density, C_d the drag coefficient and A the wetted area of the hull. The drag coefficient formulation can be found in literature for simple geometries. The viscous damping in the heave direction is not considered since the hull motion along the vertical axis does not contribute to the power extraction in this WEC. Moreover, it is decoupled for the surge and pitch DoFs due to the symmetry of the hull on the transversal plane.

2.2.3. Drift Forces

The drift force is required in order to describe properly the hydrodynamic behaviour of the hull along the surge DoF. The derivation of this action for the ISWEC device can be found in the work of [29]. Here the time series of wave drift force for irregular sea state were derived through the Newman approximation [30]:

$$F_{dx}(t) = 2\left(\sum_{h=1}^{W} \eta_h \sqrt{f_d(\omega_h)} cos(\omega_h t + \theta_h)\right)^2 \tag{7}$$

where the subscript h indicates the h-th harmonic component of the wave spectrum, W is the number of frequencies of the spectrum discretization, η_h the harmonic amplitude of the wave spectrum, $f_d(\omega_h)$ the drift force coefficient for each frequency component ω_h of the wave spectrum and θ_h the phase angle.

2.2.4. Mooring System

The mooring system is modelled through a quasi-static approach following the formulation proposed by [29]. The static equilibrium of the system is studied by varying the x coordinate and the z coordinate of the connection point of the mooring to the hull. Then, computing the equilibrium condition of the mooring line for all the different possible positions of the device, the mooring tensions are identified. In the numerical model, F_m is obtained with MATLAB® look-up tables that map the mooring forces in respect to the hull planar motion. As shown in Figure 3, the ISWEC mooring system consists of a slack catenary type with multiple mooring lines, jumpers and clump-weights. Two bridles connect the hull to a central joint to prevent the roll motion of the device. To guarantee the weather-vaning of the device in respect to the wave direction, the mooring connection points are placed towards the bow, with respect to the centre of gravity of the device. On each catenary, a sub-surface buoy and clump-weight are installed to enhance the elastic recall of the system and avoid snatches [31].

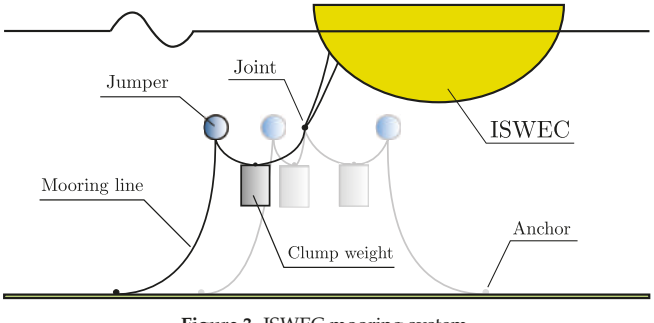

Figure 3. ISWEC mooring system.

2.2.5. Gyroscope Reactions

The gyroscope dynamics can be described through the Newton's law and derived from the conservation of the flywheel angular momentum. The non-linear numerical model considers all the contributions of the gyroscope reaction along the x, z and δ DoFs. Through a linearization of the angular momentum of the gyroscope around the y_1 axis, the expression of the gyroscopic reaction discharged on the pitch DoF of the hull can be determined [32]:

$$F_{g\delta}(t) = J\dot{\varphi}\dot{\varepsilon}(t)cos(\varepsilon(t)) \tag{8}$$

where J is the flywheel moment of inertia, and $\dot{\varepsilon}(t)$ and $\varepsilon(t)$ are the gyroscope speed and angular position around the precession axis y_1, respectively. This torque acts on the pitch axis representing the third component of the F_g term in Equation (2). In this work, the gyroscope reaction is considered as a known input of both KF and NN as it can be computed through the measurements of the gyroscope kinematics. The complete derivation of the gyroscope dynamic equation can be found in [32].

2.2.6. Wave Excitation Force Modelling

The linear wave theory describes the irregular water surface as superposition of harmonic waves with different frequencies, phases and directions [33,34]. In this work, only unidirectional waves are considered since the ISWEC device is described only in its longitudial plane. Then, the wave signal can be approximated through a Fourier series of any arbitrary number N of harmonic wave components [35]:

$$\eta(t) = \sum_{n=1}^{N} A_n cos(\omega_n t + \alpha_n) \tag{9}$$

where A_n is the amplitude, ω_n the angular frequency and α_n the n-th phase associated with the n-th harmonic. Traditionally, Power Spectral Densities (PSD) of real waves are modelled analytically and parametrized according to their spectral properties. In literature, different analytical PSD functions are proposed. Given the wave spetrum, the amplitude of the sinusoidal n-th wave component of $\eta(t)$ is obtained by the following relation [35]:

$$\eta_n = \sqrt{2S_{\eta\eta}(\omega_n)\Delta\omega} \tag{10}$$

where $\Delta\omega$ is the PSD frequency resolution and $S_{\eta\eta}$ is the value of spectral energy density. Therefore, the WEF associated to the j-th DoF can be calculated given the geometry of the floater and sea-state characteristics [36]:

$$F_{wj}(t) = \sum_{n=1}^{N} |f_j(\omega_n)|\eta_n cos(\omega_n t + \theta_n + \angle f_j(\omega_n)) \tag{11}$$

where $f_j(\omega_n)$ is the Froude-Krylov and diffraction coefficient associated to the j-th DoF and the n-th wave frequency. In this work, the Joint North Sea Wave Project (JONSWAP) spectrum [37] is considered to define 35 different irregular sea-states to evaluate the estimation performances. However, only four sea-states are employed to tune the KF and NN models according to the operating conditions of the ISWEC device. The JONSWAP spectrum can be identified using three parameters: Significant wave Height (H_s), Energy Period (T_e) and Peak Shape (γ). These spectral parameters are reported in Table 1 for each sea-states used for the tuning process, sorted in ascending order of wave Power density (P_d).

Figure 4 gives a qualitative representation of annual wave energy of the sea-states considered. Data refer to a typical annual distribution of the wave energy in the Adriatic Sea (Italy) acquired during an experimental campaign started in 2018. The data are normalized on their maximum value. The squared blue marker represents the four waves used for the tuning process.

Table 1. Tuning wave data.

Id	T_e(s)	H_s(m)	γ	P_d(kW/m)
1	4.00	0.75	3.30	1.10
2	5.00	1.25	3.30	3.83
3	5.85	1.75	3.30	8.87
4	6.75	2.25	3.30	16.74

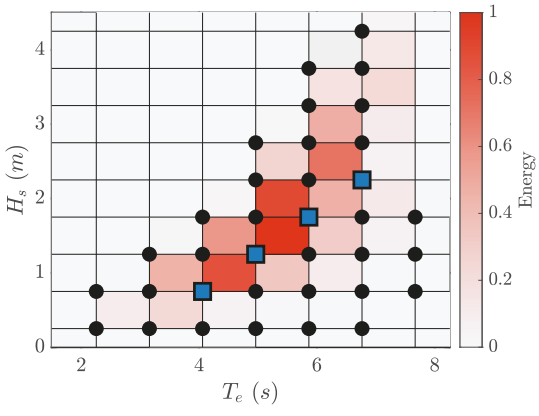

Figure 4. Normalized annual wave energy of the 35 irregular sea-states, indicated with black dots and squares.

2.2.7. Sensor and Acquisition System Model

The ISWEC device installed in the Adriatic Sea is equipped with a Data AcQuisition (DAQ) system to record experimental signals of the physical quantities of interest. The motion of the three DoFs of interest of the hull has to be acquired. Moreover, to complete the estimation the precession motion of the gyroscope as well as the flywheel speed are required. The linear accelerations, angular orientations and rates of the hull are provided by an Inertial Unit of Measurement (IMU) Xsens MTi-30 AHRS [38] fixed inside the floater. The sensor is rigidly fixed inside the hull, appropriately oriented in respect to the hull reference system. An internal data processor uses the velocity and orientation increments and, through a strapdown integration algorithm, gives in output the orientations on the three rotational DoFs. The measurements considered from the IMU are: the linear acceleration along the surge and heave directions ($\ddot{x}(t)$ and $\ddot{z}(t)$), the angular position and velocity of the hull ($\delta(t)$ and $\dot{\delta}(t)$). Two digital encoders Heidenhain Ecn 413 [39] are mounted on the gyroscope and flywheel shaft, respectively. The measurements available from the encoders used for computing the gyroscope reaction $F_g(t)$ are: the flywheel speed ($\dot{\varphi}(t)$), the angular position and speed of the gyroscope ($\varepsilon(t)$ and $\dot{\varepsilon}(t)$). The data acquisition is managed by a National Instrument compactRIO NI cRIO-9030 [40] which is a dual core 1.33 GHz real time control unit. These sensors and hardware, together with temperature, umidity, voltage and current measurements compose the actual ISWEC DAQ.

Unlike the majority of PA type WECs, the ISWEC device is slack-moored to the seabed and a precise measure of its absolute position is not trivial. In this context, a Differencial GPS (DGPS) is considered to acquire the position and elevation of the WEC. The differential positioning technique enhance the GPS position accuracy of geo-location by comparing their data with those recorded in the same time interval by other multiple GPS receivers. The measurements given by the DGPS are: the position $x(t)$ and the elevation $z(t)$. The measures of IMU and DGPS can be combined to perform the well-known sensor fusion technique [41,42]. Sensor fusion represents a foundamental part of localization and position tracking and can be applied to estimate the absolute positions and

velocities with high accuracy. In this context, Motion Reference Units (MRU) are meant for measuring positions, velocities, accelerations, angular rates and orientations representing an all-in-one solution for acquiring the WEC motion. The MRU are more precise than IMU units and returns absolute positions and velocities relative to a specified equilibrium point. These sensors are employed in modern navigation systems and dynamic positioning applications. The measurements available from the MRU are: the positions ($x(t)$ and $z(t)$), velocities ($\dot{x}(t)$ and $\dot{z}(t)$) and acceleration ($\ddot{x}(t)$ and $\ddot{z}(t)$) along the surge and heave directions, the angular position and velocity of the hull ($\delta(t)$ and $\dot{\delta}(t)$). Table 2 reasumes all the frameworks considered in this work and their noise standard deviations σ.

Table 2. Measurement frameworks available. Four cases are considered: Full Measurement (FM), Motion Reference Unit (MRU), Inertial Measurement Unit with Differencial GPS (IMU+DGPS) and Inertial Measurement Unit (IMU).

Measures	FM	MRU		IMU+DGPS		IMU	
	Data	Data	σ	Data	σ	Data	σ
x (m)	•	○	0.05	○	0.5	–	–
$\dot{x}$ (m/s)	•	○	0.03	–	–	–	–
$\ddot{x}$ (m/s^2)	•	○	0.001	○	0.01	○	0.01
z (m)	•	○	0.05	○	0.5	–	–
$\dot{z}$ (m/s)	•	○	0.03	–	–	–	–
$\ddot{z}$ (m/s^2)	•	○	0.001	○	0.01	○	0.01
δ (rad)	•	○	5×10^{-4}	○	0.01	○	0.01
$\dot{\delta}$ (rad/s)	•	○	10^{-4}	○	0.002	○	0.002
ε (rad)	•	○	0.02	○	0.02	○	0.02
$\dot{\varepsilon}$ (rad/s)	•	○	0.001	○	0.001	○	0.001
$\dot{\varphi}$ (rad/s)	•	○	0.001	○	0.001	○	0.001

The Full Measurements (FM) configuration represent an ideal measurement framework in which all measures are available. Filled black dots in Table 2 indicates that the FM framework considers measurements without noise. This framework is the referance case where maximum estimation performances are expected. The angular acceleration along the pitch DoF $\ddot{\delta}(t)$ is not considered since none of the available sensors provide it. Encoders data are considered available for all the configurations. It is worth pointing out that missing measurements in IMU+DGPS and IMU frameworks can be obtained by numerical derivation/integration of position, velocity and acceleration signals. However, in this work, only raw measurements obtained directly from the sensors are considered.

2.3. ISWEC Model Block Diagram

The block diagram of the ISWEC plant is shown in Figure 5. The input of the system are the *Wave Excitation Force* $F_w(t)$ and the *Wave Drift Fore* $F_d(t)$. First, the Equation (2) is integrated inside the block *Hull*. The output of this block are the hull positions $X_f(t)$, velocities $\dot{X}_f(t)$ and accelerations $\ddot{X}_f(t)$ that represent the input of the *Gyroscope* block. Here the dynamic equation of the gyroscope is solved computing the gyroscope motion $\varepsilon(t)$ and $\dot{\varepsilon}(t)$ around the precession axis and the gyroscope reaction $F_g(t)$ that is feedback to the *Hull*. The *Mooring* block computes the recall $F_m(t)$ in respect to the hull position $X_f(t)$. Then, the block *Power Take-Off* computes the generator torque $T_\varepsilon(t)$ and sends feedbacks back to the *Gyroscope*. The control algorithm implemented by the *Power Take-Off* is described in detail in [15]. The motion of the hull is acquired through the *IMU* [38] and the gyorscope and flywheel angular speeds with two *Encoders* [39]. The measurements are tainted with noise $w_{IMU}(t)$ and $w_E(t)$ and sampled at 10 Hz with the cRIO unit [40] to obtain the discrete data with pedix d.

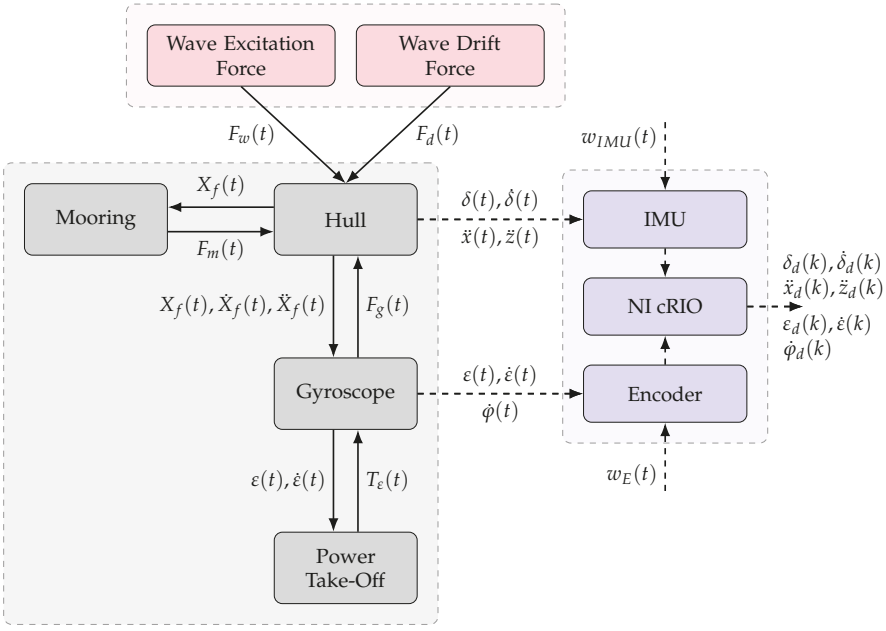

Figure 5. ISWEC device block diagram. Forces and motions in continuos line, signals and disturbances in dashed line.

3. Wave Excitation Force Estimation with Kalman Filter

One solution to estimate the WEF could be measuring directly the pressure acting on the wetted surface of the hull [8]. However, this method could be expensive as it requires a large number of sensors. Furthermore, since the pressure measured on the wetted surface is the combination of all the hydrodynamics forces it could be challenging to distinguish the contribution of the WEF. Another method relies on the measurement of the hull dynamics and an estimation is performed. The KF is ubiquitous in many applications to estimate the current state of a linear dynamic system from a set of measurements affected by uncorrelated Gaussian noise with known covariance. Under these assumptions, this estimator is defined as optimal because it estimates the system states minimizing the covariance of the estimation error. In this work, the estimation procedure is carried out by modelling the WEF as an unknown state to be estimated [4]. In order to obtain the KF formulation the Equation (2) is taken into account. First, the non-linear model is simplified considering the drift forces included into the $F_{wx}(t)$ contribution. The viscous damping along the pitch direction is linearized and the surge damping action is neglected in order to obtain a 3-DoF linear state space model. Then, the state space model of the ISWEC is discretized in the time domain to derive the KF formulation. The mooring forces are identified and the filter is designed to decouple them from the WEF. These steps are described in detail in the following sub-sections.

3.1. Linear 3-DoF ISWEC Model

The non-linear model described in the previous chapter is simplified to achieve a compromise between the computational effort required to solve the KF algorithm and the accuracy of the estimation. The non-linear viscous force along the pitch DoF defined by Equation (5) has to be linearized for inclusion in the estimation process. Four simulations are performed in four different sea-states using the non-linear 3-DoF numerical model and wave data of Table 1. The pitching rate amplitude time series is extracted and its mean is computed for each simulation. The mean is substituted into Equation (5) and β_{lin} is defined as the product between the viscous damping β and the mean pitching amplitude:

$$F_{\beta\delta}(t) \cong \beta\dot{\bar{\delta}}\dot{\delta}(t) = \beta_{lin}\dot{\delta}(t) \tag{12}$$

For the surge direction, Figure 6 demonstrates that the viscous force along the surge DoF can be neglected in respect to the WEF.

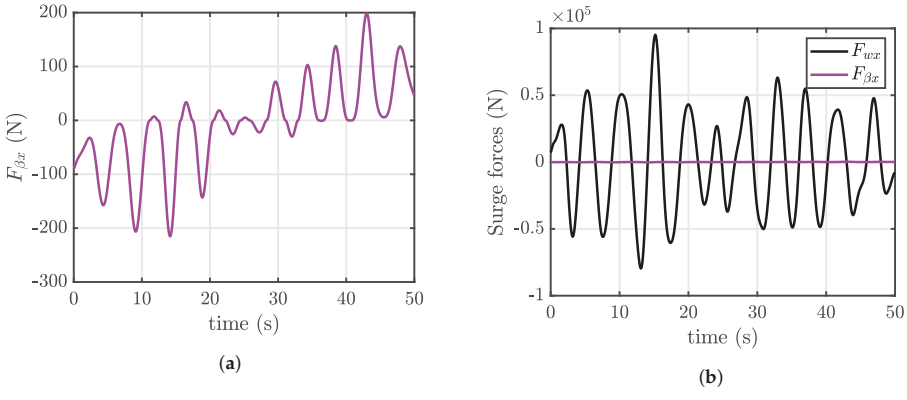

Figure 6. Viscous damping in surge direction magnitude (**a**) and comparison with WEF (**b**) (Wave Id 2). (**a**) Viscous damping in surge direction; (**b**) WEF and viscous damping in surge direction comparison.

The term $F_\beta(t)$ can be rewritten as:

$$F_\beta(t) \cong \begin{bmatrix} 0 & 0 & 0 \\ 0 & 0 & 0 \\ 0 & 0 & \beta_{lin} \end{bmatrix} \dot{X}_f(t) = B_v\dot{X}_f(t) \tag{13}$$

Substituting the Equation (13) in (2), Equation (2) can be expressed by the following linear continuous-time state-space model:

$$\begin{aligned} \dot{X}(t) &= AX(t) + BF_g(t) + B[F_w(t) + F_m(t)] \\ Y(t) &= CX(t) + DF_g(t) + D[F_w(t) + F_m(t)] \end{aligned} \tag{14}$$

where $X(t) \in \mathbb{R}^{n_S}$ and $Y(t) \in \mathbb{R}^{m_S}$ are the states and measurements vectors defined as:

$$\begin{aligned} X(t) &= \begin{bmatrix} X_f(t) & \dot{X}_f(t) & \zeta \end{bmatrix}^T \\ Y(t) &= \begin{bmatrix} X_f(t) & \dot{X}_f(t) & \ddot{X}_f(t) \end{bmatrix}^T \end{aligned} \tag{15}$$

$A \in \mathbb{R}^{n_S \times n_S}$, $B \in \mathbb{R}^{n_S \times n_D}$, $C \in \mathbb{R}^{m_S \times n_S}$ and $D \in \mathbb{R}^{m_S \times n_D}$ are given by:

$$\begin{aligned} A &= \begin{bmatrix} 0 & I & 0 \\ -KM^{-1} & -B_vM^{-1} & -C_rM^{-1} \\ 0 & B_r & A_r \end{bmatrix}, \quad B = \begin{bmatrix} 0 \\ M^{-1} \\ 0 \end{bmatrix} \\ C &= \begin{bmatrix} I & 0 & 0 \\ 0 & I & 0 \\ -KM^{-1} & -B_vM^{-1} & -C_rM^{-1} \end{bmatrix}, \quad D = \begin{bmatrix} 0 \\ 0 \\ M^{-1} \end{bmatrix} \end{aligned} \tag{16}$$

Here, $n_S = 2n_D + n_R$ is the number of states, m_S the number of outputs, I and 0 stands for identity and zero matrices according to the problem dimensions. The system (14) represents the most

general framework for a linear multi-DoF WEC model. It can be noted that, without loss of generality, gyroscope reaction $F_g(t)$ is the controlled input (e.g., the PTO action), the WEFs $F_w(t)$ the exogenous input to be estimated and the mooring forces $F_m(t)$ could be interpreted as an unknown unmodelled phenomena to be decoupled from the $F_w(t)$ estimation. The outputs of the linear model (14) are position, velocity and acceleration of the WEC body resulting in a FM configuration. However, matrices C and D can be chosen according to the measurements available on the system as well as the requirements of the observer as defined in Table 2.

3.2. Kalman Filter Problem Statement

In this work it is assumed that the excitation force $F_w(t)$ has a harmonic nature and it can be described as a linear combination of different wave components with a finite number of frequencies n_W [2–4]. In this form, the WEF can be included into the state vector as an unknown state. In Equation (14) the mooring forces are considered as a unmodelled phenomena. In real applications, it would be difficult to directly measure the action of the moorings so they are included into the state vector as unknow states to be estimate. The ISWEC mooring system is designed to minimize the impact on the pitching motion of the device, appointed to the power conversion chain [31]. As demonstrated in Figure 7b, the mooring forces have a very slow dynamics such as the surge component and a constant load in heave and pitch directions compared to the WEF. In normal working conditions, snatch loads do not appear, and the mooring forces have mainly the behaviour as shown in Figure 7a. $F_m(t)$ is synthesised using the same method that was detailed for $F_w(t)$, using a harmonic model to describe its behaviour. For the sake of simplicity, the mooring forces are modelled with only one frequency for each component representing their main spectral nature.

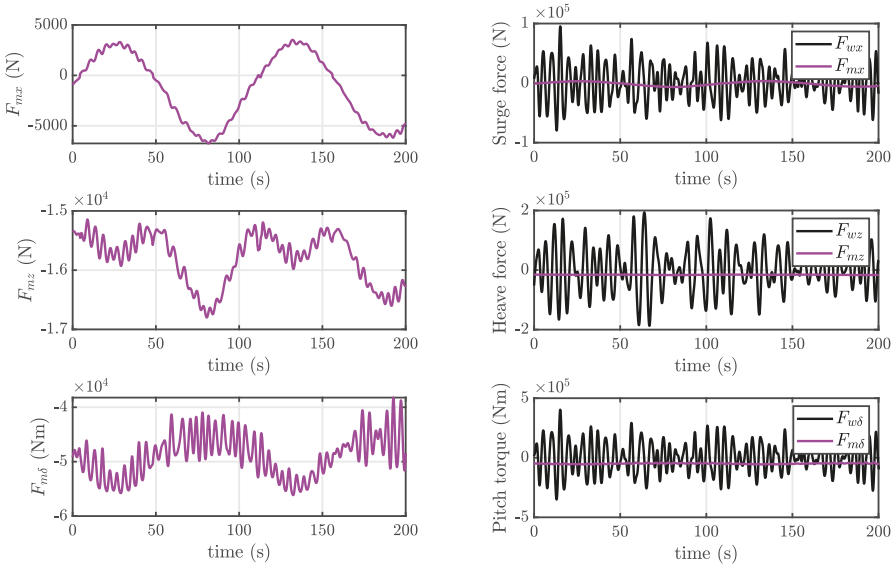

Figure 7. Mooring forces magnitude (**a**) and comparison with WEFs (**b**) (Wave Id 2). (**a**) Mooring forces; (**b**) WEFs and mooring forces comparison.

Under these assumptions the state vector $X(t)$ is augmented including the estimation of $F_w(t)$ and $F_m(t)$ and the System (14) is re-written:

$$\begin{aligned} \dot{X}_a(t) &= A_a X_a(t) + B_a F_g(t) \\ Y(t) &= C_a X_a(t) + D_a F_g(t) \end{aligned} \tag{17}$$

where $X_a(t) \in \mathbb{R}^{n_F}$ is the augmented state vector defined as:

$$X_a(t) = \begin{bmatrix} X(t) & \hat{F}(t) & \dot{\hat{F}}(t) \end{bmatrix}^T \tag{18}$$

Here $n_F = n_S + 2n_D(n_W + 1)$ is the augmented state vector dimension. $\hat{F} \in \mathbb{R}^{n_D \times (n_W+1)}$ is the unknown force to be estimated:

$$\hat{F}(t) = \begin{bmatrix} \hat{F}_x(t) & \hat{F}_z(t) & \hat{F}_\delta(t) \end{bmatrix}^T \tag{19}$$

The j-th compoenent of the estimated force is given by the WEF harmonics and the mooring force as follows:

$$\hat{F}_j(t) = \begin{bmatrix} \hat{F}_{wj_1}(t) & \hat{F}_{wj_2}(t) & \dots & \hat{F}_{wj_{n_W}}(t) & \hat{F}_{mj}(t) \end{bmatrix}^T \tag{20}$$

Therefore, the estimated $\hat{F}_w(t)$ is obtained by summing up all the harmonic contributions for each of its components:

$$\hat{F}_w(t) = \begin{bmatrix} \sum_{i=1}^{n_W} F_{wx_i}(t) & \sum_{i=1}^{n_W} F_{wz_i}(t) & \sum_{i=1}^{n_W} F_{w\delta_i}(t) \end{bmatrix}^T \tag{21}$$

The augmented matrices $A_a \in \mathbb{R}^{n_F \times n_F}$, $B_a \in \mathbb{R}^{n_F \times n_D}$, $C_a \in \mathbb{R}^{m_S \times n_F}$ and $D_a \in \mathbb{R}^{m_S \times n_D}$ are given by:

$$\begin{aligned} A_a &= \begin{bmatrix} 0 & I & 0 & 0 & 0 \\ -KM^{-1} & -B_v M^{-1} & -C_r M^{-1} & M^{-}1N & 0 \\ 0 & B_r & A_r & 0 & 0 \\ 0 & 0 & 0 & 0 & I \\ 0 & 0 & 0 & -\Omega & 0 \end{bmatrix}, \quad B_a = \begin{bmatrix} 0 \\ M^{-1} \\ 0 \\ 0 \\ 0 \end{bmatrix} \\ C_a &= \begin{bmatrix} I & 0 & 0 & 0 & 0 \\ 0 & I & 0 & 0 & 0 \\ -KM^{-1} & -B_v M^{-1} & -C_r M^{-1} & M^{-}1N & 0 \end{bmatrix}, \quad D_a = \begin{bmatrix} 0 \\ 0 \\ M^{-1} \end{bmatrix} \end{aligned} \tag{22}$$

Again, I and 0 are identity and zero matrices according to the context. $N \in \mathbb{R}^{n_D \times (n_W+1)}$ is defined as:

$$N = \begin{bmatrix} I_{1,n_W+1} & 0 & 0 \\ 0 & I_{1,n_W+1} & 0 \\ 0 & 0 & I_{1,n_W+1} \end{bmatrix} \tag{23}$$

where I_{1,n_W+1} is a $1 \times (n_W + 1)$ vector of ones. $\Omega \in \mathbb{R}^{3(n_W+1) \times 3(n_W+1)}$ is the diagonal matrix with the frequencies identified to approximate the unknown forces along the three DoFs:

$$\Omega = \begin{bmatrix} \Omega_x & 0 & 0 \\ 0 & \Omega_z & 0 \\ 0 & 0 & \Omega_\delta \end{bmatrix} \tag{24}$$

In Equation (24), $\Omega_x \in \mathbb{R}^{(n_W+1) \times (n_W+1)}$, $\Omega_z \in \mathbb{R}^{(n_W+1) \times (n_W+1)}$ and $\Omega_\delta \in \mathbb{R}^{(n_W+1) \times (n_W+1)}$ are diagonal matrices containing the frequencies for unknown force components: